
**Tesis Doctoral**

# FUNDAMENTAL STUDIES OF VIBRATED FLUIDIZED BEDS

Autor
Eduardo Cano Pleite

Director
Antonio Acosta Iborra

DEPARTAMENTO DE INGENIERÍA TÉRMICA Y DE FLUIDOS

Leganés, diciembre 2016


Tesis doctoral

# FUNDAMENTAL STUDIES OF VIBRATED FLUIDIZED BEDS

Autor: Eduardo Cano Pleite

Director de Tesis: Antonio Acosta Iborra

Firma del Tribunal Calificador:

Firma

Presidente
Miguel Menéndez Sastre
Secretario
David J. Pallarès i Tella
Vocal
J. Ruud van Ommen

Calificación:

Leganés, 12 de diciembre de 2016

*En memoria de*
*Justo, Santiago, Francisco e Inma*

DEPARTAMENTO DE INGENIERÍA TÉRMICA Y DE FLUIDOS
Escuela Politécnica Superior

**PhD Thesis**

# FUNDAMENTAL STUDIES OF VIBRATED FLUIDIZED BEDS

Ph.D. Program in Mechanical Engineering and Industrial Organization

Author
Eduardo Cano Pleite

PhD Advisor
Antonio Acosta Iborra

Leganés, December 2016

*The thing that doesn't fit*
*is the thing that's the most interesting:*
*the part that doesn't go*
*according to what you expected.*

Richard P. Feynman

*Terminó su guerra, los pies en la tierra*
*y su mano a un corazón.*
*Su pensar tranquilo, su pena, un olvido*
*y su alma, una pasión.*

Va a escampar. La Vela Puerca

# Preface

The present PhD Thesis was carried out in the Department of Thermal and Fluid Engineering at Carlos III University of Madrid, under the supervision of Prof. Dr. Antonio Acosta Iborra.

This thesis has been partially funded by the Spanish Ministry of Economy and Competitiveness (projects ENE2015/00188/001 and DPI2009-10518), the Autonomous Community of Madrid (Project S2009/ENE-1660) and the Carlos III University of Madrid (beca PIF y ayudas a la movilidad 2014 y 2015).

During the accomplishment of this thesis, two collaboration frameworks were established. During September-December 2014, the author made a research stay in the Department of Applied Chemistry at Kyushu Institute of Technology (Japan), under the supervision of Prof. Dr. Yoshihide Mawatari. During July-September 2015, the author made a research stay in the Laboratory of Energy Science and Engineering at ETH Zürich (Switzerland), under the supervision of Prof. Dr. Christoph R. Müller.

All the results presented in this work were obtained by the author unless otherwise specified.

Eduardo Cano Pleite
Department of Thermal and Fluid Engineering,
Carlos III University of Madrid
December 2016.

# Acknowledgements

I would like to thank the personnel of the research groups of the Department of Applied Chemistry at Kyushu Institute of Technology and of the Laboratory of Energy Science and Engineering at ETH Zürich. In particular, my special thanks go to Prof. Mawatari and Prof. Müller for allowing me to collaborate with their groups. My thanks are extended to Prof. Tsuji for all the fruitful discussions during my stay at ETH.

I am also grateful to all the wonderful people I met at Kitakyushu and Zürich. You made my research stays unforgettable.

# Agradecimientos

Cuando uno se sienta delante del teclado a escribir la sección de agradecimientos, existe un lapso de tiempo en el que se plantea cómo expresar su gratitud a todas aquellas personas que le han acompañado a lo largo de este camino. Tras varios minutos, he llegado a la conclusión de que no hay palabras suficientes para agradecer a Antonio todo lo que ha hecho por mí durante estos años. Gracias por ser un magnífico director, compañero, papi y amigo. No es sólo lo que me has enseñado (que es muchísimo), sino lo que he aprendido de ti, y eso no hay forma de expresarlo con palabras. Muchas gracias también a Fer, porque empezamos con la broma de los hermanitos, pero me ha aconsejado y cuidado (tanto dentro como fuera de la Universidad) como si realmente lo fuera, y para eso tampoco hay palabras que lo puedan agradecer lo suficiente.

Gracias a toda la gente del Departamento con la que he compartido un ratito (algunas veces un ratazo) dentro y fuera de la Universidad. Cafés aparte, todo esto sería mucho menos llevadero sin vosotros. Gracias a Mariano, por tantas y tantas horas de todo un poco y porque sé que le hará ilusion que su nombre aparezca aquí. A Luismi, porque tiene un corazón que no le cabe en el pecho. Gracias también a Antonio S., por su dedicación y por estar siempre dispuesto a echar una mano tanto en lo personal como en lo profesional. Muchas gracias a los técnicos de laboratorio, por su paciencia y esfuerzo en la construcción del lecho. Mención aparte merecen mis compañeros de despacho por aguantarme durante todos estos años, Alberto y, en especial, Dániel. Estos últimos meses me he dado cuenta de que tengo un muy buen compañero dentro del despacho y un gran amigo fuera de él.

No quisiera olvidarme de todos mis compañeros de carrera, amigazos desde el primer día que puse un pie en la Universidad. Gracias a Andŕes, Carlos y Jontxu, por estar ahí día a día. A los Musmen, a los Superlópez, a los viñarockeros, a toda la gente maravillosa que conocí en París y Burdeos y a todos los que han estado a mi lado durante estos años. Gracias a todos por aguantarme a mí y a mis quejas, especialmente durante los últimos meses. Si no fuera por vuestro apoyo no hubiera conseguido esta tesis, así que una buena parte de ella es gracias a vosotros.

A mi familia, que aunque sigan sin saber muy bien lo que hago, siempre están ahí dispuestos a animarme y darme su cariño y su apoyo. A mis padres, por todo. Y si alguien merece palabras de agradecimiento son mis hermanos. Las tres personas a las

que más debo, espejo en el que mirarme y ejemplo del que aprender.

Y de nuevo, otro lapso de tiempo pensando cómo cerrar esta sección de agradecimientos. Vienes tú a mi cabeza, tío, vienes ahora y vienes todos los días. Gracias por todo lo que nos enseñaste. Esta tesis es para ti.

# Resumen

La fluidización es un proceso ampliamente utilizado en las industrias química, energética y de tratamiento de materiales debido a su buen rendimiento en el mezclado de sólidos y a su buena eficiencia de contacto, tanto sólido-sólido como gas-sólido. Entre las operaciones que hacen uso de lechos fluidizados se encuentran, por ejemplo, el craqueo catalítico (FCC), gasificación, combustión de combustibles sólidos, síntesis de Fischer-Tropsch, secado, granulación y recubrimiento de partículas. Sin embargo, la facilidad con la que las partículas fluidizan puede verse afectada por diversos factores. Por ejemplo, las partículas finas tienden a aglomerarse, lo que puede llegar a defluidizar el lecho o a formar caminos preferentes de gas en el mismo. Se han empleado múltiples estrategias para eliminar la aglomeración y mejorar la homogeneidad de fluidización. Entre estas estrategias se encuentra la vibración de un lecho fluidizado convencional, la cual es una tecnología prometedora consistente en la introducción de energía cinética en el sistema mediante la vibración mecánica de la vasija del lecho. Esta vibración proporciona la energía necesaria para romper los enlaces entre partículas, prevenir su aglomeración y evitar la canalización del gas en el lecho.

A pesar de sus ventajas, la vibración introduce complejidades en la dinámica del lecho que están aún lejos de ser plenamente comprendidas. El conocimiento de estos fenómenos físicos complejos derivados de la vibración de un lecho fluidizado podría ser utilizado para la mejora del diseño y control de los lechos fluidizados vibrantes existentes, así como para aumentar su rango de operación en nuevas aplicaciones. Por todo lo anterior, un estudio de carácter fundamental del efecto de la vibración en el movimiento de la fase densa del lecho y de las burbujas presentes en el sistema es de suma importancia para entender la dinámica de este tipo de dispositivos. Este es el objetivo de la presente tesis doctoral, cuya estructura y resultados principales se indican en los párrafos siguientes.

En el primer capítulo se presentan brevemente los fenómenos de fluidización y los métodos experimentales y numéricos comúnmente empleados para caracterizar lechos fluidizados convencionales y vibrantes. En el Capítulo 2 se resumen las estrategias experimentales, numéricas y de procesamiento de datos seguidas para la caracterización de lechos fluidizados vibrantes llevada a cabo en esta tesis.

El efecto de la vibración de la vasija en el comportamiento de la fase densa en un lecho delgado (pseudo-2D) en condiciones de mínima fluidización se presenta en el Capítulo 3.

Además de las evidencias experimentales, en este capítulo se analizan los resultados derivados de un modelo unidimensional específicamente desarrollado en este capítulo y de simulaciones de dos fluidos de tipo Euleriano-Euleriano. Estos análisis sirven, en primer lugar, para entender el efecto de la vibración sobre la fase densa cuando no hay burbujas presentes en el sistema y, en segundo lugar, como un punto de partida para la interpretación del comportamiento de lechos burbujeantes más complejos. Los resultados obtenidos muestran que, además de las ondas de presión de gas, existen ondas de compresión y de expansión de la fase densa que ascienden y modifican la velocidad de las partículas a lo largo de la altura del lecho. Estas ondas son causadas por la interacción de la parte inferior del lecho con el distribuidor. Tanto los experimentos como los métodos numéricos empleados en este capítulo muestran que la vibración de la vasija del lecho promueve una compresión y expansión cíclica de la fase densa y la aparición de diferencias entre las velocidades relativas de las partículas en las partes superior e inferior del lecho.

En el Capítulo 4 se analiza el movimiento de una burbuja aislada ascendiendo en un lecho pseudo-2D sometido a vibración. Este análisis se hace de dos formas: experimentalmente (por medio de técnicas de análisis digital de imágenes y de velocimetría por imagen de partículas) y numéricamente (mediante simulaciones del modelo de dos fluidos). Los experimentos revelan que los comportamientos medio y oscilatorio de las burbujas se ven fuertemente afectados por la oscilación cíclica de la fase densa. En particular, para las partículas estudiadas, un aumento de la amplitud de vibración disminuye la velocidad de la burbuja para un determinado tamaño de la misma. La vibración también promueve un retraso en fase de las propiedades de la burbuja en función de la su posición vertical en el lecho. Además, las simulaciones numéricas ponen de manifiesto la importancia de considerar la compresibilidad del gas para una correcta predicción de las oscilaciones de la fase densa y del retraso en fase de las propiedades de la burbuja. En este capítulo se observa que las oscilaciones de las propiedades de la burbuja se transmiten a una velocidad similar a la velocidad del sonido en un lecho fluidizado, lo que de nuevo manifiesta que la compresibilidad del gas juega un papel esencial en la transmisión de ondas de compresión-expansión a lo largo de la altura del lecho.

En el Capítulo 5 se caracteriza la distribución de presiones y el movimiento de los sólidos alrededor de burbujas aisladas ascendiendo en el lecho. Se obtiene que la perturbación de presión causada por el ascenso de la burbuja en el lecho vibrante es similar a la esperada para una burbuja ascendente en un lecho sin vibrar y concuerda con el modelo de flujo potencial desarrollado por Davidson & Harrison. Esto sugiere que las fluctuaciones de presión de gas producidas por la vibración del lecho no interfieren de manera coherente con la perturbación de presión producida por la burbuja. Es más, la aplicabilidad del modelo de flujo potencial de Davidson & Harrison es también confirmada en cuanto a la descripción cualitativa del movimiento de sólidos alrededor de una

burbuja ascendiendo en un lecho vibrado. Adicionalmente, los experimentos mostrados en el Capítulo 5 se utilizan para dar explicación a la forma ondulada de burbujas en lechos fluidizados vibrados. Los resultados además revelan que el volumen de partículas arrastrado por la estela de la burbuja crece al aumentar tanto la amplitud como la frecuencia de vibración, estando dicho volumen intensamente afectado por el movimiento oscilatorio de la vasija.

El Capítulo 6 estudia un lecho vibrado operado en régimen completamente burbujeante y muestra que el comportamiento medio de las burbujas se encuentra fuertemente afectado por la vibración. En particular, cerca del distribuidor, la velocidad de las burbujas disminuye al aumentar la amplitud de vibración de la vasija del lecho ya que las burbujas son más pequeñas, están menos confinadas, y se comportan como burbujas aisladas. El análisis del comportamiento oscilatorio de burbujas en el lecho revela que el retraso en fase de las propiedades de las burbujas se conserva incluso si el lecho es operado en régimen burbujeante y las burbujas interactúan continuamente entre ellas.

Por último, en el Capítulo 7 se estudian dos aplicaciones de lechos fluidizados vibrados. La primera aplicación comprende un estudio experimental de la segregación de partículas en un lecho fluidizado vibrante formado por partículas de tamaños similares y diferentes densidades. En este lecho, la vibración y la velocidad superficial del gas tienen papeles contrapuestos en la segregación. Por un lado, la vibración sin inyección de gas promueve la mezcla de las partículas. Por otro lado, la combinación de bajas intensidades de vibración con la inyección de gas promueve la segregación de las partículas densas hacia la sección inferior del lecho. La segunda aplicación presentada en este capítulo caracteriza experimentalmente los diferentes patrones granulares que aparecen al vibrar la vasija de un lecho de forma triangular, lo cual tiene implicaciones para lechos con geometría cónica. Los resultados muestran que existe una combinación de la intensidad de vibración y la velocidad superficial de gas para la cual el sentido de la circulación convencional de las partículas en el lecho puede verse invertido.

En resumen, la presente tesis doctoral revela, tanto experimentalmente como con la ayuda de modelos numéricos, que (i) la compresibilidad del gas afecta a las oscilaciones de la fase densa de un lecho fluidizado vibrado, (ii) la presencia ondas de compresión y de expansión de sólidos y de gas causadas por la la vibración de la vasija domina el comportamiento de burbujas aisladas en el lecho, (iii) estas ondas se generan en la base del lecho y viajan en dirección ascendente modificando el comportamiento medio y oscilatorio de las propiedades de las burbujas en función de la distancia al distribuidor, (iv) esto es aplicable a lechos operados en régimen burbujeante en los que existe una continua interacción entre burbujas y (v) la vibración introduce un grado extra de libertad que permite controlar la segregación y modificar los patrones de movimiento de las partículas en el lecho.

# Abstract

Fluidization is a process extensively used in the energy, chemical and materials processing industries owing to the good performance in solid mixing and the high solid-solid and gas-solid contact efficiencies it provides. Among the operations making use of gas fluidized beds are fluid catalytic cracking (FCC), gasification, combustion of solid fuels, Fischer-Tropsch synthesis, drying, granulation and coating. However, the ease with which particles fluidize may be affected by diverse factors. For example, fine particles tend to agglomerate, which can end up defluidizing the bed. Several strategies have been employed to eliminate agglomeration and improve the fluidization homogeneity. Among these strategies, vibration of a conventional fluidized bed is a promising technology consisting in introducing kinetic energy to the system by mechanical vibration of the bed vessel. Vibration provides the necessary energy to break interparticle bonds and prevent agglomeration and gas channeling. Despite its advantages, vibration introduces complexities in the dynamics of the bed that are still far from being fully understood. Knowledge of these complex physical phenomena arising from vibration of a fluidized bed could be used to improve design and control of the existing vibrated beds and to increase their range of operation to new applications. Therefore, a fundamental study of the effect of vibration on the bulk motion and the bubbles rising in a fluidized bed is paramount to understand the dynamics in this kind of gas-solids systems. This is the aim of the present dissertation, whose structure and main results are described in the following paragraphs.

The first chapter of the dissertation briefly introduces the fluidization phenomena and the experimental and numerical methods typically used to characterize conventional fluidized beds. Chapter 2 summarizes the experimental, numerical and data processing strategies followed for the fundamental characterization of vibrated beds carried out in this work.

The effect of vibration of the bed vessel on the behavior of the solids bulk of a bed of small thickness (pseudo-2D bed) aerated at minimum fluidization conditions is presented in Chapter 3. In addition to the experimental evidence, results arising from a one-dimensional model specifically developed in this chapter and from Eulerian-Eulerian, two-fluid model simulations are analyzed. These analyses serve firstly as a basis to understand the effect of vibration on the bed bulk when no bubbles are present in the system, and

secondly as a starting point to later interpret the behavior of the more complex vibrated bubbling beds. The obtained results show that, in addition to gas pressure waves, there exist compression and expansion waves of the dense phase that travel upwards in the bed and change the velocity of the particles along the bed height. These waves are caused by the interaction of the bottom of the bed bulk with the distributor plate. Both the experiments and the numerical methods show that vibration of the bed vessel promotes a cyclic compression and expansion of the bed bulk leading to opposite velocities of particles in the upper and the lower sections of the bed.

In Chapter 4, the motion of a bubble rising alone in a pseudo-2D vibrated fluidized bed is analyzed. This is done in a twofold way: experimentally (by means of Digital Image Analysis and Particle Image Velocimetry) and numerically (by means of Two-Fluid Model simulations). The experiments reveal that the mean and oscillatory behaviors of bubbles are strongly affected by the cyclic oscillation of the bed bulk. In particular, for the particles studied, increasing the vibration amplitude decreases the measured bubble velocity for a given bubble size. Vibration also promotes the presence of a phase delay of the bubble characteristics as a function of the bubble position along the bed height. Besides, the numerical simulations reveal the importance of considering the gas compressibility to correctly predict the oscillations of the bed bulk and the phase delay of bubble characteristics. It is found that oscillations of bubble characteristics are transmitted at a velocity similar to the sound velocity in a fluidized bed, which again manifests that the gas compressibility plays an important role in the generation of compression-expansion waves traveling along the bed height.

The pressure distribution and the motion of solids around bubbles rising alone in the bed are experimentally characterized in Chapter 5. It is found that the pressure perturbation caused by a bubble rising in the vibrated bed is similar to that expected for a bubble rising in a bed without vibration and in accordance with the Davidson & Harrison's potential flow model. This suggests that the gas pressure fluctuations produced by vibration of the bed do not interfere coherently with the pressure perturbation produced by the bubble. The applicability of the Davidson & Harrison's potential flow model is also qualitatively confirmed with regard to the motion of solids around a bubble in a vibrated bed. The experiments of Chapter 5 are also used to give an explanation to the characteristic wavy shape of bubbles in the vibrated fluidized bed. The results also reveal that the volume of particles dragged by the wake increases when increasing the vibration amplitude and frequency and is strongly affected by the oscillatory motion of the bed vessel.

Chapter 6 studies a vibrated bed operated in freely bubbling regime, showing that the mean behavior of multiple interacting bubbles is strongly affected by vibration. In particular, close to the distributor, the bubble velocity decreases when increasing the

vibration amplitude of the bed vessel because bubbles are smaller and less confined and they behave like isolated bubbles. The analysis of the oscillatory behavior of bubbles in the bed reveals that the phase delay of bubble characteristics observed for isolated bubbles is preserved even if the bed is operated in freely bubbling regime.

Finally, in Chapter 7, two applications of vibrated fluidized beds are studied. The first application comprises an experimental study of the particle segregation in a vibrated fluidized bed filled with particles of approximately the same size and different densities. It is found that vibration and the gas superficial velocity play counteracting roles on segregation. Vibration alone leads to mixing, whereas low vibration strengths, in combination with the injection of gas, promote percolation that causes the segregation of the denser particles to the lower section of the bed. The second application is devoted to the experimental characterization of the different granular patterns appearing when vibrating a bed of triangular shape, with implications to beds of conical geometry. The results show that there is a combination of the vibration strength and the gas superficial velocity in which the direction of the conventional gulf stream circulation of particles inside the bed can be reversed.

In summary, the present PhD thesis principally reveals, both experimentally and with the aid of numerical models, that (i) gas compressibility affects the oscillations of the bed bulk in vibrated fluidized beds, (ii) the presence of compression and expansion waves of solids and gas caused by the vibration of the bed vessel commands the behavior of isolated bubbles in the bed, (iii) these waves are generated at the base of the bed and travel upwards modifying the mean and the oscillatory behavior of bubble characteristics as a function of the distance to the distributor, (iv) this is also applicable to beds in bubbling regime with multiple interacting bubbles and (v) vibration introduces an extra degree of freedom to control segregation and modify the patterns of particle motion in the bed.

# Contents

CHAPTER
**ONE**

# The phenomena of fluidization and the effect of mechanical vibration

## Contents



## 1.1 Fluidization and fluidization improvement

Fluidization is an operation by which solid particles are transformed into a fluid-like state through suspension in a gas or liquid. This method of contacting has some unique characteristics, and fluidization engineering puts them to good use.

Gas-fluidized beds have been widely used in the chemical, energy and process industries because of their favorable heat transfer and particle mixing characteristics. This type of beds is employed for numerous operations such as fluid catalytic cracking (FCC), gasification of coal and biomass, coating, drying, adsorption, synthesis reactions, etcetera. Despite the fact that the use of fluidized beds is not new, the dynamics of fluidized beds is

not fully understood owing to its multiscale characteristics and stochastic behavior. This lack of understanding includes not only complicate termochemical reactions in gas-solid flows but also the basic dynamics of cold beds. Therefore, correct design and control of fluidized beds are still open questions and require further development due to the complex and chaotic behavior of these gas-solid systems.

### 1.1.1 The fluidization phenomena

A gas fluidized bed consists basically of a bed of particles. This bed is situated over a distributor plate and is laterally limited by walls. The distributor plus the walls constitute the bed vessel. A fluid, which is typically gas, is introduced through the distributor by means of simple orifices, tuyeres, porous plates or other kind of gas injection devices.

Depending on the velocity of the gas injected through the distributor and the difference of densities of the phases (solid and fluid phases) involved, several flow regimes of the bed dynamics appear. These fluidization regimes are schematized in Figure 1.1 and described in the following lines.

In general, if a gas passes through a bed of particles at a low flow rate, the gas merely percolates through the void spaces between the particles, which remain static. This state of the bed is called a 'fixed bed'. When the flow rate is further increased, particles move apart and vibrate in restricted regions, increasing the volume of the bed. This state is known as 'expanded bed'. There is a gas flow rate where the particle buoyancy (usually negligible) and the drag force of the gas on the particles counterbalance the weight of the bed so that the particles are just suspended by the upward-flowing gas adopting a uniform distribution. At this point the bed is considered to be just fluidized or at 'minimum fluidization' (Figure 1.1(a)). The gas velocity necessary to reach this fluidized state is the so-called minimum fluidization velocity ($U_{mf}$). This velocity is typically expressed in the form of a superficial gas velocity, which is the gas total volumetric fluid flow rate divided by the horizontal section area of the whole bed.

Generally, in gas-solid systems, large instabilities with bubbling and channeling of gas are observed when increasing the gas velocity beyond minimum fluidization conditions. In this situation, clearly distinguishable voids are formed. These voids are known as bubbles since their behavior is similar to that of bubbles in a gas-liquid system. The bubbles rise in the bed as a consequence of their buoyancy, like gas bubbles in liquids. In general, the particles outside the bubble are in a fluidized state similar to minimum fluidization conditions. In consequence, two different phases appear in the bed, the bubble phase and the dense phase (Davidson & Harrison, 1963). Depending on the gas flow rate in the bed, different bubbling regimes can be observed. If bubbles are small (as compared to the cross-sectional area of the bed), they are generally not influenced by

the lateral walls. This regime is called 'bubbling regime' (Figure 1.1(b)). Bubbles can grow and coalesce as they rise inside the bed. If the gas flow is further increased, the diameter of the bubbles may eventually become large enough to spread across the whole cross-sectional area of the bed vessel. This is known as 'slugging regime' (Figure 1.1(c)).

When fine particles are fluidized at a sufficiently high gas flow rate, the terminal velocity of the solids (i.e. the gas velocity when the sum of the drag force and buoyancy of an individual equals the downward force of gravity) is exceeded and, instead of bubbles, a turbulent motion of solid clusters and voids of gas of various shapes and sizes is observed. This is called 'turbulent fluidization' (Figure 1.1(d)). By increasing gas velocity the 'fast fluidization' regime appears, in which particles move upwards in clusters through the middle of the bed cross section (Figure 1.1(e)). Near the walls, particles move downward. Particle mixing in both axial and radial directions is very intensive in this regime and the concentration of particles decreases exponentially in the vertical direction. With a further increase in the gas velocity, solids are carried off the bed vessel, arriving to a 'pneumatic transport' (see Figure 1.1(f)).

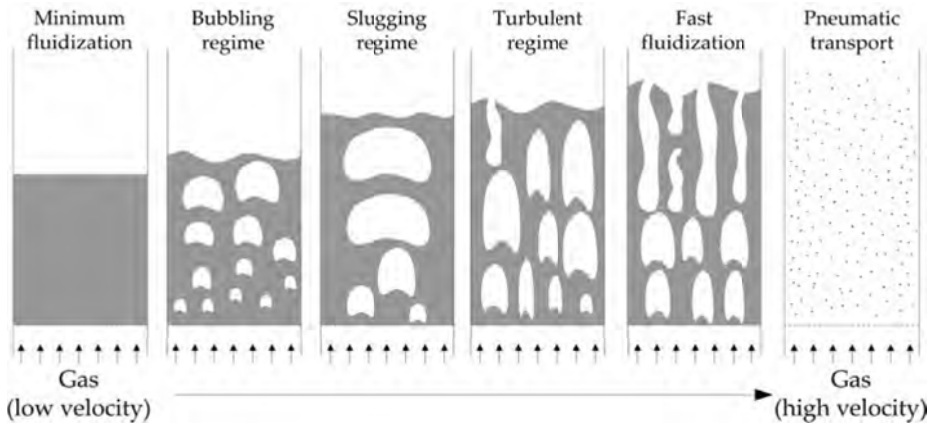


**Figure 1.1:** Summary of different operating conditions of a fluidized bed.

### 1.1.2 Particle classification

The different fluidization regimes previously described provide a macroscopic description of the fluidization state of the bed. Numerous attempts have been made to find a criterion able to predict the bed fluidization regime and the transition from one regime to another. By observing the fluidization of different kinds and sizes of solids, Geldart (1973) proposed their classification into four recognizable kinds of particles, that are linked to their fluidization behavior, as shown in Figure 1.2.

The four groups of particle behavior according to the Geldart's classification are the

following.

- Group C: cohesive or very fine powders. Normal fluidization of this kind of particles is extremely difficult given the high interparticle forces. These particles fluidize under conditions that are very difficult to achieve and may require the application of an external force, such as mechanical agitation.
- Group A: aeratable, small size or low density particles with density smaller than 1.4 g/cm$^3$. These solids fluidize easily yielding small bubbles at higher gas velocities.
- Group B: sandlike particles. These solids fluidize well with vigorous bubbling and bubbles can reach large sizes.
- Group D: spoutable large and/or dense particles. Fluidization of this group requires very high gas velocities and it is typically associated with high levels of abrasion of the bed walls and the bed internals. Examples of these particles are drying grains and peas, roasting coffee beans, gasifying coals, and some roasting metal ores. These particles are usually processed in shallow beds or in spouting beds.

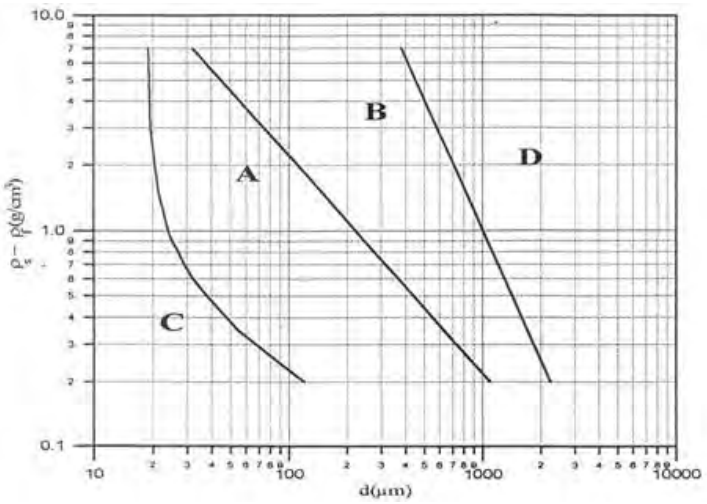


**Figure 1.2:** Geldart's classification of particles. From Geldart (1973).

### 1.1.3 Fluidization improvement: vibration of the bed

Diverse factors can affect the ease with which particles fluidize and the range of operating conditions that sustain fluidization. One of them is the particle size distribution.

Generally, fine particles tend to agglomerate, which can end up defluidizing the bed (van Ommen *et al.*, 2012). Thus, the bed must be agitated to maintain satisfactory fluidization conditions. A mechanical stirrer can be employed as an intrusive way to do this (Kuipers *et al.*, 1996). Also, the operation of the bed at high gas velocities could be a method to avoid agglomeration. In a similar way, flow pulsation has also shown to be an effective technique for the fluidization of nanoparticles, increasing the homogeneity of the fluidization, structuring chaotic patterns and reducing the minimum fluidization velocity (Coppens & van Ommen, 2003; Sadiq & Asif, 2012).

Another factor affecting fluidization is the fluid-solid density ratio. Normally, liquid-solid systems fluidize homogeneously, but gas-solid beds can present large heterogeneities in their interior leading to bubbles but also to agglomeration and channeling. In this situation, bubbles tend to channel along preferential paths, which create imperfect mixing of the bed particles. Many efforts have been made to modify the particle and bubble behavior inside a fluidized bed also by external means. For example, ferromagnetic particles subjected to magnetic fields can change the way the bed fluidizes, extending the bubble-free operation range in fluidization state (Rosenweig, 1979) or diminishing the bubble size (Jovanovic & Jovanovic, 1993). Similarly, acoustic fields have also been employed for the improvement of the fluidization quality of group C cohesive powders (Nowak *et al.*, 1993).

Additionally, the use of special methods of gas injection has been considered to improve the fluidization quality. Sobrino *et al.* (2008) studied the use of a rotatory distributor in order to improve solid mixing and the bubble distribution. The particle radial dispersion is promoted by this distributor, reducing the bubble channeling in the bed. In this line, Nakamura *et al.* (2013) proposed the improvement of particle mixing and fluidization quality by the inclined injection of the fluidizing air.

When agglomeration and channeling are severe, the improvement of fluidization requires methods capable of introducing high levels of energy in all the bed volume. In this regard, mechanical vibration of fluidized beds, i.e. 'Vibrated Fluidized Beds' (VFB), is a promising technology consisting in introducing a vibration to a conventional fluidized bed (Gupta & Mujumdar, 1980; Mori *et al.*, 1990; Noda *et al.*, 1998; Zhou *et al.*, 2001). This can be done by applying an oscillatory displacement to the bed-containing vessel, which means that vibration can be introduced non-intrusively. Vibration of the bed provides the necessary energy to break interparticle bonds, reduce agglomerates and avoid channeling.

If conventional fluidized beds are complex to understand, vibration of fluidized beds enriches even more the intricate physics of the gas-solid interaction. This explains why, at present, vibrating fluidized beds remain insufficiently understood and their characterization constitutes a challenge for the scientific community. The present PhD thesis

contributes to the characterization of these vibrated systems.

### 1.1.4 Applications of vibrated fluidized beds

Pioneer works on the application of vibration to a conventional fluidized bed were performed by Mujumbar (1987) and were devoted to drying processes of granular material. Besides, due to its unique characteristics, vibrated fluidized beds have proven to be of great use in several other operations such as the fluidization of cohesive particles (Kuipers *et al.*, 1996; Mawatari *et al.*, 2005*b*; Barletta & Poletto, 2012), granulation (Pan *et al.*, 2009), coating (Morley, 1991), catalysis (Nelson *et al.*, 2007; Latifi *et al.*, 2014), fluidization of nanoparticles (van Ommen *et al.*, 2012) and operations related to particle segregation (Luo *et al.*, 2008; He *et al.*, 2015; Zhao *et al.*, 2015). Additionally, some potential applications of vibrated beds are described in the work by Squires (2004), which include: a reactor for non-steady-state heterogeneous reaction kinetics, a heat exchanger, a reactor for flash coal pyrolysis or flash shale oil distillation, a pressurized duct to use Geldart A powders as a heat carrier in chemical processes, a counter-current heat exchanger between a gravel and a Geldart A powder and an apparatus for the distillation of oil shale rock.

The use of VFBs is widely extended in the chemical, food, pharmaceutical and other industries. The following properties make vibrated fluidized systems of great interest for these industries:

- Vibration provides the necessary energy to break agglomerates and allows the fluidization of fine cohesive powders (Mawatari *et al.*, 2005*b*; Barletta *et al.*, 2013).

- The heat and mass transfer properties of the bed can be controlled by separately changing the vibration amplitude and frequency of the bed vessel.

- The minimum fluidization velocity is decreased (Mawatari *et al.*, 2003), which decreases the necessary gas mass flow to fluidize the bed.

- Both the vibration and the gas velocity tend to fluidize the bed material. Hence, the gas flow can be set according to a requirement of heat in the bed and not by a requirement of fluidization.

- Vibration can be used to help segregate particles according to their size and density (Luo *et al.*, 2008; He *et al.*, 2015).

## 1.2 State of the art of the characterization of fluidized beds

### 1.2.1 Experimental techniques

The main experimental techniques used in the literature for the research of fluidized beds are summarized in the following lines. The principle of operation and some of their advantages and disadvantages are enumerated:

- **Digital Image Analysis (DIA)** (Busciglio *et al.*, 2008*b*). It comprises the set of methods devoted to the analysis of digital images to obtain visually discernible properties like the bubble size in a bed. *Advantages:* This technique is non-intrusive and provides good temporal and spatial resolutions. *Disadvantages:* Optical access to the bed is needed, hence, its applicability is reduced to pseudo two-dimensional (pseudo-2D) facilities.

- **Particle Image Velocimetry (PIV**) (Laverman *et al.*, 2008; Hernández-Jiménez *et al.*, 2011). Consists in the particle seeding and measurement of the displacement of the particles with a high-speed camera (see Section 1.2.1). *Advantages:* As DIA, it is a non-intrusive technique and provides good temporal and spatial resolution. *Disadvantages:* Optical access to the bed is needed, which again limits its applicability to pseudo-2D facilities.

- **Pressure signal analysis** (Bi, 2007; van Ommen *et al.*, 2011). Pressure fluctuations in the plenum or in the bed are measured by pressure probes. *Advantages:* It is a non intrusive technique which allows a real-time determination of the pressure fluctuations inside the bed. *Disadvantages:* Although it provides information on the pressure fluctuations in the whole bed, the measurements provided are local.

- **Optical fiber probes** (Ishida & Shirai, 1980; Glicksman *et al.*, 1987). The particles reflect the light, which is received by an optical fiber sensor. *Advantages:* The cross-correlation of the signals obtained by two fibers allows the calculation of the velocity of bubbles and particles and the instantaneous void fraction in 2D and 3D beds. *Disadvantages:* The optical fiber sensors are difficult to calibrate and yield noisy signals. Also, the probes are intrusive and provide local information of the bed.

- **Laser Doppler Anemometry (LDA)** (Mathiesen *et al.*, 2000). This technique is based on the doppler shift produced on a laser beam by the particle velocity. *Advantages:* It is a non-intrusive technique which does not require calibration and

provides a high temporal resolution. *Disadvantages:* The obtained results only provide punctual measurements of the solids velocity.

- **Capacitance probes** (Sharma *et al.*, 2000). The capacitance probes detect variations of the dielectric constant between two plates caused by changes in the solids concentration. *Advantages:* This method is extensively used, as it can provide information about the solid concentration and the bubble dynamics in a non-intrusive way. *Disadvantages:* The measurements are local and can be perturbed by the distortion of the electric field.

- **Electrical capacitance tomography (ETC)** (van Ommen & Mudde, 2008; Makkawi & Wright, 2002). ETC is based on the measurement of the electrical capacitance, which varies as a function of the void fraction of the bed. *Advantages:* It is a non-intrusive technique that allows to obtain three-dimensional measurements. *Disadvantages:* The number of sensors typically employed is small, which difficults capturing high-resolution images.

- **X-Ray tomography** (Mudde, 2010). It is based on the attenuation of X-Rays when crossing the bed. This attenuation depends on the chemical composition, concentration and the volume of particles being penetrated by the X-Ray beam. *Advantages:* This technique is non-intrusive and three-dimensional measurements can be obtained at a high temporal resolution, which makes it very interesting for the characterization of fluidized beds. *Disadvantages:* The spatial resolution of the images is still not very high.

- **Planar laser induced fluorescence** (Solimene *et al.*, 2006). It consists in recording an excited substance, like acetone, with a high-resolution camera. *Advantages:* It is a non-intrusive technique that permits highly sensitive concentration measurements of the gas flow and mixing patterns information. *Disadvantages:* Despite its advantages, the surface of analysis is limited to the size of the laser sheet.

- **Magnetic resonance imaging (MRI)** (Müller *et al.*, 2008). The MRI is an imaging technique based on the principles of Nuclear Magnetic Resonance (NMR) that detects nuclei with non-zero spin quantum number. It can measure the concentration and velocity of the gas and solids phases. *Advantages:* Apart from being non-intrusive, these facilities provide temporally resolved results in surfaces in any of the three dimensions of the bed. *Disadvantages:* The particles or/and the gas phases have to be detectable by MRI. Also, the size of the fluidized bed is limited to the size of the MRI facility.

- **Radioactive particle tracking** (Lin. *et al.*, 1985). It is based on the tracking of the gamma radiation of a radioactive tracer particle identical to the solid particles. *Advantages:* It is a non-intrusive technique which allows for the calculation of the solids motion in the bed. *Disadvantages:* The information provided by the tracer is local and needs of a distance-intensity and redundancy calibration. Also, there exist secondary emissions of the radioactive tracer.

- **Magnetic tracer Particle Tracking (MPT)** (Buist *et al.*, 2014; Sette *et al.*, 2015). It consists in the tracking of a magnetic tracer particle in the bed, which provides the particle tracer trajectory. *Advantages:* Allows the tracking of the particle trajectory in three dimensions and the possibility of using non-magnetic powders. *Disadvantages:* The information provided by the tracer is local.

- **Infrared camera technique** (Dang *et al.*, 2013). The local concentration and temperature of a gas non-transparent to radiation is analyzed by DIA of images acquired with an infrared and a high-speed camera *Advantages:* It is a non-intrusive technique. *Disadvantages:* The bed has to be constructed with a material transparent to radiation. Also, commonly used particles do not allow visualization of the gas phase as they are not transparent to radiation. Thus, only the gas concentration in bubble voids is observed.

The DIA, PIV and pressure signal analysis techniques were the three experimental methods employed in this work because of their availability in the different laboratories and their well balanced characteristics. The three of them are non-intrusive techniques, i.e. the fluidized bed is not perturbed by the measurement system. The following lines describe in more detail these techniques.

### Digital Image Analysis (DIA) in pseudo-2D beds

Beds of small thickness, i.e. the so called pseudo two-dimensional beds, are lab-scale beds of simplified geometry that have been crucial for the understanding of the dynamics of gas-particle systems (Shen *et al.*, 2004; Busciglio *et al.*, 2008*b*; Laverman *et al.*, 2008; Hernández-Jiménez *et al.*, 2011). Pseudo-2D fluidized bed systems typically have a transparent front wall in order to allow optical access to the system. The back wall of the bed is separated to the front wall by a narrow distance to ensure that the visualization is representative of the whole system. The optical access to the bed allows the use of measurement techniques aimed to understand the bed and bubble dynamics such as PIV (Hernández-Jiménez *et al.*, 2011) or DIA (Shen *et al.*, 2004; Busciglio *et al.*, 2008*b*; Laverman *et al.*, 2008). However, despite the advantages of pseudo-2D beds, great attention has been paid during the last few years to the frictional effect of the bed front and

rear walls of beds with this geometry. These walls restrict the solids motion, which may lead to a different flow behavior of the bed to that observed in fully three-dimensional systems (Hernández-Jiménez *et al.*, 2011, 2013*b*; Li & Zhang, 2013).

DIA consist on recording the fluidized bed with a CCD camera. To allow visualization of the interior of the bed, it has to be optically accessible (i.e. having a transparent wall). The opacity of the solids allows the distinction between the solid phase and the bubbles inside the bed. However, given this opacity of the solids, thin beds are normally used in DIA.

The images captured using DIA represent the spatial distribution of the bubbles and dense phase near the walls of the bed. The images are first transformed into grayscale. In consequence, good illumination and good grayscale contrast between particles and the bed background is necessary. This is generally achieved by painting the rear wall of the bed or illuminating the bed from behind, which allows the penetration of light through the bubbles. Once the transformation to grayscale is performed, each pixel will present a value between 0 and 255, 0 being black and 255 being white. A correct determination of a threshold value allows to discern bubble phase from the dense phase. Other kinds of information such as the dense phase segregation or mixing can be extracted using DIA.

The use of pseudo-2D beds in combination with DIA has been successfully applied to VFBs and has proven to be a useful technique to investigate their bed and bubble behavior (Eccles & Mujumdar, 1997; Zhou *et al.*, 2001, 2004, 2005; Mawatari *et al.*, 2005*a*; Cano-Pleite *et al.*, 2014, 2016).

### Particle Image Velocimetry (PIV)

The PIV technique has been also crucial for the understanding of fluidized beds, as demonstrated by the numerous works making use of this technique (Santana *et al.*, 2005; Almendros-Ibáñez *et al.*, 2006; Müller *et al.*, 2007; Laverman *et al.*, 2008; Sánchez-Delgado *et al.*, 2010; Hernández-Jiménez *et al.*, 2011; Zeilstra *et al.*, 2013). PIV uses two consecutive image frames separated a time lapse $\Delta t$ to measure the displacement of the particles in horizontal and vertical directions, $\Delta x$ and $\Delta y$. Thus, the instantaneous horizontal and vertical components of the solids velocity can be calculated as:

$$u(x, y, t) = \frac{\Delta x(x, y, t)}{\Delta t} \tag{1.1}$$

$$v(x, y, t) = \frac{\Delta y(x, y, t)}{\Delta t} \tag{1.2}$$

In typical PIV applications, the flow is seeded with tracer particles small enough to be able to faithfully follow the flow field (Strumillo & Pakowski, 2007). The flow is generally illuminated with a laser light and the displacement of the tracer particles between two

consecutive frames is calculated by means of statistical cross-correlation methods.

As commented in Section 1.2.1, one of the main disadvantages of PIV is that optical access to the bed bulk is needed. Thus, the PIV technique is limited to pseudo-2D beds. The bed is uniformly illuminated through the front view and the bed material is typically seeded with a low percentage (e.g. around 5% (Sánchez-Delgado *et al.*, 2010)) of particles with the same properties but different color as the particles in the bed. This increases the contrast between the particles and facilitates the cross-correlation process between two consecutive images. The images captured by the CCD camera are divided in small windows of a user-specified size called interrogation windows, among which the cross-correlation process is carried out. Windows of 8 to 64 pixels side and 50% overlap are typically chosen in fluidized beds.

Generally, combined DIA and PIV techniques are employed for the calculation of the solids velocity in a pseudo-2D bed. Firstly, DIA is used to apply a mask to the image, so that the bubbles are differentiated from the dense phase. This mask is used by the PIV, avoiding the calculation of the solids velocity inside bubbles, which would lead to unrealistic results.

Figure 1.3 shows an example of the motion of solids around an isolated bubble rising in a VFB (Chapter 5). The bubble volume was detected from Figure 1.3(a) by means of DIA and removed from the PIV calculation of the solids velocity vectors between two consecutive frames in Figure 1.3(b).

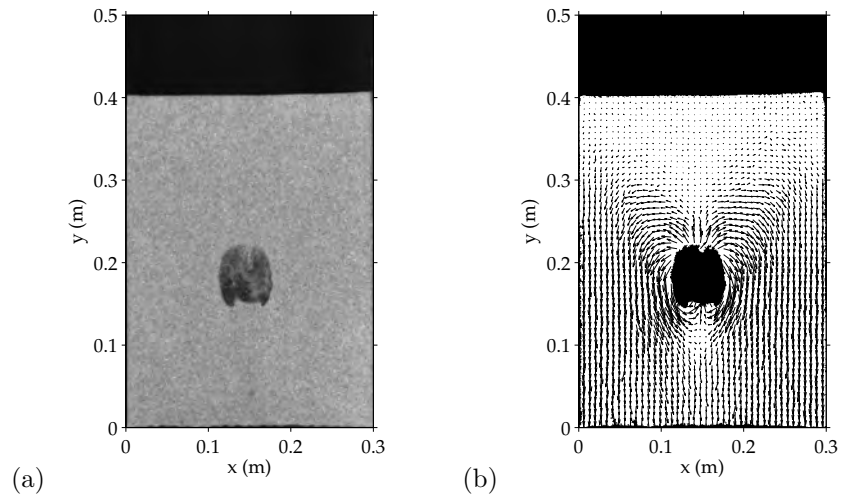


**Figure 1.3:** Example of DIA and PIV processing (a) orginal particle image; (b) bubble mask and PIV solids phase velocity vectors. Chapter 5.

**Pressure signal analysis**

Pressure signal analysis in the domain of time or in the domain of frequency is a technique extensively used in research and in plant operation (van der Schaaf *et al.*, 1998; Bi, 2007; Sasic *et al.*, 2007; Croxford & Gilbertson, 2011; van Ommen *et al.*, 2011). In gas-fluidized beds, the pressure in the gas or in the plenum is measured by virtue of pressure transducers, which generally work on the principle of the variation of their conductivity when subjected to changes of pressure. These transducers are connected to the bed and, through an acquisition card, pressure data can be transformed and monitored in a computer for later data analysis.

This method allows a real-time determination of the pressure fluctuations. Pressure signal analysis can be employed to obtain a huge amount of information concerning the fluidized bed. For instance, pressure fluctuations can be used for the determination of the fluidization regimes inside the bed, as shown in Figure 1.4.

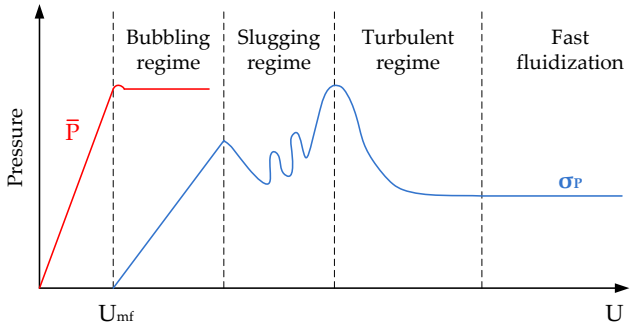


**Figure 1.4:** Schematic evolution of the pressure mean and standard deviation as a function of the superficial velocity.

### 1.2.2 Numerical modeling

One of the main challenges in modeling hydrodynamics in gas-solid fluidized beds is the description of the motion of the solid and gas phases and their interaction in space and time.

Five main simulation approaches are reported in the literature, differing in their temporal and spatial resolution and, in consequence, in computational time. Figure 1.5 shows examples of the different simulation methodologies arranged by level of detail and computational cost. The most computationally demanding approach is the Direct Numerical Simulation (DNS) of the local flow around each particle and the movement and interaction between particles. This approach is typically computed using Lattice

Boltzmann methods (Ladd & Verberg, 2001; Third *et al.*, 2016). Going a step lower in computational cost, in discrete Lagrangian-Eulerian models such as the so called Discrete Element Method (DEM), the gas-flow field is described as a continuum medium skipping local details around particles. Nevertheless, the movement of each particle is followed individually. This results in the computation of each particle-particle and particle-wall collision, making this method highly computationally demanding and still restricted to beds of small dimensions or filled with a reduced number of particles (i.e. order of $10^6$) (Cundall & Strack, 1979; Tsuji *et al.*, 1992; Deen *et al.*, 2007).

Simulation of medium size and moderately big fluidized beds is commonly undertaken using an Eulerian-Eulerian approach known as Two-Fluid Model (TFM). The advantage of this Euler-Euler approach (Gidaspow, 1994; van Wachem & Almstedt, 2003) is that particles are not defined individually but grouped as an equivalent continuous fluid that is interpenetrated by the gas phase. As in the Lagrangian-Eulerian description, a model of gas-solid interaction is needed in the TFM. Furthermore, given the lack of micro-scale information on the particle phase in the Eulerian-Eulerian description, the solids interaction has to be introduced in the simulation by means of additional closure models. As a result of these simplifications, the computational cost is dramatically decreased compared to the Lagrangian-Eulerian methods. Nevertheless, two-fluid models provides satisfactory results in terms of temporal and spatial resolution.

The spatial resolution is further reduced in the Discrete Bubble Model (DBM) approach, which makes an extensive use of phenomenological methods. In DBM only macroscopic characteristics of the bed are computed, such as bubble displacement and growth and the general dense phase motion (Briongos *et al.*, 2011). Given its phenomenological nature, the computational cost of this method is lower than that of the other three, making it suitable for numerical estimations of big facilities.

The last numerical approach is a purely phenomenological model in which all the spatial details of the bed are usually lost and the system is characterized by using temporal or spatially averaged values, function of local phenomena of the bed. These kind of phenomenological models are computed effortlessly allowing for the optimization and design of complex cold and reacting beds.

Given the characteristics of the experimental facilities used in the present PhD thesis and the level of resolution required to characterize the bubble oscillation, an Eulerian-Eulerian model was selected for the simulations performed in this dissertation. This Euler-Euler simulation strategy will be detailed in Chapter 2.

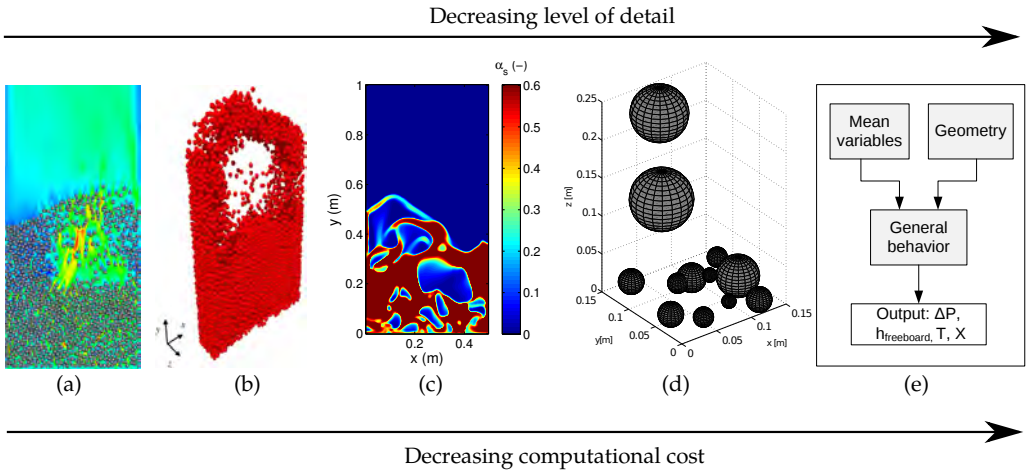


**Figure 1.5:** Simulation strategies of fluidized beds. (a) DNS, (b) DEM, (c) Two-fluid model, (d) DBM, (e) Pure phenomenological model. Adapted from Hernández-Jiménez (2013).

### Two-fluid model

In the last two decades, the use of two-fluid models for the understanding of fluidized beds hydrodynamics is emerging as an encouraging alternative given the advancement of computational capabilities. Two-fluid models can be solved with standard well known CFD techniques. The two-fluid modeling with the closure models of the Kinetic Theory of Granular Flow (KTGF), where the motion of the particles is defined analogously to the kinetic theory of gases (Gidaspow, 1994), is the most extended in the simulation of fluidized beds (Gidaspow, 1994; van Wachem & Almstedt, 2003). As an alternative to this model, Patil *et al.* (2004) evaluated the simpler Constant Viscosity Model (CVM), in which the solid phase viscosity is considered to be constant. Patil *et al.* (2004) studied the bubble dynamics (i.e. bubble diameter and velocity and visible bubble flow rate). They found that the KTGF results were in better agreement with the experimental data and correlations from the literature than the CVM.

Many works have demonstrated that the KTGF is the best option in two-fluid modeling. For example, using a commercial CFD software, Taghipour *et al.* (2005), studied the hydrodynamics of a gas-solid two-dimensional fluidized bed, characterizing the effects of the different gas-solid drag closure models and the restitution coefficient. Similarities between the hydrodynamics of simulations and experiments on the general bed behavior were found in the work by Taghipour *et al.* (2005).

Lim *et al.* (2006) studied the dynamics of a bubbling fluidized, given the fact the global understanding of this is regime of great importance for its control. An examination of the frequency content of the bed void and bubble fraction was performed in this work,

providing information about the physics of the bed dynamics. The introduction of simple empirical models had shown to give a good prediction of the state of a fluidized bed in terms of the bubble distribution and pressure fluctuations.

Busciglio *et al.* (2008*a*,*b*), making use of DIA techniques combined with two-fluid model simulations, characterized the bubble behavior in a pseudo-2D fluidized bed. Many features of the bubbles were studied in these works, that were used for the practical validation of the simulation code. These features comprised the time-average bed height, distribution of bubble diameters, bubble aspect ratio or bubble velocity. Global indicators were found to provide a good agreement between experimental conditions and bubble simulations.

Subsequent works (e.g. Hernández-Jiménez *et al.* (2011, 2013*a*); Acosta-Iborra *et al.* (2012); Cano-Pleite *et al.* (2015); Li (2015); Julián *et al.* (2016)) have shown the good predictive capacities and usefulness of two-fluid models.

The review presented above illustrates the great research activity concerning experiments and simulations of conventional fluidized beds. However, the literature regarding vibrated fluidized-beds is comparatively scarce. Studies in vibrated fluidized beds can be divided in two main branches, experimental and simulation studies, which are usually combined in the publications.

### 1.2.3 Experimental and numerical studies on vibrated fluidized beds

#### Experimental studies

There is an ongoing effort to experimentally understand the fundamental behavior of VFBs. Existing experimental studies in VFBs are mainly centered on beds working in bubbling regime (Eccles & Mujumdar, 1997; Zhou *et al.*, 2001, 2004, 2005; Mawatari *et al.*, 2005*a*) and beds with aggregation problems due to the utilization of fine powders (Barletta *et al.*, 2008; Barletta & Poletto, 2012). Global indicators such as the bubble mean diameter and velocity (Eccles & Mujumdar, 1997; Zhou *et al.*, 2001; Mawatari *et al.*, 2005*a*; Zhou *et al.*, 2005), air pressure and void fraction fluctuations (Barletta & Poletto, 2012), aggregate diameters (Barletta & Poletto, 2012), as well as solids circulation promoted by vibration (Zeilstra *et al.*, 2013) are included in these works. Some works have also investigated the effect of different vibration modes (e.g. vertical, horizontal and twist vibrations) in a fluidized bed (Mawatari *et al.*, 2001; Zhou *et al.*, 2001, 2004), revealing that both vertical and horizontal vibrations change the flow patterns and the bubble behavior in the bed. The size and distribution of bubbles within a fluidized bed are of great importance for the understanding of the bed dynamics.

Eccles & Mujumdar (1997) studied the influence of the vessel vibration on a train of bubbles injected through a central aperture in the distributor plate and for three different kinds of particles of type A, B and D. They found that there is a resonant frequency in which the bubble diameter reaches maxima whilst the bubble velocity passes through a minimum value. Also in Eccles & Mujumdar (1997), experiments in an incipiently fluidized bed with small bubbles above the distributor were conducted using particles of 100 $\mu$m, and they revealed that the bubble diameter increases and the bubble velocity decreases when increasing the vibration frequency at a constant vibration amplitude. Zhou *et al.* (2001) carried out experiments to study the particle flow pattern and its interaction with bubble paths, pressure drop and bed expansion ratio in a pseudo-2D bed filled with spherical particles of 198 $\mu$m and subjected to horizontal and vertical vibration. They found that, for gas fluidization velocities above the minimum fluidization conditions, the effect of sinusoidal vibration was only significant when applied in vertical direction. Zhou *et al.* (2004, 2005) measured the mean diameter and velocity of bubbles passing through two fringes of 2 cm in the upper half of a bubbling bed filled with particles of 198 $\mu$m and subject to high vibration amplitudes ($A > 5$ mm). Results in Zhou *et al.* (2004, 2005) show that, in those fringes, both the bubble diameter and velocity increase when introducing vibration in the system. These results are in agreement with the measurements performed by Mawatari *et al.* (2005*a*) concerning the mean bubble velocity and diameter of bubbles in a bed filled with particles of 60 $\mu$m mean diameter. Mawatari *et al.* (2005*a*) also observed that, for sufficiently high vibration strengths, the flow pattern changed and that affected the bubble behavior.

In contrast, the number of experimental works analyzing the oscillatory behavior of the bed bulk and bubbles in a vertically vibrated fluidized bed is still scarce (Wang *et al.*, 1997, 2000; Barletta *et al.*, 2013; Cano-Pleite *et al.*, 2014, 2015). Wang *et al.* (1997) studied the wave propagation in both a packed and a fluidized bed operated in bubbling regime. In their results, when the superficial gas velocity was below the minimum fluidization velocity, the interaction between the bed bulk and the distributor was by collision occurring locally at the base of the bed. However, when $U > U_{mf}$, the action of vibration on the bed was found to be through a continuous pressure wave propagation in a pseudo-continuous and pseudo-elastic medium. The wave propagation mechanism was further studied by Wang *et al.* (2000) in a vertically vibrated cylindrical bed of 200 mm inner diameter filled with particles of 20 $\mu$m mean diameter and fluidized with air. By the use of a set of pressure probes placed at different heights from the distributor, they studied the oscillations induced by vibration on the pressure of the air in the bed. They observed that in a VFB there exists a propagation of pressure waves originated at the base plate of the bed. According to their findings, these pressure waves are reflected at the surface of the bed, so that the wave energy is mainly dissipated in

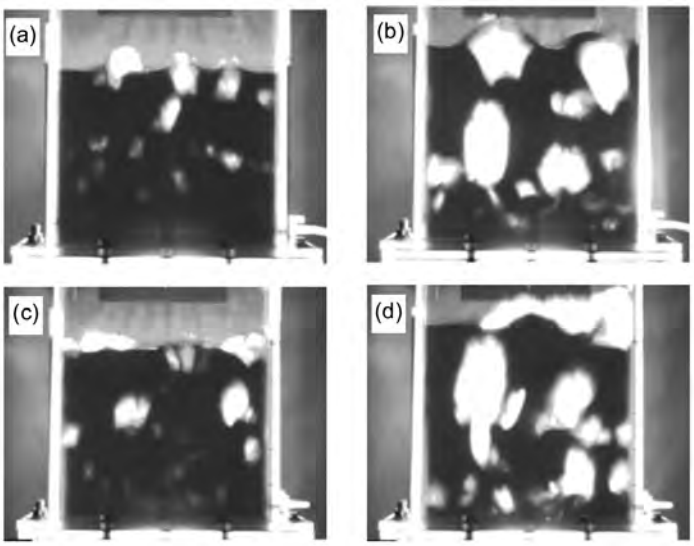


**Figure 1.6:** Bubble distribution for (a,c) low and (b,d) high superficial gas velocities in a vertically vibrated fluidized bed of particles with a mean diameter of $d_p = 198$ $\mu$m. (a,b) No vibration, (c,d) Vibration. From Zhou *et al.* (2005).

the bed. Regarding the oscillatory behavior of a vibrated fluidized bed, Barletta *et al.* (2013) studied the dynamic response of a vibrated fluidized bed of 85 mm of internal diameter filled with fine and cohesive powders of Geldart A and C classification. They characterized the oscillation of the bed height by means of DIA for a superficial gas velocity just above the minimum fluidization at the chosen vibration conditions. They observed that the phase delay between the bed vessel vibration and the bed height oscillation tended to increase when increasing the vibration frequency. When the bed was filled with particles until a static bed height of 0.27 m, they found a wide range of vibration frequencies that caused an opposition in phase between the bed height and the bed vessel, revealing a cyclic compression and expansion of the bed bulk.

In recent years, several works have analyzed the effect of vibration on particle segregation in processes involving vibrated fluidized beds, such as coal beneficiation (Luo *et al.*, 2008; He *et al.*, 2015), fine coal cleaning (Yang *et al.*, 2013) and lignite cleaning (Zhao *et al.*, 2015). In Luo *et al.* (2008) and He *et al.* (2015), a dense medium vibrated fluidized bed was employed for the separation of fine coal particles of different densities and sizes (<6 mm in Luo *et al.* (2008) and 1-3 mm, 3-6 mm in He *et al.* (2015)). In Luo *et al.* (2008), the segregation degree was measured after 20 s of separation time, whereas in He *et al.* (2015) the effect of the separation time was experimentally investigated by collecting the lignite of the bed at different time instants. These works showed that the separation performance for coal was improved when the gas and vibration operative

conditions of the vibrated fluidized bed were optimized.

### Numerical studies

Numerical simulation of fluidized beds can be employed as a tool to improve the understanding of the complex behavior of fluidized beds during vibration. Besides, once a simulation model is experimentally validated, it can also be used for the design and scale-up of vibrating fluidized beds due to the unrestricted availability of data, the lack of interferences and the null measurement errors present in the simulation. Two main kinds of models have been reported in the literature for the simulation of vibrated fluidized beds: the Lagrangian-Eulerian and the Eulerian-Eulerian models. Nearly all the reported simulations of VFBs resort to the Lagrangian-Eulerian model based on the discrete element modeling of the bed particles.

Tatemoto *et al.* (2004) and Xiang *et al.* (2010) employed the Lagrangian-Eulerian (CFD-DEM) method to simulate the motion of particles in a reduced two-dimensional VFB in which the bed thickness of the simulated bed was equal to the particle diameter and 1500 particles were considered. Particle velocity and concentration of particles were studied, giving a qualitative understanding of the VFB behavior and the vibration energy transmission (Xiang *et al.*, 2010). A study on gas velocity and the change of void fraction and pressure fluctuations as a function of the time under different vibration modules was carried out in the work by Tatemoto *et al.* (2004). However, as stated in Xiang *et al.* (2010), a quantitative understanding of this kind of results is difficult given the low number of particles employed in the simulations. Three-dimensional simulations were performed by Limtrakul *et al.* (2007) in a cylindrical vibrated fluidized bed of 2.41 mm of diameter filled with cohesive particles. The effects of particle type, superficial gas velocity and vibration amplitude and frequency on particle movement and velocity vectors were analyzed. More recently, Zeilstra *et al.* (2013) used combined PIV measurements and CFD-DEM simulations to study solid circulation rates in a pseudo-2D vibrated fluidized bed. Although the results obtained were in good qualitative agreement with the experiments and the literature, the bed size was still small (15 x 1.5 x 60 $cm^3$) and the particle size was relatively large (1 mm diameter) because of restrictions caused by the high computational cost of the CFD-DEM simulations.

As an answer to the difficulties of the Lagrangian-Eulerian (CFD-DEM) simulations, Acosta-Iborra *et al.* (2012) proposed the simulation of vibrated fluidized beds by solving the two-fluid (Eulerian-Eulerian) model CFD equations (Gidaspow, 1994; van Wachem & Almstedt, 2003) in a coordinate system that moves with the bed. Thus, vibration is transformed into acceleration terms that are introduced in the simulations as body forces in both the gas and particle phases. Using this methodology, the size of the bed

and number of particles represented by the two-fluid model can be increased dramatically compared to the Lagrangian-Eulerian alternatives, making affordable the numerical simulation of bigger VFBs facilities. Since particles are treated as a continuum interpenetrated by the gas phase in TFM simulations, additional closure models to those used in DEM simulations are required in two-fluid models to reproduce the particle-particle and particle-wall interactions (van Wachem & Almstedt, 2003). Normal frequencies of vibration (of order of 10 Hz) are smaller than the expected frequency of particle collision due to granular temperature, hence, the closure models of the bed are still valid for vibration.

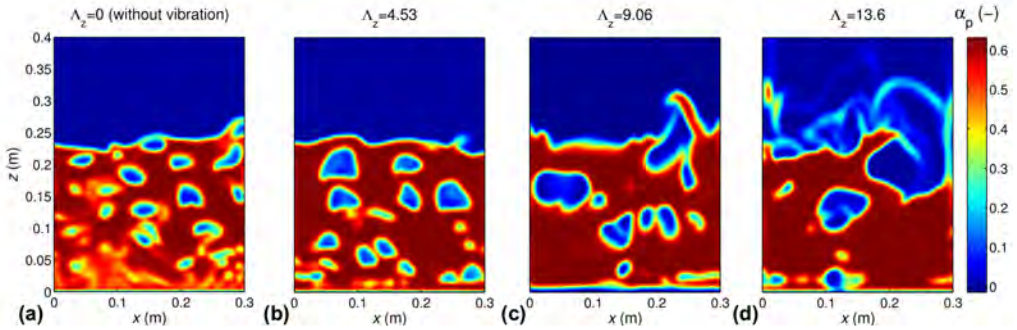


**Figure 1.7:** Example of snapshots of the solids volume fraction of two fluid model simulations of a vertically vibrated fluidized bed of particles with a mean diameter of $d_p = 198$ $\mu$m. The snapshots have been obtained from the two-fluid simulations at $f = 15$ Hz and different vibration strengths $\Lambda_z = A(2\pi f)^2/g$. From Acosta-Iborra *et al.* (2012).

The segregation phenomena have been also investigated by means of numerical simulations. Making use of the methodology proposed by Acosta-Iborra *et al.* (2012), Sun *et al.* (2014) studied, by means of 2D DEM simulations, the segregation induced by density of a mixture of particles of 1400 and 2000 kg/m$^3$ and similar size ($d_p = 3$ mm) in a gas fluidized bed of 0.15 x 0.7 m$^2$. When varying the operative conditions of the bed, they observed that segregation reached a maximum for certain vibration amplitudes, frequencies and superficial gas velocities. The time evolution of segregation during the 20 s of simulation time was analyzed. The final segregation index at the end of the simulation was found to decrease if the vibration amplitude, frequency or the superficial gas velocity were further increased beyond their optimal values.

## 1.3 Challenges on the understanding of vibrated fluidized beds

All the previously mentioned works represent a large step on the understanding of fluidized bed systems and, in particular, of vibrating fluidized beds. However, there are many topics regarding the dynamics of the bed bulk and the bubbles in a vibrated fluidized bed that are still not fully understood. The present dissertation aims at answering some of those questions by the use of experiments, modeling and numerical simulations.

Previous works in vibrated fluidized beds have shown a cyclic compression and expansion of the bed bulk and the presence of pressure waves traveling through the bed. However, it is not clear how the solid particles behave during these compression and expansion stages and the mutual interaction of the bubbles and the bed bulk motion. This interaction may have a profound impact on the bubble behavior depending on the vertical position of the bubble in the bed and the local bulk oscillation. Besides, the effect of vibration on the motion of solids around a bubble rising in a VFB is an unexplored topic. A fundamental study on the motion of solids around bubbles rising in a vibrated bed would not only provide information about that topic, but also provide valuable information regarding the volume of particles dragged by a bubble when the system is vibrated and give an explanation to the occurrence of the characteristic wavy contour of bubbles rising in VFBs.

Furthermore, to the author's best knowledge, results regarding the bubble characteristics in VFBs operated in bubbling regime are relatively scarce and provide only information in horizontal fringes at specific vertical coordinates in the bed. This complicates the elucidation of clear trends on the bubble behavior along the bed height and the direct effect of vibration on the mean and oscillatory behavior of bubbles present in the system.

Moreover, some works in the literature mentioned in Section 1.2 make use of the segregation properties of VFBs to separate mixtures in diverse fluidized bed processes. Nevertheless, these studies employ particles that differ in density and size. From the author's point of view, a fundamental understanding on the main mechanisms affecting density segregation in a vibrated fluidized bed is still needed.

Lastly, there is a lack of reported information concerning the effect of vibration on the particle motion in conical or analogous fluidized beds, though this configuration appears in common devices such as hoppers or spouted beds assisted by vibration.

## 1.4 Scope of the thesis

On view of the motivation, the state of the art and the challenges on the understanding of vibrated systems, the present PhD thesis is aimed at the following studies:

- The experimental characterization of the bed bulk oscillation in a pseudo-2D vibrated fluidized bed using DIA, PIV and numerical modeling techniques. This fundamental study can further clarify the origin and nature of vibration waves propagating in a fluidized bed.
- The development of a simplified 1-D model able to reproduce and help to better understand the bed bulk motion and the propagation of waves inside a vibrated fluidized bed at minimum fluidization conditions and with the same characteristics of the ones used in the experiments and the simulations.
- The use of DIA and two-fluid model simulation techniques for the characterization of the mean and oscillatory motion of an isolated bubble rising in a vibrated fluidized bed.
- The determination of the motion of solids and the pressure distribution around an isolated bubble rising in a vibrated fluidized bed by means of PIV and pressure signal analysis techniques.
- The understanding of the mean and the oscillatory behavior of the bed bulk and the bubbles in a vibrated fluidized bed operated in bubbling regime.
- The effect of vibration on the density segregation of particles of similar sizes in a vibrated fluidized bed.
- The solids motion and granular pattern formation in a vibrated fluidized bed of triangular shape.

## 1.5 Methodology

The methodology used in the present thesis combines the analysis of experimental, modeling and simulation data. Regarding the experimental data, DIA, PIV and pressure measurements were carried out in four different experimental facilities.

The experimental results presented in Chapters 3 and 4 were collected by the author in the pseudo-2D vibrated fluidized bed at the Department of Thermal and Fluid Engineering of Carlos III University of Madrid. This bed was especially designed and built for the accomplishment of the present PhD thesis. The experimental results presented

in Chapter 6 were obtained in one of the pseudo-2D vibrated fluidized beds present at the Department of Applied Chemistry of Kyushu Institute of Technology. Lastly, two fluidized beds were designed and constructed by the author at the Laboratory of Energy Science and Engineering of ETH Zürich, in order to obtain the experimental measurements shown in Chapter 7.

Concerning the numerical simulations, the two-fluid (Eulerian-Eulerian) model was used employing the open source code MFIX (Multiphase Flow with Interphase eXchages, NETL) for the solution of the governing equations. This code was selected in account of its good behavior in gas-solid fluidized beds simulations and also due to the unrestricted access and algorithm modification allowed by the code. The simulations were carried out in personal computers, the workstation *Ipy* and the cluster *Caracol*, all of them at the Department of Thermal and Fluid Engineering of Carlos III University of Madrid.

Except for the MatPIV code used for the PIV technique in Chapters 3 and 5, all the postprocessing codes were developed by the author. The Matlab® software platform was used to develop the codes and create the graphics of results.

The bibliographic references used in this PhD thesis were obtained thanks to subscription to databases and science journals provided by Carlos III University of Madrid as well as the books available at the library of this same institution.

## 1.6 Outline of the thesis

The thesis is structured attending to the globality of the results, from more fundamental to more global. Thus, the chapters are ordered as studies on the: bed bulk, isolated bubbles, beds operated in bubbling regime and applications of vibrated fluidized beds. This order was not chronologically followed by the author during the accomplishment of the present PhD thesis but was selected in this document attending to the different questions and needs that progressively arose when presenting the results of VFBs.

After a first introductory chapter of fluidization and vibrated fluidized beds, Chapter 2 describes the different experimental setups and the data processing techniques used along the present contribution.

In the third chapter of this dissertation, the oscillatory motion of the bed bulk is experimentally studied. Thanks to the use of combined DIA and PIV techniques, the effect of vibration on the bed bulk motion was characterized. It could be observed that there exist compression and expansion waves of solids that travel inside the bed bulk that modify the way the particles behave inside the bed. This promotes different relative velocities of particles in the upper and lower sections of the bed. A simple 1-D model, used to characterize the oscillatory displacement and the wave propagation mechanism in a vertically vibrated fluidized bed, is also presented in Chapter 3 and the results are

compared with experimental evidence and a two-fluid model simulation.

Chapter 4 attends to the motion of isolated bubbles in the VFB as affected by the bed vessel vibration. This is done by a threefold way. Firstly, the effect of vibration on the mean bubble characteristics was assessed by virtue of DIA and PIV techniques. The results showed that there exists a phase delay of the bubble characteristics between the upper and the lower sections of the bed, revealing that the bubbles are strongly affected by the cyclic compression and expansion mechanism observed in Chapter 3. The DIA results presented in Chapter 4 were compared, in this same chapter, with numerical evidences using compressible and incompressible gas models. It is shown that the compressible gas model simulations are in good agreement with the experiments, whereas the incompressible gas model simulations fail to predict the bed and bubble behavior.

Chapter 5 presents results concerning the motion of solids and the pressure distribution around an isolated bubble rising in a VFB. The PIV results depicted in this chapter confirm the applicability of the Davidson & Harrison (1963) potential flow model for the solids motion and the pressure distribution around the bubble in spite of the fact the bed is vertically vibrated.

Once the motion of an isolated bubble rising alone in the bed has been studied. The mean and oscillatory behavior of the bed bulk and individual bubbles rising in a VFB operated in bubbling regime is studied in Chapter 6. This allowed to determine the effect of vibration on a bed in which multiple bubbles interact with each other. It was observed that the bubble behavior changes as a function of the distance to the distributor, revealing, as in the case of isolated bubbles, the existence of a phase delay between the oscillations of bubble characteristics in the lower and upper sections of the bed.

Chapter 7 studies the effect of vibration on the fundamentals on two applications of vibrated fluidized beds. In the first section of Chapter 7, the segregation of a bed filled with particles of the same size and different densities is studied. In the second section of Chapter 7, the effect of the injection of gas in a vibrated bed of triangular shape and the appearance of granular patterns appearing in the bed is studied.

Finally, the results obtained in this thesis and the future prospects are summarized in Chapter 8.

The chart shown in Figure 1.8 schematizes the structure and overall scope of the thesis.

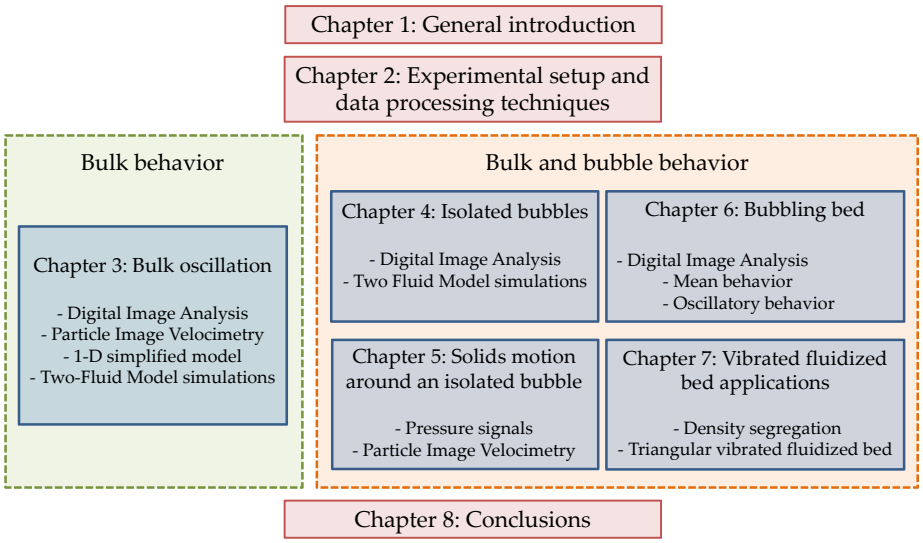


**Figure 1.8:** Chart describing the structure and scope of the thesis.

# References

Acosta-Iborra, A., Hernández-Jiménez, F., de Vega, M. & Briongos, J.V. 2012 A novel metodology for simulating vibrated fluidized beds using two-fluid models. *Chem. Eng. J.* 198-199, 261–274.

Almendros-Ibáñez, J.A., Sobrino, C., de Vega, M. & Santana, D. 2006 A new model for ejected particle velocity from erupting bubbles in 2-d fluidized beds. *Chem. Eng. Sci.* 61, 5981–5990.

Barletta, D., Donsi, G., Ferrari, G., Poletto, M. & Russo, P. 2008 The effect of mechanical vibration on gas fluidization of a fine aeratable powder. *Chem. Eng. Res. Des.* 86, 359–369.

Barletta, D. & Poletto, M. 2012 Aggregation phenomena in fluidization of cohesive powders assisted by mechanical vibrations. *Powder Technol.* 2012, 93–100.

Barletta, D., Russo, P. & Poletto, M. 2013 Dynamic response of a vibrated fluidized bed of fine and cohesive powders. *Powder Technol.* 237, 276–285.

Bi, H. 2007 A critical review of the complex pressure fluctuation phenomenon in gas-solids fluidized beds. *Chem. Eng. Sci* 62, 3473–3493.

Briongos, J. V., S anchez Delgado, S., Acosta-Iborra, A. & Santana, D. 2011 A novel approach for modeling bubbling gas-solid fluidized beds. *AIChE Journal* 57(7), 1733– 1750.

Buist, K.A., van der Gaag, A.C., Deen, N.G. & Kuipers, J.A.M. 2014 Improved magnetic particle tracking technique in dense gas fluidized beds. *AIChE J.* 60(9), 3133–3142.

Busciglio, A., Giuseppa, V., Micale, G. & Rizzuti, L 2008*a* Analysis of the bubbling behavior of 2D gas-solid fluidized beds part II: Comparison between experiments and numerical simulations via digital image analysis technique. *Chem. Eng. J.* 148, 145–163.

Busciglio, A., Vella, G., Micale, G. & Rizzuti, L. 2008*b* Analysis of the bubbling behaviour of 2D gas solid fluidized beds: Part I. digital image analysis technique. *Chem. Eng. J.* 140, 398–413.

Cano-Pleite, E., Hernández-Jiménez, F. & Acosta-Iborra, A. 2015 Compressible-gas two-fluid modeling of isolated bubbles in a vertically vibrated fluidized bed and comparison with experiments. *Chem. Eng. J.* 271, 287–299.

Cano-Pleite, E., Hernández-Jiménez, F., de Vega, M. & Acosta-Iborra, A. 2014 Experimental study on the motion of isolated bubbles in a vertically vibrated fluidized bed. *Chem. Eng. J.* 255, 287–299.

Cano-Pleite, E., Shimizu, Y., Acosta-Iborra, A. & Mawatari, Y. 2016 Effect of vertical vibration and particle size on the solids hold-up and mean bubble behavior in a pseudo-2D fluidized bed. *Chem. Eng. J.* 304, 384–398.

Coppens, M.O. & van Ommen, J.R. 2003 Structuring chaotic fluidized beds. *Chem. Eng. J.* 96, 117–124.

Croxford, A.J. & Gilbertson, M.A. 2011 Pressure fluctuations in bubbling gas-fluidized beds. *Chem. Eng. Sci.* 66(16), 3569–3578.

Cundall, P.A. & Strack, O.D.L. 1979 Discrete numerical-model for granular assemblies. *Geotechnique* 29, 47–65.

Dang, T.Y.N., Kolkman, T., Gallucci, F. & van Sint Annaland M. 2013 Development of a novel infrared technique for instantaneous, whole-field, non invasive gas concentration measurements in gas-solid fluidized beds. *Chem. Eng J.* 219, 545–557.

Davidson, J.F. & Harrison, D. 1963 *Fluidised Particles*. Cambridge University Press, Cambridge.

Deen, N.G., Van Sint Annaland, M., Van der Hoef, M.A. & Kuipers, J.A.M. 2007 Review of discrete particle modeling of fluidized beds. *Chem. Eng. Sci.* 62, 628–44.

Eccles, E.R.A. & Mujumdar, A.S. 1997 Bubble phenomena in aerated vibrated beds of small particles. *Drying Technol.* 15:1, 95–116.

Geldart, D. 1973 Types of gas fluidization. *Powder Technol.* 7, 285.

Gidaspow, D. 1994 *Multiphase flow and Fluidization*. Academic Press. Boston.

Glicksman, L.R., Lord, W.K. & M., Sakagami 1987 Bubble properties in large-particle fluidized beds. *Chem. Eng. Sci.* 42, 479–491.

Gupta, R. & Mujumdar, A.S. 1980 Aerodynamics of a vibrated fluid bed. *Can. J. Chem. Eng.* 58, 332–338.

He, J., Zhao, Y., Zhao, J., Luo, Z., Duan, C. & He, Y. 2015 Separation performance of fine low-rank coal by vibrated gas-solid fluidized bed for dry coal beneficiation. *Particuol.* 23, 200–108.

Hernández-Jiménez, F., Gómez-García, A., Santana, D. & Acosta-Iborra, A. 2013*a* Gas interchange between bubble and emulsion phases in a 2D fluidized bed as revealed by two-fluid model simulations. *Chem. Eng. J.* 215-216, 479–490.

Hernández-Jiménez, F., Sánchez-Delgado, S., Gómez-García, A. & Acosta-Iborra, A. 2011 Comparison between two-fluid model simulations and particle image analysis & velocimetry (PIV) results for a two-dimensional gas-solid fluidized bed. *Chem. Eng. Sci.* 66, 3753–3772.

Hernández-Jiménez, F., Sánchez-Prieto, J., Soria-Verdugo, A. & Acosta-Iborra, A. 2013*b* Experimental quantification of the particle-wall frictional forces in pseudo-2D gas fluidised beds. *Chem. Eng. Sci.* 102, 257–267.

Hernández-Jiménez, F. 2013 Numerical and experimental investigations on pseudo-2D gas fluidized beds. *PhD. Thesis* .

Ishida, M. & Shirai, T. 1980 Measurement of the velocity and direction of flow of solid particles in a fluidized bed. *Powder Technol.* 27, 1–6.

Jovanovic, G.N. & Jovanovic, Z.R. 1993 Bubble size and fluidization regimes in magnetically controlled fluidized beds. In *AIChE Annual Meeting, St. Louis, MO, U.S.A.*.

Julián, I., Herguido, J. & Menéndez, M. 2016 Experimental and simulated solids mixing and bubbling behavior in a scaled two-section two-zone fluidized bed reactor. In *Chem. Eng. Sci.*, , vol. 143, pp. 240–255.

Kuipers, N.J.M., Stamhuis, E.J. & Beenackers, A.A.C.M. 1996 Fluidization of potato starch in a stirred vibrated fluidized bed. *Chem. Eng. Sci.* 51, 2727–2732.

Ladd, A.J.C. & Verberg, R. 2001 Lattice-boltzmann simulations of particle fluid suspensions. *J. of Statistical Physics* 104, 1191–1251.

Latifi, M., Berruti, F. & Briens, C. 2014 A novel fluidized and induction heated microreactor for catalyst testing. *AIChE J.* 60, 3107–3122.

Laverman, J.A., Roghair, H., van Sint Annaland, M. & Kuipers, H. 2008 Investigation into the hydrodynamics of gas-solid fluidized beds using particle image velocimetry coupled with digital image analysis. *Can. J. Chem. Eng.* 86, 523–535.

Li, Tingwen 2015 Validation of a 2.5d cfd model for cylindrical gas–solids fluidized beds. *Powder Technol.* 286, 817–827.

Li, T. & Zhang, Y. 2013 A new model for two-dimensional numerical simulation of pseudo-2D gas–solids fluidized beds. *Chem. Eng. Sci.* 102, 246–256.

Lim, C.N., Gilberston, M.A. & Harrison, A.J.L. 2006 Measurement and simulation of bubbling fluidised beds. *Powder Technol.* 170, 167–177.

Limtrakul, S., Rotjanavijit, W. & Vatanatham, T. 2007 Lagrangian modeling and simulation of effect of vibration on cohesive particle movement in a fluidized bed. *Chem. Eng. Sci.* 62, 232–245.

Lin., J.S., Chen, M.M. & Chao, B.T. 1985 A novel radioactive particle tracking facility for measurement of solids motion in gas fluidized beds. *AIChE Journal* 31(3), 465–473.

Luo, Z.F., Fan, M.M., Zhao, Y.M., Tao, X.X., Chen, Q.R. & Chen, Z.Q. 2008 Density-dependent separation of dry fine coal in a vibrated fluidized bed. *Powder Technol.* 187, 119–123.

Makkawi, Y.T. & Wright, P.C. 2002 Fluidization regimes in a conventional fluidized bed characterized by means of electrical capacitance tomography. *Chem. Eng. Sci.* 57, 2411–2437.

Mathiesen, V., Solberg, T. & Hjertager, B.H. 2000 An experimental and computational study of multiphase flow behavior in a circulating fluidized bed. *Int. J. Multiphase Flow* 26, 387–419.

Mawatari, Y., Koide, T., Tatemoto, Y., Takeshita, T. & Noda, K. 2001 Comparison of three vibrational modes (twist, vertical and horizontal) for fluidization of fine particles. *Adv. Powder Technol.* 2, 157–168.

Mawatari, Y., Tagawa, K., Tatemoto, Y. & Noda, K. 2005*a* Bubbling characteristics under vertical vibration in a two-dimensional fluidized bed. *Chem. Eng. Jpn.* 38, 18–23.

Mawatari, Y., Tatemoto, Y. & Noda, K. 2003 Prediction of minimum fluidization velocity for vibrated fluidized bed. *Powder Technol.* 131, 66–70.

Mawatari, Y., Tsunekawa, M., Tatemoto, Y. & Noda, K. 2005*b* Favorable vibrated fluidization conditions for cohesive fine particles. *Powder Technol.* 154, 54–60.

Mori, S., Yamamoto, A., Iwata, S., Haruta, T., Yamada, I. & Mizutani, E. 1990 Vibro-fluidization of group c particles and its industrial applications. *AlChE Symp. Series.* 86, 88–94.

Morley, D.B. 1991 Evaluation of vibrated fluidized bed techniques in coating hemosorbents. *Int. J. Artif. Organs* 14(6), 371–9.

Mudde, R.F. 2010 Time-resolved x-ray tomography of a fluidized bed. *Powder Technol.* 199(1), 55–59.

Mujumbar, A.S. 1987 *Handbook of Industrial Drying*. Marcel Dekker, New York.

Müller, C.R., Davidson, J.F., Dennis, J.S. & Hayhurst, A.N. 2007 A study of the motion and eruption of a bubble at the surface of a two-dimensional fluidized bed using particle image velocimetry (PIV). *Ind. Eng. Chem. Res.* 46, 1642–1652.

Müller, C.R., Holland, D.J., Sederman, A.J., Scott, S.A., Dennis, J.S. & Gladden, L.F. 2008 Granular temperature: Comparison of magnetic resonance measurements with discrete element model simulations. *Powder Technol.* 203, 241–253.

Nakamura, H., Kondo, T. & Watano, S. 2013 Improvement of particle mixing and fluidization quality in rotating fluidized bed by inclined injection of fluidizing air. *Chem. Eng. Sci.* 91, 70–78.

Nelson, R.J., Flakker, C.L. & Muggli, D.S. 2007 Photocatalytic oxidation of methanol using titania-based fluidized beds. *Appl Catal B.* 69(3-4), 189–195.

Noda, K., Mawatari, Y. & Uchida, S. 1998 Flow patterns of fine particles in a vibrated fluidized bed under atmospheric or reduce pressure. *Powder Technol.* 99, 11–14.

Nowak, W., Hasatani, M. & Derczynski, M. 1993 Fluidization and heat transfer of fine particles in an acoustic field. *AIChE Symp. Ser.* 89, 137–149.

van Ommen, J.R., Valverde, J.M. & Pfeffer, R. 2012 Fluidization of nanopowders: a review. *J. Nanopart. Res.* 314, 737.

van Ommen, R. J. & Mudde, R.F. 2008 Measuring the gas-solids distribution in fluidized beds – a review. *Int. J. Chem. R. Eng.* 6, R1.

van Ommen, R. J., Sasic, S., van der Schaaf, J., Gheorghiu, S., Johnsson, F. & Coppens, M.O. 2011 Time-series analysis of pressure fluctuations in gas-solid fluidized beds - a review. *Int. J. Multiphase Flow* 37, 403–428.

Pan, X., Ye, S., Zhang, Z., Zhang, L. & Zhu, X. 2009 A study of spray granulation in vibrated fluidized bed with internal heating tubes. *Front. Chem. Eng. China* 3, 78.

Patil, D.J., van Sint Annaland, M. & Kuipers, J.A.M. 2004 Critical comparison of hydrodynamics models for gas-solid fluidized beds- partii: freely bubbling gas-solid fluidized beds. *Chem. Eng. Sci.* 60, 73–84.

Rosenweig, R.E. 1979 Fluidization: hydrodynamic stabilization with a magnetic field. *Science* 204, 57–60.

Sadiq, S.A. & Asif, M. 2012 Fluidization of nano-powders: Effect of flow pulsation. *Powder Technol.* 225, 86–92.

Sánchez-Delgado, S., Marugán-Cruz, C., Acosta-Iborra, A. & Santana, D. 2010 Dense-phase velocity fluctuation in a 2-d fluidized bed. *Powder Technol.* 200, 37–45.

Santana, D., Nauri, S., Acosta, A., Garcia, N. & Macias-Machín, A. 2005 Initial particle velocity spatial distribution from 2-d erupting bubbles in fluidized bed. *Powder Technol.* 150, 1–8.

Sasic, S., Leckner, B. & Johnsson, F. 2007 Characterization of fluid dynamics of fluidized beds by analysis of pressure fluctuations. *Prog. Energy Combust. Sci.* 33, 453–496.

van der Schaaf, J., Schouten, J.C. & van den Bleek, C.M. 1998 Origin, propagation and attenuation of pressure waves in gas-solid fluidized beds. *Powder Technol.* 95, 220–233.

Sette, E., Pallarès, D., Johnsson, F., Ahrentorp, F., Ericsson, A. & C., Johansson 2015 Magnetic tracer-particle tracking in a fluid dynamically down-scaled bubbling fluidized bed. *Fuel Process. Technol.* 138, 368–377.

Sharma, A.K., Tuzla, K., Matsen, J. & Chen, J.C. 2000 Parametric effects of particle size and gas velocity on cluster characteristics in fastfluidized beds. *Powder Technol.* 111, 114–122.

Shen, L., Johnsson, F. & Leckner, B. 2004 Digital image analysis of hydrodynamics two-dimensional bubbling fluidized beds. *Chem. Eng. Sci.* 59, 2607–2617.

Sobrino, C., Almendros-Ibáñez, J.A., Santana, D. & de Vega, M. 2008 Fluidization of group b particles with a rotating distributor. *Powder Technol.* 181, 273–280.

Solimene, R., Marzocchella, A., Passarelli, G. & Salatino, P. 2006 Assessment of gas-fluidized beds mixing and hydrodynamics by zirconia sensors. *AIChE Journal* 52, 185–198.

Squires, A.M. 2004 Chemical process opportunities for vibrated powders: 2. in the field. *Powder Technol.* 147(1-3), 10–19.

Strumillo, C. & Pakowski, Z. 2007 *Particle Image Velocimetry, A Practical Guide.* Springer, Berlin.

Sun, L., Zhao, F., Zhang, Q., Li, D. & Lu, H. 2014 Numerical simulation of particle segregation in vibration fluidized bed. *Chem. Eng. Technol.* 37(12), 2109–2115.

Taghipour, F., Ellis, N. & Wong, C. 2005 Experimental and computational study of gas-solid fluidized bed hydrodynamics. *Chem. Eng Sci.* 60, 6857–6867.

Tatemoto, Y., Mawatari, Y., Yasukawa, T. & Noda, K. 2004 Numerical simulation of particle motion in vibrated fluidized bed. *Chem. Eng. Sci.* 59, 437–447.

Third, J.R., Chen, Y. & Müller, C.R. 2016 Comparison between finite volume and lattice-boltzmann method simulations of gas-fluidised beds: bed expansion and particle–fluid interaction force. *Comp. Part. Mech.* 3, 373.

Tsuji, Y., Tanaka, T. & T., Ishida 1992 Lagrangian numerical-simulation of plug flow of cohesionless particles in a horizontal pipe. *Powder Technol.* 71, 239–250.

van Wachem, B.G.M & Almstedt, A.E. 2003 Methods for multiphase computational fluid dynamics. *Chem. Eng. J.* 96, 81–98.

Wang, T.J., Jin, Y., Tsutsumi, A., Wang, Z. & Cui, Z. 2000 Energy transfer mechanism in a vibrating fluidized bed. *Chem. Eng. J.* 78, 115–123.

Wang, T., Jin, Y., Wang, Z. & Yu, Z. 1997 The characteristics of wave propagation in a vibrating fluidized bed. *Chem. Eng. Technol.* 20, 606–611.

Xiang, L., Shuyan, W., Huilin, L., Goudong, L., Juhui, C. & Yikun, L. 2010 Numerical simulation of particle motion in vibrated fluidized beds. *Powder Technol.* 197, 25–35.

Yang, X., Zhao, Y., Luo, Z., Song, S., Duan, C. & Dong, L. 2013 Fine coal dry cleaning using a vibrated gas-fluidized bed. *Fuel Process. Technol.* 106, 338–343.

Zeilstra, C., van der Hoef, M.A. & Kuipers, J.A.M. 2013 Experimental and numerical study of solids circulation in gas-vibro fluidized beds. *Powder Technol.* 248, 153–160.

Zhao, P., Zhao, Y., Chen, Z. & Luo, Z. 2015 Dry cleaning of fine lignite in a vibrated gas-fluidized bed: Segregation characteristics. *Fuel* 142, 274–282.

Zhou, T., Kage, H., Funaoka, S., Ogura, H. & Matsuno, Y. 2001 Fluidization behaviour of glass beads under different vibration modules. *Adv. Powder Technol.* 12, 559–575.

Zhou, T., Kage, H. & Li, H. 2005 Bubble characteristics in a two-dimensional vertically vibro-fluidized bed. *China Partic.* 3, 224–228.

Zhou, T., Ogura, H., Yamamura, M. & Kage, H. 2004 Bubble motion pattern and rise velocity in two-dimensional horizontal and vertical vibro-fluidized beds. *Can. J. Chem. Eng.* 82, 236–242.

CHAPTER
**TWO**

# Experimental setups, numerical modeling and data processing

**Contents**



## 2.1 Experimental setups

Four different experimental installations were used along this PhD thesis. The first installation is a pseudo-2D bed in which the bed bulk and the isolated bubble analyses were carried out (Chapters 3, 4 and 5). A different pseudo-2D bed was used for the bubbling bed analysis. These results are shown in Chapter 6. Finally, two additional beds were employed in Chapter 7: one to study the segregation in a vibrated fluidized bed and another to characterize the formation of granular patterns in a triangular pseudo-2D bed.

### 2.1.1 Vibrated fluidized bed for bulk and isolated bubble characterization

The pseudo-2D bed used for the analysis of the bulk motion and the behavior of isolated bubbles in Chapters 3, 4 and 5, was built *ad-hoc* for the investigations of the present PhD thesis in the Department of Thermal and Fluid Engineering, Carlos III University of Madrid. The facility consisted of a pseudo-2D bed of dimensions 0.3 x 0.6 x 0.01 $m^3$ (width W, height H and thickness K, respectively). The bed vessel was placed on a vibrating structure that was built in the framework of a previous research project. Figure 2.1 shows a sketch of the experimental facility. The front and rear walls of the bed were made of glass and the rear wall was painted in black to increase contrast of the front images. The fluidizing gas was air, which was injected to the bed through a gas distributor consisting of 20 aligned holes of 1 mm that are spaced 1.5 cm apart. The pressure drop of the gas distributor was experimentally measured and follows the quadratic law $\Delta P_d = 7.6 \cdot 10^4 U^2$, with $\Delta P_d$ in Pa and $U$ in m/s. The gas mass flow was measured by means of two different mass flow meters: either a mass flow meter with a resolution of 1 L/min (0.005 m/s) or one with a resolution of 2 L/min (0.01 m/s).

Two different digital cameras (either a CCD camera or a high speed camera) were employed to record images of the front view of the bed bulk at different frame rates. The camera was mounted on a tripod that was not subjected to vibration. Two spotlights were symmetrically placed at each side of the bed to provide a uniform illumination of the bed bulk. Two accelerometers (Brüel and Kjaer 4507 B005/30092) were connected to the plenum in order to measure *in situ* the amplitude and frequency of the vertical and transversal vibrations of the bed. In the experiments of Chapter 5, in addition to the accelerometers, two pressure probes (Kistler 7261 with a Kistler amplifier 5015) were attached to the rear wall of the bed at a vertical distance of $y_{p1} = 0.15$ m and $y_{p2} = 0.25$ m above the distributor. The output coming from the accelerometers and the pressure probes were connected to a PC through an acquisition card NI 9233. The software Labview® was used for the storage and monitoring of the data acquired. The accelerometry and the pressure signals were simultaneously acquired at 2000 Hz. However, these acquisitions were not automatically synchronized with the captured images. In order to synchronize the exact vertical displacement of the bed with the image acquisition at any time, an optical method was used. It consisted of small square films glued to the front wall of the bed near its upper corners or to the plenum. The vertical instantaneous position of the whole bed was obtained from the vertical position of the centroids of the squared films, calculated for each image using DIA. The vibration frequency obtained by means of DIA was calculated by performing a frequency domain analysis (Welch periodogram) of the instantaneous position of the bed and was always

in agreement with the main vibration frequency obtained from the vertical component of the accelerometry signal. The transversal components of the accelerometry signal were very low compared to the vertical component, and the left corner square moves identically to the right corner square, indicating that the vibration of the system was correctly aligned in the vertical direction. Since the bed vessel followed a sinusoidal displacement, the equivalent amplitude and velocity of vibration of the bed vessel for each experiment was calculated as:

$$A_{eq} = \sigma_{\delta(t)}\sqrt{2} \tag{2.1}$$

$$V_{eq} = \sigma_{v(t)}\sqrt{2} \tag{2.2}$$

where $\delta(t)$ is the instantaneous bed vessel displacement, $v(t) = d\delta(t)/dt$ is the instantaneous velocity of the bed vessel and $\sigma$ is the standard deviation of the time evolution of $\delta$ or $v$ with regard to their mean.

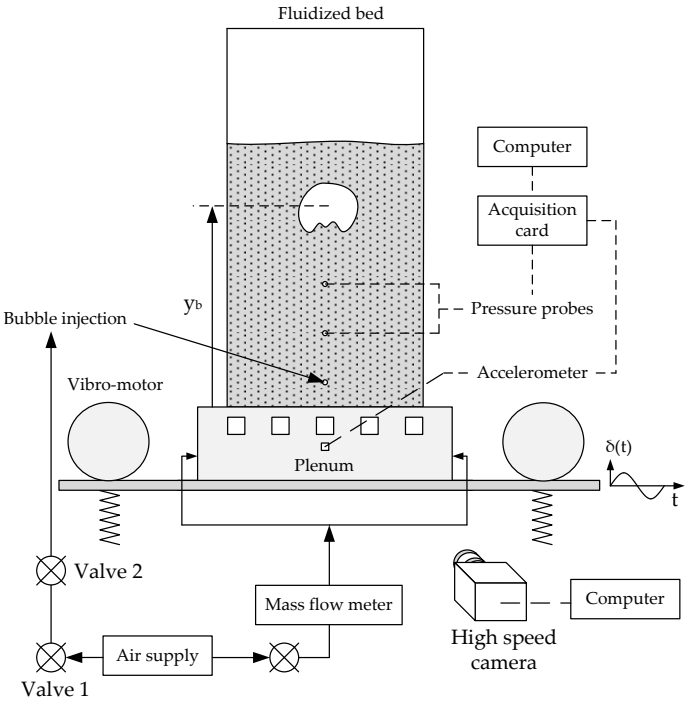


**Figure 2.1:** Sketch of the experimental facility used in Chapters 3, 4 and 5.

To induce vibration on the bed, two vibro-motors (Italvibras MVSI 10/310 SO2) were symmetrically disposed at both sides of the bed on a horizontal structure on which the

bed vessel was firmly attached (Figure 2.1). The amplitude of the vibration displacement was regulated by the variation of the relative position of two groups of two masses inside each of the vibro-motors, obtaining the maximum amplitude when the masses positions were aligned. Setting an exact value of the vibration amplitude was not trivial. The relative position of the masses was set manually at graduated angles of finite resolution marked by the manufacturer on the vibro-motor. Thus, only rounded values of this scale were used in order to minimize the chance of misalignment between the masses of the two vibro-motors. The vibration frequency was controlled by changing the turning velocity of the motors, using a variable frequency drive that allowed the variation of the frequency of excitation between 0 and 50 Hz. The oscillating frequency of the system was proportional to the excitation frequency, and the top frequency of vibration of the bed was 17.2 Hz. However, variations of the frequency affected the amplitude of vibration for a given relative position of the masses of the vibro-motors, which complicated the fixing of the amplitude of vibration while varying the frequency. Note that resonance frequencies of the facility, which were at about 5 Hz and their harmonics, were avoided during the measurements in all the chapters.

Two air supply lines were employed in this bed (see Figure 2.1). The first line was connected to the plenum of the vibrated bed and the air flow rate was adjusted for each experiment to reach minimum fluidization conditions. The secondary air supply line was connected to a hole drilled in the rear part of the bed, which was 5 cm above the distributor. Bubbles were created in the bed by fast opening and closing of a valve in the secondary air supply in Chapter 4, whereas a more controlled volume of gas injection was used in Chapter 5 by controlling the pressure and volume of gas confined between two valves (see Valve 1 and Valve 2 in Figure 2.1).

### 2.1.2 Vibrated bed for freely bubbling operation

The experimental facility used in Chapter 6 belongs to the Department of Applied Chemistry at Kyushu Insitute of Technology (Japan). This facility is a pseudo-2D bed of vessel dimensions 0.2 x 1.3 x 0.01 $m^3$ (width $W$, height $H$, and thickness $K$). The top section of the bed vessel is firmly attached to a vibrating structure (see Figure 2.2). All the vessel walls are transparent to allow optical access to the bed. Dry nitrogen ($N_2$) was employed as fluidizing gas to eliminate the moisture effect, which allows the use of the facility for a broad range of bed materials, including particles of small size (e.g. Geldart A particles). Nevertheless, as $N_2$ properties are quite similar to those of air, no significant variation of the results would be expected if dry air were used instead of $N_2$. The nitrogen was introduced to the bed through a porous plate distributor made of sintered stainless steel with nominal filtration accuracy equal to 2 $\mu$m, which produced a

uniform generation of bubbles in the lower section of the bed. The pressure drop of the gas distributor was experimentally measured and follows the linear law $\Delta P_d = 3.4 \cdot 10^4 U$. The flow rate of nitrogen introduced to the bed was controlled by means of a mass flow controller, which had a resolution of 0.1 L/min ($8.3 \cdot 10^{-4}$ m/s).

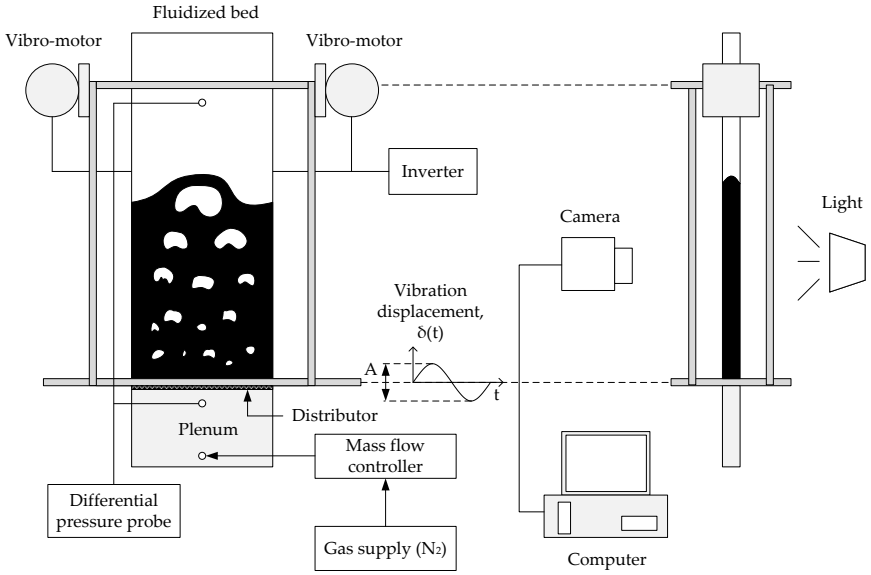


**Figure 2.2:** Sketch of the experimental facility used in Chapter 6.

Vibration was induced to the system by means of two vibro-motors symmetrically situated at both sides of the bed (see Figure 2.2). As in Section 2.1.1, each vibro-motor had two pair of eccentric masses attached to its shaft, so that their rotation produced a sinusoidal displacement (vibration) of the bed vessel in the vertical direction, $\delta(t) = A \sin(2\pi f t)$. The amplitude of the vibration, $A$, was set by changing the relative position of the eccentric masses. The frequency of the vibration, $f$, was controlled by a frequency inverter that set the turning frequency of the two vibro-motors. The amplitude of the vibration was measured with a vibration meter (Showa 1332). The amplitude of vibration was also measured with DIA (Digital Image Analysis) by following the displacement of several small circular openings in the bed vessel structure, which let the light penetrate and allowed for the determination of the bed instantaneous position. The vibration meter was used to monitor the vibration amplitude of the bed vessel of the experiments, whereas DIA was employed to give a more exact figure of this vibration amplitude. It was observed that the two measures led to results that differ only slightly.

The bed and bubble behavior were measured using DIA of the front section of the bed. Images were taken by a high speed CCD camera (Fastcam 1024pci). To obtain a good

contrast between the bubbles and the emulsion phase, the bed was uniformly illuminated through its back wall using two spotlights, each one of 180 W. The light was able to penetrate through the bubbles, making their contours easily distinguishable from the emulsion phase. The bed was first fluidized with nitrogen, and then vibration of the bed was produced by the vibro-motors several seconds before triggering the camera to avoid recording of start-up effects. The spatial resolution of the images was approximately 0.4 mm side per pixel for all the experiments performed.

### 2.1.3 Vibrated bed for the characterization of particle segregation

The segregation experiments analyzed in Chapter 7 were conducted in a pseudo-2D bed of dimensions 0.2 x 0.5 x x 0.01 $m^3$ (width $W$, height $H$, and thickness $K$), as shown in Figure 2.3. The bed was constructed by the author in the Laboratory of Energy Science and Engineering at ETH Zürich (Switzerland). The walls of the bed were constructed of anti-static PMMA in order to allow optical access to the bed. The fluidizing gas was air, which was continuously introduced at the bottom of the bed through a perforated plate distributor with 50 holes of 0.7 mm of diameter. The pressure drop of the gas distributor was experimentally measured and follows the quadratic law $\Delta P_d = 2.1 \cdot 10^4 U^2$. The air flow rate was controlled by a pressure regulator and it was measured by means of a mass flow controller (Analyt−MTC 35816). A gas humidifier was situated between the mass flow meter and the bed plenum to eliminate static forces arising between the different types of particles used in Chapter 7. In all the cases, the amount of humidity introduced was small and did not create agglomeration of particles, which were of type D according to Geldart's classification.

The bed was mounted onto an electrodynamic shaker (Labworks Inc., ET-139), which generated vibration in the form of a vertical sinusoidal displacement $\delta(t) = A\sin(2\pi ft)$. A controller (Labworks Inc. VL−144), an amplifier (Labworks Inc., PA−138−1) and an accelerometer (PCB Piezotronics Inc., J352C33) were used to control and monitor the semi-amplitude, $A$, and frequency, $f$, of vibration. Four square pieces of paper were glued on the front wall of the bed as a reference to obtain the instantaneous position of the bed vessel. The front part of the bed was uniformly illuminated by two LED spotlights symmetrically disposed at each side of the bed. A high speed CCD camera (Optronics CL 600 x2/M) was used to record images of the bed through its front wall at a frame rate of 50 images per second. DIA of the captured images was used to characterize the rate and extent of particle segregation with time.

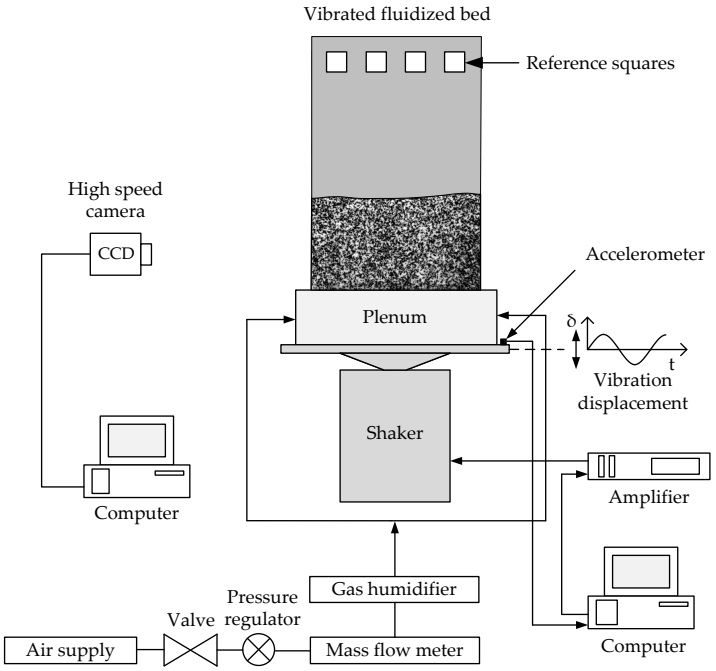


**Figure 2.3:** Sketch of the experimental facility used for the segregation experiments of Chapter 7.

### 2.1.4 Vibrated triangular bed for the characterization of solids motion patterns

The triangular bed used in Chapter 7 was also constructed by the author in the Laboratory of Energy Science and Engineering at ETH Zürich (Switzerland). The experimental facility consists of a triangular pseudo-2D bed that was fluidized with air and vibrated in the vertical direction. The dimensions of the bed are 0.206 x 0.203 x 0.01 $m^3$ (span, height from the vertex of the bed and thickness), as shown in Figure 2.4. The bed front and back walls were made of antistatic PMMA in order to allow optical access to the fluidized bed. The same electrodynamic shaker as the one described in Section 2.1.3 was used to vertically vibrate the bed. Air was introduced to the bed through each of the inclined walls, which form an angle of 45° with the horizontal. The air mass flow was regulated by means of a mass flow controller (Analyt-GFC47) and entered a first plenum and then a second plenum through a gas distributor consisting of 50 holes of 1 mm of diameter (see Figure 2.4). Then, the air enters the bed through the lateral inclined walls, which were perforated with 80 holes of 0.5 mm of diameter (40 holes in each wall). The pressure drop of the gas distributor was experimentally measured and follows the

quadratic law $\Delta P_d = 3.7 \cdot 10^4 U^2 + 4.5 \cdot 10^3 U$. Due to the configuration of the bed, air was not injected through the vertex of the triangular bed. Nevertheless, particles located in the vertex of the bed were not static as they were affected by vibration and the motion of the surrounding particles.

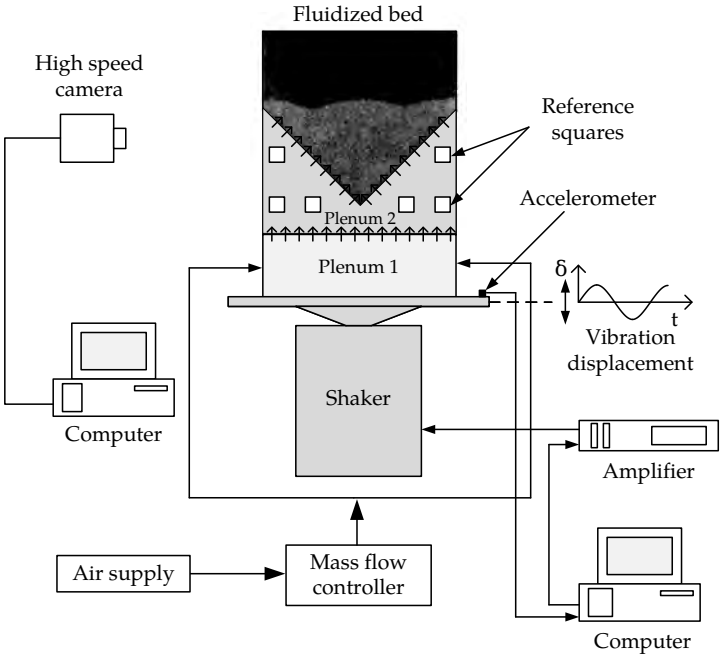


**Figure 2.4:** Sketch of the experimental facility used for the triangular bed experiments of Chapter 7.

A controller (Labworks Inc. VL-144), amplifier (Labworks Inc., PA-138-1) and an accelerometer (PCB Piezotronics Inc., J352C33) were used to generate and control a sinusoidal vibration $\delta(t) = A\sin(2\pi f t)$. The front part of the bed was uniformly illuminated by two LED spotlights symmetrically disposed at each side of the bed. A high speed CCD camera (Optronics CL 600 x2/M) was used to record images of the bed through its front wall at a frame rate of 200 images per second. Combined DIA and PIV techniques were applied to the captured images in order to characterize the patterns of solids velocity in the bed.

## 2.2 Two-Fluid modeling of vibrated fluidized bed

As commented in Chapter 1, the TFM allows for an Eulerian-Eulerian description of the fluidized bed, the gas phase (g) and the particles or solids phase (p) being modeled

as two interpenetrating continua. The MFIX code (Multiphase Flow with Interphase eXchanges) (Syamlal *et al.*, 1993; Benyahia *et al.*, 2012) was used to solve the conservation equations of mass and momentum for each of the phases (see Equations T2.1-2.4 in Table 2.1) and the equation of transport of granular temperature $\Theta$, which accounts for the level of random fluctuation of particle velocity due to collisions (Equation T2.5 in Table 2.1). The MFIX code uses an extension of the SIMPLE method to integrate the governing equations in a finite volume domain. An iterative procedure is used to satisfy the conservation equations of both phases in each of the cells. A staggered grid is used in this code. Thus, the scalars (e.g. gas pressure, void fraction, etc.) are saved at the cell centers and the velocities are defined at the cell faces. The numerical technique of the MFIX code uses a semi-implicit scheme that automatically adjusts the time-step depending on the convergence of the simulation.

The Kinetic Theory of Granular Flow (KTGF) (Gidaspow, 1994) was used for the closure of the solids pressure and stress terms. For the calculation of the drag coefficient between the gas and the particles, $K_{gp}$, the drag model by Gidaspow (1994) was selected because of its robustness during the start-up of the simulation. Other closure models employed in the present dissertation are summarized in Appendix A.

**Table 2.1:** Governing equations

Continuity equations

$$\frac{\partial}{\partial t}(\varepsilon_p \rho_p) + \nabla \cdot (\varepsilon_p \rho_p \boldsymbol{U}_p) = 0 \qquad \text{(T2.1)}$$

$$\frac{\partial}{\partial t}(\varepsilon_g \rho_g) + \nabla \cdot (\varepsilon_g \rho_g \boldsymbol{U}_g) = 0 \qquad \text{(T2.2)}$$

Momentum equations

$$\left[\frac{\partial}{\partial t}(\varepsilon_p \rho_p \boldsymbol{U}_p) + \nabla \cdot (\varepsilon_p \rho_p \boldsymbol{U}_p \boldsymbol{U}_p)\right] = -\varepsilon_p \nabla P_g + \nabla \cdot \boldsymbol{\tau}_p + \boldsymbol{I}_{gp} + \varepsilon_p \rho_p \boldsymbol{f}_{m,eq} \qquad \text{(T2.3)}$$

$$\left[\frac{\partial}{\partial t}(\varepsilon_g \rho_g \boldsymbol{U}_g) + \nabla \cdot (\varepsilon_g \rho_g \boldsymbol{U}_g \boldsymbol{U}_g)\right] = -\varepsilon_g \nabla P_g + \nabla \cdot \boldsymbol{\tau}_g - \boldsymbol{I}_{gp} + \varepsilon_g \rho_g \boldsymbol{f}_{m,eq} \qquad \text{(T2.4)}$$

Granular temperature equation

$$\frac{3}{2}\rho_p \left[\frac{\partial \varepsilon_p \Theta}{\partial t} + \nabla \cdot (\varepsilon_p \boldsymbol{U}_p \Theta)\right] = \nabla \cdot (\kappa_\Theta \nabla \Theta) + (-P_p \bar{\bar{I}} + \boldsymbol{\tau}_p) : \nabla \boldsymbol{U}_p + \Pi_p - \varepsilon_p \rho_p J_p \qquad \text{(T2.5)}$$

Following the methodology proposed by Acosta-Iborra *et al.* (2012) (see Figure 2.5), the procedure conducted to introduce the oscillatory displacement of the bed vessel in the simulation consists in the solution of the governing equations using a system of reference that moves with the base of the bed vessel. After performing this change in the governing equations, vibration appears in the two-fluid model constitutive equations as an equivalent mass force (see Table 2.1) acting in both the gas and the solid momentum balance equations:

$$\boldsymbol{f}_{m,eq} = \boldsymbol{g} - \boldsymbol{a}(t) \tag{2.3}$$

where $\boldsymbol{g}$ is the gravity acceleration vector and $\boldsymbol{a}(t)$ accounts for the acceleration of the bed vessel induced by vibration. This methodology is described in Figure 2.5.

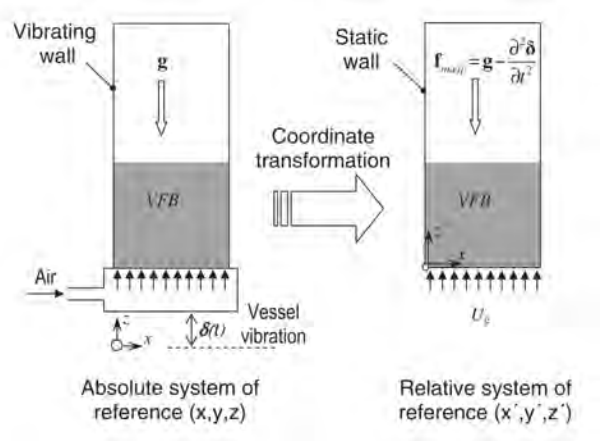


**Figure 2.5:** Transformation of coordinates from an absolute to a relative system of reference attached to the bed vessel in a vibrating fluidized bed (VFB). From Acosta-Iborra *et al.* (2012).

Considering a vertical sinusoidal displacement of the bed vessel, $\delta(t) = A\sin(\omega t)\boldsymbol{u}_y$, the bed vessel acceleration term in the vertical direction can be expressed as follows:

$$\boldsymbol{a}(t) = \frac{\partial^2 \delta(t)}{\partial t^2} = -A\omega^2 \sin(\omega t)\boldsymbol{u}_y \tag{2.4}$$

where $A$ represents the vibration semi-amplitude, $\omega = 2\pi f$ is the angular frequency of vibration, $f$ is the vessel vibration frequency and $\boldsymbol{u}_z$ is the vertical unitary vector. More information concerning this transformation of equations can be found in Acosta-Iborra *et al.* (2012).

### 2.2.1 Treatment of gas compressibility

The presence of an oscillatory vibration displacement of the bed vessel promotes the generation of compression-expansion waves which travel through the bed bulk, as seen in (Musmarra *et al.*, 1995; van der Schaaf *et al.*, 1998) and experimental results shown in the present dissertation. These waves may affect the gas density of the bed. Thus, the compressibility of the gas phase was considered in the numerical models employed in this PhD thesis using the ideal gas law to calculate the gas density at each point and time instant during the two-fluid model simulation:

$$\rho_g = \frac{P_g}{R_g T_g} \tag{2.5}$$

where $P_g$ is the gas pressure, $T_g = 298$ K is the gas temperature, and $R_g = 287$ J/kg K is the ideal gas constant for air. It is assumed that the process in all the bed is isotherm since real particles accumulate heat and damp small fluctuations of temperature (Roy *et al.*, 1990). The compressible gas TFM simulations were compared to those in which the gas phase was considered incompressible ($\rho_g = 1.22$ kg/m$^3$).

## 2.3 Data processing

The following sections summarize the different data processing techniques used along the present dissertation. Some of the techniques, as for example the averaging of cycles methodology, are used in more than one chapter and not only for experimental data but also for simulation results. The adaptations of each of the techniques to each of the chapters are also specified in the subsequent sections.

### 2.3.1 Bubble detection

#### Isolated bubbles

In all the chapters, the software Matlab® was employed for the processing of the digital images taken of the fluidized bed. Using a constant threshold value obtained from the grey level histogram of the experimental images (Otsu, 1979), each pixel in the image was computed to have a value of 0 (black, inside the bubble) or 1 (white, outside the bubble), making the contour of the studied bubble easily identifiable. The threshold was also used to eliminate the particle rain at the top region of the bubble so that the bubble shape and diameter were correctly captured.

The bubbles in the simulation were identified by setting a common threshold value of $\varepsilon_{p,th} = 0.2$ (Boemer *et al.*, 1997; Hulme *et al.*, 2005) on the instantaneous solids volume

fraction. Visual inspection of the results showed that both the experimental threshold and the chosen value of $\varepsilon_{p,th}$ ensured the robustness of the location of the bubble contour in the VFB experiments and simulations. Greater values of $\varepsilon_{p,th}$ led to a growth of the bubble contour oscillation with a lost of resolution in defining the bubble contour. As in the experiments, for each simulation frame of solid volume fraction, a point in the image was assigned a value of 0 if $\varepsilon_p < \varepsilon_{p,th}$ or 1 if $\varepsilon_p > \varepsilon_{p,th}$, making the contour of the bubble easily identifiable.

In all the chapters, the bubble equivalent diameter was calculated as the diameter of a circle having the same area, $A_b$, of the bubble:

$$D_b = \sqrt{\frac{4A_b}{\pi}} \tag{2.6}$$

The instantaneous vertical position of a bubble, $y_b(t)$, was calculated as the vertical distance of the bubble centroid to the distributor of the bed. This position can be computed in a relative or absolute system of reference if the distance is calculated from the instantaneous or the time-averaged location of the distributor, respectively. Expressing the bubble position variation in an absolute or relative system of reference does not change significantly the mean values since the differences arising from the two reference systems are compensated when the results are time-averaged. In order to obtain the bubble rising velocity, the vertical distance between the bubble centroid in a frame, at time $t$, and the bubble centroid in the following frame, at time $t + \Delta t$, was divided by the time interval between frames:

$$V_b = \frac{y_b(t + \Delta t) - y_b(t)}{\Delta t} \tag{2.7}$$

Note that, since velocity was calculated from the displacement of the bubble centroid, changes of shape of a bubble may produce an apparent displacement that is difficult to separate from the main bubble motion.

### Bubbling bed

A double thresholding methodology was used to identify the dense and bubble phases in the bubbling fluidized bed used in Chapter 4. This double threshold method combines a constant and an adaptive threshold to correctly discriminate all the bubble sizes, including bubbles whose contour is not easily observable due to particle rain.

Figure 2.6 shows an example of the double thresholding methodology. A constant threshold based on the maximum entropy method (Kapur *et al.*, 1985) was applied to the grayscale image (Figure 2.6(a)) for distinguishing between bubble and emulsion phases (Figure 2.6(b)). Visual inspection of the images indicated that the size of bigger bubbles

obtained after this first thresholding was slightly overestimated and did not capture correctly the splitting of bubbles produced by particle rain in their interior. Subsequently, a second threshold was applied to the thresholded image. This second thresholding was adaptive (Bradley & Roth, 2007) and aimed at reducing the bubble size overestimation and improving the detection of both big and small bubbles. During the second threshold, pixels previously assigned with a value of 1 (white, dense phase) in the first threshold (Figure 2.6(b)) can be modified to a value of 0 (black, dense phase) based on the graylevel and average brightness of the surrounding pixels in a window of specified size (i.e. 30 pixels side). This improves the detection of the contours of bubbles, as shown in Figure 2.6(c).

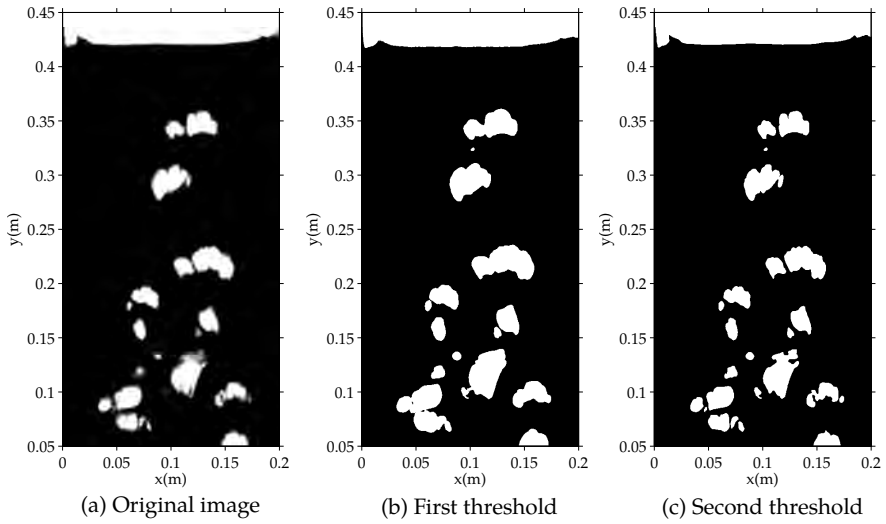


**Figure 2.6:** Example of snapshots of the bed described in Section 2.1.2. (a) Grayscale raw image taken by the CCD camera, (b) binarized image after the first (constant) threshold and (c) binarized image after the second (adaptive) threshold. Chapter 6.

In the bubbling bed employed in Chapter 6, it was found that bubbles close to the distributor were insufficiently illuminated. When approaching to the bed surface, bubbles were deformed just prior eruption. Therefore, only bubbles whose centroids were within 5 to 40 cm (i.e. $\Delta h = 0.35$ m) over the distributor and have not erupted at the surface of the bed were considered for data averaging. Bubbles of area smaller than 1 cm$^2$ were eliminated from the analysis since their contours were not clearly distinguishable. To study bubble characteristics as a function of the distance to the distributor, the bed height was divided in vertical intervals (i.e. in horizontal stripes) of 20 cm width and 2 cm height, and bubbles were assigned to an interval according to the location of their centroids.

To avoid mismatching of bubbles in consecutive image frames and to skip the perturbation of the centroid position due to bubble splitting, coalescence and break up, Equation (2.7) was only applied to bubbles before they split, erupt in the freeboard of the bed, or coalesce with other bubbles. Bubbles with more than 20% diameter change between consecutive frames were discarded in the analysis because they were considered to be highly perturbed by coalescence or splitting. Note that the time step between consecutive frames is $\Delta t = 8$ ms, which represents approximately a 0.5% of the total bubble residence time in the bed.

In addition to the bubble size and velocity, the bubble fraction and the bubble number density were also calculated in Chapter 6. The bubble fraction was computed as the summation of all the valid bubble areas in all the frames and the result was divided by the number of frames and the area of analysis (see Equation (2.8)). The bubble fraction is therefore a normalized time-averaged value of the area simultaneously occupied by the bubbles per unit area of the front view of the bed:

$$F_b = \frac{\sum_{i=1}^{N_{bub}} A_{b,i}}{N_{f,tot} W \Delta h} \tag{2.8}$$

Where $A_{b,i}$ is the bubble front area, $N_{bub}$ is the total number of valid bubbles along all the images, $N_{f,tot}$ is the total number of frames of the experiment (i.e. 6400 frames in Chapter 6), $W$ is the bed width and $\Delta h$ is the height of the vertical interval in which $F_b$ is calculated.

The bubble number density was calculated as the total number of valid bubbles divided by the averaging area, $W\Delta h$, and the total number of frames of the experiment:

$$n_b = \frac{\sum_{i=1}^{N_{bub}} N_{b,i}}{N_{f,tot} W \Delta h} \tag{2.9}$$

Where $N_{b,i}$ is the number of valid bubbles in the $i^{th}$ frame whose centroid is within a vertical interval. The definitions given in Equations (2.8) and (2.9) correspond to a vertical interval defining a thin stripe ($\Delta h = 0.02$ m), sensitivity analysis of the results to the size of the stripe thickness showed that $\Delta h = 0.02$ m is sufficient to obtain statistically significant results with a good spatial resolution in the vertical direction. Processing of consecutive intervals allows the calculation of $F_b$ and $n_b$ as a function of the distance to the distributor sampling areas. Also, if the sampling area approaches the whole bed ($y = 0.05 - 0.4$ m, $\Delta h = 0.35$ m) the results represent global values in all the bed.

In Chapter 6, the center of mass position is calculated as the instantaneous position of

the centroid of the dense phase of the bed excluding the volume occupied by the bubbles obtained by the double thresholding methodology. Also, as the base of the bed is not discerned in the captured images, the first 0.05 m of the bed are not considered for the calculation of the bed centroid position.

**Bubble tracking** In order to study the oscillation of the characteristics of individual bubbles as they rise in the bed, a bubble tracking methodology was developed in the framework of Chapter 6. In this methodology, all the bubbles present in an image frame of the bubbling bed are individually tracked during consecutive image frames until they break, coalesce or erupt in the freeboard of the bed. As in the case of the calculation of the bubble velocity, bubbles with more than 20% diameter change between consecutive frames are discarded.

**Solids hold-up** To analyze the solids hold-up in the bed, all the grayscale images of the bed were averaged and divided by the temporal standard deviation of the grayscale images. This operation was performed individually for each pixel of the image area. The result of this operation is a normalized mean grayscale map of the distribution of solids in the bed:

$$\widetilde{GS}(i,j) = \frac{\sum_{k=1}^{N_{f,tot}} GS(i,j)_k / N_{f,tot}}{\sigma_{GS}(i,j)} = \frac{\overline{GS}}{\sigma_{GS}} \tag{2.10}$$

Where $GS(i,j)_k$ is the grayscale image corresponding to the k$^{th}$ frame, $i$ and $j$ are the pixel location indexes in the image and $N_{f,tot}$ is the total number of frames recorded by the CCD camera. In Equation (2.10), normalization is carried out by means of $\sigma_{GS}(i,j)$, which is the standard deviation of the variation of $GS(i,j)$ with time at a given pixel location $(i,j)$. The normalized mean average grayscale image, $\widetilde{GS}(i,j)$ enhances the visualization of bubble paths, including those created by small bubbles, and allows to compare different experiments. In Equation (2.10), the presence of bubbles in a given pixel location, $(i,j)$, increases the mean value $\overline{GS}$. For the bed studied in this chapter, the values of $\widetilde{GS}(i,j)$ are typically comprised between 0 (regions with few bubble passing) and 1 (maximum bubble passing).

**Bubble distribution index** The normalized mean grayscale image defined in Equation (2.10) provides valuable qualitative information of how bubble and dense phase are spatially distributed in the bed. However, in order to perform a quantitative analysis, a distribution index of bubbles ($DI$) is proposed. $DI$ is calculated as the root mean square average, $\sigma_{rms,j}$, of the local standard deviation of the grayscale images within a horizontal

stripe of vertical thickness $\Delta h = 2$ cm at a given distance of j pixels from the distributor. The result is normalized with the standard deviation of the local time-averaged gray level $\overline{GS}$ on this same horizontal stripe ($\sigma_{\overline{GS}_j}$):

$$DI_j = \frac{\sigma_{rms,j}}{\sigma_{\overline{GS}_j}} = \frac{\left(\frac{1}{M}\sum_{i=1}^{M}\frac{1}{N_s}\sum_{k=j-N_s/2}^{j+N_s/2}\sigma_{GS}^2(i,k)\right)^{1/2}}{\left[\frac{1}{M}\sum_{i=1}^{M}\left(\sum_{k=j-N_s/2}^{j+N_s/2}\frac{\overline{GS}(i,k)}{N_s}\right)^2 - \left(\frac{1}{M}\sum_{i=1}^{M}\left(\sum_{k=j-N_s/2}^{j+N_s/2}\frac{\overline{GS}(i,k)}{N_s}\right)\right)^2\right]^{1/2}} \tag{2.11}$$

Where $M$ is the number of pixels along the horizontal direction in the bed image and $N_s$ is the number of pixels in vertical direction in the horizontal stripe of thickness $\Delta h$. If the bubble path is not well distributed in the horizontal direction, $\sigma_{rms,j}$ decreases and $\sigma_{\overline{GS}_j}$ increases, which diminishes $DI_j$. Thus, $DI = 0$ for a perfectly uneven distribution of bubbles in the bed (i.e. one vertical line of white pixels in the bed) and $DI \to \infty$ for a perfectly distributed bed.

### 2.3.2 Averaging of cycles methodology

An averaging of cycles method is employed for the study of the oscillatory behavior of the bulk and bubbles cyclic behavior. This oscillation is obtained with DIA in the experiments. Figure 2.7 describes the averaging of cycles method used to obtain the average oscillation of bubbles in the bed.

It is considered that the fluctuation of a given variable, $z(t)$, over its averaged value is influenced by the bed vessel vibration. Assuming a periodic vibration, the oscillation of the vertical position of the bed vessel, $\delta(t)$, is repeated periodically on time, so that:

$$\delta(t) = \delta(t + nT) = \delta\left(\frac{\phi + 2\pi n}{\omega}\right) \tag{2.12}$$

Where $T = 1/f$ is the time period of vibration, $n$ is an arbitrary integer, $\omega = 2\pi f$ is the angular frequency and $f$ is the frequency of vibration. As an example, Figure 2.7(a) shows the instantaneous vertical position of a bubble, obtained from the bubbling bed described in Section 2.1.2. The instantaneous oscillation of a given variable, $z(t)$, with regard to its mean is calculated as:

$$\Delta z(t) = z(t) - \widehat{z}(t) \tag{2.13}$$

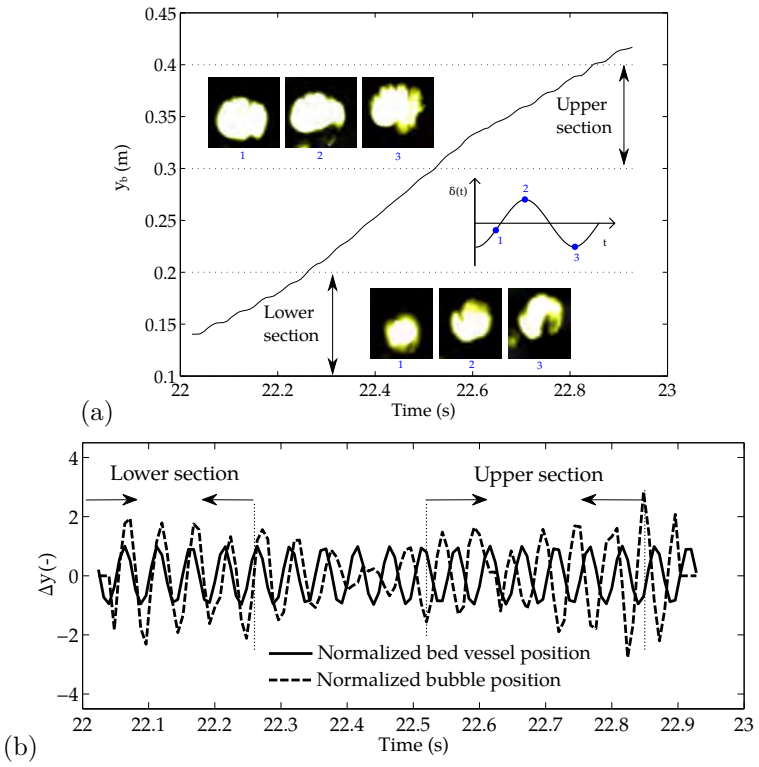


**Figure 2.7:** Processing of the oscillation of bubble characteristics. (a) Example of the oscillation of a bubble centroid position as a function of time. The numbers in the figure indicate the approximate phase of the bubble snapshots. (b) Normalized oscillation of the bed and the bubble position. The solid line indicates the normalized oscillation of the bed vessel position. Chapter 6, experiment with $d_p = 60$ $\mu$m, $f = 20$ Hz, $A = 2$ mm and $U/U_{mf} = 8$.

where $\widehat{z}(t)$ is the moving average of $z$ over a time interval $[-T/2, T/2]$, with $T = 1/f$ being the time period of oscillation. Figure 2.7(b) shows the normalized oscillation of the bubble position shown in Figure 2.7(a) together with the normalized bed vessel position.

It can be observed in Figure 2.7(b), that $\Delta y_b$ oscillated with a frequency that matches the frequency of vibration of the bed vessel. In consequence, each instantaneous value of $\Delta z(t)$ can be associated to a phase $\phi$, where $\phi = 0$ corresponds to the beginning of a cycle (bed vessel at its central position, $\delta(t_0) = 0$, and moving upwards) and $\phi = 2\pi$ to the end of the cycle (bed vessel at its central position, $\delta(t_0 + T) = 0$, and moving again upwards). Thus, for every image in the experiment, a data point in the phase domain ($\phi = 0 - 2\pi$) is obtained.

**Isolated bubbles** The averaging process followed in Chapter 4 for isolated bubbles rising in the VFB is schematized in Figure 2.8.

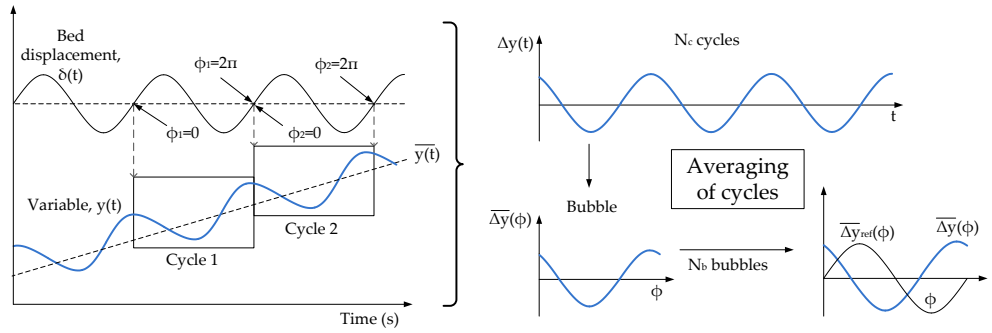


**Figure 2.8:** Sketch of the averaging of cycles method. The left hand side of the figure shows the time evolution of the reference signal (bed displacement) and the studied variable ($z(t)$). The right hand side of the figure sketches the averaging of cycles procedure performed for all the cycles of a bubble ($N_c$) and all the bubbles in an experiment ($N_b$).

Since bubbles can be sequentially followed from the bottom to the top of the bed bulk, an average oscillation $\overline{\Delta z}(t)$ is computed independently for each of the bubbles, which averages the value of $\Delta z$ over all the periodic cycles of each bubble at a phase interval $\phi_k$.

$$\overline{\Delta z_n}(\phi_k) = \frac{1}{N_k} \sum_{i=1}^{N_{dat}} \Delta z_i \delta_{i,k} \beta_n \tag{2.14}$$

Where $\phi_k$ is the phase, which has been discretized in $N_\phi = 20$ intervals ($k = 1$ to 20), $\Delta z_i = z_i - \widehat{z}_i$ is the fluctuation at the sampling instant $t_i$. In Equation (2.14), $N_k$ is the number of time instants whose phase is within $\phi_k \pm \pi/N_\phi$ and belong to the $n^{th}$ bubble,

$$N_k = \sum_{i=1}^{N_{dat}} \delta_{i,k} \beta_n \tag{2.15}$$

where $N_{dat}$ is the total number of time instants used to calculate $\overline{\Delta z}(\phi)$ and $\delta_{i,k}$ is equal to the unity if $t_i$ is in the phase interval of $\phi_k$:

$$\delta_{i,k} = \begin{cases} 1 & \text{if } \frac{T}{N_\phi}(k-1+n) < t_i < \frac{T}{N_\phi}(k+n) \\ 0 & \text{otherwise} \end{cases} \tag{2.16}$$

Finally, for each phase interval $\phi_k$, the average oscillation of $z$ was obtained by averaging the results encountered for each of the bubbles:

$$\overline{\Delta z}(\phi_k) = \frac{1}{N_b} \sum_{n=1}^{N_b} \overline{\Delta z_n}(\phi_k) \tag{2.17}$$

A basic polynomial data fitting was included together with the average oscillation for enhancing the visual inspection of the results. To analyze the variation of the bubble behavior with the distance to the distributor, the averaging of cycles performed in Equation (2.17) was done for bubbles whose centroids were situated in the lower height interval $y = 0.1 - 0.275$ m (lower half volume of the bed) and, separately, for bubbles whose centroids were in the upper height interval $y = 0.275 - 0.45$ m (upper half volume of the bed).

**Center of mass and bubbling bed characteristics** The averaging of cycles procedure described above was also employed for the determination of the oscillation of the vertical position of the center of mass of the bed bulk in Chapters 3 and 6 and the bubble characteristics in Chapter 6. However, due to the multiple interaction of bubbles in Chapter 6, an average oscillation for each bubble was difficult to obtain.

In this case, each instantaneous value of oscillation $\Delta z(t)$ is associated to a phase $\phi$. As for the isolated bubbles in Chapter 4, two regions of analysis for the bubble behavior are chosen in Chapter 6: $y = 0.1 - 0.2$ m and $y = 0.3 - 0.4$ m, namely the lower and upper sections of the bed, respectively.

As an example, all the normalized values of $\Delta y_{b_i}$ corresponding to the position of every tracked bubble in the two sampling regions shown in Figure 2.7(a) and as a function of $\phi$ are shown in Figure 2.9. A polynomial data fitting, $\Delta z_f$, is then performed for enhancing the visual inspection and quantifying the results (see dashed and dashed-dotted lines in Figure 2.9). As a reference, the normalized oscillation of the vertical position of the bed vessel is also included in Figure 2.9.

In Chapter 3, the local bed bulk velocity, especially close to the distributor, presented a cyclic displacement whose behavior differed from that of a sinusoidal displacement. Thus, a smoothing spline of $\Delta z_f$ was chosen to represent the results of the velocity oscillation in the interval $\phi = 0 - 2\pi$.

### Phase delay of oscillations

The phase delay $\phi_d$ is the retardation in phase $\phi$ of the oscillation of a variable with respect to a reference signal, $\overline{\Delta z}_{ref}$ (i.e. the bed vessel displacement or velocity). This

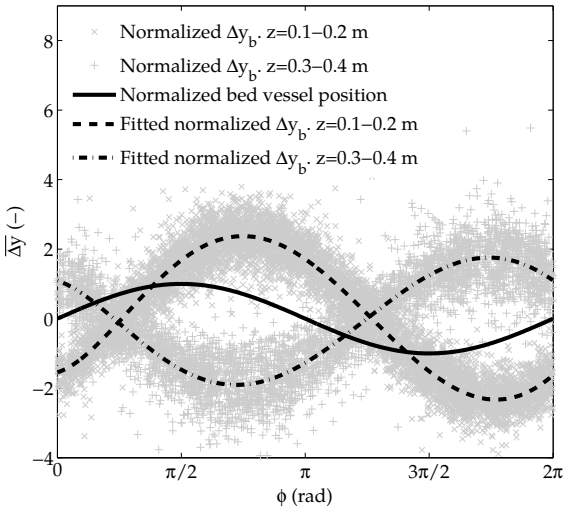


**Figure 2.9:** Example of the normalized oscillation of the bubble position in the lower and upper sections of the bed. Each point in the figure corresponds to a bubble and the dashed lines are obtained by polynomial fitting to the points in the figure. The solid line indicates the normalized oscillation of the bed vessel position. Chapter 6, experiment with $d_p = 60$ $\mu$m, $f = 20$ Hz, $A = 2$ mm and $U/U_{mf} = 8$.

phase delay was estimated using Equation (2.18):

$$\min_x \left(\sum_{i=1}^{N_\phi} [\overline{\Delta z}_i - A_{\overline{\Delta z}} \sin(\phi_i - x)]^2\right) \longrightarrow \phi_d = x \tag{2.18}$$

In Equation (2.18), $x$ is the value that minimizes the squared difference between the average fluctuation signal ($\overline{\Delta z}$) and a reference sinusoidal signal. The amplitude of the reference sinusoidal signal, $A_{\overline{\Delta z}}$, is made equivalent to the amplitude of $\overline{\Delta z}$, by means of Equation (2.19):

$$A_{\overline{\Delta z}} = \sigma_{A_{\overline{\Delta z}}} \sqrt{2} \tag{2.19}$$

Where $\sigma_{A_{\overline{\Delta z}}}$ is the standard deviation of $\overline{\Delta z}$. Positive values of $x$ in Equation (2.18) correspond to a positive phase delay, i.e. $\overline{\Delta z}$ is retarded in time with respect to the bed vessel displacement. Note also that the reference signal is a cosine instead of a sine in Equation (2.18) when the reference signal is the bed vessel velocity instead of the position. Sensitivity analysis of the results showed that increasing the number of intervals $N_\phi$ employed to represent the oscillations of a given variable has little influence on $\phi_d$.

### 2.3.3 Particle Image Velocimetry

The velocity of the bed particles at an instant between each two consecutively recorded images was obtained by means of PIV, which is based on the cross-correlation of consecutive images, as described in Section 1.2.1. For that, the multigrid code MATPIV (Sveen, 1998-2014) was used. For the analysis of the bed bulk oscillation described in Chapters 3 and 7, a final interrogation window of 32 x 32 pixels and 50% overlapping was employed. However, a smaller interrogation window of 16 x 16 pixels with a 50% overlapping was used in Chapter 5 for the study of the solids motion around an isolated bubble.

In the case of the triangular bed described in Section 2.1.4, to improve the accuracy and stability of the velocimetry technique, before performing the PIV calculations, each of the particle images were vertically displaced a distance equal to minus the instantaneous displacement of the bed vessel, calculated by means of DIA of several square films (see Section 2.1.4). Thus, instead of using an absolute reference system in which the bed is oscillating, the PIV algorithm calculates the displacement of particles in a relative reference system that moves with the bed vessel.

The solid velocities obtained with PIV were also analyzed as a function of the vibration phase by means of the averaging of cycles method. Each complete period of oscillation of the bed bulk, $T$, was divided into $M$ phase intervals of phase $\phi \in [0, 2\pi]$ to capture the oscillatory behavior of the bed bulk as a function of the bed vessel phase. The velocity vectors of all the oscillation periods pertaining to a given phase interval were averaged, obtaining a velocity map for each of the phase intervals in which the period of oscillation was divided.

The standard deviation of the temporal evolution of each PIV vector of solids relative velocity was obtained by means of Equation (2.20):

$$\sigma_{U_s} = \sqrt{\frac{1}{N}\sum_{i=1}^{N}(U_{s,i}(x,y) - U_{s,avg})^2} \tag{2.20}$$

where $U_{s,avg}$ is the time-averaged solids velocity in each window calculated along the $N_{f,tot}$ frames of an experiment:

$$U_{s,avg} = \sum_{i=1}^{N_{f,tot}} U_{s,i}(x,y)/N_{f,tot} \tag{2.21}$$

### Bubble averaging method

To statistically characterize the particle velocity around bubbles in Chapter 5, a method to average the bubble contour is proposed. This method consists in averaging all the bubbles identified along an experiment in order to obtain the average velocity distribution around a representative bubble. This bubble statistically represents all the analyzed bubbles. The procedure followed is described in the following lines and schematized in Figure 2.10.

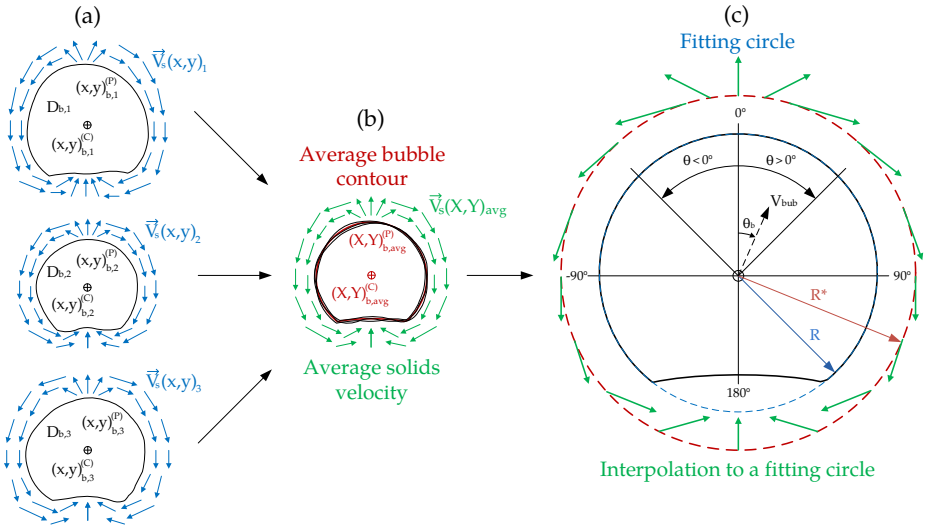


**Figure 2.10:** Sketch of the bubbling averaging method. The left hand side of the figure shows the averaging of multiple bubbles and solids velocities to produce the average bubble contour and solids velocity. The right hand side of the figure sketches the fitting circle and the definition of the angle $\theta$.

For every image (numbered with $i$) in which an isolated bubble is present in the system, the instantaneous area-equivalent bubble diameter ($D_{b,i}$), velocity ($V_{b,i}$), the coordinates describing its centroid, ($(x,y)_{b,i}^{(C)}$) and its perimeter ($(x,y)_{b,i}^{(P)}$) are obtained by means of DIA. The contour of the bubble is normalized and translated to a new system of coordinates defined by a normalized pair of coordinates $(X,Y)$. In this new coordinate system, the bubble centroid is assigned to the origin, $X=0, Y=0$, and the bubble contour is normalized with the radius of the bubble. By this, all the bubbles' centroids are placed at $X=0, Y=0$ with a radius equal to unity. Thus, the normalized bubble contour in the new coordinate system is:

$$(X,Y)_{b,i}^{(P)} = \frac{2[(x,y)_{b,i}^{(P)} - (x,y)_{b,i}^{(C)}]}{D_{b,i}} \tag{2.22}$$

This operation is repeated for all the bubble contours identified along an experiment, which comprise several bubbles injected one after the other. The average contour $(X,Y)^{(P)}_{b,avg}$ is defined as the contour that averages all the analyzed bubbles, as schematized in Figure 2.10(b):

$$(X,Y)^{(P)}_{b,avg} = \frac{\sum_{i=1}^{N_b}(X,Y)^{(P)}_{b,i}\beta_{i,k}}{\sum_{i=1}^{N_b}\beta_{i,k}} \tag{2.23}$$

where $N_b$ is the number of analyzed bubbles and $\beta_{i,k}$ is equal to the unity if the $i^{th}$ bubble centroid is within a specific distance from the distributor, $y_{b,i} \in [y_{b,min}, y_{b,max}]$ and the phase of the bed vessel is within the $k^{th}$ phase interval in which the period of oscillation is discretized:

$$\beta_{i,k} = \begin{cases} 1 & \text{if } \left(\frac{2(k-1)}{M}\pi < \phi_i < \frac{2k}{M}\pi\right) \text{ and } (y_{b,min} < y_{b,i} < y_{b,max}) \\ 0 & \text{otherwise} \end{cases} \tag{2.24}$$

The same operation is carried out for the instantaneous solids velocity vectors, $\vec{V}(x,y)_i$, around the bubble. In this case, normalization is carried out in terms of the mean velocity of the centroid of the analyzed bubbles. Thus, the instantaneous value of the normalized solids velocity in the new coordinate system for each of the bubbles is calculated as:

$$\vec{V}(X,Y)_{norm,i} = \frac{\vec{V}(x - x^{(C)}_{b,i}, y - y^{(C)}_{b,i})_i}{\frac{1}{N_b}\sum_{i=1}^{N_b} V_b} \tag{2.25}$$

where $N_b$ is the number of bubbles comprised in the height interval under analysis, $y_{b,i} \in [y_{b,min}, y_{b,max}]$.

Note that the position of the velocity vectors, $\vec{V}(X,Y)_{norm,i}$ for each of the frames in the new system of coordinates $(X,Y)$ may vary from one frame to another, since they are displaced during the normalization of $x$ and $y$. Thus, the average velocity around the bubble is obtained by dividing the new system of coordinates in $N_{bins}$ averaging windows. These windows have approximately the same size as the PIV interrogation windows. The velocity vectors of each bubble $\vec{V}(X,Y)_{norm,i}$ are linearly interpolated to the center of each of the averaging windows, obtaining the average velocity $\vec{V}(X,Y)_{avg}$ of solids around the averaged bubble contour, $(X,Y)^{(P)}_{b,avg}$, as shown in Figure 2.10(b).

Once all the bubble contours and the velocity vectors are averaged in the new coordinate system, the normalized mean solids velocity of the particles as a function of the angle around a bubble, $\theta$, could be determined (see Figure 2.10(c)). Here, $\theta$ is the angle between the position of the velocity vector and a vertical line passing through the

bubble centroid. In order to do this, firstly the coordinates of the circle, $(X,Y)^{(F)}$ that better fits the average bubble contour $(X,Y)^{(P)}_{b,avg}$ in an angle range $\theta \in [-120°, 120°]$ (i.e. the circle with radius $R$ in Figure 2.10) are calculated. Secondly, to avoid the effect of particle rain on the calculation of the solids motion around the bubble, a new fitting circle, $(X,Y)^{(F)}_n$ is used. This new circle is obtained by increasing the radius of the fitting circle $(X,Y)^{(F)}$ to a radius $R^*$ in which the velocity of the particles at $\theta = 0°$ of the new circle reaches a maximum positive value (see Figure 2.10(c)). This radius $R^*$ defines the minimum distance to the bubble centroid for which the experimental solids velocity presents a decrease with the radius, as predicted by the potential flow theory. Results for distances to the bubbles smaller than $R^*$ do not show this decrease of $\vec{V}_{avg}$ and, hence, are considered severely affected by the particles rain and the irregularities of the bubble contour.

As schematized in Figure 2.10(c), the average solids velocity as a function of $\theta$ was obtained by interpolating the velocity vectors $\vec{V}(X,Y)_{avg}$ to the contour of the new circle $(X,Y)^{(F)}_n$.

### 2.3.4 Segregation Index

The Lacey index (Lacey, 1954) was used to quantify the extent of particle segregation with time in Chapter 7. The Lacey index is based on a statistical analysis conceived for discrete systems. In the images of the bed, particles are difficult to distinguish individually and, instead, they appear like a speckle pattern. Therefore, an adaptation of the Lacey index to particle images is proposed here. The segregation index presented in this section takes a value $SI = 1$ if the mixture is completely segregated and $SI = 0$ for a completely mixed mixture, as shown in Figure 2.11.

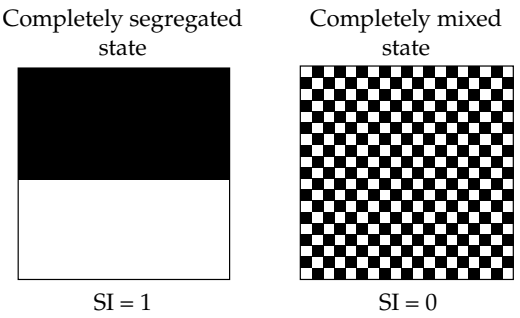


**Figure 2.11:** Schematic drawing of the completely segregated and a completely mixed states.

Firstly, the bed image is divided in $N_{cell} = 1950$ cells of 17 x 17 ($N_x$ x $N_y$) pixels (i.e. cells of 8 mm side) in the horizontal and vertical directions. A sensitivity analysis showed

a small variation of the results with $N_{cell}$ for the range of number of cells employed in Chapter 7. Secondly, the normalized area concentration of the denser, white, particles in each cell is calculated as:

$$c_k = \frac{1}{N_x N_y} \sum_{x_k=1}^{N_x} \sum_{y_k=1}^{N_y} \frac{GS_{x_k,y_k} - GS_{min}}{GS_{max} - GS_{min}} \chi_k \tag{2.26}$$

Where $\chi_k$ is the fraction of the $k^{th}$ cell occupied by the bed particles (i.e. $\chi_k = 1$ if the cell is fully occupied by particles and $\chi_k = 0$ if there are no particles in the cell), $GS_{x_k,y_k}$ is the grayscale level of each of the pixels in the cell (from $GS = 0$ black to $GS = 255$ white). For each image of the experiments $GS_{min} = 0$, as the brightness level of the black particles is $GS = 0$, and $GS_{max} = min(255; \overline{GS} + \sigma_{GS})$. $\overline{GS}$ and $\sigma_{GS}$ are, respectively, the mean value and the standard deviation of the grayscale level for all the pixels of the bed in the image (excluding the freeboard). A change of system of reference to one moving with the bed vessel is performed so that the bed does not move in this new system of reference and the location of the cells in the bed is preserved along the data processing. This is done by following the position of the reference squares shown in Figure 2.3 and displacing the image vertically to preserve their location.

Thirdly, the variance of the concentration of the white particles in all the cells of the bed is defined as:

$$\sigma_c^2 = \frac{1}{N_{cell} - 1} \sum_{k=1}^{N_{cell}} (c_k - \overline{c})^2 \tag{2.27}$$

where $\overline{c}$ is the average concentration of white particles in the whole bed calculated with

$$\overline{c} = \frac{1}{N_{cell}} \sum_{k=1}^{N_{cell}} c_k \tag{2.28}$$

Finally, the segregation index, based on Lacey's mixing index is defined at each instant as:

$$SI = 1 - \frac{\sigma_0^2 - \sigma_c^2}{\sigma_0^2 - \sigma_R^2} \tag{2.29}$$

In Equation (2.29), $\sigma_R^2 = \overline{c}(1 - \overline{c})/n_p$ is the variance for a bed with a perfectly random mixture of white and black particles, $\sigma_0^2 = \overline{c}(1 - \overline{c})$ is the variance for a bed with a completely segregated mixture of particles and $n_p$ is the average number of particles observed in the area of the sampling cells.

# Nomenclature

| | |
|---|---|
| $A$ | vibration amplitude (mm) |
| $A_b$ | bubble area ($m^2$) |
| $A_{eq}$ | vibration equivalent amplitude (mm) |
| $\boldsymbol{a}(t)$ | instantaneous acceleration ($m/s^2$) |
| $c$ | concentration of dense particles (-) |
| $DI$ | distribution index (-) |
| $D_b$ | bubble equivalent diameter (m) |
| $\overline{D}_b$ | averaged $D_b$ (m) |
| $d_p$ | particle diameter ($\mu$m) |
| $F_b$ | bubble fraction (-) |
| $f$ | vibration frequency (Hz) |
| $\boldsymbol{f}_{m,eq}$ | equivalent mass force ($m/s^2$) |
| $GS$ | grayscale value () |
| $\overline{GS}$ | mean grayscale value (-) |
| $\widetilde{GS}$ | normalized mean grayscale value (-) |
| $g$ | gravity acceleration constant ($m/s^2$) |
| $H$ | bed vessel height (m) |
| $\Delta h$ | height of a sampling area in the bed (m) |
| $\boldsymbol{I}_{gp}$ | inter-phase momentum exchange ($kg/m^2s^2$) |
| $J_p$ | collisional dissipation term ($m^2/s^3$) |
| $K$ | bed vessel thickness (m) |
| $M$ | number of pixels in the horizontal direction (-) |
| $N_b$ | number of analyzed bubbles of the experiment (-) |
| $N_{bins}$ | number of windows for velocity averaging (-) |
| $N_{bub}$ | number of bubbles (-) |
| $N_c$ | number of cycles (-) |
| $N_{cell}$ | number of cells (-) |
| $N_{dat}$ | number of time instants (-) |
| $N_{f,tot}$ | total number of frames of an experiment (-) |
| $N_k$ | number of phase intervals (-) |
| $N_s$ | number of vertical pixels in a stripe (-) |
| $N_{tot}$ | total number of cycles (-) |
| $N_x$ | number of pixels horizontally (-) |
| $N_y$ | number of pixels vertically (-) |
| $N_\phi$ | number of phase intervals for averaging of cycles (-) |
| $n_b$ | bubble number density (bubbles/$m^2$) |

| | |
|---|---|
| $n_p$ | number of particles in a cell (-) |
| $P$ | pressure (Pa) |
| $\Delta P_d$ | gas distributor pressure drop (Pa) |
| $R_b$ | bubble radius (m) |
| $R_g$ | ideal gas constant (J/kg K) |
| $R^*$ | bubble extended radius (-) |
| $SI$ | segregation index (-) |
| $T$ | oscillation period, $1/f$ (s) |
| $T_g$ | gas temperature (K) |
| $t$ | time (s) |
| $U$ | superficial gas velocity (m/s) |
| $U_{mf}$ | minimum fluidization velocity (m/s) |
| $U_g$ | gas velocity (m/s) |
| $U_p$ | solids phase velocity (m/s) |
| $U_s$ | solids velocity (m/s) |
| $v(t)$ | bed vessel instantaneous velocity (m/s) |
| $V$ | bed vessel velocity (m/s) |
| $\vec{V}$ | solids velocity vector (m/s) |
| $V_b$ | bubble velocity (m/s) |
| $V_{eq}$ | vibration equivalent velocity (m/s) |
| $V_s$ | solids vertical velocity (m/s) |
| $\overline{V}_s$ | normalized solids vertical velocity (m/s) |
| $\vec{V}$ | solids velocity vector (m/s) |
| $W$ | bed vessel width (m) |
| $X$ | normalized horizontal coordinate (-) |
| $x$ | horizontal coordinate (m) |
| $(x,y)^{(C)}$ | bubble contour coordinates (m) |
| $(x,y)^{(F)}$ | fitting circle coordinates (m) |
| $(x,y)_n^{(F)}$ | new fitting circle coordinates (m) |
| $(x,y)^{(P)}$ | bubble perimeter coordinates (m) |
| $Y$ | normalized vertical coordinate (-) |
| $y$ | vertical coordinate (m) |
| $y_b$ | bubble centroid vertical coordinate (m) |
| $y_{cm}$ | bed center of mass vertical coordinate (m) |
| $y_{fb}$ | bed surface vertical coordinate (m) |
| $y_p$ | pressure sensor vertical coordinate (m) |
| $y_w$ | wave front vertical coordinate (m) |
| $z(t)$ | instantaneous variable value |

| | |
|---|---|
| $\widehat{z}(t)$ | moving average of $z$ |
| $\Delta z$ | oscillation of $z$ |

*Greek letters*

| | |
|---|---|
| $\delta(t)$ | instantaneous vibration displacement (m) |
| $\varepsilon$ | volume fraction (-) |
| $\Theta$ | granular temperature ($m^2/s^2$) |
| $\theta$ | angle from the vertical direction (°) |
| $\theta_b$ | bubble rising angle (°) |
| $\kappa_\Theta$ | granular temperature diffusion coefficient (kg/m s) |
| $\Pi_p$ | exchange terms (kg/m $s^3$) |
| $\rho$ | density ($kg/m^3$) |
| $\sigma$ | standard deviation |
| $\boldsymbol{\tau}$ | stress tensor (Pa) |
| $\phi$ | bed vessel vibration phase (rad) |
| $\phi_d$ | phase delay (rad) |
| $\chi_k$ | fraction of a cell occupied by particles (-) |
| $\omega$ | angular frequency (rad/s) |

*Subscripts*

| | |
|---|---|
| $avg$ | average |
| $f$ | fitting |
| $g$ | gas phase |
| $norm$ | normalized |
| $p$ | solids phase |
| $ref$ | reference |
| $th$ | threshold |

# References

Acosta-Iborra, A., Hernández-Jiménez, F., de Vega, M. & Briongos, J.V. 2012 A novel metodology for simulating vibrated fluidized beds using two-fluid models. *Chem. Eng. J.* 198-199, 261–274.

Benyahia, S., Syamlal, M. & O'Brien, T.J. 2012 Summary of mfix equations 2012-1. In *https://mfix.netl.doe.gov/documentation/MFIXEquations2012-1.pdf*.

Boemer, A., Qi, H. & Renz, U. 1997 Eulerian simulation of bubble formation at a jet in a two-dimensional fluidized bed. *Int. J. Numer. Meth.* 23, 927–944.

Bradley, D. & Roth, G. 2007 Adaptive thresholding using the integral image. *Journal of Graphics Tools* 12:2, 13–21.

Gidaspow, D. 1994 *Multiphase flow and Fluidization*. Academic Press. Boston.

Hulme, I., Clavell, E., van der Lee, L. & Kantzas, A. 2005 Cfd modeling and validation of bubble properties for a bubbling fluidized bed. *Ind. Eng. Chem. Res.* 44, 4254–4266.

Kapur, J.N., Sahoo, P.K. & Wong, A.K. 1985 A new method for gray-level picture thresholding using the entropy of the histogram. *Comput. Graphics Image Process.* 29, 273–285.

Lacey, P.M.C. 1954 Developments in the theory of particle mixing. *J. Appl. Chem.* 4, 257–268.

Musmarra, D., Poletto, M., Vaccaro, S. & Clift, R. 1995 Dynamic waves in fluidized beds. *Powder Technol.* 82, 255–268.

Otsu, N. 1979 A threshold selection method from gray-level histograms. *IEEE Trans. Syst. Man. Cybern.* 9, 62–66.

Roy, R., Davidson, J.F. & Tuponogov, V.G. 1990 The velocity of sound in fludised beds. *Chem. Eng. Sci.* 45, 3233–3245.

van der Schaaf, J., Schouten, J.C. & van den Bleek, C.M. 1998 Origin, propagation and attenuation of pressure waves in gas-solid fluidized beds. *Powder Technol.* 95, 220–233.

Sveen, J.K. 1998-2014 Matpiv. In *https://www.mn.uio.no/math/english/people/aca/jks/matpiv/*.

Syamlal, M., Rogers, W. & O'Brien, T.J. 1993 Mfix documentation: Theory guide. *U.S. Department of Energy (DOE), Morgantown Energy Technology Center, Morgantown, West Virginia* .

CHAPTER
**THREE**

# Bulk oscillation and solids wave propagation in a vibrated fluidized bed

## Contents



## 3.1 Introduction

In Chapter 1 the main benefits of the use of vibrated fluidized beds were summarized. However, vibration further complicates the intrinsically intricate dynamics of fluidized beds. The study of the oscillations of a vibrated fluidized bed in the absence of bubbles and the way the vibration waves propagate inside the bulk of the bed can serve as a basis for the understanding of the complex phenomena affecting the bubbles once the vibrated bed is aerated above minimum fluidization conditions.

The presence of pressure waves in conventional fluidized beds has been a field of great interest during the last decades (e.g. Roy *et al.* (1990); Musmarra *et al.* (1995); van der Schaaf *et al.* (1998); Bi (2007); Sasic *et al.* (2007)). However, as described in Chapter 1, works analyzing pressure waves and other energy propagation mechanisms in a VFB remain scarce (Wang *et al.*, 1997, 2000; Barletta *et al.*, 2013).

Besides, many efforts have been also made to analytically characterize the oscillatory motion of the bed bulk in a vibrated bed of particles (Kroll, 1954; Gutman & Davidson, 1975; Erdesz & Ormos, 1983; Goldshtein *et al.*, 1995; Matchett & Alsop, 1995; Janssen *et al.*, 1998; Akiyama *et al.*, 1998; Barletta *et al.*, 2013). However, most of the modeling works reported in the literature are concerned with granular beds with no aeration. Among these works, Gutman & Davidson (1975) accounted for the compressibility of the gas phase present in the interparticle interstices but not introduced to the bed to model the collision of the bed bulk with the bed distributor. They confirmed the suitability of the Darcy's law for non-steady conditions through a vibrated bed of particles. Matchett & Alsop (1995) presented a two-phase column elastic and piston model to study the pressure and strain distributions in a vibrated column. Goldshtein *et al.* (1995) used experimental and modeling evidence to study the compression (shock) and expansion waves through a shallow vibrated bed.

Regarding aerated beds subjected to vibration, Janssen *et al.* (1998) presented a model to successfully describe the vibratory displacement of the bed bulk both when the bed was aerated below minimum fluidization conditions and when no gas was injected through the gas distributor. However, the bed elasticity was not considered in this model, which prevented the calculation of the relative motion of solids inside the bed as a function of their vertical coordinate. Barletta *et al.* (2013) also presented a model describing the bed cyclic compression and expansion. This model considers the bed bulk as a pseudo-homogeneous medium and provides a good prediction in terms of phase and amplitude of the bed cyclic motion of the surface of the bed. However, the model does not provide information regarding the solids oscillatory motion at intermediate heights in the bed bulk. The DEM simulations carried out by Xiang *et al.* (2010) were also used to characterize the behavior of a bubbling vibrated fluidized bed and, particularly, of the interaction between the bed bulk and the bed vessel. They observed that the maximum pressure in the bed distributor occurred when the bed vessel moved up (i.e. the void fraction was minimum). Also, Xiang *et al.* (2010) observed in the simulation that the energy transfer in the VFB was by collision when the bed is moving up and by wave propagation through the bed when the bed vessel is moving down.

In view of the previously cited references, one crucial aspect to characterize is the oscillating movement of the particles in a VFB, as they influence both the bed bulk and the bubbles dynamics. In particular, oscillations of the particle movement in a VFB may be linked to the compression and expansion of the bulk of the bed, which in turn can affect the size and rise velocity of bubbles and the resulting gulf stream motion. Besides, it is not totally clear the way vibration is propagated by the particle movement in the bulk of a gas fluidized bed. All these effects can have an impact on processes like gasification, combustion, drying and granulation in VFBs. From a fundamental point of view, it is

also interesting to know the temporal and spatial distribution of the particle movement in the bed and how this movement is coupled with the oscillation of the bed bulk. These results can be also of interest for the validation and development of numerical models describing the dynamics of VFBs.

The aim of the present chapter is threefold. Firstly, the oscillations of the surface, center of mass and bulk of a vibrated pseudo-2D bed, fluidized with air at minimum fluidization, are experimentally characterized with DIA. Operation at minimum fluidization eliminates the disturbance of bubbles on the dense phase, facilitating the measurement of the impact of vibration on the bulk of the bed. Secondly, these observations are connected with the temporal and spatial distribution of the particle movement obtained with PIV measurements in the studied VFB. In this regard, a simplified one-dimensional (1-D) model considering the bed bulk as a set of masses and bed discrete volumes, similarly as in Matchett & Alsop (1995), is developed and compared with the experimental results and with two fluid model simulations.

The ultimate objective of all these results is to explain the link between the bed bulk oscillation, the gas pressure waves and the local movement of the particles phase, and to present detailed information of the oscillating velocity of particles that may help to understand VFBs and to improve existing models of their behavior.

## 3.2 Experimental setup

The experimental facility used in this chapter is the pseudo-2D bed of dimensions 0.3 x 0.6 x 0.01 $m^3$ described in Section 2.1.1. The bed material was ballotini glass beads with a density of 2500 $kg/m^3$ and a diameter range between 425-600 $\mu$m. This bed material corresponds to type B particles, according to Geldart's classification (Geldart, 1973). Approximately, 5% of the particles were painted black to enhance the correlation during the processing of results with PIV. The minimum fluidization velocity of the particles at static conditions was $U_{mf} = 0.28$ m/s, which was measured by using the mean value of the pressure signal of a pressure probe attached to the rear wall at 0.025 m above the distributor.

A high speed camera (Redlake Motion pro X3) was employed to record images of the front view of the bed bulk at a frame rate of 250 images per second. Each of the conducted experiments comprised a recording time of approximately 14 s. Firstly, the superficial gas velocity was adjusted for each experiment to set minimum fluidization conditions. Secondly, the vibration of the bed was activated. Images started to be recorded approximately 10 s after turning on the vibro-motors in order to avoid the recording of start-up effects.

Table 3.1 lists the conditions of the experiments carried out. Three different static

bed heights ($H_0$) were tested: 0.3 m, 0.375 m and 0.45 m, which correspond to $H_0/W$=1, 1.25 and 1.5, respectively. The selected nominal case was Exp. 1, which has the largest frequency allowed by the vibro-motors under the vibration conditions of the present chapter ($f$ =17.1 Hz), the largest static bed height ($H_0/W$=1.5) and the lowest amplitude $A = 4.1$ mm. These conditions were found to clearly show the main features of the bed bulk behavior. The effects of the vibration amplitude and frequency were analyzed by independently varying $f$ or $A$ for the largest static bed height $H_0/W = 1.5$. Table 3.1 also includes the value of the vibration strength parameter for each of the experiments, which is defined as the ratio of the vibration acceleration to the acceleration of gravity:

$$\Lambda = \frac{A(2\pi f)^2}{g} \tag{3.1}$$

**Table 3.1:** Experimental conditions.

| Exp. | Vibration frequency $f$ (Hz) | Vibration amplitude $A$ (mm) | Static bed height $H_0/W$ (-) | Vibration strength $\Lambda$ (-) |
|---|---|---|---|---|
| 1 | 17.1 | 4.1 | 1.5 | 4.8 |
| 2 | 17.1 | 4.7 | 1.5 | 5.5 |
| 3 | 17.1 | 5.2 | 1.5 | 6.1 |
| 4 | 13.9 | 4.2 | 1.5 | 3.3 |
| 5 | 15.6 | 4.1 | 1.5 | 4 |
| 6 | 17.1 | 4 | 1 | 4.7 |
| 7 | 17.1 | 4 | 1.25 | 4.7 |

## 3.3 Numerical modeling

### 3.3.1 Development of a 1-D model of the vibrated bed at minimum fluidization

Figure 3.1 shows an schematic drawing of the model developed for the characterization of the oscillation of the vibrated fluidized bed. As in Matchett & Alsop (1995), the bed is modeled as a set of masses, $N_B$, and elastic columns (viz. bed discrete volumes) of height $H_0/N_B$. Contrary to Matchett & Alsop (1995) the injection of gas through the bottom of the bed is considered in the present model.

In each of the bed discrete volumes delimiting the masses there is a mixture of the gas and solid phases. Each volume expands and contracts to contain the same volume

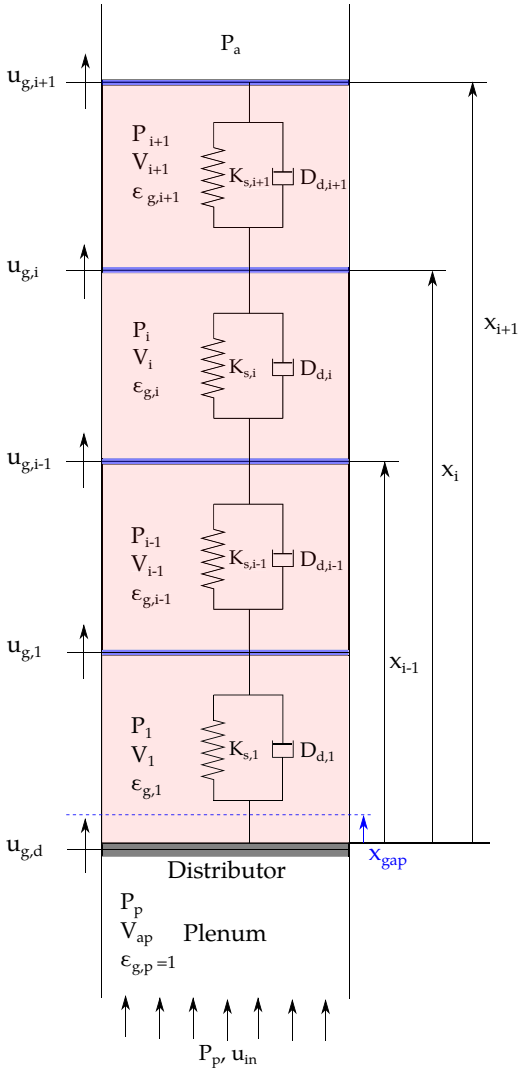


**Figure 3.1:** Schematic diagram of the simplified 1-D model of the bed.

of particles at any time. In addition, there exists elasticity and energy dissipation in the volumes due to the inherent elasticity of the bed material at compression and the contact between the masses. This elasticity is described as a set of spring-damper systems in series and connected to the center of each of the masses (see Figure 3.1). As a first approximation, the spring-damper elements between the masses are only activated in the case the masses collide, that is, when the void fraction of the bed volume within the $i^{th}$ bed discrete volume is smaller than a prescribed value $\varepsilon_{g,i} = 0.4$.

The presence of gas between each of the masses is accounted for in terms of the

pressure of the gas phase, which directly acts upon the masses. If no interchange of particles is considered between the different bed discrete volumes, the compression of the bed bulk will reduce the volume of the interstices between the particles, which, in turn, promotes an increase of the gas pressure in the bed volumes. Similarly, an expansion of the bed bulk promotes a reduction of the pressure within the different bed discrete volumes. In this simplified model, no transport of particles is considered between the bed discrete volumes. Besides, the gas phase is transported along the bed height at a velocity that was calculated using Darcy's law (see Appendix B). The gas mass flow exerts a drag force upon the masses, which is also considered in the present model.

The local bed motion can be characterized by variation of the vertical position of each of the masses in which the system was divided. Equation (3.2) represents the equation of motion of each of the masses, $i$, which considers all the forces described in the previous paragraphs. In order of appearance on the right hand side of Equation (3.2), the forces per unit mass over the masses are: gravity force, force caused by the pressure gradient inside the bed discrete volumes, force caused by the drag of the gas, forces due to the interaction of the solid masses and the acceleration force due to vibration.

$$\frac{\mathrm{d}^2 x_i}{\mathrm{d}t^2} = -g + \frac{N_B}{H_0 \rho_b} \varepsilon_i (P_i - P_{i+1}) + F_{drag,i} + \frac{N_B F_{spring-damper,i}}{\rho_b H_0 A_{bed}} + A\omega^2 \sin(\omega t) \quad (3.2)$$

Here, the number of masses used was $N_B = 20$, which was considered large enough to characterize the bed bulk oscillation without incurring in a large computational cost. Appendix B describes the equations used by the 1-D model.

### 3.3.2 Two fluid model simulations

In order to reproduce the VFB system described in the simplified 1-D model and the experiments, a two-dimensional two-fluid model simulation of the fluidized bed described in the experimental setup section (Section 2.2) was carried out. To fully account for the effect of the plenum in the simulation, the domain has a plenum of equivalent height $H_{eq}$ (Sasic *et al.*, 2005). Here, $H_{eq} = V_{ap}/A_{bed}$, where $V_{ap}$ and $A_{ap}$ are, respectively, the plenum chamber volume and the cross-sectional area of the experimental bed. In this computational domain, the air distributor was numerically modeled as an internal semipermeable surface, which prevents the particles from falling to the plenum and allows the gas to cross the distributor with a pressure drop made equal to that of the actual distributor. That is, the pressure drop through the simulated distributor follows the potential relation $\Delta P_d = 7.6 \cdot 10^4 U_g^2$, where $\Delta P_d$ is expressed in Pa and $U_g$ is the superficial gas velocity in m/s. The computational domains are discretized with a square grid of cell size equal to 4 mm in the section occupied by the solids. The cells are slightly

elongated in the sections on top of the bed and in the plenum, where only gas is present.

In this chapter, no attempt was made to simulate using an incompressible gas model, as it would lead to unrealistic results. A thorough description on the effect of including the gas compressibility and the plenum in the two-fluid model simulations can be found in Chapter 4.

The simulation results were performed using the MFIX code and were exported each 0.001 s over a period of 30 s of physical time. To make the plenum configuration as general as possible, the air was uniformly introduced through the bottom of the plenum at a given velocity $U_g$, to set the bed under minimum fluidization conditions. At the exit, a pressure outlet boundary condition was specified, with a static pressure equal to one atmosphere. At the walls of the bed and the plenum, no-slip conditions were imposed for the gas phase. For the solids, partial-slip conditions of Johnson & Jackson (1987) were specified at the walls with a standard specularity coefficient of $\Phi = 0.6$. A restitution coefficient, $e$, of 0.9 was used for both the particle-particle and particle-wall collisions. Similarly to the experiments, the static bed height in all the cases was set to $H_0 = 0.45$ m. More details about the simulation procedure and the treatment of gas compressibility can be found in Chapter 2 and Appendix A.

Table 3.2 summarizes the conditions used in the 1-D model and the two-fluid model simulation. Those variables that are exclusively used by the TFM simulations or the 1-D model are marked in the table as *sim.* and *model*, respectively.

**Table 3.2:** Simulation conditions

| Parameter | Value | Parameter | Value |
|---|---|---|---|
| $W$(mm) | 300 | $H$(mm) | 600 |
| $A$(mm) | 0.0041 | $f$(Hz) | 17.1 |
| $d_p(\mu$m) | 512.5 | $\rho_p$(kg/m$^3$) | 2500 |
| $H_0$(m) | 0.45 | $H_{eq}$(m) | 0.84 |
| $K_d$(kg/m$^3$) | $7.6 \cdot 10^4$ | $\mu_g$ (Pa·s) | $1.86 \cdot 10^{-5}$ |
| $P_a$(Pa) | 101300 | $T_g$(K) | 298 |
| $\varepsilon_0$(-) | 0.4 | $e$(-) (sim.) | 0.9 |
| $N_B$(-) (model) | 20 | $\chi$(-) (model) | 700 |
| $U_g$ (m/s) (sim.) | 0.17 | $\varepsilon^*$(-) (sim.) | 0.4 |
| $\theta(^o)$ (sim) | 30 | $\Delta t_{exp}$(s) (sim.) | 0.001 |

## 3.4 Results and discussion

The results obtained in this chapter are presented in four interrelated ways. Firstly, the oscillatory behavior of the bed bulk is experimentally studied by using the averaging of cycles method described in Section 2.3.2. Secondly, the PIV results concerning the bed solids oscillatory motion are analyzed altogether with their sensitivity to the static bed height, the vibration amplitude and the vibration frequency. Some experimental results revealing the wave propagation phenomenon through the bed bulk are presented and discussed. The last section shows and analyzes the results resorting from the two-fluid model simulation and the simplified 1-D model.

### 3.4.1 Experimental results

#### Oscillatory behavior of the bed bulk

Figure 3.2(a) shows a snapshot of the bed bulk at a time instant corresponding to an initial phase of the bed vessel oscillation $\phi \sim 0$ rad (i.e. the bed moving upwards and at its central position) for the nominal case (Exp. 1). The images depicted in Figure 3.2(b) and (d) show, respectively, a zoomed region of the bed surface and the bed bottom. Figure 3.2(c) shows the oscillation with time of the bed center of mass ($z = y_{cm,rel}$ in Equation (2.13)), surface position ($z = y_{fb}$) and the bed vessel position ($z = \delta$). The time increment between consecutive snapshots in Figure 3.2(b) and (d) is $\Delta t = 0.016$ s (i.e. every four recorded frames), which corresponds to an increment in phase of approximately $\Delta\phi \sim 0.275$ rad. The lines superimposed to the snapshots represent the oscillation of the bed surface (Figure 3.2(b)) and the bed vessel position (Figure 3.2(d)). It can be observed in Figure 3.2 that both the absolute position of the center of mass and the surface of the bed oscillate with a frequency equal to that of the bed vessel. Interestingly, the absolute position of the bed surface presents an oscillatory displacement in opposition of phase with the displacement of the bed vessel position. That means that when the bed vessel goes up the bed surface goes down and vice versa. Reversely, as shown in Figure 3.2(d), the bed vessel goes down when the bed surface goes up. This manifests a cyclic compression and expansion of the bed volume, similarly to the one encountered in other related experiments (Barletta *et al.*, 2013). On the other hand, the absolute position of the center of mass of the bed oscillates with a phase equal to that of the bed vessel, as it is mainly affected by the oscillation of the whole bed bulk caused by the vessel vibration.

The oscillatory behavior of the surface and the center of mass of the bed can be further studied by means of the averaging of cycles method described in Section 2.3.2. Figure 3.3 shows the results concerning the absolute and relative positions of $y_{fb}$ and

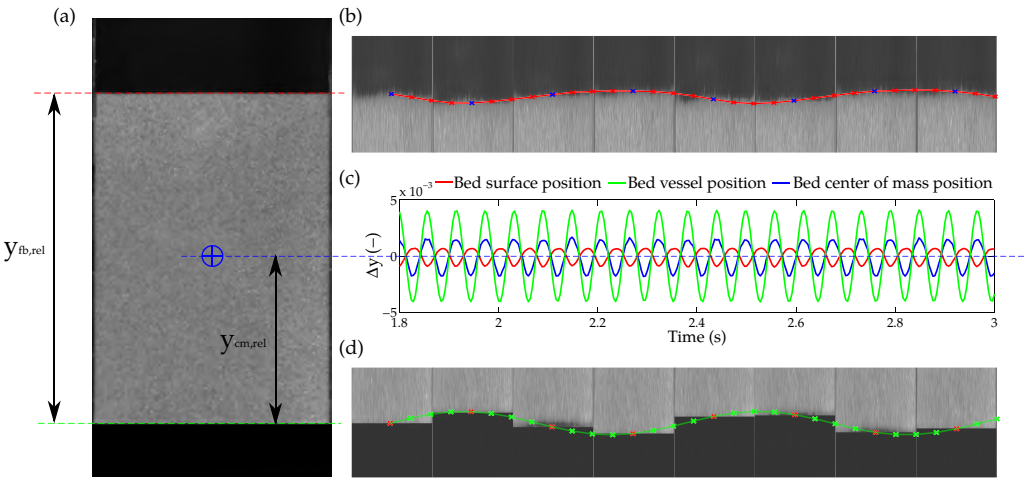


**Figure 3.2:** Oscillation of the bed bulk at minimum fluidization. (a) Snapshot of the bed taken by the high speed camera. (b) Zoomed snapshots of the bed surface superimposed by the oscillation of the bed surface. (c) Evolution with time of the oscillation of the bed surface, the bed position and the bed center of mass. (d) Zoomed snapshots of the bed base position superimposed by the oscillation of the bed position. Exp. 1.

$y_{cm}$ as a function of the phase of the bed vessel $\phi$ and normalized with the vibration amplitude $A$. Recall that $\phi = 0$ rad corresponds to the beginning of a vibration cycle and $\phi = 2\pi$ rad to the end of the cycle. As in Figure 3.2, it can be observed in Figure 3.3 that both the absolute and the relative oscillations of $y_{fb}$ present an opposition of phase with regard to the bed vessel oscillation. Also, the bed bulk expansion and compression caused by vibration is larger than the oscillation of the bed vessel. The origin of that may be attributed, in the expansion stage ($\phi = \pi/2 - 3\pi/2$ rad), to the ease of the particles on the upper region of the bed bulk to maintain their upward velocity due to inertia despite the fact the bed bulk commences to descend. In addition, in the compression stage, the decrease of the bed bulk height ($\phi = 3\pi/2 - \pi/2$ rad of the next cycle) is larger than the bed vessel displacement. During this compression stage, the bulk viscosity of particles is expected to damp the change of the bed volume because of the higher collisional stress due to the larger compaction of the bed (Moon *et al.*, 2006). Figure 3.3 also shows the normalized bed volume, which is calculated with the instantaneous front area occupied by the bed particles in the image divided by $W \cdot A$. Again, a cyclic compression and expansion of the bed volume in opposition in phase with the oscillation of the bed vessel is observed. As expected, the normalized oscillation of the bed volume is very close to that of the relative position of the bed surface. The differences encountered between the two curves can be attributed to the slight changes in the shape of the oscillation of the bed volume caused by the separation of the bulk from the bed base (see Figure 3.2(d)), which takes place when the bed commences to descend ($\phi = \pi/2$ rad).

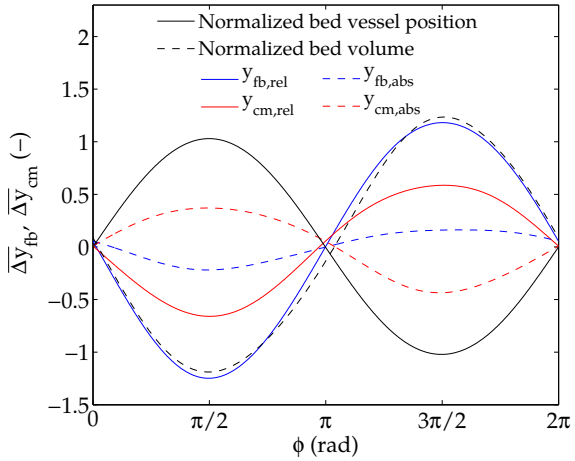


**Figure 3.3:** Oscillation of the bed vessel position, the bed volume and the absolute and relative positions of the freeboard and the center of mass of the bed. Exp. 1.

### Wave propagation in the bed

Figure 3.4 presents the results of the averaging of cycles of the absolute velocity vectors together with the contours of the solids velocity magnitude for the Exp. 1 (see Table 3.1). The velocity vectors and contours are averaged over intervals of $\Delta\phi = \pi/4$ rad. As in Figure 3.3, $\phi$ represents the phase of the bed vessel displacement, with $\phi = 0 - \pi/2$ rad corresponding to the bed vessel moving upwards from the middle to the highest vertical position. It can be observed in the figure that the particles pertaining to the upper section of the bed (i.e. the bed volume close to the freeboard) present absolute velocities that are different to those pertaining to the lower section of the bed (i.e. the bed volume close to the distributor). When the particles in the upper section of the bed are moving up, the particles in the lower section are moving down and vice versa.

In Figure 3.4(f), the particles in the lower region of the bed have a downwards displacement, whereas in Figure 3.4(g) the particles move upwards in that region. This implies that the bed bulk impacts the bed vessel and the particle velocity changes in a phase close to $\phi = 3\pi/2$ rad, which corresponds to the beginning of the ascending stroke of the bed vessel. Besides, in the phase interval $\phi = 3\pi/2 - 7\pi/4$ rad (Figure 3.4(g)), the particles belonging to the upper section of the bed maintain their descendant displacement, as the information of the impact of the bulk with the bed vessel has not arrived yet to the bed upper region.

Figure 3.4 has shown that the impact of the bed bulk with the base of the bed creates a disturbance that travels through the fluidized bed in the form of a wave. This is in

harmony with the gas pressure wave reported by Wang *et al.* (2000), on the basis of the same impact disturbance in a cylindrical vibrated fluidized bed. Therefore, it seems that the pressure wave is another manifestation of the velocity wave seen in Figure 3.4. The wave caused by the impact of the bed vessel with the distributor has a front horizontally extended and travels upwards the bed bulk until it reaches the upper region of the bed around a phase $\phi \simeq \pi/4$ rad (of the next cycle). In that phase, the bed vessel commences to descend and, as the particles in the upper region of the bed still maintain their inertial displacement, two clearly distinguishable regions are formed in the bed in the phase interval $\phi = \pi/2 - 3\pi/4$ rad. In the upper section of the bed particles move up and in the lower section of the bed the particles move down as a consequence of the descending motion of the bed vessel. In Figure 3.4(c-f) there exists an expansion wave that travels upwards the bed and separates the bed in two regions of downward velocity of solids (close to the distributor) and upwards velocity of solids (in the upper section of the bed). In the phase interval $\phi = 3\pi/4 - \pi$ rad a small region of particles in the upper section of the bed still preserves its upward motion, which causes a smaller velocity of particles in the upper region in the subsequent phase intervals $\phi = \pi - 3\pi/2$ rad. Again, in a phase around $3\pi/2$ rad the bed bulk impacts the distributor and the bulk behavior previously described is cyclically repeated. The presence of this wave propagation mechanism is in harmony with the DEM simulations of Xiang *et al.* (2010), as commented in the introduction section of the present chapter.

In order to qualitatively study the propagation of the wave produced at the base of the bed, Figure 3.5 shows a detail of Figure 3.4 for a phase interval $\phi = 3\pi/2 - 2\pi$ rad. This interval is decomposed in Figure 3.5 in small phase intervals of size $\Delta\phi = 0.0625\pi$ rad. In Figure 3.5(a-b) it can be clearly observed the formation of a wave caused by the impact of the bed bulk with the distributor that propagates upwards in the bed. In Figure 3.5(b-h) the wave delimits two regions of upward and downward absolute velocity of solids in the bed bulk. Also, in Figure 3.5(b-c) the wave presents a 'U' shape. This shape is caused because the wave generated on the distributor appears earlier close to the left and right corners than on the distributor center ($x = 0.15$ m). Near the corners, the friction of the particles with the lateral walls reduces the difference between the particles and the bed vessel velocities. This makes that the particles close to these corners impact the base of the bed with a smaller phase delay than the particles on the distributor center. When the wave is sufficiently far from the distributor (Figure 3.5 (c-h)) particles in the region under the wave present an upward velocity equal to the bed vessel ascending velocity as they move with the same velocity of the distributor. On the other hand, the particles above the wave present downward velocity and they cover a progressively smaller area.

Similarly to Figure 3.5, in Figure 3.6 the expansion wave generated in the vertically vibrated bed in the phase interval $\phi = \pi/2 - \pi$ rad was studied, which corresponds to a

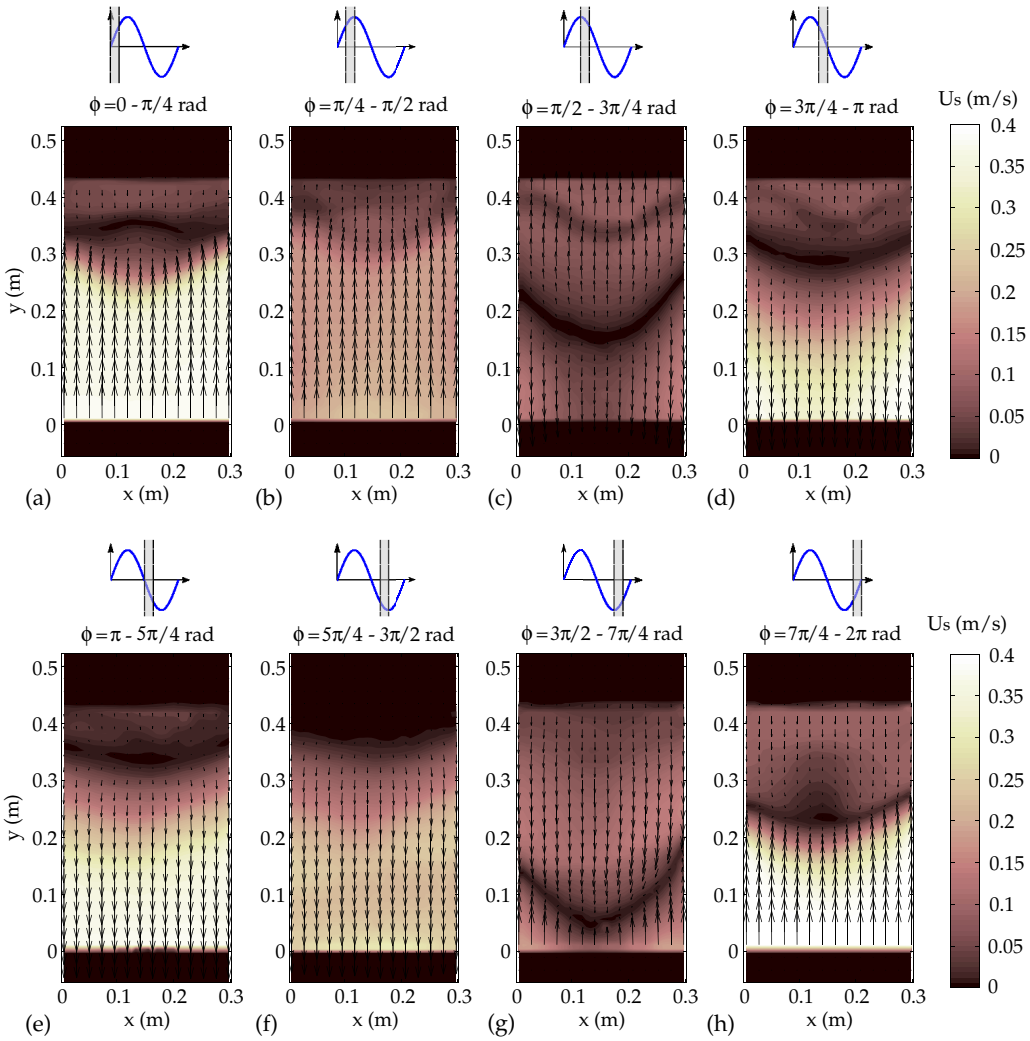


**Figure 3.4:** Averaging of cycles of the absolute velocity of solids in the vertically vibrated fluidized bed for eight different phase intervals of size $\Delta\phi = \pi/4$ rad over a total interval $\phi = 0 - 2\pi$ rad. The velocity vectors are shown superimposed to the velocity magnitude contours. Exp. 1.

phase range of the expansion wave in which it can be clearly appreciated. This expansion wave clearly differentiates the bed bulk into two regions. The formation of the expansion wave corresponds to the descending stroke of the bed vessel. In this phase interval, the bed vessel commences to move downwards ($\phi = \pi/2$ rad) and the particles belonging to the lower section of the bed start to descend as they loose contact with the distributor. In Figure 3.6(c-d), a progressively larger volume of particles in the lower section of the bed is affected by this downward motion, which promotes the wave front to move upwards. However, particles belonging to the upper section of the bed maintain their upward

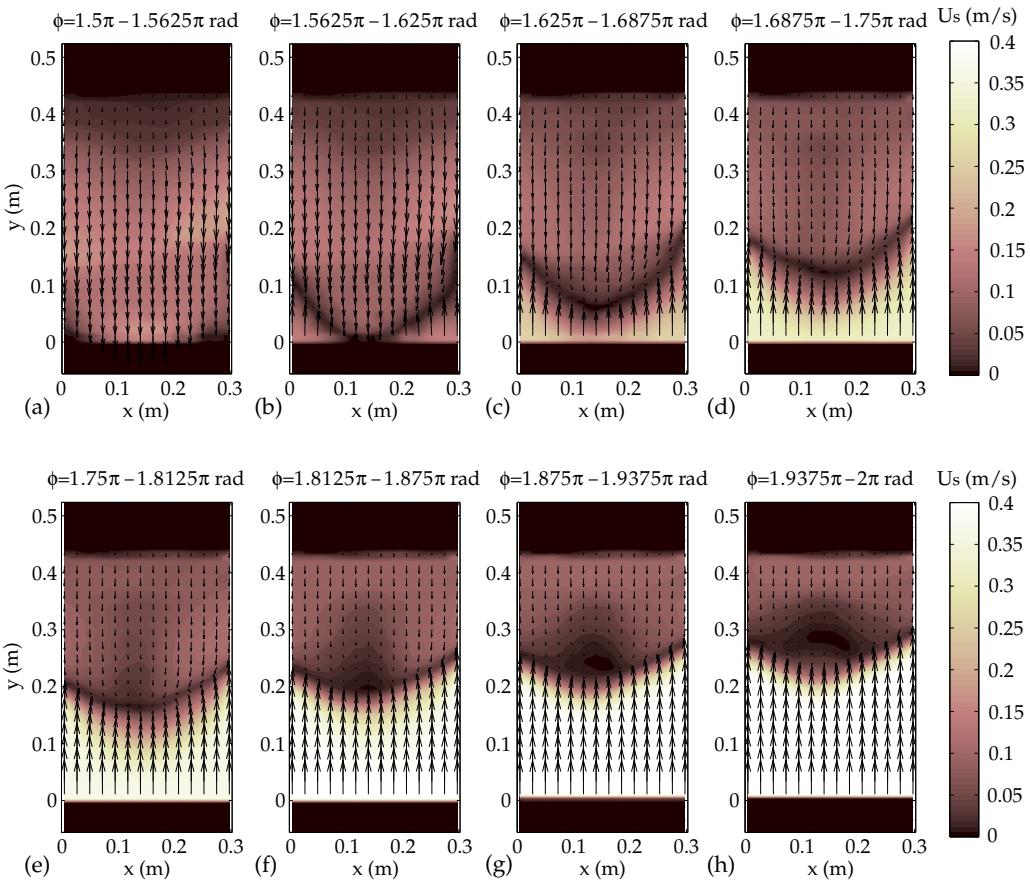


**Figure 3.5:** Averaging of cycles of the absolute velocity of solids in the vertically vibrated fluidized bed for eight different phase intervals of size $\Delta\phi = \pi/16$ rad over a total interval $\phi = 1.5\pi - 2\pi$ rad. The velocity vectors are shown superimposed to the velocity magnitude contours. Exp. 1.

inertial displacement and cover a progressively smaller area in Figure 3.6(e-h).

Figure 3.7 shows the averaged (in the horizontal direction) normalized oscillation of the relative vertical velocity of solids along lines of constant absolute positions, $y$, situated at different heights from the distributor and as a function of the phase of the bed vessel. The horizontal lines in which the velocity is calculated are separated $\Delta y = 0.05$ m. The normalization is carried out by means of the bed vessel velocity, which was calculated using Equation (2.2), thus:

$$\overline{\Delta V}_s = \frac{\Delta V_s}{V} \tag{3.3}$$

As commented in Section 2.3.2, the averaging of cycles curves are obtained after smoothing all the experimental data within $\phi = 0 - 2\pi$ rad. In the case of Figure 3.7,

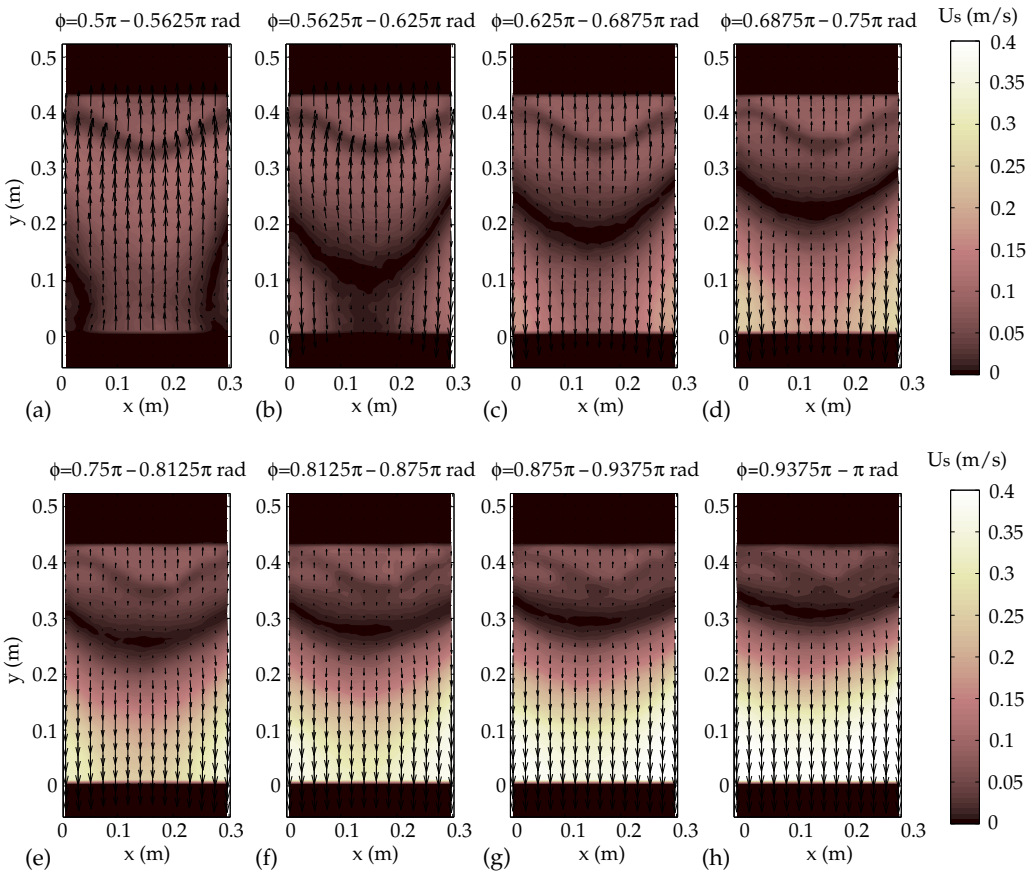


**Figure 3.6:** Averaging of cycles of the absolute velocity of solids in the vertically vibrated fluidized bed for eight different phase intervals of size $\Delta\phi = \pi/16$ rad over a total interval $\phi = 0.5\pi - \pi$ rad. The velocity vectors are shown superimposed to the velocity magnitude contours. Exp. 1.

the standard deviation of the data points of the relative velocity is between 0.01 and 0.06 when dividing the phase range in phase intervals of similar span than the smoothing spline ($\Delta\phi \simeq 2\pi/100$ rad). This indicates that the data dispersion and the relative uncertainty of the results are low. For the rest of the PIV results of this chapter, low values of the data dispersion are also found.

In Figure 3.7, the oscillation of the solids velocity is larger as they are further from the distributor because they are more free to move due to the smaller mass of particles above them. This creates a delay of about $\pi$ rad between the particles and the bed vessel velocity. Note that the relative velocity of the solids in the upper section of the bed, $y > 0.3$ m, is slightly larger than the velocity of the bed, $\overline{\Delta V}_s > 1$. This is attributed to the inertial displacement of the particles in the upper section of the bed when the

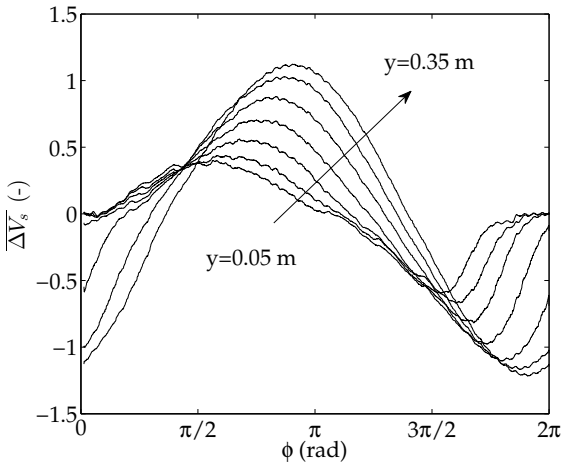


**Figure 3.7:** Oscillation of the normalized relative vertical velocity of solids at different distances from the distributor. The lines in which the particle velocity is calculated are separated $\Delta y = 0.05$ m. Exp. 1.

bed vessel is moving downwards. In the lower region of the bed, the particles are more confined due to the weight of the bed bulk above them and that decreases the amplitude and delay of their velocity with respect to the vessel velocity. In addition, also in the lower region of the bed, the oscillation of the vertical velocity of solids follows a nearly sinusoidal displacement in the first half of the cycle $\phi = 0 - \pi$ rad, which corresponds to the fraction of the cycle in which the bed vessel commences to decelerate and the velocity changes from positive to negative values. This creates a positive oscillation of the relative vertical velocity of the bed bulk, as particles maintain their upward velocity. In the second half of the cycle ($\phi = \pi - 2\pi$ rad) the bed vessel velocity commences to increase from negative to positive values and that causes a decrease of the bed bulk relative velocity. As shown in Figure 3.5, the bed bulk impacts the distributor at a phase around $\phi \simeq 3\pi$ rad. This is reflected in Figure 3.7 through the sudden increase of the oscillation of the vertical velocity of solids occurring at $\phi > 3\pi/2$ rad for the smaller distances from the distributor ($y = 0 - 0.2$ m). After impacting the distributor, the particles close to it adopt the vessel velocity, which leads to $\overline{\Delta V}_s = 0$ for $\phi \simeq 7\pi/4$ rad. The perturbation caused by the interaction of the bed particles with the distributor is transmitted upwards with a finite velocity, as evidenced in Figure 3.7 with the progressive phase delay of the increase of $\overline{\Delta V}_s$ with $y$ for $\phi > 3\pi/2$ rad. Again, when the bed vessel commences to decelerate at $\phi = 0$ rad, the oscillation of the bed relative velocity becomes greater than zero and the whole process is cyclically repeated.

To quantitatively analyze the vertical distribution of the velocity wave, Figure 3.8

shows the evolution, for different time instants, of the normalized relative vertical velocity of solids along the vertical direction. The solids velocity has been sampled from a vertical fringe of a width of $\Delta x \simeq 0.02$ m (three PIV windows) situated in the central section of the bed ($x = W/2$) and also from two vertical fringes of the same width but close to the bed walls ($x = W/4$ and $x = 3W/4$). The velocity within each fringe is averaged horizontally to reduce noise. The figure shows a set of time instants separated $2\Delta t = 0.008$ s (i.e. $\Delta\phi = 0.86$ rad). The first time instant is $t_0$, which has a phase equal to $\phi = 0.08$ rad. It can be observed in Figure 3.8 that the behavior of the solids velocity in the different fringes along the horizontal direction presents only a slight variation, which is caused by the non perfectly symmetrical impact of the bed bulk with the bed vessel, as seen in Figure 3.5. For $t = t_0$, the compression wave has already been generated at the bottom of the bed and the front of the velocity wave, which divides the bed in two regions with different relative velocities, is easily discernible. In $t = t_0 + 2\Delta t$, the bottom section of the bed presents a positive relative velocity, whereas there still exists a small region in the upper region of the bed in which particles are descending (in relative coordinates). In the subsequent time steps the relative velocity of the particles in all the bed bulk is positive and, when the bed commences to decelerate, it increases in the upper region of the bed. There is an instant, around $t = t_0 + 10\Delta t$ and $t = t_0 + 12\Delta t$, in which the bed bulk impacts the base of the bed and this cyclic behavior is repeated.

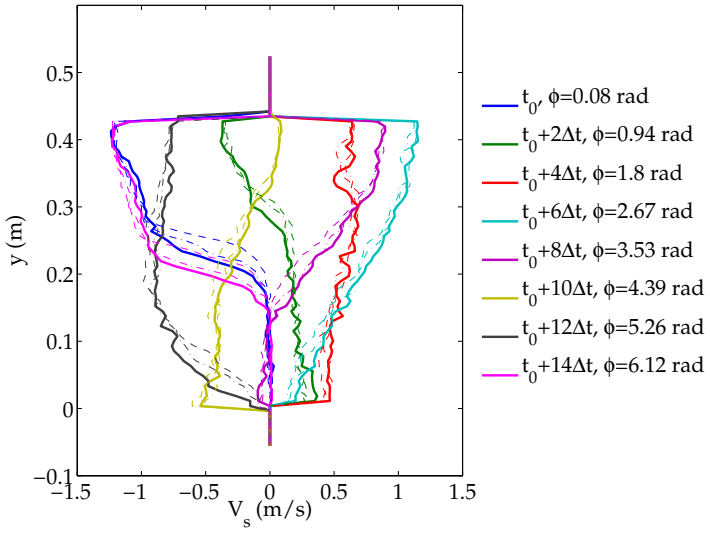


**Figure 3.8:** Time evolution of the normalized relative vertical velocity of solids along the vertical direction. Solid line: vertical fringe at $x = W/2$. Dashed-dotted and dashed lines: vertical fringes situated at $x = W/4$ and $x = 3W/4$. Exp. 1.

Considering that the bed presents a cyclic behavior, it could be of interest to study the behavior of solids and the wave propagation phenomenon in the bed as a function of the phase of the bed vessel. In this regard, Figure 3.9 presents the phase evolution of the solids velocity along a vertical fringe in the central section of the bed ($x = W/2$ and width of the fringe of $\Delta x \simeq 0.02$ m). In Figure 3.9, every line averages the solids velocity pertaining to a phase $\phi = \phi_0 + i\Delta\phi$ $(i = 1, 2, ..., M)$ along a complete experiment. In this case, $M = 32$ and $\Delta\phi = \pi/16$ rad, which ensures the averaging of approximately 100 time instants for every phase interval. The results are normalized with the velocity of the bed vessel $V$.

Figure 3.9(a) shows the evolution of the relative particle velocity with the phase in a phase interval $\phi = 5.2 - 1.1$ rad (of the next cycle) as it represents the phase interval in which there is an upward compression wave inside the bed. It can be observed that, just before the bed bulk impacts the bed vessel, the whole bed bulk presents a net negative relative velocity ($\phi = 5.2$ rad in Figure 3.9(a)). From that phase interval on, the bed is clearly divided into two regions, which are separated by the compression wave front observed in Figure 3.5. One region with a relative vertical velocity of solids $V_s = 0$ as particles are being drifted upwards due to the presence of the base of the bed; and a region in which particles maintain their negative relative velocity, as could be qualitative observed in Figure 3.5. There is a phase, around $\phi = 0.2$ rad, in which the relative velocity of particles at the bottom of the bed is positive, which indicates that the bed bulk in that region is moving faster than the base of the bed, which is probably caused by the upward inertial velocity of the particles while the bed is decelerating.

Figure 3.9(b) represents the evolution of the particle velocity with the vibration phase in the phase interval $\phi = 1.3 - 5$ rad. There exist two clearly distinguishable subintervals of phase in Figure 3.9(b) concerning the behavior of the solids velocity. In the first one, marked in Figure 3.9 as 'A', the relative velocity of the particles in the lower section of the bed scarcely varies whereas the bulk velocity in the upper section of the bed progressively increases. This corresponds to the fraction of the cycle in which the bed vessel commences to move downwards and the bed bulk detaches from the base of the bed. In the upper region of the bed, the particles maintain their inertial displacement and present a progressively larger upward velocity. At a phase close to $\phi = \pi/2$ rad the bed commences to expand as the relative velocity of the particles in the upper region of the bed is larger than in the lower region of the bed. Also, in Figure 3.9, the expansion wave described in Figure 3.6 commences to be observable in the subinterval 'B' in Figure 3.9(b). In this subinterval, the particles in the whole bed bulk commence to reduce their velocity and the velocity in the upper region of the bed is larger than in the lower section of the bed, which promotes the expansion of the bed bulk observed in Figures 3.3 and 3.4. However, the upwardly advancing front of the expansion wave observed in "B" in

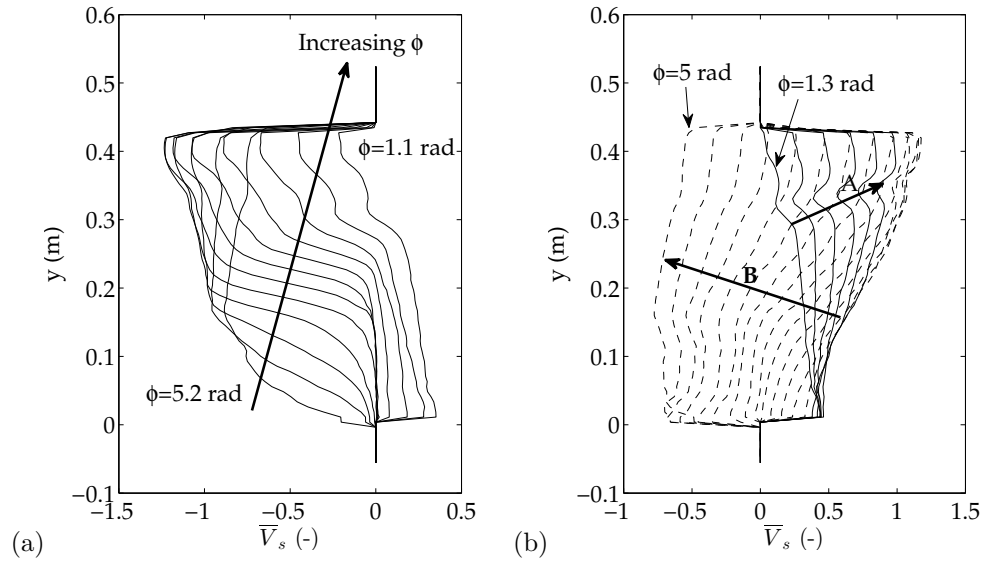


**Figure 3.9:** Vertical evolution of the normalized relative vertical velocity of the solids in the bed for different phase intervals: (a) Phase interval comprising the compression wave propagation in the bed, (b) phase interval comprising the expansion of the bed bulk and the expansion wave propagation until the bed bulk impacts the distributor. Exp. 1.

Figure 3.9(b) is less pronounced as it produces a softer change in the relative vertical velocity of solids in the bed as the compression wave in Figure 3.9(a). As commented before, for a phase $\phi > 3\pi/2$ rad (4.7 rad), the bed bulk contacts the distributor and this cyclic behavior is repeated.

### Effect of the static bed height

Figures 3.10 to 3.13 analyze the effect of the static bed height on the oscillatory behavior of the bed bulk and the wave propagation inside the bed. The amplitude of the vessel vibration, $A$, is similar in all the experiments of these figures. Firstly, similarly to Figure 3.3, the normalized oscillation of the bed surface and the bed center of mass is analyzed as a function of the vibration phase (see Figure 3.10) for different fill levels of the bed. It can be observed that the amplitude and phase of both the oscillation of the bed surface and the center of mass of the bed bulk remain practically unaffected regardless of the static bed height. This indicates that the oscillation of $y_{fb}$ and $y_{cm}$ are mainly caused by the bed vessel oscillatory displacement.

As in Figure 3.7, the effect of the static bed height on the oscillation of the relative velocity of particles as a function of the vibration phase at different heights $y$ from the

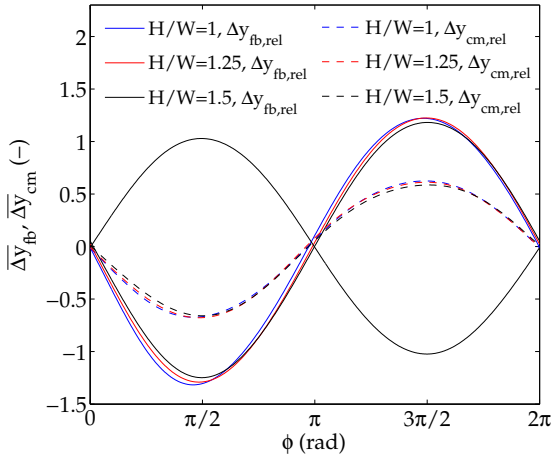


**Figure 3.10:** Effect of the static bed height on the oscillation of the bed vessel position and the absolute and relative positions of the freeboard and the center of mass of the bed. The solid black line indicates the normalized bed vessel position. Exp. 1, 6 and 7.

distributor is shown in Figure 3.11. For the three static bed heights the oscillation of the bed bulk velocity presents a qualitative behavior similar to that described in Figure 3.7. However, quantitatively, the particles oscillate more vigorously (for the same distance to the distributor) when the static bed height is decreased. As in previous figures, this is attributed to the smaller amount of particles above the horizontal fringe of analysis, which permits particles to move more freely and with a larger velocity. For the same reason, the oscillation of the particle velocity presents a slightly larger delay when the static bed height is decreased. This is attributed to the less force needed to lift the weight of particles in a bed of small static bed height due to both the smaller mass of the bed bulk and the more reduced friction with the vessel walls. If the volume of particles in the bed is smaller, the vibration of the bed vessel is able to fully detach the bed bulk from the distributor and create a larger air gap above it than when volume of the bed is larger. This ultimately promotes an earlier impact of the bed with the larger static bed height, as observed in Figure 3.11 for $\phi > 3\pi/2$ rad.

To study the possible effect that the static bed height may have on the oscillation of the bed bulk and the regions of different oscillation velocities in the bed, Figure 3.12 shows the contour maps of the normalized standard deviation of the velocity of particles in the bed for the three static bed heights tested (see Equation (2.20)). Here, the standard deviation of the solids velocity is normalized with the bed velocity as shown in Equation (3.4).

$$\overline{\sigma}_{U_s} = \frac{\sigma_{U_s}}{V} \tag{3.4}$$

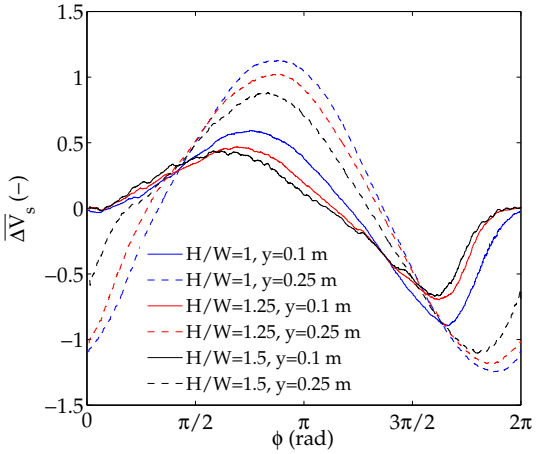


**Figure 3.11:** Effect of the static bed height on the oscillation of the normalized relative vertical velocity of solids at different distances from the distributor. Exp. 1, 6 and 7.

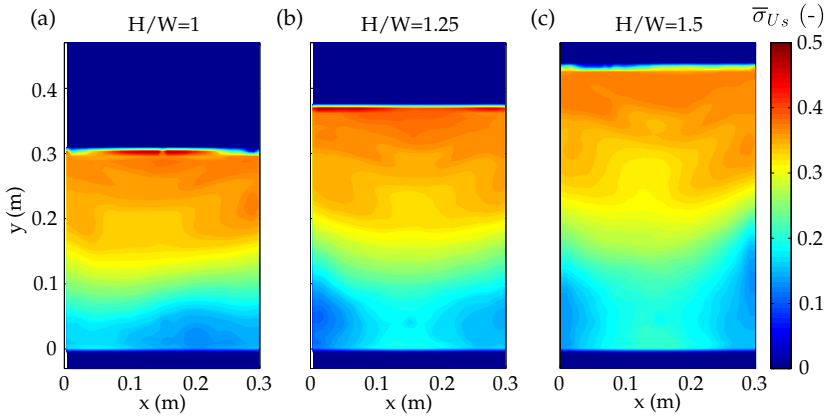


**Figure 3.12:** Effect of the static bed height on the normalized standard deviation contour map of the solids velocity. Exp. 6, 7 and 1.

It can be observed in Figure 3.12 that the behavior of the bed is similar for the three experiments. That is, when $H_0$ is decreased, in the upper section of the bed the contour maps present a progressively larger standard deviation of the velocity. This is due to the larger oscillation of particles when they have a smaller mass of solids above them. It is clear from Figure 3.12 that, in average, the velocity of the particles in the upper section of the bed oscillates more than in the lower section. This can explain why previous studies (Cano-Pleite *et al.* (2014, 2015, 2016), results that are shown in the subsequent chapters) have observed a change of bubble characteristics when passing from the lower to the upper sections of the bed. Noticeably, the upper section in which the particles oscillate

more vigorously covers a slightly larger volume as the static bed height is increased. This suggests that the behavior of bubbles rising in a vibrated fluidized bed may also differ depending on the static bed height.

The effect of the static bed height on the variation of the solids velocity in phase intervals of $\Delta\phi = \pi/16$ rad and along the bed height is studied in Figure 3.13 in a phase range $\phi = 0 - \pi$ rad (Figure 3.13(a)) and $\phi = \pi - 2\pi$ rad (Figure 3.13(b)). For simplicity, results of each $\Delta\phi = \pi/8$ rad are shown in Figure 3.13. The two regions in which the bed bulk is divided by the compression wave propagation along the bed height can be easily appreciated in Figure 3.13(a) in the phases in which the relative velocity of the solids in the lower section of the bed is close to zero and is negative in the upper section of the bed. Although in a lower extent, the expansion wave generated by the expansion of the bed bulk is also observable in the last phases of Figure 3.13(a) and in Figure 3.13(b), and it divides the bed bulk into two regions of smaller (lower section) and greater (upper section) relative vertical velocity of solids. In Figure 3.13(a), the compression wave in the bed with the smaller static bed height is ahead of the compression waves in the bed with larger $H_0$ because, in the former bed, the two regions of the different relative solids velocity have a smaller volume. However, no significant qualitative differences of the behavior of the bed bulk are encountered for the different $H_0/W$ under study. In all the cases tested, the bed compresses and expands cyclically due to the different relative velocities of solids in the upper and lower sections of the bed.

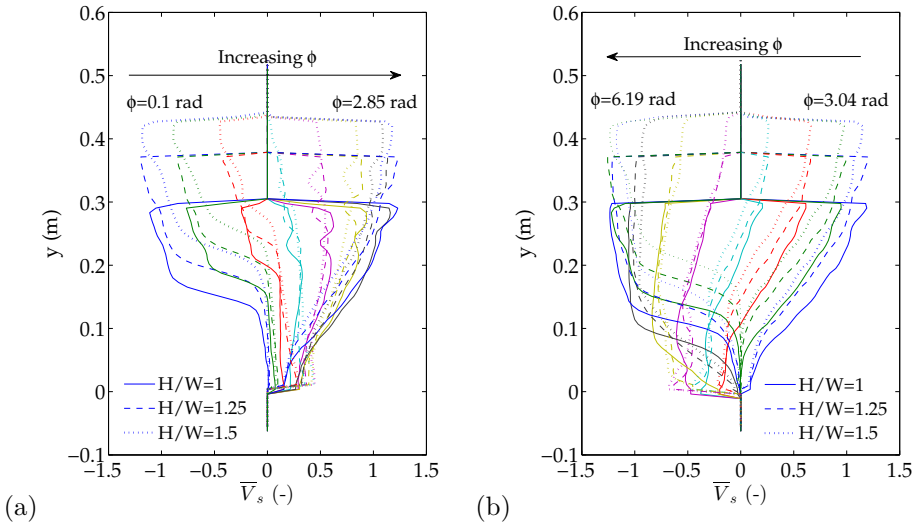


**Figure 3.13:** Vertical evolution of the normalized relative vertical velocity of the solids in the bed for different phase intervals and static bed heights. (a) $\phi = 0 - \pi$ rad, (b) $\phi = \pi - 2\pi$ rad. Exp. 1, 6 and 7.

**Effect of the vibration amplitude and frequency**

Figure 3.14 studies the effect of the vibration amplitude and frequency on the oscillatory behavior of the relative velocity of the particles of the bed bulk on horizontal lines at different distances from the distributor. Three different vertical coordinates are chosen in Figure 3.14: $y = 0.1$ m above the distributor, $y = 0.25$ m and $y = 0.35$ m (i.e. a distance of 0.1 m to the static bed height). Figure 3.14(a) shows that the normalized oscillation of $V_s$ increases accordingly with $A$ (i.e. $\Delta V_s = A \cdot \overline{\Delta V_s}$). The only remarkable difference encountered in Figure 3.14(a) among the different vibration amplitudes tested is found close to the distributor ($y = 0.1$ m). In that region, the phase $\phi$ in which the bed bulk impacts the distributor has a large influence on the phase delay of the solids in the lower section of the bed.

As for the variation of the vibration amplitude, the effect of the vibration frequency on the oscillation of the normalized relative particle velocity (Figure 3.14(b)) is also weak. In particular, prior to the impact of the bed vessel with the bed bulk, the oscillation of the normalized relative velocity of the particles in the lower region of the bed is smaller for smaller frequencies ($f = 13.9$ Hz) than for larger frequencies. The increase of the bed velocity caused by the increase of the vibration frequency affects slightly more the velocity of the particles inside the bed, contrary to the variation of the vibration amplitude in Figure 3.14(a). Note that, if the vibration frequency increases, the vibration strength, $\Lambda$, increases by a square factor, which makes the particles to be subjected to a larger acceleration. This is more noticeable in the lower sections of the bed, where the motion of particles is directly driven by the acceleration of the bed vessel.

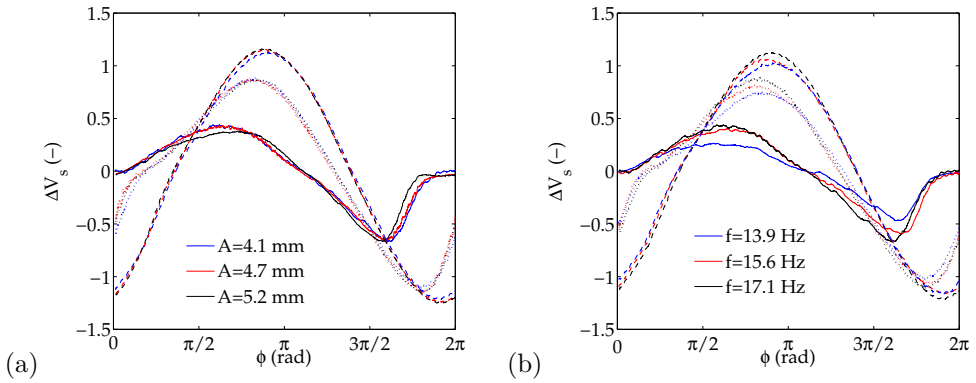


**Figure 3.14:** Normalized oscillation of the solids relative vertical velocity at different distances from the distributor. Solid lines: $y = 0.1$ m. Dotted lines: $y = 0.25$ m. Dashed lines $y = 0.35$ m. (a) Variation with the vibration amplitude (Exp. 1, 2 and 3), (b) variation with the vibration frequency. (Exp. 1, 4 and 5).

Figure 3.15 shows the normalized standard deviation contour maps obtained for different vibration amplitudes (Exp. 1, 2 and 3 in Figure 3.15(c-e)) and the vibration frequency (Exp. 1, 4 and 5 in Figure 3.15(a-c)). As in Section 3.4.1, the standard deviation of the solids velocity was normalized with the bed vessel velocity by means of Equation (3.4). As in Figure 3.12, the standard deviation delimits two regions in the bed: an upper region, $y > 0.2$ m and a lower region $y < 0.2$ m. In all the cases, the upper region has the largest values of the normalized standard deviation (i.e. the bed velocity oscillates more vigorously). As commented previously, the particles belonging to the upper region of the bed oscillate more vigorously as they are less confined by the weight of the bed. Also, Figure 3.15 indicates that the volume of the two regions is independent of both the vibration amplitude and frequency. Counteracting effects of the vibration amplitude and frequency seem to be affecting the behavior of the particles in the lower region of the bed, where the normalized oscillation of the particle velocity is smaller. When increasing the vibration frequency in Figure 3.15(a-c), the normalized standard deviation of the particle velocity in the lower region of the bed slightly increases, which is probably due to a higher average voidage in the lower section promoted by the increase of the vibration frequency, which allows for the particles to move more freely. On the contrary, when increasing the vibration amplitude in Figures 3.15 (c-e), $\overline{\sigma}_{U_s}$ slightly decreases for $y \lesssim 0.05$ m. This indicates that the oscillation of the particle velocity in the lower region of the bed might be damped by large amplitudes of vibration that densely pack the bed in that region and impede the particle movement.

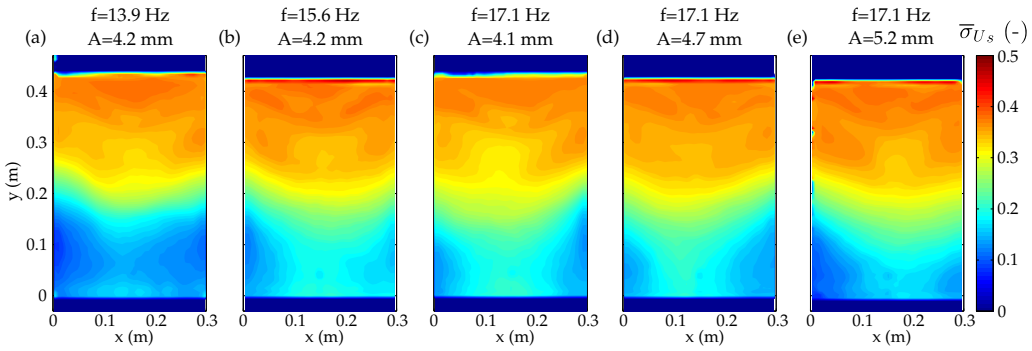


**Figure 3.15:** Normalized standard deviation contour map of the velocity of solids. (a-c) Variation with the vibration frequency (Exp. 4, 5 and 1), (c-e) variation with the vibration amplitude (Exp. 1, 2 and 3).

The effect of the vibration frequency and amplitude on the phase variation of the normalized vertical velocity of solids in a vertical stripe of width $\Delta x = 0.02$ m situated in the middle of the bed is depicted in Figure 3.16. As in Figure 3.13, phase intervals of $\Delta\phi = \pi/16$ rad with phase steps of $\Delta\phi = \pi/8$ rad within the different curves

in Figure 3.16 were chosen. Figures 3.16(a,c) show the results of the phase intervals belonging to $\phi = 0 - \pi$ rad, whereas Figures 3.16(b,d) depict results within the range $\phi = \pi - 2\pi$ rad. The effect of the different vibration amplitudes on the normalized solids velocity can be appreciated in the first phases of the wave propagation in the bed in Figure 3.16(b), which correspond to the phase range $\phi = 5.01 - 6.19$ rad. The compression wave of velocity generated for $A = 4.1$ mm is slightly forward in phase with respect to the cases of $A = 4.7$ mm and $A = 5.2$ mm. This is probably caused by the higher distance the bed lifts from the distributor when increasing the vibration amplitude, which delays (in phase) the impact of the bed vessel and the bed bulk. The effect of the vibration frequency on the normalized vertical velocity of solids is shown in Figure 3.16(c-d). Here, the lines corresponding to the different vibration frequencies are nearly overlapped except in the phase intervals in which the wave is in the lower region of the bed ($\phi = 5.01 - 6.19$ rad of Figure 3.16(d)). From all this, it can be extracted that the mechanism of wave propagation and the normalized velocity profiles of solids in the bed appear to be slightly affected by the vibration amplitude and frequency in the present range of conditions studied. This means that the amplitude of the velocity wave depends directly on the velocity of the bed vessel; that is, if the normalization of the velocity is undone, it is nearly proportional to $A$ and $f^2$.

**Wave propagation velocity**

As commented in the previous sections, the results show that there exists a compression wave that is generated at the bottom of the bed vessel and travels inside the bed. There is also an expansion wave going upwards. Thus, it would be interesting to characterize the velocity at which the velocity waves travel inside the bed bulk.

Firstly, the instantaneous position of the front of a compression wave with a velocity equal to that of the particles inside the bed was obtained by means of the averaging of cycles method for the absolute vertical velocity of the particles in the bed (similarly as in Figure 3.9). In this case, the absolute velocity of particles was discretized in $M = 64$ phase intervals in order to have a sufficient number of phase points in which the wave position was determined without compromising the statistical accuracy of the results. The wave vertical position was calculated as the vertical coordinate, in a vertical stripe of $\Delta x \sim 0.02$ m in the center of the bed, at which the absolute vertical velocity of the particles is equal to a threshold value that separates the maximum to the minimum vertical velocity of solids in the wave. This threshold is taken equal to half the maximum vertical velocity of solids in the vertical stripe. As the bed impacts the bed vessel in a phase $\phi \sim 3\pi/2$ rad, the compression wave position is calculated in an interval starting at $\phi = 3\pi/2$ rad and ending at $\phi = 7\pi/2$ rad (i.e. $\pi/2$ rad of the next cycle), which corre-

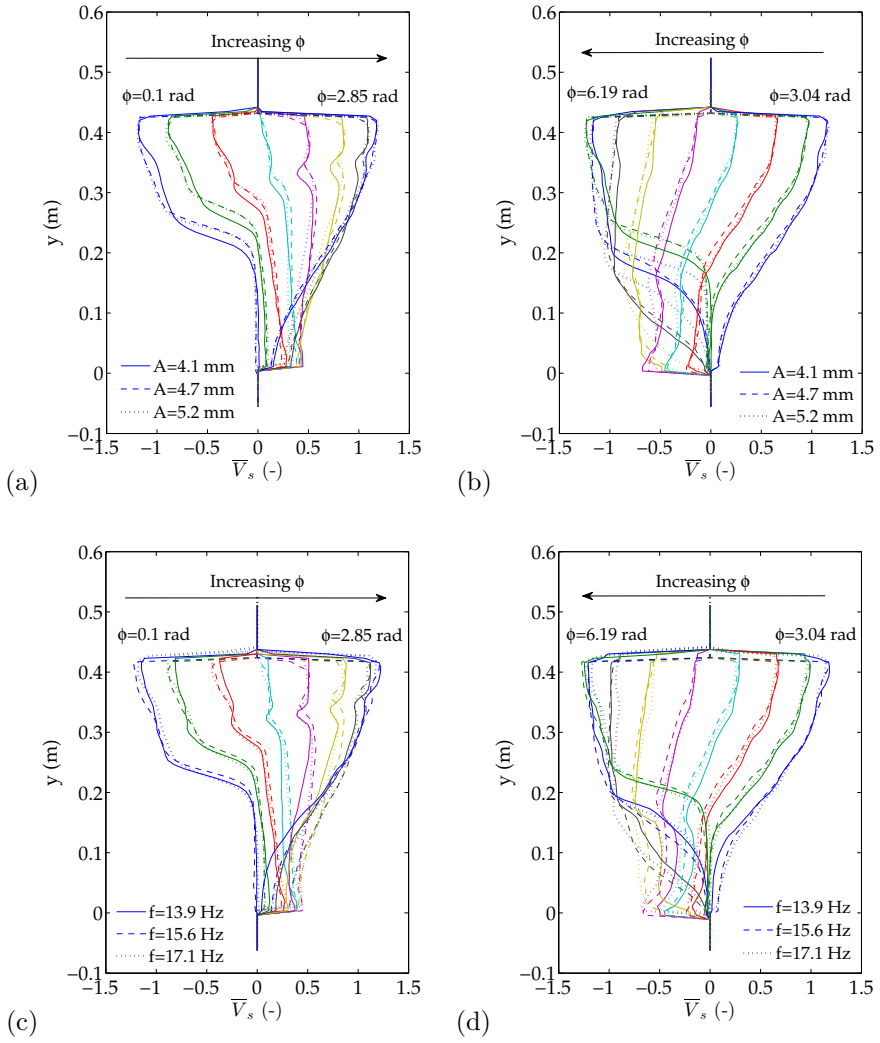


**Figure 3.16:** Vertical evolution of the normalized vertical velocity of the solids in the bed for different phase intervals. (a-b) Effect of the vibration amplitude (Exp. 1, 2 and 3). (c-d) Effect of the vibration frequency (Exp. 1, 4 and 5). (a,c) Phase interval $\phi = 0 - \pi$ rad, (b,d) phase interval $\phi = \pi - 2\pi$ rad.

sponds to the whole ascending stroke of the bed vessel. Equivalently, the expansion wave position is calculated in a phase interval $\phi = \pi/2 - 3\pi/2$ rad. Note that, in some phase intervals, the compression and the expansion waves are attenuated and their position is potentially less accurate. This occurs during the transition phases between compression and expansion waves, which corresponds to the shadowed regions in Figure 3.17.

Figure 3.17 shows the evolution of the position of the front of the compression and expansion velocity waves as a function of the vibration phase for the different experiments listed in Table 3.1. Two clearly distinguishable regions are observed in the compression wave region. In the lower section of the bed ($y < 0.2$ m), a fast increase of the compression wave front position appears, which is attributed to the more efficient wave transmission due to the denser packing of particles in this lower section of the bed. When the wave is sufficiently far from the distributor ($y > 0.2$ m), the position of the wave front increases less rapidly and more linearly. The upward displacement of the expansion wave front can be appreciated at $\phi \geq 0.7\pi$ rad and $y \geq 0.1$ m. In general, the position of this expansion wave front presents a nearly linear increase with a slightly smaller slope than the compression wave front.

Comparison of the different experiments depicted in Figure 3.17 shows that a similar trend is followed by the evolution of the waves position regardless the vibration amplitude and frequency of the bed. Reducing the static bed height for the same vibration conditions in Figure 3.17 seems to reduce the region in which the compression wave position presents a fast increase. Also, the front of the compression waves present in the bed filled with a smaller $H_0/W$ travels slower in the lower section of the bed, than in beds filled with a larger static bed height. This is probably associated to the larger confinement of particles in the lower region of the bed for larger $H_0/W$, which allows for a faster traveling of the perturbation along the bed (Bi, 2007). Additionally, when reducing the static bed height, the expansion wave manifests in a lower vertical coordinate, as this wave appears during the expansion stage of the bed bulk and depends on the vertical coordinate in which the particles commence to move downwards.

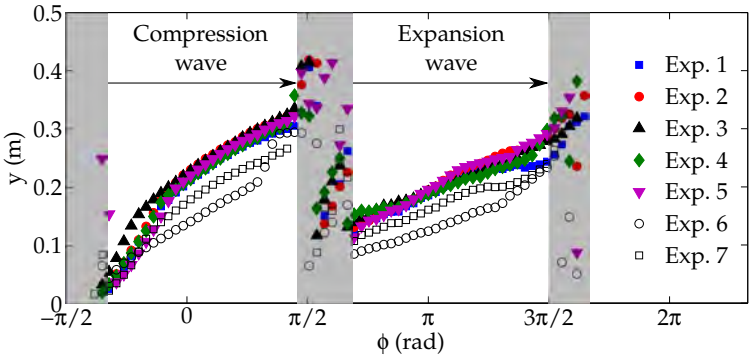


**Figure 3.17:** Evolution of the compression and expansion wave front positions as a function of the vibration phase.

The velocity of propagation of the wave inside the bed was calculated by means of Equation (3.5).

$$V_{prop} = \left( \frac{\omega \Delta y}{\Delta \phi} \right) \tag{3.5}$$

where $\omega = 2\pi f$ is the angular frequency of vibration and $\Delta y$ and $\Delta \phi$ denote, respectively, the variation of the absolute vertical position and the phase interval between two consecutive positions of the waves fronts in Figure 3.17.

Figure 3.18 presents the results of the wave propagation velocity calculated by means of Equation (3.5). The compression wave propagation velocity shows a maximum value when the wave is close to the distributor ($y < 0.2$ m), which corresponds to the larger slope of the wave position in Figure 3.17. According to Figure 3.18, the maximum wave velocity increases when the vibration amplitude and frequency are augmented. This observation suggests that, right after being generated, the wave propagation velocity is directly affected by the bed vessel acceleration, which densely packs the lower section of the bed, promoting a faster wave front. After this maximum value, $V_{prop}$ progressively decreases and remains in the range $V_{prop} = 5 - 10$ m/s for all the experiments. This progressive decrease of $V_{prop}$ may be caused by the progressively increasing voidage of the bed bulk as the wave front travels upwards. This is probably caused by the smaller confinement of particles in the upper region of the bed (see Section 3.4.1) where the wave propagation velocity decreases because the bed is less densely packed (Bi, 2007). Figure 3.18 also shows the velocity of the expansion wave front, which is around 5 m/s for all the cases tested.

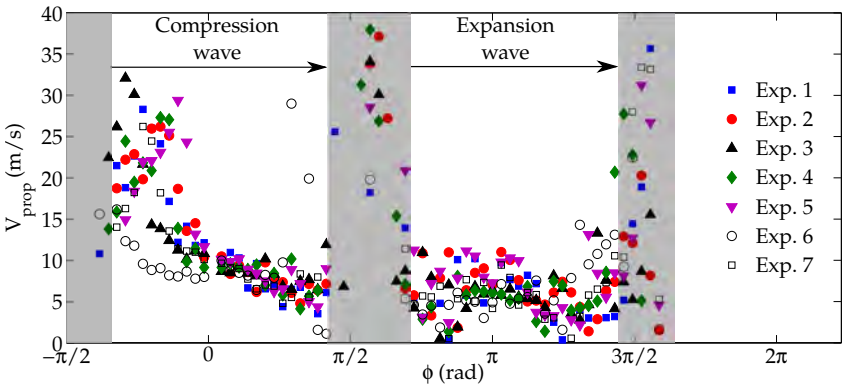


**Figure 3.18:** Evolution of the compression wave front velocity as a function of the vibration phase.

To see the sensitivity of the compression wave velocity on the acceleration of the bed, Figure 3.19 shows the mean, median and maximum value of the results of $V_{prop}$ shown in Figure 3.18. The results in Figure 3.19 are represented as a function of the vibration strength for the experiments with the same bed heights. It is clear from the figure that when $\Lambda$ is increased, the mean velocity of the wave and, especially, the median, are weakly affected because these velocities are principally affected by the numerous data of wave propagation far from the distributor ($\phi > 0$ rad in Figure 3.18) and less by the wave propagation data close to the distributor ($\phi < 0$ rad). In contrast, the standard deviation and the maximum velocity of the compression wave grow with $\Lambda$, in correspondence with the dispersion of data with $A$ and $f$ in Figure 3.18 that is only important for $\phi < 0$ rad.

In general, the mean and median values of the compression wave propagation velocity in the vibrated fluidized bed are in accordance to the classical values of the sound propagation velocity in a fluidized bed (Bi, 2007). Alternatively, in Xiang *et al.* (2010) the pressure wave propagation velocity is calculated in a vibrated fluidized bed as a function of the vibration frequency in a bed in bubbling regime. They observed that the propagation velocity increased with the vibration frequency. However, for the particles and the range of vibration amplitudes and frequencies tested in the present chapter, the wave propagation velocity presents a small variation with the vibration frequency. All these results show that, once the bed bulk impacts the base of the bed and the compression wave is generated, it travels in the bed at a velocity that is weakly affected by the vibrating conditions (e.g. $\Lambda$), excepting for a region close to the distributor.

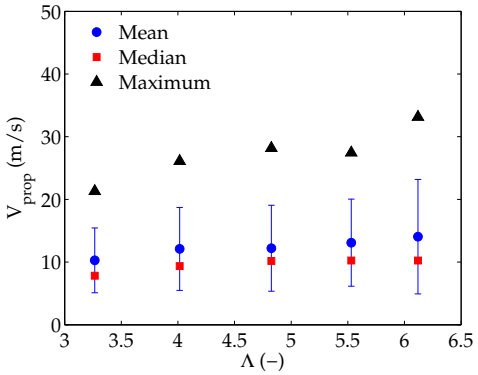


**Figure 3.19:** Mean, median, maximum and standard deviation bars of the wave absolute propagation velocity in the bed as a function of the vibration strength $\Lambda$. Exp. 1-5.

### 3.4.2 Numerical results

The present section analyzes the results obtained by the simplified 1-D model and the two-fluid model simulation described in Sections 3.3.1 and 3.3.2 and compares them with the experimental evidence presented in Section 3.4.1. Figure 3.20 shows the oscillation of the position of the center of mass and the surface of the bed predicted by the experiments (Figure 3.20(a)), the two-fluid model simulation (Figure 3.20(b)) and the 1-D model (Figure 3.20(c)). In the figure, both the 1-D model and the two-fluid model simulation provide a good description of the cyclic compression and expansion of the bed bulk observed in the experiments. This cyclic compression and expansion is evidenced by the opposed phase between the bed vessel position and the oscillations of the bed volume and the surface of the bed. In harmony with the experiments, the model and the compressible gas simulations also predict a cyclic compression and expansion of the bed bulk caused by vibration with an amplitude larger than the amplitude of vibration. Despite its simplicity, the 1-D model is capable of predicting the presence of the air gap between the bed bulk and the bed vessel. This is manifested by the different behavior between the oscillation of the relative position of the surface of the bed and the normalized bed volume in Figure 3.20.

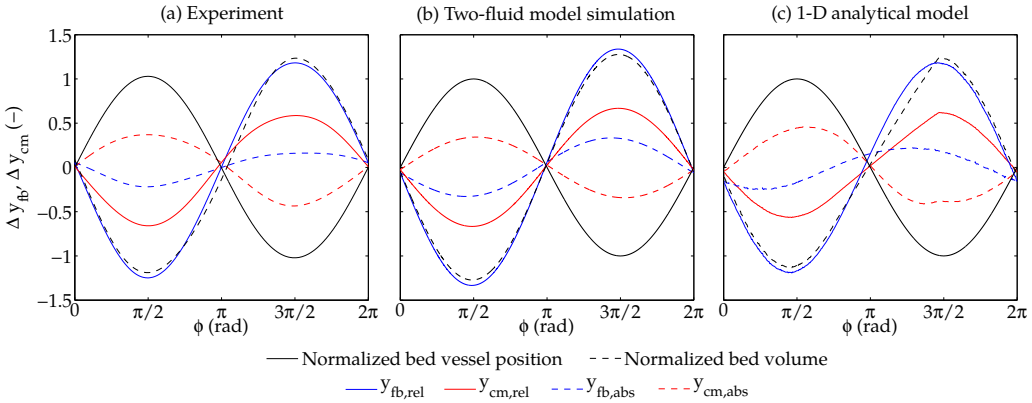


**Figure 3.20:** Oscillation of the bed vessel position, the normalized bed volume, the absolute and relative positions of the bed surface and the center of mass of the bed. (a) Experimental, (b) two-fluid model simulation and (c) 1-D model results. Conditions of Exp. 1.

The validity of the 1-D model and the numerical simulations was examined in Figure 3.21 in terms of the oscillation of the normalized solids velocity in the vertical direction. Figure 3.21 compares the experimental, modeling and the simulation results. Note that, in the 1-D model, the solids velocity is assumed to be that of the masses dividing each of the bed volumes. To obtain results at the same vertical coordinates in the bed, the

results of the experiments and the simulations were calculated at the average position of the masses in the model. Additionally, as in Figure 3.7, an averaging of cycles method was used to represent the cyclic behavior of the results depicted in Figure 3.21.

Commonly, one input value selected *ad hoc* in DEM simulations is the spring stiffness, which is closely related to the damping coefficient (Moon *et al.*, 2006). In the present 1-D model (see Appendix B) the spring-damper submodel is an oversimplification of the complex dynamic interaction of particles by collisions and drag within the discrete bed volumes. Hence, a sensitivity analysis of the effect of increasing the damping coefficient was carried out. It was observed that increasing the damping coefficient by a factor $\chi = 700$ led to results qualitatively similar to the experimental and two-fluid model results, as shown in Figure 3.21. The range of $\chi$ that provide qualitatively realistic results is in fact narrow. Values below $\chi = 500$ were unable to reproduce the impact of the bed bulk with the bed vessel. Besides, increasing this factor up to values of around $\chi = 900$ led to computationally expensive calculations that yielded similar qualitative results to those obtained with $\chi = 700$ but with a smaller velocity fluctuation in the lower section of the bed. Similar qualitative results of the bed expansion and the solids velocity in the upper section bed were found in the range $\chi = 500 - 900$. Further increasing of $\chi$ led to a very rigid or even an unstable system which was unable to reproduce the interaction of the bottom of the bed bulk with the bed vessel.

The 1-D model and the simulation results provide a good qualitative (and quantitatively reasonable) description of the oscillation of the solids velocity. The smaller oscillation of the solids velocity is found in all the cases in the lower section of the bed bulk and increases with the distance to the distributor. In Figure 3.21(a-c) the maximum oscillation of the solids velocity takes place in the upper section of the bed at an approximate phase of $\phi = \pi$ rad. This oscillation is larger than the normalized velocity of the bed vessel (i.e. $\overline{\Delta V}_s > 1$), which is in harmony with the experimental results. As shown in Figure 3.5, the bed bulk impacts the distributor at a phase around $\phi \simeq 3\pi/2$ rad. This is reflected in Figure 3.21(a-c) through the fast increase of the vertical velocity of solids. This perturbation is propagated upwards, as manifested by the latter increase of $\overline{\Delta V}_s$ with $y$. Both the model and the simulation are able to predict this increase of the solids velocity, which is less pronounced in the two-fluid model simulation, probably due to its smaller rigidity. Nevertheless, in the case of the 1-D model, the velocity of the masses presents some cyclic perturbations in the phase interval $\phi = 1.75\pi - 0.25\pi$ rad, arising from the presence of spring and damper systems.

The great availability of data at continuous vertical coordinates provided by the two-fluid model simulations can be used to determine the void, velocity and pressure variations in the vibrated fluidized bed as a function of the bed height. This valuable information can be used to determine the origin of the compression and expansion waves

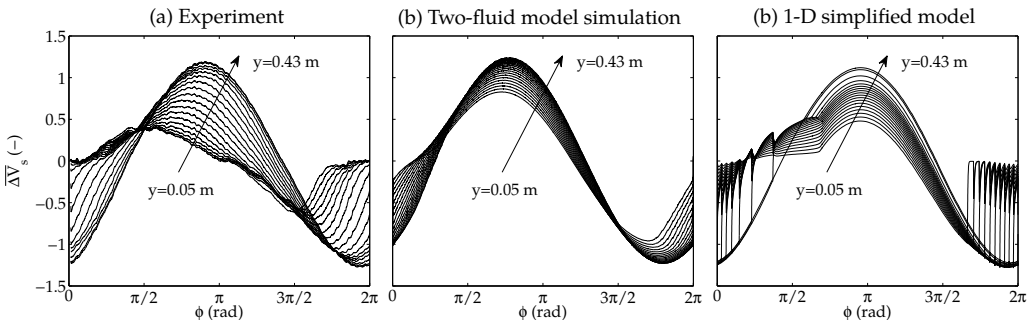


**Figure 3.21:** Oscillation of the normalized relative vertical velocity of solids at different distances from the distributor. (a) Experimental, (b) two-fluid model simulation and (c) 1-D model results. Conditions of Exp. 1.

traveling through the bed bulk. In this regard, Figure 3.22, shows the time evolution of the gas volume fraction, the gas pressure and the normalized solids velocity along a vertical fringe that, for each vertical coordinate, averages the values of the whole width of the bed.

As in the experiments, the impact of the bed bulk with the distributor of the bed promotes a progressive compression of the bed bulk along the bed height. This effect can be observed in Figure 3.22(a) by a sudden decrease of the void fraction, which can be clearly appreciated in the phase range $\phi = 0 - 0.51\pi$ rad. This void fraction perturbation travels upwards in the bed. The presence of the compression wave traveling through the bed bulk is also manifested by the fast decrease of the normalized solids velocity in the phase range $\phi = 0 - 0.5\pi$ rad in Figure 3.22(c). When the bed vessel commences to descend ($\phi > 0.5\pi$ rad), the compression wave has already reached the top section of the bed and the bed bulk commences to expand (see Figure 3.20). This is manifested by the increase of the void fraction and the smaller velocity of particles in the lower section of the bed than in the upper section in the phase range $\phi = 0.51\pi - 1.54\pi$ rad.

The pressure fluctuation along the bed height shown in Figure 3.22(b) seems to be largely affected by the cyclic oscillation of the bed bulk. The maximum pressure reached at the bottom of the bed is found in the phase $\phi = 1.88\pi$ rad, which corresponds to the last phase instant in which the compression wave is not observable in Figure 3.22(a,c) and it is attributed to a combination of both the maximum expansion of the bed bulk (minimum gas velocity and an increase of the gas pressure by the Bernoulli effect) and the commencement of the compression of the gas phase at the bottom of the bed.

Also, the presence of the compression wave in the bed vessel is linked to a perturbation in the pressure distribution along the bed height, as can be observed by the changes on the slope of the pressure curves at $\phi = 0.17\pi - 0.34\pi$ rad in Figure 3.22(b), which

take place at the same vertical coordinates as the void and velocity perturbations in Figure 3.22(a,c). This change of slope of the vertical pressure profile represents the front of a pressure wave traveling upwards as the solids compression wave.

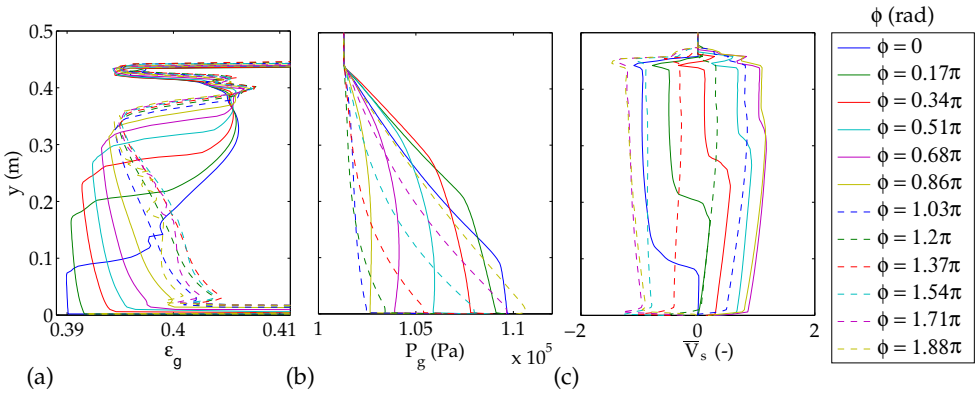


**Figure 3.22:** Vertical evolution with time of the (a) void fraction, (b) gas pressure and (c) normalized relative vertical velocity of the solids in the bed for different phase intervals of $\Delta\phi = 0.25\pi$ rad over a total phase range $\phi = 0 - 2\pi$ rad. Two-fluid model simulation. Exp. 1.

From all of the above, it is clear that, after the bed impacts the distributor, both the disturbance created in the solids velocity and the bed void fraction follow closely the disturbance on the gas pressure profile in the bed. Nevertheless, the relative importance of the particle collisions and the pressure fluctuations in the propagation of information through the bed bulk cannot be trivially extracted from the two-fluid model simulations because of its complex formulation. Instead, the simplified 1-D model presented in Equation (3.2) can be used. To this aim, Figure 3.23 shows each of the forces of Equation (3.2) (per unit of mass) acting over the bed discrete masses situated at $y_m = 0.0225$ m, $y_m = 0.225$ m and $y_m = 0.45$ m as a function of the vibration phase. Close to the distributor (Figure 3.23(a)), the main force affecting the motion of the masses is the damping force. This force is maximum when the bed vessel commences to ascend due to the compression of the bed discrete volumes in the lower section. The damping force is still dominant in the mass situated at $y_m = 0.225$ m (Figure 3.23(b)). However, the damping force manifests in a later phase and its magnitude is smaller than the one for the mass at $y_m = 0.0225$ m. This is attributed to the progressive damping within the bed of the energy of the bulk-distributor impact, which causes a higher compaction of the particles close to the distributor than in the upper layer of the bed.

Interestingly, the dominant forces in the upper section of the bed (Figure 3.23(c)) are the drag and the pressure gradient forces. In Figure 3.23(c), the effects of the spring and damper systems are very small because the bed compaction is very reduced. In the upper

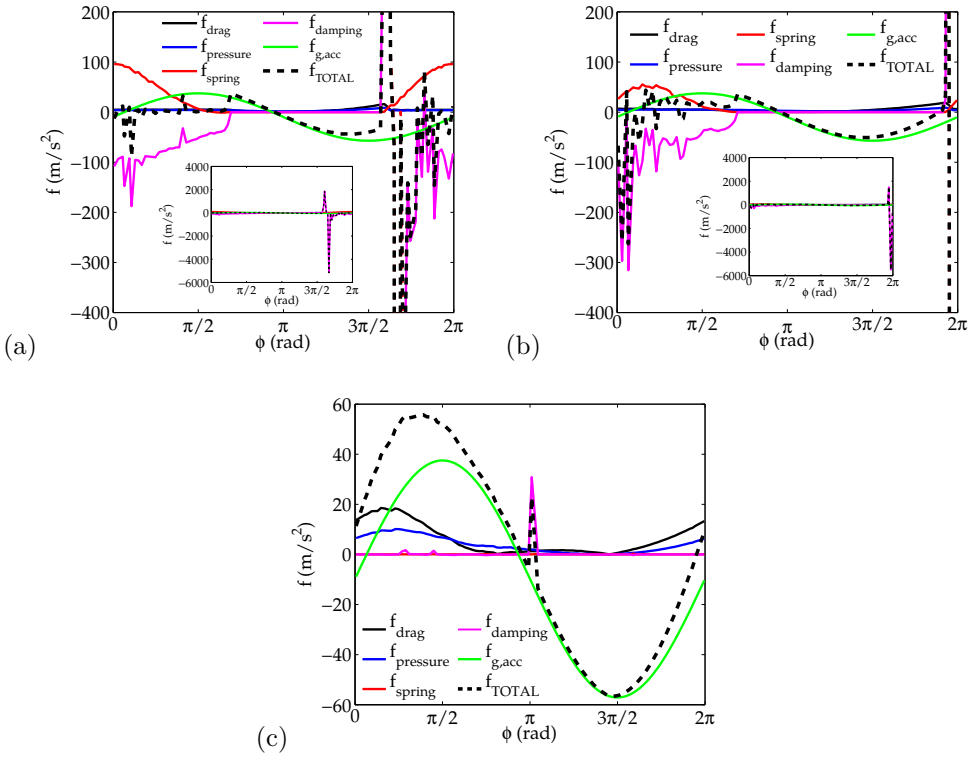


**Figure 3.23:** Forces per unit of mass as a function of the vibration phase acting over the masses situated at (a) $y_m = 0.0225$ m, (b) $y_m = 0.225$ m and (c) $y_m = 0.45$ m. 1-D model results. Exp. 1.

section of the bed, the pressure and drag forces are maximum in a phase $\phi = 0.3\pi$ rad, which is close to the phase of the maximum upwards acceleration force ($\phi = \pi/2$ rad). This promotes an increase of the total force in the phase interval $\phi = 0-\pi$ rad, which may be one of the effects causing an oscillation of the bed surface larger than the oscillation of the bed vessel (i.e. $y_{fb,rel} > 1$ in Figure 3.20).

The 1-D model can be also used to visualize the forces affecting the masses motion as a function of the vibration phase. Figure 3.24 shows the forces per unit of mass acting over the bed masses and for 16 intervals of phase of $\Delta\phi = 0.125\pi$ rad. Due to the different magnitudes of the forces, and to provide a better inspection of the evolution of the forces along the bed height, Figures 3.24(a,b,c,d) show, respectively, the drag, pressure, spring and damping forces acting on each of the bed masses.

The maximum values of the drag and pressure gradient forces are found in the phase interval $\phi = 1.5\pi - 0.125\pi$ rad (of the next cycle). These maximum values are caused by the increase of both the pressure and the gas interstitial velocity (at low void fraction)

when the bed bulk impacts the distributor and propagate upwards in the subsequent phases at an approximate velocity of $V_{prop} = 21.5$ m/s.

Regarding the forces exerted by the damping effect in the 1-D model, the maximum values belong to the interval $\phi = 1.75\pi - 2\pi$ rad. As anticipated in Figure 3.23, the maximum values of this force propagate upwards in the bed and their magnitude decrease, as the bed compaction is progressively smaller along the bed height. In the phase range $\phi = 0.5\pi - 1.5\pi$ rad the bed commences to expand and the void fraction in each of the volumes increases, which reduces drastically the force exerted by the damping effect.

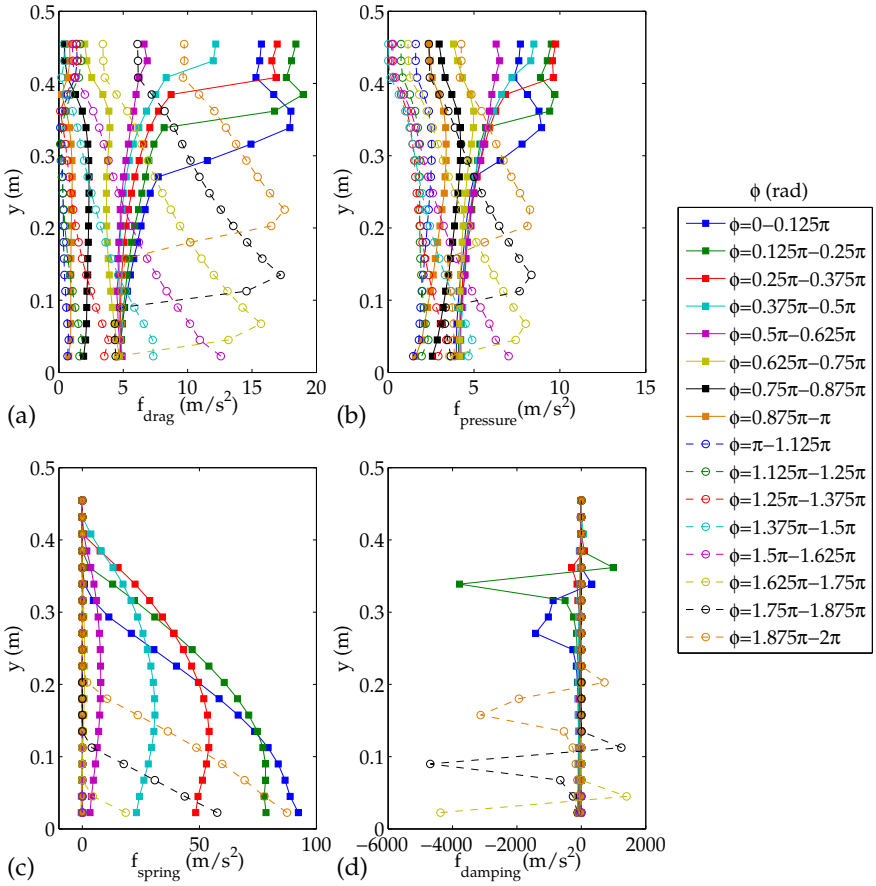


**Figure 3.24:** Forces per unit of mass acting over the bed masses and for 16 intervals of phase of $\Delta\phi = 0.125\pi$ rad over a phase range $\phi = 0 - 2\pi$ rad. (a) Drag, (b) pressure, (c) spring and (d) damping forces. 1-D model results of Exp. 1.

Noticeably, the damping force is slightly delayed in phase with regard to the gas drag and pressure forces. Note, for example, that the pressure and gas drag forces reach a maximum at $y = 0.135$ m for $\phi = 1.75\pi - 1.875\pi$ rad, whereas the value of the forces

exerted by the spring and the damper at that height and phase interval are very reduced ($f_{spring}$ = 0.002 m/s$^2$, $f_{damping}$ = 4.576 m/s$^2$). Therefore these results indicate that, according to the 1-D model, the solids velocity wave is primarily caused by the pressure gradients inside the bed, which are associated to the presence of a pressure wave. This pressure wave is cyclically generated at the base of the bed when the bed bulk impacts the distributor and travels through the bed bulk. This important outcome may explain the fact that the compression waves of solids traveling through the bed bulk (Section 3.4.1) present a velocity similar to the velocity of propagation of sound in a fluidized bed.

## 3.5 Conclusions

The oscillatory behavior of the bed bulk and the particles in a vertically vibrated fluidized bed were experimentally studied in this chapter by means of DIA and PIV. Experiments comprising beds of Geldart B particles aerated at minimum fluidization velocity and with different static bed heights and vibration amplitudes and frequencies were carried out. An averaging of cycles methodology was employed for the analysis of the oscillation of the bed surface and the center of mass of the bed as well as for the characterization of the periodic distribution of the solids velocity.

The results showed that the bed presents a cyclic compression and expansion caused by the vibration of the bed vessel. Analysis of the PIV results revealed that there exists a compression wave of solids velocity that spans the whole bed width. This wave is generated by the impact of the bed bulk with the gas distributor and travels upwards dividing the bed into two regions with different relative velocities. That is, the particles under the wave move upwards and the particles above the wave move downwards. It was also found that during the expansion phase of the bed, a less intense wave appears and travels upwards with particles under the wave moving downwards and particles above the wave moving upwards.

The effects of the static bed height and the vibration amplitude and frequency on the oscillation and the wave propagation of solids velocity were also studied. When the static bed height is increased, the spatial distribution of the oscillation of solids velocity presents the same qualitative behavior. However, the amplitude of the oscillation of the solids velocity at a given vertical position decreases because the column of particles above this position augments when the bed height is increased. The vibration amplitude changes proportionally to the amplitude of the oscillation of the particles velocity in the bed. An increase of the vibration frequency increases the amplitude of the solids velocity oscillation. Close to the distributor of the bed, the velocity of the compression wave presents a maximum which is directly produced by the upward displacement of the gas distributor in cooperation with the dense packing of particles in that region during the

compression phase of the vibration cycle. Far from the distributor, the velocity of the compression wave reaches values between 5 to 10 m/s, which are nearly independent of the static bed height and the vibration frequency and amplitude. The expansion wave front presents a velocity around 5 m/s.

A simplified 1-D model was developed and a two-fluid model simulation was carried out to better understand the solids wave propagation mechanism in the bed. Both the numerical simulation and the modeling results resemble the experimental results and have demonstrated to be of great help for the understanding on the dynamics underlying the compression waves of solids traveling through the bed. In both models, when the bed bulk impacts the distributor, a perturbation on the solids velocity travels upwards the bed. This perturbation is propagated through the bulk by collision of the particle layers, whereas the main forces acting on the particles in the upper layers of the bed are the drag force and the one arising from the pressure gradients in the bed. The 1-D model results indicated that the gas pressure gradients in the bed generate primarily the solids waves in the bed bulk.

The oscillation of the bed bulk and the propagation of velocity waves analyzed in this chapter can help to understand the fundamental mechanisms of particle-vessel interaction and the bubble behavior in vibrated fluidized beds. Thus, the results here presented can help to shed light on the different behaviors of bubbles and pressure signals reported in previous works regarding vibrating fluidized beds and in Chapters 4, 5 and 6.

## Nomenclature

| | |
|---|---|
| $A$ | vibration amplitude (mm) |
| $A_{bed}$ | cross-sectional area of the bed ($m^2$) |
| $d_p$ | particle diameter ($\mu$m) |
| $e$ | restitution coefficient (-) |
| $f$ | vibration frequency (Hz) |
| $F$ | force (N/kg) |
| $g$ | gravity acceleration constant ($m/s^2$) |
| $H$ | bed height (m) |
| $H_{eq}$ | plenum equivalent height (m) |
| $H_0$ | static bed height (m) |
| $K_d$ | gas distributor pressure drop ($kg/m^3$) |
| $M$ | number of phase intervals for averaging of cycles (-) |
| $N_B$ | number of bed discrete volumes (-) |
| $P$ | pressure (Pa) |
| $t$ | time (s) |

| | |
|---|---|
| $\Delta t_{exp}$ | simulation data exporting time-step (s) |
| $U_{mf}$ | minimum fluidization velocity (m/s) |
| $U_g$ | gas velocity (m/s) |
| $U_s$ | solids velocity (m/s) |
| $V$ | bed vessel velocity (m/s) |
| $V_i$ | volume of the $i^{th}$ discrete volume ($m^3$) |
| $V_{ap}$ | plenum volume ($m^3$) |
| $V_{prop}$ | wave front propagation velocity (m/s) |
| $V_s$ | solids vertical velocity (m/s) |
| $\overline{V}_s$ | normalized solids vertical velocity (m/s) |
| $W$ | bed width (m) |
| $x$ | horizontal coordinate (m) |
| $x_{gap}$ | air gap height (m) |
| $x_i$ | bed mass position (m) |
| $y$ | vertical coordinate (m) |
| $y_{fb}$ | bed surface vertical coordinate (m) |
| $y_{cm}$ | bed center of mass vertical coordinate (m) |
| $y_w$ | wave front vertical coordinate (m) |

*Greek letters*

| | |
|---|---|
| $\Delta P_d$ | distributor pressure drop (Pa) |
| $\delta(t)$ | instantaneous vibration displacement (m) |
| $\varepsilon$ | void fraction (-) |
| $\varepsilon^*$ | packed bed void fraction (-) |
| $\theta$ | angle of internal friction (°) |
| $\Lambda$ | vibration strength (-) |
| $\mu$ | viscosity (Pa s) |
| $\rho$ | density ($kg/m^3$) |
| $\sigma$ | standard deviation |
| $\Phi$ | specularity coefficient (-) |
| $\phi$ | bed vessel vibration phase (rad) |
| $\chi$ | damping increasing factor (-) |
| $\omega$ | angular frequency (rad/s) |

*Subscripts*

| | |
|---|---|
| *abs* | absolute |

| | |
|---|---|
| $b$ | bed bulk |
| $g$ | gas phase |
| $rel$ | relative |

## References

Akiyama, T., Aoki, K.M., Yamamoto, K. & Yoshikawa, T. 1998 Experimental study on vibration-induced convection and heaping in granular beds. *Granul. Matter* 1, 15–20.

Barletta, D., Russo, P. & Poletto, M. 2013 Dynamic response of a vibrated fluidized bed of fine and cohesive powders. *Powder Technol.* 237, 276–285.

Bi, H. 2007 A critical review of the complex pressure fluctuation phenomenon in gas-solids fluidized beds. *Chem. Eng. Sci* 62, 3473–3493.

Cano-Pleite, E., Hernández-Jiménez, F. & Acosta-Iborra, A. 2015 Compressible-gas two-fluid modeling of isolated bubbles in a vertically vibrated fluidized bed and comparison with experiments. *Chem. Eng. J.* 271, 287–299.

Cano-Pleite, E., Hernández-Jiménez, F., de Vega, M. & Acosta-Iborra, A. 2014 Experimental study on the motion of isolated bubbles in a vertically vibrated fluidized bed. *Chem. Eng. J.* 255, 287–299.

Cano-Pleite, E., Shimizu, Y., Acosta-Iborra, A. & Mawatari, Y. 2016 Effect of vertical vibration and particle size on the solids hold-up and mean bubble behavior in a pseudo-2D fluidized bed. *Chem. Eng. J.* 304, 384–398.

Erdesz, K. & Ormos, Z. 1983 Hydrodynamic studies on fluidized beds(iv)-bed expansion and pressure drop in vibrofluidized layers. *Hung. J. Ind. Chem.* 11, 21–32.

Geldart, D. 1973 Types of gas fluidization. *Powder Technol.* 7, 285.

Goldshtein, A., M., Shapiro, L., Moldavslky & M., Fichman 1995 Mechanics of collisional motion of granular materials. part 2. wave propagation through vibrofluidized granular layers. *J. Fluid Mech.* 287, 349–382.

Gutman, R.G. & Davidson, J.F. 1975 Darcy's law for oscillatory flow. *Can. J. Chem. Eng.* 30, 89–95.

Janssen, L.P.B.M., Marring, E., Hoogerbrugge, J.C. & A.C., Hoffmann 1998 The mechanical behaviour of vibrated beds of glass and starch powders. *Chem. Eng. Sci.* 53, 761–772.

Johnson, P.C. & Jackson, R. 1987 Frictional-collisional constitutive relations for granular materials, with application to plane shearing. *J. Fluid Mech.* 176, 67–93.

Kroll, W. 1954 Uber das verhalten von schuttgut in lotrecht schwingenden gefassen. *Forshung* 20, 2–15.

Matchett, A.J. & Alsop, S. 1995 A two-phase elastic model of vibration in a bed of particulates. *Powder Technol.* 83, 13–28.

Moon, S.J., Kevrekidis, I.G. & Sundaresan, S. 2006 Compaction and dilation rate dependence of stresses in gas-fluidized beds. *Phys. Fluids* 18, 083304.

Musmarra, D., Poletto, M., Vaccaro, S. & Clift, R. 1995 Dynamic waves in fluidized beds. *Powder Technol.* 82, 255–268.

Roy, R., Davidson, J.F. & Tuponogov, V.G. 1990 The velocity of sound in fluidised beds. *Chem. Eng. Sci.* 45, 3233–3245.

Sasic, S., Leckner, B. & Johnsson, F. 2005 Fluctuations and waves in fluidized bed systems: The influence of the air-supply system. *Powder Technol.* 153, 176–195.

Sasic, S., Leckner, B. & Johnsson, F. 2007 Characterization of fluid dynamics of fluidized beds by analysis of pressure fluctuations. *Prog. Energy Combust. Sci.* 33, 453–496.

van der Schaaf, J., Schouten, J.C. & van den Bleek, C.M. 1998 Origin, propagation and attenuation of pressure waves in gas-solid fluidized beds. *Powder Technol.* 95, 220–233.

Wang, T.J., Jin, Y., Tsutsumi, A., Wang, Z. & Cui, Z. 2000 Energy transfer mechanism in a vibrating fluidized bed. *Chem. Eng. J.* 78, 115–123.

Wang, T., Jin, Y., Wang, Z. & Yu, Z. 1997 The characteristics of wave propagation in a vibrating fluidized bed. *Chem. Eng. Technol.* 20, 606–611.

Xiang, L., Shuyan, W., Huilin, L., Goudong, L., Juhui, C. & Yikun, L. 2010 Numerical simulation of particle motion in vibrated fluidized beds. *Powder Technol.* 197, 25–35.

CHAPTER
**FOUR**

# The shape and motion of isolated bubbles in a vibrated fluidized bed

**Contents**



## 4.1 Introduction

As stated in Chapter 1, despite the advantages of vibrated fluidized beds, vibration substantially increases the complexity of the fluidized bed behavior and introduces new phenomena that are still not completely understood or are even unexplored. These are, for example, the presence of compression and expansion waves of solids traveling through the bed, as manifested in Chapter 3. Additionally, the complexity of the system is magnified by the interaction between multiple bubbles when the bed is operated in bubbling regime. Therefore, there is a need of fundamental experimental and simulation characterization of the bubble behavior in vibrated fluidized beds. In this regard, the characterization of the behavior of a bubble rising alone in the bed is paramount for the understanding of the fundamental effect of vibration on the oscillation of bubbles in the bed.

Many efforts have been made to understand the motion of the bed bulk and the bubbles in VFBs, as commented in Chapter 1 (Eccles & Mujumdar, 1997; Wang *et al.*, 2000; Mawatari *et al.*, 2001; Zhou *et al.*, 2001, 2004, 2005; Mawatari *et al.*, 2005; Barletta

*et al.*, 2008; Barletta & Poletto, 2012; Barletta *et al.*, 2013). However, the oscillating behavior of an isolated bubble in a vibrated fluidized bed remains nearly unstudied, despite the fact that it could provide clear and valuable information on the impact of the vibration on the fundamental bubble behavior in fluidized beds. In the related field of gas bubbles in liquid columns, this methodology of studying isolated bubbles has been successfully applied for the understanding of the effects of vibration on bubbles (Baird, 1963; Jameson & Davidson, 1966; Rubin, 1968; Ellenberg & Krishna, 2007*b*,*a*; O'Hern *et al.*, 2012). In one of these works, Jameson & Davidson (1966) analyzed the time oscillations of the displacement of a bubble in the vibrated liquid column using a phase representation of averaged oscillation cycles. This method allowed the comparison of the amplitude and the relative phase of the bubble and liquid displacements.

Some of the numerical works of VFBs consider the gas phase as a compressible medium (Limtrakul *et al.*, 2007; Xiang *et al.*, 2010; Zeilstra *et al.*, 2013). However, it is not totally clear whether the compressibility of the gas phase plays an important role on the VFB behavior and, in particular, on the oscillatory motion of bubbles. Also, existing numerical studies regarding vibrating fluidized beds do not investigate the influence of the gas phase compressibility on the fluctuations induced by vibration in the bed and the bubbles present in the system.

The aim of the present chapter is to study both experimentally and numerically the effect of the vertical vibration on the bed bulk motion and the resulting behavior of an isolated bubble rising alone in a VFB. These results can be useful for clarifying the essential mechanisms affecting a bubble in the vibrated bed, which constitutes a necessary first step in the understanding of more complex bubbling beds dryers and reactors subjected to vibration. The results are presented using a phase frame of reference, so that the local fluctuations caused by the bed vibration on the bed bulk motion and bubble properties, i.e. bubble diameter and velocity, can be systematically analyzed. Besides, the effect of the vibration amplitude and frequency on the oscillation and mean motion of isolated bubbles in a fluidized bed is studied. The results show that the vibration amplitude and frequency have a complex and coupled impact on the bed bulk behavior and the bubble size and motion.

The two-fluid model simulations carried out in this chapter are used to unveil the importance of the compressibility of the gas phase on the wave propagation mechanism (i.e. solids and pressure waves) observed in Chapter 3. The results show that the two-fluid model simulation with compressible gas phase is capable of well reproducing the experimental behavior of isolated bubbles in a vibrated fluidized bed, whereas this is not true if the gas is simulated as an incompressible phase. This important outcome suggests that the gas compressibility, together with particle collision, are key parameters in the propagation of oscillations inside the bed.

## 4.2 Experimental setup

The facility used in the experimental section of this chapter is the vibrated fluidized bed described in Section 2.1.1. The bed was filled with ballotini glass beads with a density of 2500 kg/m$^3$ and a size range between 150-250 $\mu$m (Geldart's classification type B). The settled bed height was fixed to $H_0 = 0.45$ m. For static conditions, the minimum fluidization velocity was measured using a pressure probe placed in the plenum, resulting on a value of $U_{mf} = 0.055$ m/s.

The bulk of the bed and the bubble behavior were recorded using a digital camera, BASLER A640, which took images of the front view of the fluidized bed. The resolution of the camera for the frequency of acquisition set in the experiments was 312 x 658 pixels, resulting in approximately 1 mm/pixel. Thus, the location of a bubble has an intrinsic uncertainty of $5{\cdot}10^{-5}$ m, which is equal to half pixel size divided by the square root of the number of pixels defining the contour of a bubble (typically more than 100 pixels).

Each of the conducted experiments comprised a maximum of 2 minutes of time to avoid overheating of the vibro-motors. The first 20 seconds were not analyzed to avoid transient effects during the experiment start-up. Several bubbles were sequentially injected and recorded during each experiment, in order to acquire statistically significant values. Table 4.1 lists the conditions of the experiments carried out. The amplitude and frequency were varied from the base conditions, $f = 13.9$ Hz and $A = 2.7$ mm (Exp. 1). Here, the amplitude $A$ refers to the amplitude of the vertical oscillation with respect to the mean vertical position of the bed, so that the total peak-to-peak oscillation is $2A$.

**Table 4.1:** Experimental conditions.

| **Exp.** | Vibration frequency $f$ (Hz) | Vibration amplitude $A$ (mm) |
|---|---|---|
| 1 | 13.9 | 2.7 |
| 2 | 13.9 | 4.1 |
| 3 | 13.9 | 5.7 |
| 4 | 10.8 | 3.0 |
| 5 | 17.2 | 2.5 |

## 4.3 Numerical solution and boundary conditions

In order to reproduce the VFB system described in Section 4.2, two simulation domains are proposed. The two domains are two-dimensional reproductions of the fluidized bed described in the experimental setup section (Section 4.2). In the first domain, the air flow velocity through the distributor is directly imposed, as usually done, excluding the

simulation of the plenum. The second domain, similarly to the domain used in Chapter 3, adds a plenum of equivalent height $H_{eq}$. Both computational domains are discretized with a square grid of cell size equal to 4 mm in the section occupied by the solids. As in Chapter 3, the cells are slightly elongated in the sections on top of the bed and in the plenum, where only gas is present (see Figure 4.1). Sensitivity results in previous works (Acosta-Iborra *et al.*, 2012) showed a good reproduction of bubble characteristics for a mesh of greater cell size. Given the large number of cases considered, and the need of computing the transient solution for a physical time period sufficiently large to obtain statistically meaningful results, no attempt was made to simulate the pseudo-2D bed in three dimensions.

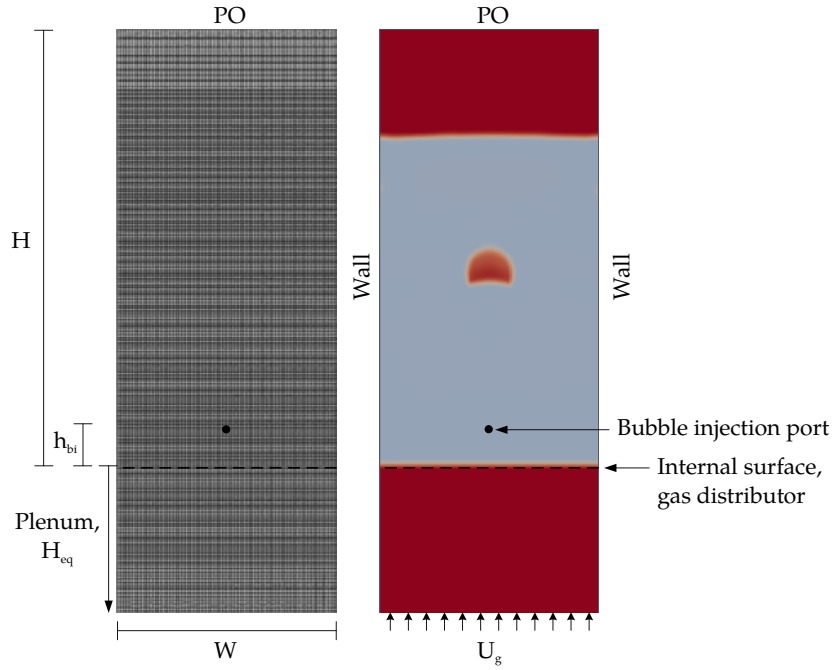


**Figure 4.1:** Computational domain (case with plenum) and boundary conditions of the simulations.

To study bubble oscillating characteristics, the simulation results were exported each $5 \cdot 10^{-3}$ s over a period of 120 s of physical time in each of the cases conducted. The air was uniformly introduced through the bottom of the computational domain at a given velocity $U_g$, to set the bed under minimum fluidization conditions. In order to reproduce the experimental conditions of Section 4.2, bubbles were injected in the bed through a punctual source of air of 4 mm x 4 mm situated 5 cm above the distributor. The amount of mass injected in each of the bubbles in the subsequent simulations was set to statistically match the size of the bubbles found in the experiments. The mean and the

standard deviation of the bubble diameter were obtained from the experiments and these values were introduced in the simulations by means of Equation (4.1), which incorporates a random function that accounts for the different volume injected in each bubble of the experiments. In particular, for each bubble, air was injected until the area-equivalent diameter (Equation (2.6)) of the bubble $D_{inj}$ reached:

$$D_{inj} = D_{inj,exp} + 2\sqrt{3}\sigma_{inj,exp}(\text{Rand} - 0.5) \tag{4.1}$$

where $D_{inj,exp}$ and $\sigma_{ink,exp}$ are, respectively, the experimental mean bubble diameter and the bubble diameter standard deviation. Rand stands for a randomly generated number between 0 and 1 with a uniform distribution. Equation (4.1) gives a diameter distribution of mean value and standard deviation similar to the experiments.

Pressure outlet boundary conditions (PO) were imposed for the gas phase at the exit. At the walls of the bed and the plenum, no-slip conditions were specified for the gas and partial-slip conditions of Johnson & Jackson (1987) with a standard specularity coefficient $\Phi = 0.6$ for the solids. A restitution coefficient of $e = 0.9$ was used for the particle-particle and particle-wall collisions. The simulation conditions are summarized in Table 4.2. More details about the simulation conditions and constitutive equations can be found in Chapter 2 and in Appendix A.

**Table 4.2:** Simulation conditions

| Parameter | Value | Parameter | Value |
|---|---|---|---|
| $W$(m) | 0.3 | $H$(m) | 0.6 |
| $d_p(\mu$m) | 213 | $\rho_p$(kg/m$^3$) | 2500 |
| $U_g$ (m/s) | 0.04 | $\mu_g$(Pa s) | $1.86 \cdot 10^{-5}$ |
| $H_0$(m) | 0.45 | $H_{eq}$(m) | 0.84 |
| $h_{bi}$(m) | 0.05 | $e$(-) | 0.9 |
| $\varepsilon_0$(-) | 0.4 | $\varepsilon^*$(-) | 0.4 |
| $\theta(^o)$ | 30 | $\Delta t_{exp}$(s) | 0.005 |

The simulation cases carried out are listed in Table 4.3. The base conditions of vibration frequency and amplitude are $f = 13.9$ Hz and $A = 2.7$ mm. As in the experiments, to account for the effects of not introducing gas compressibility, an initial case with constant $\rho_g$ was considered (Case-1). Investigations on the effect of not including the plenum when the gas is compressible are performed by means of Case-2. Finally, the effect of vibration amplitude and frequency is studied with the rest of cases of Table 4.3. In Cases 3, 4 and 5 the vibration amplitude is varied whereas Cases 3, 6 and 7 comprise different vibration frequencies.

**Table 4.3:** List of simulated cases

| Case | Gas phase | Plenum | $f$ (Hz) | $A$ (mm) |
|---|---|---|---|---|
| 1 | Incompressible | No | 13.9 | 2.7 |
| 2 | Compressible | No | 13.9 | 2.7 |
| 3 | Compressible | Yes | 13.9 | 2.7 |
| 4 | Compressible | Yes | 13.9 | 4.1 |
| 5 | Compressible | Yes | 13.9 | 5.7 |
| 6 | Compressible | Yes | 10.8 | 3 |
| 7 | Compressible | Yes | 17.2 | 2.5 |

## 4.4 Results and discussion

The results presented in this chapter are divided into two main sections.

In Section 4.4.1, the effect of vibration on the displacement of the bed bulk and the bubble behavior is experimentally analyzed by means of the averaging of cycles method presented in Section 2.3.2. Using this same method, the effect of variating the frequency and amplitude of vibration on the behavior of a bubble is studied.

In the second section, Section 4.4.2, the numerical simulations are compared to the experimental results. The bed general motion, the effect of gas compressibility and the presence of the plenum in the bed model are studied by the use of a two-fluid model. The same methodology is followed to numerically investigate the effect of vibration on bubble diameter and velocity fluctuations caused by vibration and their variation with the bed vessel vibration amplitude and frequency.

### 4.4.1 Experimental results

#### Bed and bubble general motion

Vertical vibration of the gas fluidized bed generates an oscillation of the bulk of the bed that is coupled with the motion of an injected bubble. To analyze this, the bed was vibrated at frequency $f = 13.9$ Hz and amplitude $A = 2.7$ mm (Exp. 1 of Table 4.1). Individual bubbles at a rate of 30 per minute were injected as described in Section 4.2.

Figure 4.2 shows consecutive snapshots of a single bubble in the vibrated fluidized bed for several instants of time comprising a whole period of the bed vessel oscillation. The position of the centroid of the bubble is also indicated on each of the images. As the bubble rises in the bed, its position and diameter is influenced by vibration. Note, for example, that the bubble seems to rise faster in the first half of the period (upper row of images) than in the last part of it (lower row). Also, between $\phi = \pi$ rad and $\phi = 2\pi$ rad the bubble boundary is deformed and part of the wake of the bubble penetrates into it,

forming two distinct waves at the bubble bottom. This wavy contour at the bottom of the bubble was observed in all the vibration cases tested and seems to be characteristic of bubbles in vibrated fluidized beds.

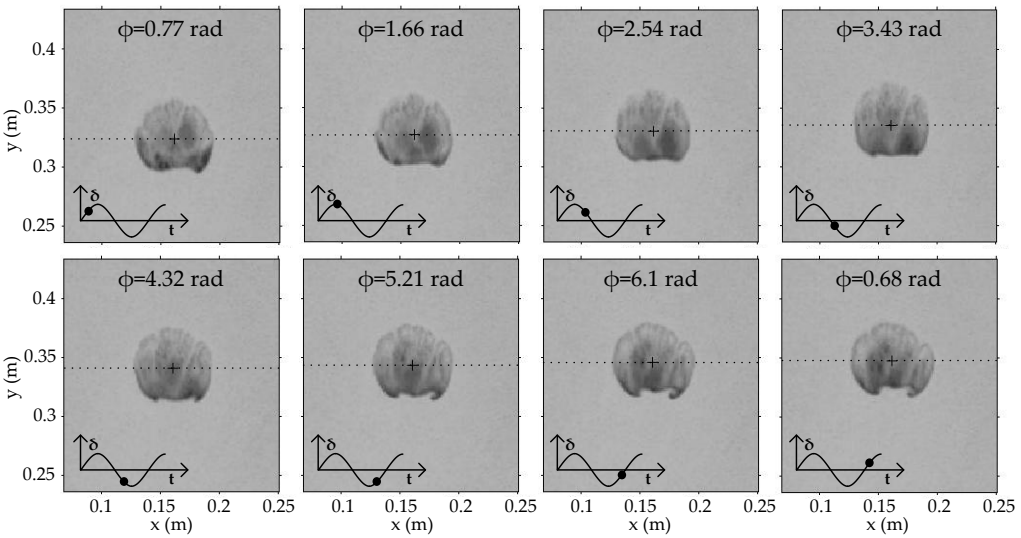


**Figure 4.2:** Grayscale digital images of an isolated bubble rising in the vibrating fluidized bed captured at different vibration phases. The dotted horizontal line indicates the vertical position of the bubble centroid. The vertical displacement $\delta$ of the bed vessel is also indicated. $f = 13.9$ Hz, $A = 2.7$ mm, (Exp. 1).

Figure 4.3(a) shows the time evolution of the bed volume together with the vertical coordinate of the bed surface, $y_{BS}$; and Figure 4.3(b) contains the vertical coordinate of the bed center of mass, $y_{CM}$, together with the vertical coordinate of the centroid of a bubble, $y_b$. The bed volume is calculated from the digital images of the bed as the bed thickness, $K$, multiplied by the total area (including bubbles) between the distributor and the surface of the bed. The vertical coordinate in Figure 4.3 is calculated in an absolute system of reference, whose origin is at the time-averaged vertical position of the distributor of the bed. The bed volume and the vertical position of the bed surface are normalized dividing by $KWH_0$ and $H_0$ respectively. Figure 4.3 only comprises an experiment of the rise of a bubble, but the results analyzed in subsequent figures are taken from the repetition of about 60 isolated bubbles rising like the one shown in Figure 4.3. According to Figure 4.3(a), once the bubble is formed (at $t = 34.6$ s in the figure), the volume of the bed oscillates with the same frequency as the vessel. The normalized height of the bed surface oscillates with less amplitude than the normalized volume. As in Chapter 3, this indicates that there is a cyclic compression-expansion of the whole bed induced by vibration. In Figure 4.3(a) the mean values of the bed height and volume

slightly increase with time due to the bubble growth. The effect of the bubble growth is not significant since the bubble volume constitutes only a small fraction of the bed volume. Once eruption of the bubble occurs (at $t = 35.7$ s in Figure 4.3(a)), both the bed height and volume decrease because the bubble is not present in the system. In this situation the frequency and amplitude of oscillation of the bed height and volume are similar to those observed for a bed with a bubble rising inside. Similarly, Figure 4.3(b) shows that the centroid of the bubble experiences an oscillation of its vertical position overimposed to the expected bubble rise in the bed. The center of mass of the bed also oscillates with a frequency equivalent to that of the bed vessel. The descending displacement of the center of mass of the bed is due to the bubble rising in the bed (Figure 4.3(b)). It is difficult from Figure 4.3 to analyze whether the compression-expansion of the bed and the bubble centroid oscillations are in phase with the bed vibration. Therefore, a characterization of the oscillation with the vibration phase, as described in Chapter 2, is performed in the subsequent paragraphs.

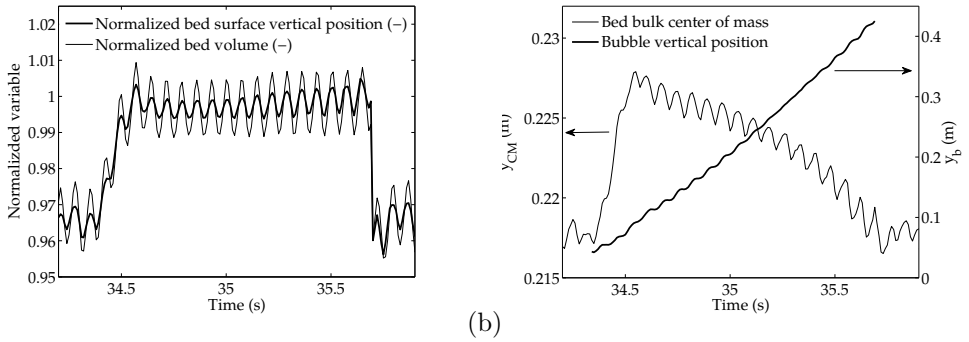


**Figure 4.3:** (a) Time evolution of the normalized vertical position of the bed surface together with the normalized bed volume and (b) time evolution the center of mass of the bed together with the vertical position of the bubble centroid $y_b$. $f = 13.9$ Hz and $A = 2.7$ mm (Exp. 1).

The average oscillations of the bed volume and the surface of the bed, together with the local standard deviation of the data for each of the phase intervals, are presented in Figure 4.4. As a reference, the normalized bed vessel displacement $\delta(\phi)/A_{eq}$ has been included, where $A_{eq} = \sigma_\delta\sqrt{2}$ is the equivalent amplitude and $\sigma_{\delta(t)}$ is the standard deviation of $\delta$, which was obtained by means of DIA. As in Chapter 3, when no bubble was present in the system, Figure 4.4 reflects an opposition in phase between the bed surface and the bed vessel displacement, i.e. when the vessel is moving upwards the bed surface line is moving downwards and vice versa. This effect can be understood as a cyclic compression and expansion of the bed bulk, which can be also observed in the dense phase area fluctuations in Figure 4.4.

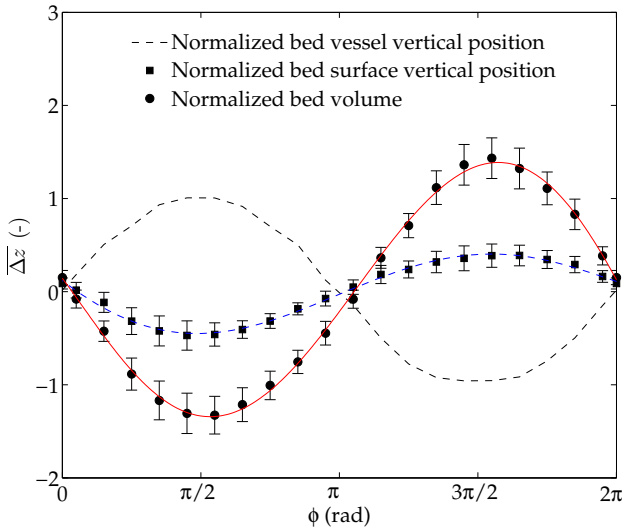


**Figure 4.4:** Normalized bed vessel position, bed surface position and bed volume as a function of the vibration phase. $f = 13.9$ Hz and $A = 2.7$ mm (Exp. 1).

### Oscillatory behavior of isolated bubbles

The oscillating motion of a bubble in the vibrated bed can be firstly studied in terms of the vertical position of the bubble centroid in an absolute system of reference. Figure 4.5 shows the results obtained for the height intervals described in Chapter 2. Normalization of the bubble absolute vertical position $y_b$ in Figure 4.5 is performed in this case using the equivalent amplitude of the bed vibration:

$$\overline{\Delta y_b}(t) = \frac{y_b(t) - \widehat{y}_b(t)}{A_{eq}} \tag{4.2}$$

The uncertainty of each experimental data point in Figure 4.5 is below the oscillation amplitude of the bubble centroid position. Table 4.4 contains the experimental data dispersion, $S$, in terms of the local standard deviation of the results in each phase interval in Figure 6 and averaged for all the phase intervals. In addition, Table 4.4 shows that the average data dispersion is also relatively small for the normalized diameter and velocity of bubbles that are studied in this same section.

When the bubble is in the lower height interval of the bed ($y = 0.1 - 0.275$ m), the fluctuation of the bubble centroid position is close in terms of phase and amplitude to the oscillatory displacement of the vibrating bed vessel. Besides, as the height of the bubble increases ($y = 0.275 - 0.45$ m), the bubble motion is not only subjected to the movement

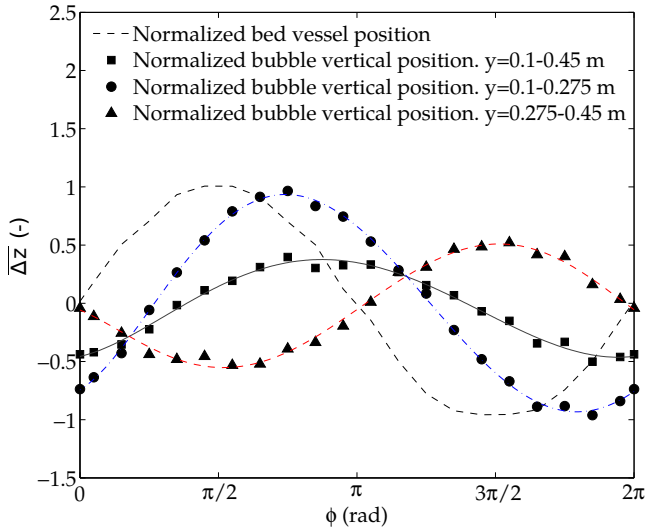


**Figure 4.5:** Normalized absolute vertical position of the bubble centroid versus the vibration phase. $f = 13.9$ Hz and $A = 2.7$ mm (Exp. 1).

**Table 4.4:** Average data dispersion of the bubble oscillations. $f = 13.9$ Hz and $A = 2.7$ mm (Exp. 1).

| | $y = 0.1 - 0.275$ m | $y = 0.275 - 0.45$ m | $y = 0.1 - 0.45$ m |
|---|---|---|---|
| $S_{\overline{\Delta y_b}}$ | 0.23 | 0.27 | 0.29 |
| $S_{\overline{\Delta D_b}}$ | 0.012 | 0.013 | 0.0094 |
| $S_{\overline{\Delta V_b}}$ | 0.21 | 0.26 | 0.28 |

of the vessel, but also influenced by the movement of the bulk and the surface of the bed. In consequence, as the bubble rises in the bed, the amplitude of the oscillations of the bubble centroid decreases and the displacement of the centroid is no longer in phase with the bed vessel oscillation. An intermediate result is obtained if the averaging of cycles is performed for the whole height interval ($y = 0.1 - 0.45$ m). More results concerning the phase delay between oscillations are presented later in this section.

Figure 4.6 presents the results regarding the oscillations of the bubble diameter and velocity. The bubble diameter oscillation in Figure 4.6(a) is normalized in order to obtain general results independent of the size and growth of each bubble in the experiment. Here, normalization is done with the instantaneous moving average of the bubble diameter as

follows:

$$\overline{\Delta D}_b = \frac{D_{bi} - \widehat{D}_{bi}}{\widehat{D}_{bi}} \tag{4.3}$$

Therefore, the vertical axis of Figure 4.6(a) represents the change of bubble diameter over its mean value. For the size of the bubbles studied here ($D_b \sim 5-8$ cm), oscillations of diameter around 2% are observed when the bed is vibrated at $f = 13.9$ Hz and $A = 2.7$ mm.

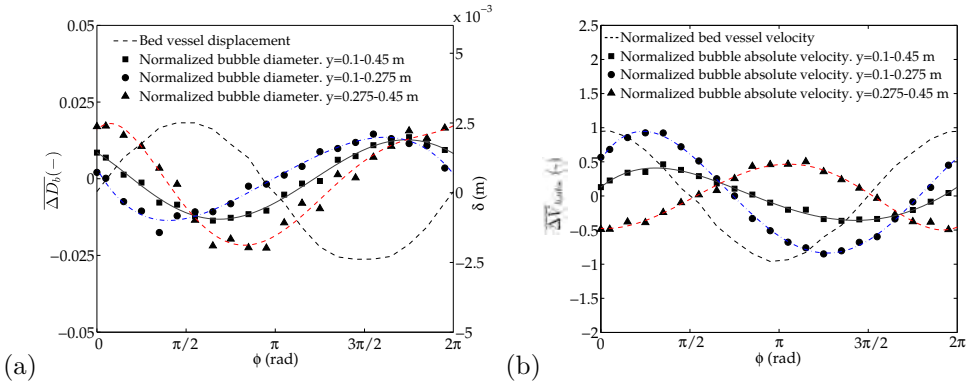


**Figure 4.6:** (a) Normalized bubble equivalent diameter and (b) absolute vertical velocity versus vibration phase. $f = 13.9$ Hz and $A = 2.7$ mm (Exp. 1).

It is clear from Figure 4.6(a) that the bubble tends to shrink when the bed is contracting, i.e. the bed vessel is close to the upper position ($\phi = \pi/2$ rad), as shown in Figure 4.4, and tends to grow when the bed bulk is expanding, i.e. the bed vessel is close to its lower position ($\phi = 3\pi/2$ rad). Thus, the origin of the cyclic shrinking and growing of the bubble size in a vibrated fluidized bed seems to be the same as the bed volume expansion and compression observed in Figure 4.4.

In Figure 4.6(b), the absolute vertical velocity of the bubble was normalized with the vertical velocity of the bed vessel:

$$\overline{\Delta V}_{b,abs} = \frac{V_{bi} - \widehat{V}_{bi}}{2\pi f A_{eq}} \tag{4.4}$$

It can be observed in Figure 4.6(b) that the magnitude of the velocity oscillation of isolated bubbles crossing the lower half of the bed is close to the velocity oscillation of the vessel. The oscillation of the bubble velocity becomes weaker as the bubble rises in the bed. As it happens with the bubble centroid position, bubbles tend to follow the

general movement of the bed vessel as they are closer to the distributor.

**Effect of vibration amplitude and frequency on the bubble oscillations**

As indicated in the previous subsection, bubbles are subjected to the main oscillatory displacement of the bed vessel when they are close to the distributor. Therefore, it is interesting to study the effect of amplitude and frequency of vibration on a bubble located in the lowest half section of the bed ($y = 0.1 - 0.275$ m).

Figure 4.7 shows the normalized bubble equivalent diameter as a function of the vibration phase for different vibration amplitudes and frequencies. It can be seen in Figure 4.7(a) that, as long as the vibration amplitude increases (Exp. 1, 2 and 3), the bubble diameter fluctuations become higher in amplitude. The rationale of this effect is similar to that of previous sections; that is, the bubble size tends to follow the oscillatory change of the bed volume. In particular, an increase of vibration amplitude of the bed vessel introduces a larger amount of kinetic energy of particles, which augments the oscillation amplitude of the bed volume. During the bed expansion, the voidage in the bed bulk increases and allows for a bubble to grow more easily. Reversely, during the compression of the bed the bubble tends to shrink following the fluidized medium. Thus, increasing the amplitude of the vessel vibration leads to an increase of the amplitude of the oscillation of bubble diameter, as reflected in Figure 4.7(a). A slight increase of the delay between the bed vessel displacement and the bubble diameter oscillations can be observed in Figure 4.7(a) as the amplitude of the vibration increases. From Figure 4.7(b) it can be seen that there is no clear tendency of the amplitude of the bubble diameter oscillation with variations of vibration frequency. This lack of trend could be caused by the slight change of vibration amplitude with frequency (Exp. 1, 4 and 5) commented in Section 4.4.1.

Figure 4.8 shows the influence of the amplitude and frequency of vibration on the standard deviation, $\sigma$, of the oscillations of the normalized bubble diameter (i.e. the standard deviation of the points in Figure 4.7), which can be considered as a measure of the amplitude of the diameter oscillations presented in Figure 4.7. Accordingly to previous results, the amplitude of the diameter oscillations is higher as the amplitude grows. Both the lower and the higher sections of the bed present this increasing trend in Figure 4.8(a). However, although less intensely than in Figure 4.8(a), Figure 4.8(b) indicates that the oscillation of the bubble diameter increases with the vibration frequency for a bubble in the lower section of the bed and decreases with frequency for a bubble in the upper section of the bed. The fact that the amplitude of the bubble oscillations, at small vibration frequencies and amplitudes, is superior at the upper half of the bed than at the lower half (Figure 4.8) can be caused by the larger weight of the bed sup-

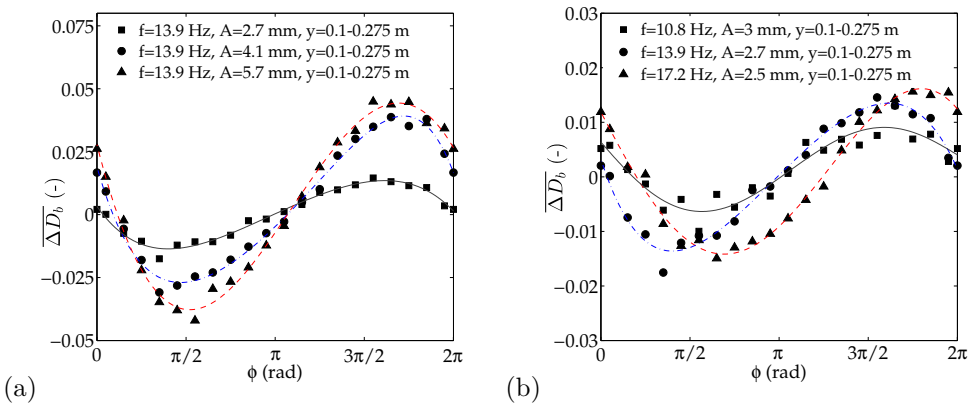


**Figure 4.7:** Normalized bubble equivalent diameter versus vibration phase. (a) Variation with vibration amplitude (Exp. 1, 2 and 3), (b) variation with vibration frequency (Exp. 1, 4 and 5).

ported in the lower half, which reduces the oscillation of the particles velocity (as shown in Chapter 3) and reduces the local compression-expansion oscillations of the bed bulk. An increase of the vibration frequency seems to promote the homogenization of the bed compression-expansion and makes the standard deviation of bubble diameter to converge to a common value in the upper and lower halves of the bed (Figure 4.8(b)).

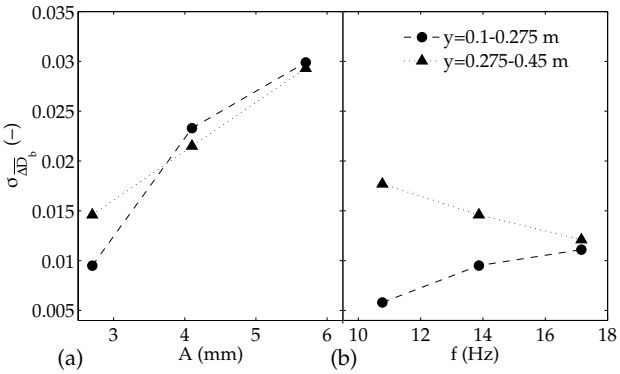


**Figure 4.8:** Standard deviation of the oscillations of the normalized equivalent bubble diameter. (a) Variation with vibration amplitude (Exp. 1, 2 and 3) and (b) variation with vibration frequency (Exp. 1, 4 and 5).

The influence of vibration amplitude and frequency on the oscillations of bubble velocity is shown in Figure 4.9. No clear trends in phase nor amplitude of the oscillations are observed when the amplitude of the vessel vibration is varied, as shown in Figure 4.9(a). The amplitude of the velocity oscillations seems to reach a minimum at $A = 4.1$ mm. However, since the distance between curves in Figure 4.9(a) is smaller than their local standard deviation, which is about 0.27, more experimental data comprising additional amplitudes of the vessel vibration would be required to confirm the presence of a minimum. Doubling the amplitude from $A = 2.7$ mm to $A = 5.7$ mm does not seem to change significantly the amplitude of the normalized bubble velocity oscillations, and the relative phase of the bubble velocity oscillations remains practically unchanged. Considering that the bubble motion is mainly subjected to the oscillatory motion of the bed bulk, this result is in accordance with the experimental observations of the bed bulk oscillation shown in Chapter 3. In Chapter 3, the normalized oscillation of the particle velocity in the lower section of bed remains nearly the same when varying the vibration amplitude. Additionally, an increase on the vibration frequency reduces the amplitude of the bubble velocity fluctuations (Figure 4.9(b)), especially at positive displacements of the bed vessel ($\delta > 0$). One explanation for that might be that increasing the frequency of the vessel vibration makes the bubble velocity to fluctuate faster, which augments the dissipation rate of the particle kinetic energy and leads to a softening of the amplitude of the bubble velocity oscillations. It is considered that the small change of vibration amplitude with frequency of the bed vessel is not the main cause of the softening of the amplitude of the bubble velocity oscillations, since this effect is not observed in Figure 4.9(a) for a larger amplitude variation.

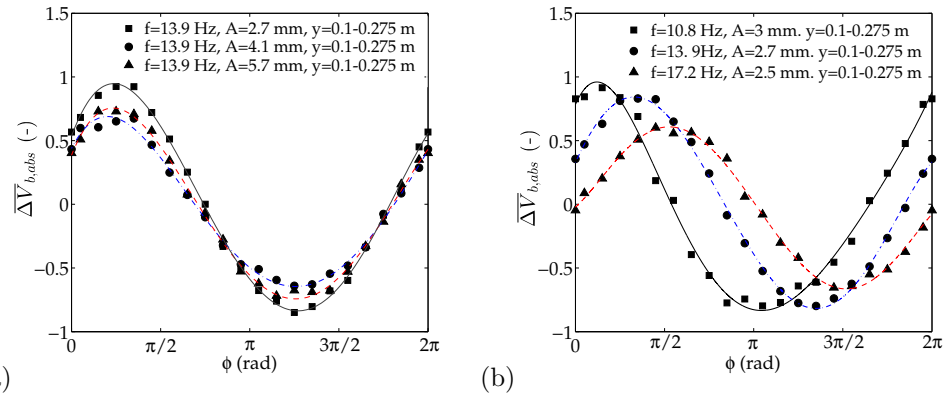


**Figure 4.9:** Normalized bubble vertical absolute velocity. (a) Variation with vibration amplitude (Exp. 1, 2 and 3), (b) variation with vibration frequency (Exp. 1, 4 and 5).

To see this tendency more explicitly, the standard deviation of the oscillations of the normalized absolute velocity of isolated bubbles is depicted in Figure 4.10 as a function of $A$ and $f$. In Figure 4.10(a), an increase in the vibrating amplitude from $A = 2.7$ mm to $A = 4.1$ mm seems to decrease the velocity fluctuations in the lower part of the bed. The movement of the bulk of particles near the bed surface directly influences the bubble displacement of bubbles far from the distributor. An increase of the vibration amplitude of the bed vessel augments the oscillations of amplitude of the bed near its surface and that causes the growth of $\sigma_{\overline{\Delta V_b}}$ with $A$ in the upper interval ($y = 0.275 - 0.45$ m). The increase of vibration frequency decreases the amplitude of velocity fluctuations, as observed previously in Figure 4.9(b). However, according to Figure 4.10(b) this effect is not reflected in the standard deviation of $\overline{\Delta V}_b$ for bubbles close to the distributor. This is probably due to the differences in the shape of the oscillation curve for positive and negative values of $\overline{\Delta V}_b$ (Figure 4.9(b)).

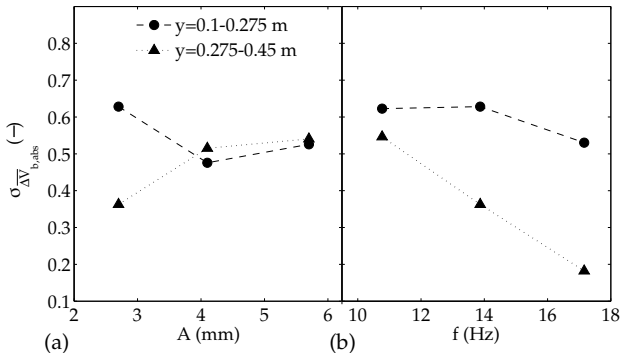


**Figure 4.10:** Standard deviation of the oscillations of the normalized bubble absolute vertical velocity. (a) Variation with vibration amplitude (Exp. 1, 2 and 3), (b) variation with vibration frequency (Exp. 1, 4 and 5).

### Phase delay and propagation velocity of oscillations

As explained in Chapter 2, the phase delay is the retardation in phase (i.e. time retardation multiplied by $2\pi f$) of the bubble oscillations with respect to a reference signal. Figure 4.11 shows the influence of the amplitude and frequency of vibration on the phase delay, $\phi_d$, of the bubble diameter with respect to the bed vessel displacement, $\delta$. When the bubble is situated in the lower part of the vessel, the change in diameter is in close phase with the expansion-compression of the bed volume. The expansion-compression of the bed is opposite to the bed displacement (see Figure 4.4), which explains why $\phi_d \simeq \pi$ rad in Figure 4.11 for isolated bubbles within $y = 0.1 - 0.275$ m. As the bubble rises in the bed, there seems to be an attenuation of the relative diameter oscillation

and a retardation of its response with respect of the cyclic expansion-compression of the bed bulk. A bubble located in the lower half of the bed ($y = 0.1 - 0.275$ m) presents a slightly growing delay as the amplitude of the vibration increases, see Figure 4.11(a). The reverse behavior of the bubble diameter delay is observed in the upper half of the bed, so that the delays in the two bed halves become closer as the amplitude increases. It can also be noticed that the delay in the upper half of the bed is always higher than in the lower half.

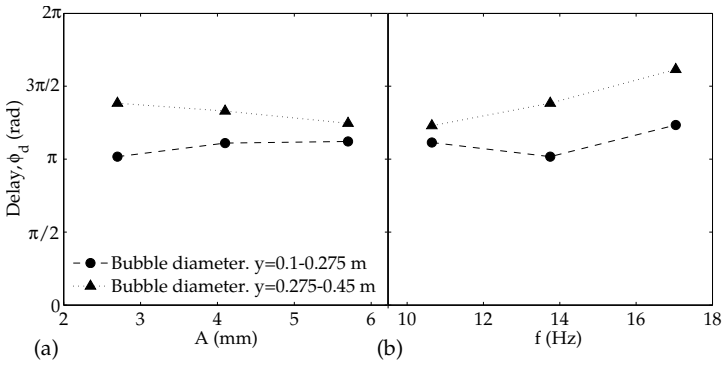


**Figure 4.11:** Phase delay of bubble equivalent diameter at different heights. (a) Variation with vibration amplitude (Exp. 1, 2 and 3), (b) variation with vibration frequency (Exp. 1, 4 and 5).

Regarding Figure 4.11(b), mixed effects of the vibration amplitude and frequency on the phase delay are revealed since the vibration amplitude decreased slightly while increasing the frequency (Exp. 1, 4 and 5). If the bubble is in the lower half of the bed, the decrease of vibration amplitude tends to slightly decrease the bubble delay (as observed in Figure 4.11(a)), in opposition to the effect of the growing frequency, which seems to contribute to its increase when passing from 13.9 Hz to 17.2 Hz. In the upper half of the bed, both the amplitude decrease and the frequency augmentation tend to increase the delay between the bed displacement and the bubble diameter variation.

Figure 4.12 contains the results for the delay of the bubble velocity oscillation relative to the phase of the vessel velocity. As previously revealed by Figure 4.9(b), the oscillation of bubble velocity is mainly influenced by the bed vessel velocity in the lower section of the bed. This behavior can be also observed in Figure 4.12. The phase delay is close to $\phi_d = 0$ rad for the lower half of the bed, indicating that the bubble velocity oscillation follows the oscillation velocity of the bed vessel. This is obtained for various vibration amplitudes (Figure 4.12(a)) and for smaller frequencies (Figure 4.12(b)). However, the bubble velocity delay in the lower half of the bed increases progressively with frequency, which can be attributed to the impossibility of a bubble to follow rapid bed oscillations.

Figure 4.12 clearly demonstrates that, in the upper half of the bed, the bubble velocity oscillates following the bed surface cyclic displacement ($\phi = \pi$ rad).

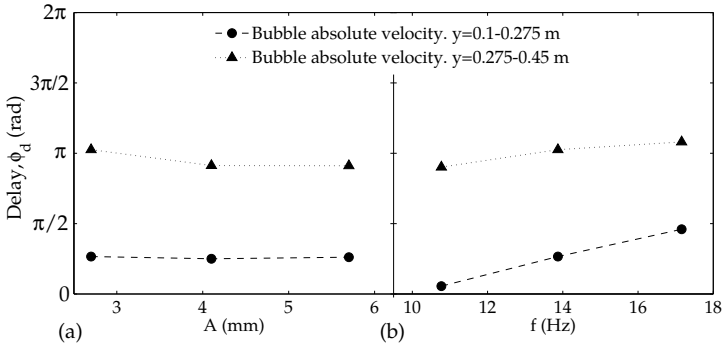


**Figure 4.12:** Phase delay of bubble absolute vertical velocity at different heights. (a) Variation with vibration amplitude (Exp. 1, 2 and 3), (b) variation with vibration frequency (Exp. 1, 4 and 5).

The fact that the delays of bubble size and velocity increase from the lower to the upper half of the bed indicates that there is a propagation mechanism between the bed vessel vibration (at the distributor) and the rest of the bed. This propagation mechanism is probably connected with the compression and expansion waves in the bulk of the bed observed in Chapter 3. Equation (4.5) can be used to determine the velocity of propagation of the vibration effects inside the bed:

$$V_{prop} = 2\pi f \frac{\Delta y}{\Delta \phi} \tag{4.5}$$

Where $\Delta y$ is calculated as the distance between the center of the lower and upper height intervals analyzed, i.e. $y_2 - y_1$, where $y_1 = 18.75$ cm, and $y_2 = 36.25$ cm and $\Delta\phi$ represents the phase delay of the oscillations of the bubble centroid $y_b$, diameter $D_b$ and velocity $V_b$ between $y_1$ and $y_2$.

The results obtained for $V_{prop}$ are presented in Table 4.5. Each column in Table 4.5 contains the propagation velocity calculated with $y_b$, $D_b$ and $V_b$. Observe that most of the values of $V_{prop}$ in Table 4.5 are of order 10 m/s. This velocity resembles the effective sound propagation velocity inside a fluidized bed, which can be calculated following the work by Roy *et al.* (1990):

$$u_s = u_{s0} \sqrt{\frac{\rho_g}{\gamma\varepsilon\left[\rho_s(1-\varepsilon) + \rho_g\varepsilon\right]}} \tag{4.6}$$

Where $u_{s0} = \sqrt{\gamma R_g T_g}$ is the velocity of sound in the gas. For the experimental conditions of this chapter ($\rho_g = 1.22$ kg/m$^3$, $\rho_s = 2500$ kg/m$^3$, $\varepsilon = 0.4$ and $\gamma = 1.4$),

Equation (4.6) yields an effective velocity of the sound in the bed equal to 13.1 m/s, which is of the same order of the values in Table 4.5. These values are also in harmony with the results presented in Chapter 3, in which the propagation velocity of the compression and expansion wave front of solids in the bed bulk was calculated by means of PIV. This corroborates the energy propagation mechanism between the bed vessel and the rest of the bed is linked with the compression and expansion of the bed bulk. The presence of a wave propagation mechanism inside the bed is in agreement with the pressure observations by Wang *et al.* (2000), who indicated that the wave propagation is the main energy transfer mechanism in a vibrated fluidized bed. If the bed were rigid, information would propagate instantaneously (Wang *et al.*, 2000). However, the phase delay of the bubble characteristics between two points in the bed (see $\Delta\phi$ in Equation (4.5)) is a sign of the bed elasticity and, as commented before, corroborates the presence of a compression wave generated by vibration at the bottom of the bed that propagates the information upwards.

**Table 4.5:** Velocity propagation of the oscillations in the bed.

| **Exp.** | $V_{prop,y_b}$, (m/s) | $V_{prop,D_b}$, (m/s) | $V_{prop,V_b}$, (m/s) |
|---|---|---|---|
| 1 | 6.62 | 13.3 | 6.39 |
| 2 | 7.55 | 22.1 | 7.32 |
| 3 | 7.37 | 39.1 | 7.46 |
| 4 | 4.6 | 32.7 | 4.45 |
| 5 | 9.77 | 15.8 | 9.68 |

The smaller standard deviation of the oscillations of bubble velocity observed in the upper half of the bed (Figure 4.10(b)) suggests that there is an attenuation of wave propagation. This attenuation of waves when traveling upwards the bed can be attributed to damping by thermal dissipation, gas-particle friction and inter-particle collisions, amongst other attenuation mechanisms (Roy *et al.*, 1990; Musmarra *et al.*, 1995; van der Schaaf *et al.*, 1998). Besides, the increase of vibration frequency may promote an augmentation of the inter-particle collisions and, in consequence, a higher damping of the wave propagation. This may explain why the standard deviation of the oscillations of bubble velocity decreases with frequency in Figure 4.10(b).

### Relation between mean bubble diameter and velocity

A classic relation of the form proposed by Davidson & Harrison (1963) can be employed to relate the time averaged bubble diameter with the time averaged bubble velocity of

an isolated bubble rising in a vibrated bed.

$$\mu = \left\langle \frac{\overline{V}_{b,i}}{\sqrt{g\overline{D}_{b,i}}} \right\rangle_{median} \tag{4.7}$$

Where $\overline{D}_{b,i}$ and $\overline{V}_{b,i}$ are the time averaged values of the bubble diameter and velocity in a cycle. Note that, due to the dispersion of $\mu$ for each oscillation cycle, the median, instead of a simple mean, has been used to calculate $\mu$ in Equation (4.7). For non-vibrating conditions, the bubble injection system used in the experiment originated bubbles that tended to break (perhaps due to their close to Geldart A behavior in that conditions), which precludes the calculation of $\mu$ for $f = 0$ and $A = 0$.

Figure 4.13 depicts the velocity coefficient $\mu$ as a function of the vibration amplitude and frequency. Previous studies of single bubbles rising in conventional fluidized beds report values of 0.711 for the bubble velocity coefficient (Davidson & Harrison, 1963) and smaller values for two dimensional bubbles (e.g. about 0.48 when referred to the area-equivalent diameter, (Raffel *et al.*, 1967)). Comparing these results with the ones in Figure 4.13, it can be stated that the introduction of the vibratory displacement on the bed tends to decrease the bubble velocity. Also, Figure 4.13 clearly shows a decrease of the velocity coefficient $\mu$ with the amplitude of vibration. As the amplitude increases, isolated bubbles of a given diameter become slower in their rising motion. This tendency was previously observed by Acosta-Iborra *et al.* (2012) and by Cano-Pleite *et al.* (2013) for simulated VFBs working under bubble regime with multiple interacting bubbles. Note that the decrease of $\mu$ with $A$ appears in both the lower and the upper half of the bed taken into consideration, the effect being more pronounced in the upper half.

As can be seen in Figure 4.13(b), the relation between bubble diameter and velocity seems to be not greatly affected by frequency variations, as $\mu$ remains around the same values for the three vibration frequencies tested and the two sections under study. This suggests that the decrease of bubble velocity might be induced not by the augmentation of energy dissipation that is linked to collisions, but to other phenomenon. The growth of inter-particle void fraction cyclically experienced by the bed and augmented by the increase of vibration amplitude, may generate bubbles with lower buoyancy in the bed, causing $\mu$ to decrease. Two additional plausible explanations of the decrease of the bubble velocity with the vibration amplitude could be (i) that vibration increases the amount of particles dragged by the bubble wake, which may reduce the velocity of the bubble, and (ii) that increasing the vibration amplitude decreases of the effective bubble diameter affecting the solids for a given visible bubble size.

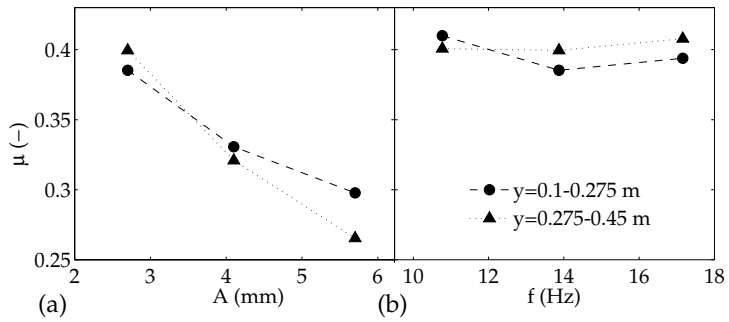


**Figure 4.13:** Bubble velocity coefficient, $\mu = \left\langle \overline{V}_b / \sqrt{g\overline{D}_b} \right\rangle_{median}$, for different heights. (a) Variation with vibration amplitude (Exp. 1, 2 and 3), (b) variation with vibration frequency (Exp. 1, 4 and 5).

### 4.4.2 Numerical simulation results

#### General dense phase and bubble behavior

Figure 4.14(a) shows the time evolution of the volume of the simulated VFB, normalized with the settled bed volume $KWH_0$, when an isolated bubble is rising in the bed. It can be observed that the volume of the bed simulated with the incompressible gas-phase model oscillates with a markedly smaller amplitude than the simulated bed with the compressible gas. According to Figure 4.14, the simulation of the bed with the plenum together with the compressible gas model (Case-3) seems to partially relax the bed fluctuations, which lead to a less vigorous oscillation of the bed volume compared with the same simulations with compressible gas but without plenum. Also, the phase of the bed volume oscillations in the incompressible case is ahead of the phase of the results calculated with the compressible gas model. Figure 4.14(b) contains the location of the centroid of the simulated bubble, $y_b$, during the period of time shown in Figure 4.14(a). While the bubble is rising, the bubble centroid vertical position increases and this movement slightly fluctuates since it is simultaneously affected by the oscillation of the bed volume.

As in Section 4.4.1, the amplitude and phase of the bed volume oscillations can be more easily analyzed by means of the averaging of cycles method described in Section 2.3.2. The simulation and experimental results are shown in Figure 4.15. The averaged oscillations of the simulated bed volume with compressible gas present an opposition in phase with respect to the bed displacement. This behavior of the simulated bed is in very good agreement with the experiments presented in Section 4.4.1, as shown in Figure 4.15. It is clear from the figure that the simulation of the bed with incompressible gas leads to inaccurate results since the phase and the amplitude of the bed volume is different to

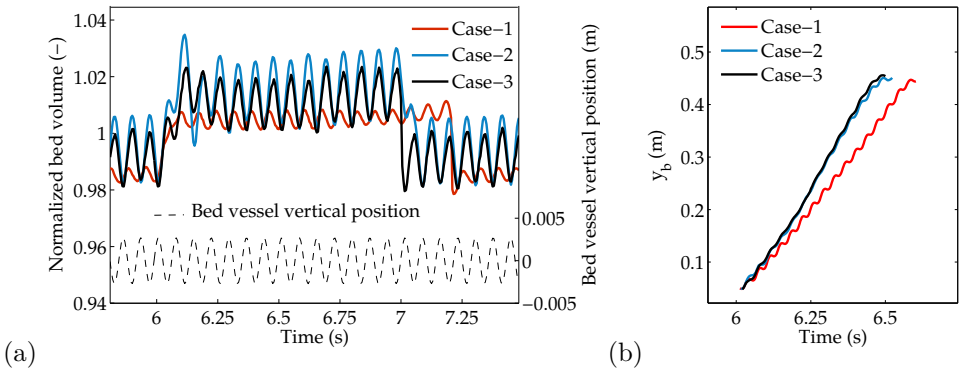


**Figure 4.14:** (a) Normalized bed volume and (b) bubble absolute vertical position as a function of the time for the incompressible gas-phase model (Case-1), compressible gas-phase model without plenum (Case-2) and compressible gas-phase model with plenum (Case-3). $f = 13.9$ Hz and $A = 2.7$ mm.

the experimental results. Thus, the results presented in Figure 4.15 can be understood as a cyclic compression-expansion of the bed facilitated by the compressibility of the gas phase and the propagation of particle collision in the bed (see Chapter 3). Besides, the magnitude of the cyclic compression-expansion of the bed is overestimated when the plenum chamber is not considered in the simulation. The fact that the presence of the plenum does not promote a change on the phase of the bed volume oscillation but decreases the amplitude of the bed volume oscillation indicates that the compressibility of the gas phase plays a key role on the cyclic expansion-compression of the bed volume. The plenum increases the gas volume of the system, which alternately accumulates by compression the mechanical energy of the system. In view of the results, it can be stated that the use of compressible gas and the inclusion of the plenum in the two-fluid model simulations clearly improves the results compared to those of the incompressible gas simulations. Figure 4.15(b) shows the normalized bed volume, for the compressible case with plenum, as a function of the vibration phase for three meshes with cells of 2, 4 and 8 mm side. It can be observed that the results remain practically unchanged when the cell size is reduced from 4 mm to 2 mm. However, the computational cost of the mesh with cells of 2 mm side is dramatically increased. Therefore, the simulation with compressible gas with plenum and a mesh with cells of 4 mm side will be taken as the base conditions in the subsequent analyses.

Concerning bubble behavior, Figure 4.16 shows four consecutive snapshots of a bubble rising in the simulation (Case-3) and a bubble of similar diameter rising in the experimental bed (Exp. 1). The location of the centroid of the bubble is also indicated on each of the images. As the bubble of the simulation raises in the bed, its position and

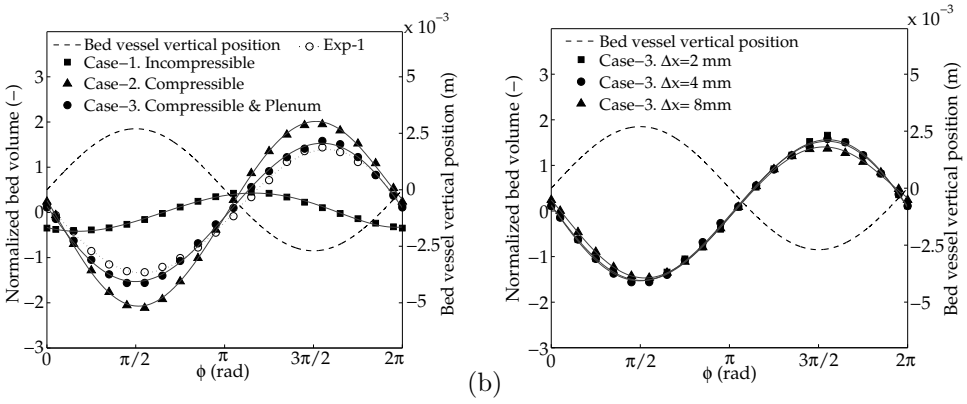


**Figure 4.15:** Normalized bed vessel position and bed volume as a function of the vibration phase. (a) Experimental results (Exp-1), incompressible gas phase model (Case-1), compressible gas phase model without plenum (Case-2) and compressible gas phase model with plenum (Case-3). (b) Case-3 for three different mesh resolutions. $f = 13.9$ Hz and $A = 2.7$ mm.

diameter are influenced by vibration. The bubble rises faster in the first half of the period, comprising the first two images in each row of Figure 4.16 (from $\phi = 0$ rad to $\phi = \pi$ rad), than in the rest of the cycle. Also, in the second half of the period (between $\phi = \pi$ rad and $\phi = 2\pi$ rad) the shape of the bubble changes and its wake partially penetrates into the bubble. The same oscillatory behavior and wake penetration are found in the experimental snapshots of Figure 4.16(b). The differences observed in terms of bubble shape may be attributed to the two-dimensionality of the model. In the experiments, the amount of particles raining in the bubble is increased by the presence of the front and rear walls. This raining phenomenon is difficult to capture in detail by the two fluid simulations due to the discrete nature of particle dynamics when the void fraction is high. Sensitivity tests for the different mesh sizes revealed that the bubble shape in the simulation is weakly affected when doubling the resolution of the mesh of Figure 4.16(a).

### Oscillatory bubble diameter

Figure 4.17 shows the averaging of cycles oscillations of the normalized bubble diameter for the simulated cases with incompressible gas, compressible gas without plenum and compressible gas with plenum (Cases 1-3). As in the experiments (Section 4.4.1), normalization is carried out in terms of the moving average of the bubble diameter.

It can be clearly observed in Figure 4.17(a) that the use of incompressible gas in the simulation fails to predict the phase of the oscillations of bubble diameter. In this case, the simulated bubble diameter tends to grow when the bed surface is moving upwards (see Figure 4.15), just the opposite to the experimental results. Also, contrary

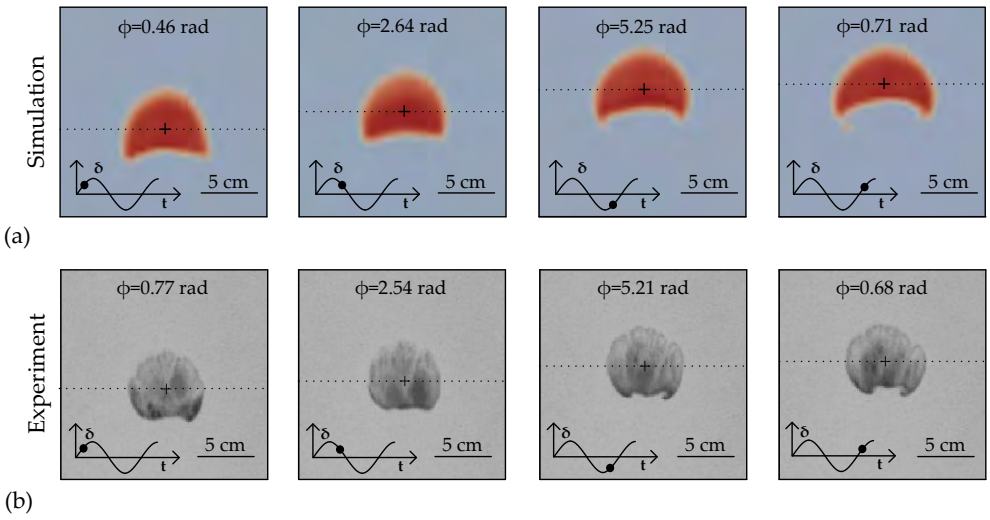


**Figure 4.16:** Comparison of (a) simulation snapshots (Case-3) and (b) grayscale digital images (Exp. 1) of an isolated bubble rising in the vibrating fluidized bed and captured at different vibration phases. The dotted horizontal line indicates the vertical position of the bubble centroid. The vertical displacement $\delta$ of the bed vessel is also indicated. $f = 13.9$ Hz, $A = 2.7$ mm.

to the experimental observations, the incompressibility of the gas yields no phase delay between the lower half section of the bed ($y = 0.1 - 0.275$ m) and its higher half section ($y = 0.275 - 0.45$ m).

In contrast, the simulations with compressible gas, Figure 4.17(b), are able to predict diameter oscillations with a phase closer to the experiments than the incompressible gas simulations. It can be appreciated in Figure 4.17(b) that there is a positive delay of the oscillation of bubble diameter when passing from the lower half of the bed to the upper half of the bed. This positive delay also happens in the experiments. Similarly to Figure 4.15, the presence of the plenum in the simulated domain promotes a softening in the oscillating movement of the whole bed, which is also reflected through a decrease in the amplitude of the bubble diameter fluctuations. Differences between the phases and amplitudes of the compressible gas simulations and the experiment could be attributed to the friction caused by the front and rear walls in the experiments (Li *et al.*, 2010; Hernández-Jiménez *et al.*, 2011, 2013), which can retard the phase of the oscillation and diminish their amplitude. This effect is not present in the two-dimensional simulation since it lacks of front and rear walls.

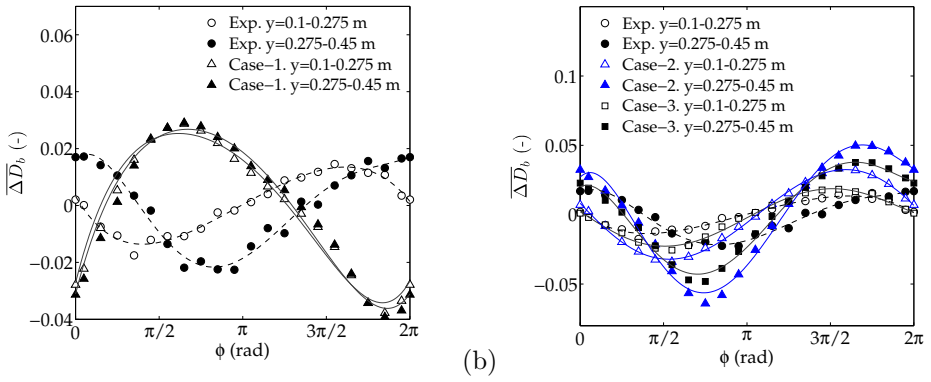


**Figure 4.17:** Normalized oscillation of bubble diameter as a function of the vibration phase. (a) Simulations with incompressible gas phase (Case 1) (b) Simulations with compressible gas without and with plenum (Cases 2 and 3). Experimental results are also included. $f = 13.9$ Hz and $A = 2.7$ mm.

The effect of the bed vessel vibration amplitude and frequency on the bubble diameter can be also studied through the averaging of cycles method. Figures 4.18 and 4.19 show the simulation and experimental results concerning the averaged oscillation of bubble diameter as a function of the amplitude (Figure 4.18) and the frequency (Figure 4.19) of the bed vessel vibration. The growth of the amplitude of the bubble diameter oscillations with the vibration amplitude observed in the experiments is well reproduced in the numerical model (see Figure 4.18(a)). Though the simulations predict amplitudes similar in the lower part of the bed to those of the experiments (Figure 4.18(b)), the amplitude of the oscillations in the upper part of the bed is always overpredicted by the simulated bed. This effect is also observed in Figure 4.19. According to the previous comments, the larger oscillation amplitude of the simulation could be explained with the lack of front and rear wall interaction in the simulated VFB. In the experiments, the friction of the bed material with the front and rear walls avoids the bubble to freely oscillate and reduces the oscillation of the bubble diameter. Nevertheless, both the experiments and the simulations agree in the fact that the variation of the vibration amplitude has a more pronounced effect on the amplitude of the diameter oscillations than the variation of vibration frequency (Figures 4.19(a) and 4.19(b)). Concerning the phase of the oscillations, the simulation reflects that the retardation in phase of the oscillation of the bubble diameter (Figure 4.19(a)) is more noticeable in the upper half section of the bed than in the lower half section. This is also in agreement with the experimental results (Figure 4.19(b)).

The value of the phase delay of bubble characteristics was calculated following the procedure indicated in Chapter 2. Note that in the simulations with incompressible gas-

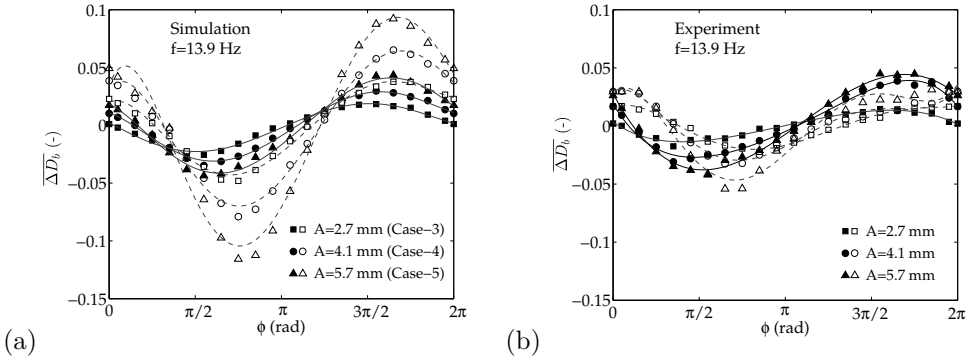


**Figure 4.18:** Normalized oscillation of bubble equivalent diameter as a function of the vibration phase for different vibration amplitudes (Cases 3, 4, and 5). (a) Simulation and (b) experimental results. The black symbols indicate the results for the lower half section of the bed ($y = 0.1 - 0.275$ m) and the white symbols for the upper half section ($y = 0.275 - 0.45$ m).

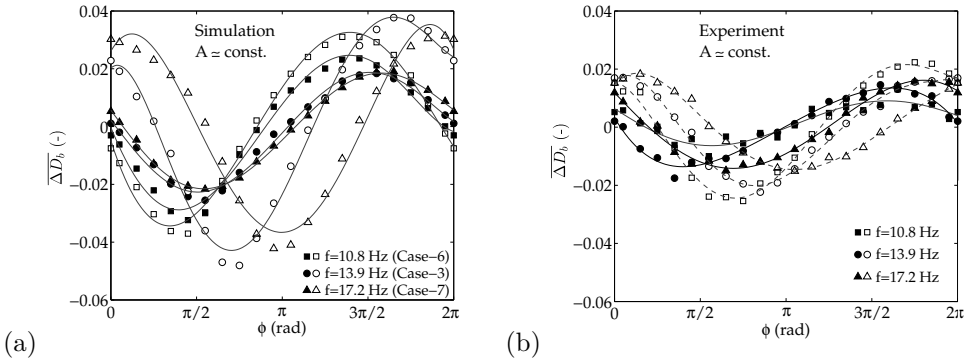


**Figure 4.19:** Normalized oscillation of bubble equivalent diameter as a function of the vibration phase for different vibration frequencies (Cases 3, 6, and 7). (a) Simulation and (b) experimental results. The black symbols indicate the results for the lower half section of the bed ($y = 0.1 - 0.275$ m) and the white symbols for the upper half section ($y = 0.275 - 0.45$ m).

phase (Case-1) bubble characteristics do not present a phase delay between the lower and the higher half sections (Figure 4.17). This unrealistic result is caused by the lack of compressibility in the gas phase when the gas density is assumed constant.

Figure 4.20 shows the phase delay of the bubble diameter, in the upper and lower sections of the bed, as a function of the bed vessel vibration amplitude and frequency. It can be observed in the figure that the bubble oscillation delays of the simulation with the compressible gas model are in good agreement with the experimental observations. In particular, it can be seen in Figure 4.20 that the delay of the bubble oscillation with

respect to the vessel displacement is about $\phi_d = \pi$ rad in both the simulation and the experiments. In view of Figure 4.15, where the bed volume also has a delay of $\pi$ rad, it can be said that the compression-expansion of the bed bulk is the principal cause of the oscillation of the bubble diameter. Besides, for all the cases shown in Figure 4.20, bubble characteristics in the lower half of the bed present a lower phase delay than bubbles in the upper half, and this is finely reproduced by the compressible gas simulation. The delay of the diameter oscillations in the higher half of the bed is slightly smaller than the experimental results. This may be attributed to the absence of the front and rear walls in the two-dimensional numerical model, which retard the response of the dense phase with respect to the bed vessel oscillation movement. Another cause of the discrepancies concerning the delay of diameter oscillation could be the differences in the way the bubble contours are defined in the simulations and in the experiments. In the experiments the bubble contours are sharper than in the simulations due to the discrete nature of particles in a real bed.

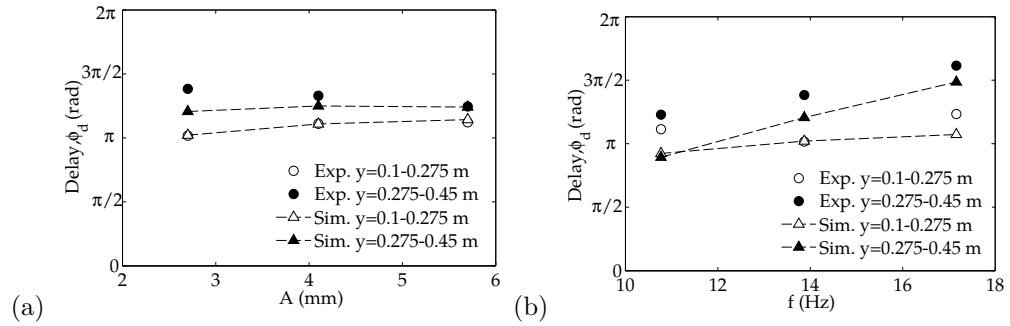


**Figure 4.20:** Phase delay of bubble equivalent diameter at different heights and comparison with experiments. (a)Variation with vibration amplitude (Cases 3, 4 and 5), (b) variation with vibration frequency (Cases 3, 6 and 7).

Nevertheless, the retardation produced by the front and rear walls, or other causes, are not greatly contributing to the delay since it is acceptably well reproduced by the two-dimensional simulations, excepting perhaps at low frequencies in Figure 4.20(b) (Case 6), where the energy introduced by vibration is smaller. All these facts confirmed by the numerical simulation support the assumption of the presence of compression-expansion waves traveling through the bed and propagating the information upwards.

As in Section 4.4.1, the propagation velocity of the simulated bubble diameter (i.e. the velocity of the compression wave in the bed bulk) can be calculated as the distance between the centers of the upper and lower sections of the bed times the vibration frequency and divided by the phase delay difference between those sections (see Equation (4.5)).

Calculating the propagation velocity of the bubble diameter for the simulation results in Figure 4.20, excluding the anomalous result at low frequency (Case 6), yields an average propagation velocity of $V_{prop,D_b,sim} = 31.2$ m/s for the simulation results and $V_{prop,D_b,exp} = 22.6$ m/s for the experiments. Despite the complexity of the simulated system and the absence of front and rear walls interactions in the 2D computations, these simulation and experimental results are reasonably similar and are of the same order of magnitude as the effective sound propagation velocity inside a fluidized bed, which can be calculated following (Roy *et al.*, 1990) and is equal to 13.1 m/s, as seen in Section 4.4.1.

### Oscillatory bubble velocity

Figure 4.21 shows the oscillation of the bubble vertical velocity normalized with the moving average of the bubble velocity ($\Delta V_{bi} = (V_{bi} - \widehat{V}_{bi})/\widehat{V}_{bi}$). The results for the simulation with incompressible gas (Figure 4.21(a)) and the compressible gas with and without plenum (Figure 4.21(b)) are compared with the experimental results. It can be seen how the simulation with the incompressible gas model fails to predict both the phase and the amplitude of the velocity oscillations. Additionally, no delay and amplitude variations are observed between the upper and lower half sections of the bed in the incompressible gas simulations, which corroborates the assumption that, in addition to the propagation of the information upwards the bed due to particle collision studied in Chapter 3, the change of the oscillation phase of bubble characteristics is also induced by the compressibility of the gas phase inside the bed.

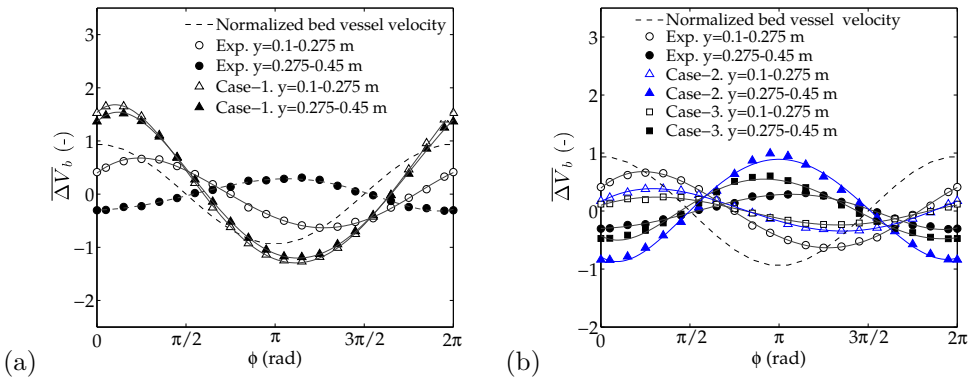


**Figure 4.21:** Normalized oscillation of bed vessel velocity and bubble absolute vertical velocity as a function of the vibration phase. (a) Simulations with incompressible gas phase (Case 1) (b) Simulations with compressible gas without and with plenum (Cases 2 and 3). Experimental results are also included. $f = 13.9$ Hz and $A = 2.7$ mm.

According to Figure 4.21(b), the two-fluid model simulations with compressible gas model clearly improve the prediction of the bubble velocity oscillation compared to the simulations with incompressible gas model. The simulations with compressible gas are able to reasonably match the experimental results in terms of phase delay and amplitude of the velocity oscillations. The simulations predict a higher amplitude of the velocity oscillation in the upper section of the bed, which could be attributed, as commented for the case of diameter oscillation, to the lack of front and rear walls in the simulation. The higher amplitude of velocity oscillations in the simulations might be also attributed to other effects such as the invariance of pressure imposed in the simulation at the top outlet of the bed, which is an approximation of what is actually occurring in a real VFB. However, the similarities between experiments and simulations are more than remarkable, given the complexity of the VFB system.

Similarly to the diameter fluctuation in Figure 4.17, the presence of the plenum in the computational domain 4.17 reduces the magnitude of the velocity oscillations in both sections of the bed in Figure 4.21. It can be seen in the figure that the introduction of the plenum in the simulation leads to results closer to the experiments.

The velocity fluctuations for the different vibration frequencies and amplitudes tested are also studied in Figures 4.22 and 4.23. The simulations with compressible gas and plenum yield a good estimation of the variation of the velocity fluctuation amplitude observed in the experiments when the amplitude of the vibration is increased. The amplitude of the normalized velocity increases in the upper and the lower sections of the bed for both the simulation (Figure 4.22(a)) and the experimental results (Figure 4.22(b)). Also, in consonance with the experimental evidence, no great changes in the phase delay of the oscillations are observed when the vibration amplitude is varied. The effect of the vibration frequency in the normalized velocity oscillations observed in the experiments (Figure 4.23(b)) is also reasonably well reproduced in the simulations (Figure 4.23(a)). Quantitatively, the simulation predicts smaller oscillations in the lower half section of the bed and greater oscillations in the upper section of the bed.

Figure 4.24 shows the values of the phase delays of the bubble velocity fluctuations with respect to the bed vessel velocity. Results are presented for both the lower and the upper half sections of the bed. The simulations yield an excellent estimation of the delay on bubble characteristics in most of the cases. As the small delay for $y = 0.1 - 0.275$ m in Figure 4.24(a) suggests, the bubble velocity close to the distributor seems to be more attached to the movement of the bed vessel than bubbles near the bed surface. While the simulation delays on Figure 4.24(a) are practically unaffected by the vibration amplitude, those in Figure 4.24(b) present a stronger variation with frequency. All these results are in harmony with the experiments. The mean propagation velocity (Equation (4.5)) corresponding to the simulated bubble velocity fluctuations is $V_{prop,V_b,sim} = 10$ m/s.

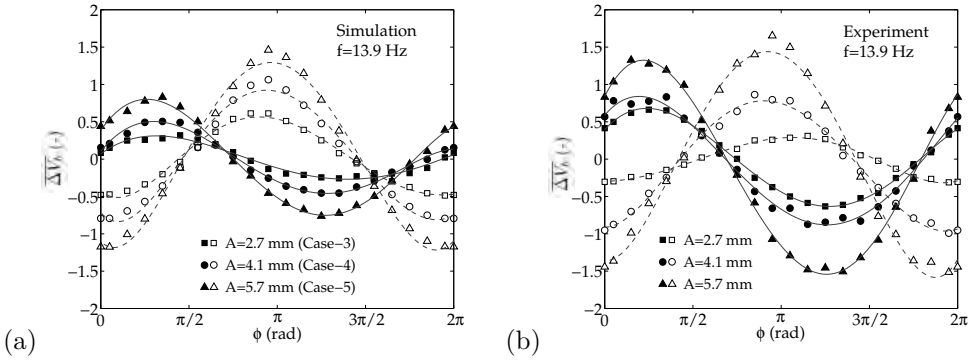


**Figure 4.22:** Normalized oscillation of bubble absolute vertical velocity as a function of the vibration phase for different vibration amplitudes (Cases 3, 4, and 5). (a) Simulation and (b) Experimental results. The black symbols indicate the results for the lower half section of the bed ($y = 0.1 - 0.275$ m) and the white symbols for the upper half section ($y = 0.275 - 0.45$ m).

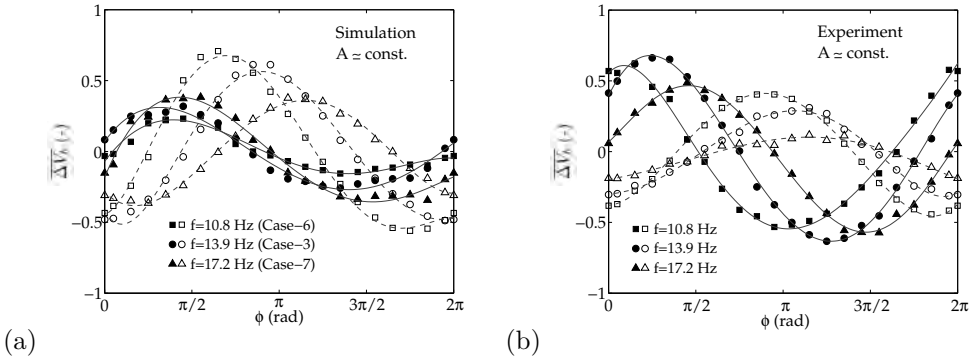


**Figure 4.23:** Normalized oscillation of bubble absolute vertical velocity as a function of the vibration phase for different vibration frequencies (Cases 3, 6, and 7). (a) Simulation and (b) Experimental results. The black symbols indicate the results for the lower half section of the bed ($y = 0.1 - 0.275$ m) and the white symbols for the upper half section ($y = 0.275 - 0.45$ m).

This is in acceptable agreement with the same result calculated with the experimental data,$V_{prop,V_b,exp} = 6.9$ m/s. As for the case of diameter oscillations, these velocities are of the same order of magnitude as the effective sound propagation velocity in a fluidized bed.

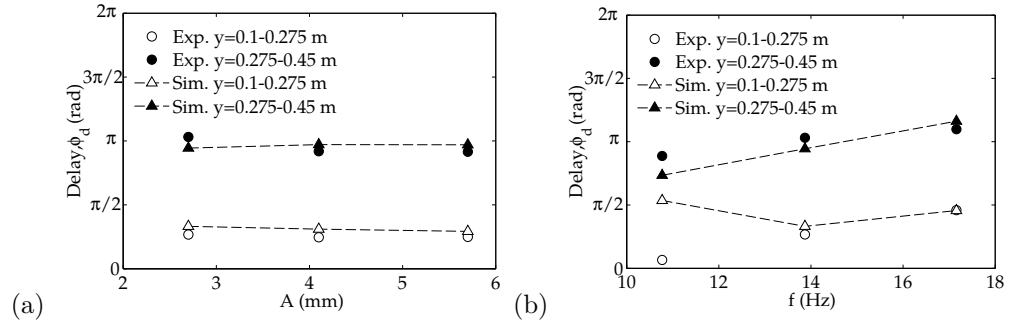


**Figure 4.24:** Phase delay of bubble absolute vertical velocity at different heights and comparison with experiments. (a)Variation with vibration amplitude (Cases 3, 4 and 5), (b) variation with vibration frequency (Cases 3, 6 and 7).

## 4.5 Conclusions

The size and motion of isolated bubbles in a pseudo-2D fluidized bed subjected to vertical vibration were experimentally and numerically studied in this chapter. Bed characteristics as well as the bubble behavior were studied using an averaging of cycles method in which the influence of the vibration on the local oscillation of the bubble is considered. The experimental results revealed that vibration of the bed vessel causes a continuous expansion and compression of the bed bulk, which has an impact on the bubble dynamics. The simulation with the fluidization air treated as an incompressible gas is unable to reproduce this cyclic compression and expansion. In contrast, the simulations using a compressible gas model for the fluidization air mimic the experiments fairly well. The vibration frequency of the bed vessel has a clear influence on the phase delay of the bubble diameter and velocity, whilst the vibration amplitude possesses a more significant effect on the amplitude of the bubble oscillations. The phase delays and amplitudes of the oscillations of the bubble diameter and velocity change with the bubble distance to the distributor. Thanks to the simulation evidence, these effects can be attributed to the compressibility of the gas-phase, in harmony with the propagation of pressure and solids waves observed in Chapter 3. The need of gas compressibility to model VFBs reinforces the idea proposed in Chapter 3 that solids compression waves are principally driven by gas pressure waves and not merely by particle collisions. Besides, the simulations revealed that the gas volume in the plenum promotes a softening of the amplitude of the bed and bubble oscillations. Most of the simulation results using the compressible gas model with plenum are quite similar to the experimental observations of bubble behavior, which is remarkable given the complexity of the VFB system. However, regarding the magnitude of

the oscillations of bubble diameter and velocity, some quantitative discrepancies between the simulations and the experiments were found. This may be attributed to the fact that the simulations were performed in two dimensions whereas the experimental pseudo-2D bed can be affected by the particles interaction with the front and rear walls of the bed vessel. Other effects such as the differences in the way the bubble contours are defined in the simulation and the experiments, might contribute to these discrepancies and their impact on results should be studied in the future. The results presented in this chapter have shown that careful selection of the vessel vibration amplitude and frequency may be used to modify the motion of bubbles in the bed increasing, for example, their residence time before they erupt. The results also reveal the potential of the two-fluid model for the simulation of medium and large scale VFBs and suggest the need of incorporating the gas-phase compressibility to the simulation of bed and bubble oscillations in VFBs and other vibrating-like systems.

## Nomenclature

| | |
|---|---|
| $A$ | vibration amplitude (mm) |
| $A_{ap}$ | bed cross-sectional area, WK ($m^2$) |
| $A_{eq}$ | oscillation equivalent amplitude (mm) |
| $A_b$ | bubble area ($m^2$) |
| $D_b$ | bubble equivalent diameter (m) |
| $D_{inj}$ | diameter of the injected bubble (mm) |
| $\overline{D}_b$ | averaged $D_b$ (m) |
| $d_p$ | particle diameter ($\mu$m) |
| $e$ | restitution coefficient (-) |
| $f$ | vibration frequency (Hz) |
| $g$ | gravity acceleration constant ($m/s^2$) |
| $H$ | bed vessel height (m) |
| $H_{eq}$ | equivalent plenum height (m) |
| $H_0$ | static bed height (m) |
| $h_{bi}$ | height of the bubble injection port (m) |
| $K$ | bed vessel thickness (m) |
| $R_g$ | ideal gas constant for air (J/kg K) |
| $S$ | average data dispersion (-) |
| $T$ | oscillation period, $1/f$ (s) |
| $T_g$ | gas phase temperature (K) |
| $t$ | time (s) |
| $U_g$ | gas velocity (m/s) |

| | |
|---|---|
| $U_{mf}$ | minimum fluidization velocity (m/s) |
| $u_s$ | equivalent sound velocity in the bed (m/s) |
| $u_{so}$ | gas velocity of sound (m/s) |
| $V_{ap}$ | plenum chamber volume ($m^3$) |
| $V_b$ | bubble velocity (m/s) |
| $\overline{V}_b$ | averaged $V_b$ (m/s) |
| $V_{prop}$ | propagation velocity of oscillations (m/s) |
| $W$ | bed width (m) |
| $x$ | horizontal coordinate (m) |
| $y$ | vertical distance to the distributor (m) |
| $y_{BS}$ | bed surface vertical coordinate (m) |
| $y_{CM}$ | bed center of mass vertical coordinate (m) |
| $y_b$ | bubble centroid vertical coordinate (m) |
| $z(t)$ | instantaneous variable value |
| $\widehat{z}(t)$ | moving average of $z$ |

*Greek letters*

| | |
|---|---|
| $\gamma$ | heat capacity ratio (-) |
| $\delta(t)$ | bed vessel vertical displacement (m) |
| $\Delta t_{exp}$ | simulation data export time-step (s) |
| $\Delta z$ | oscillation of a variable (-) |
| $\varepsilon$ | void fraction (-) |
| $\varepsilon_0$ | initial bed void fraction (-) |
| $\varepsilon^*$ | packed bed void fraction (-) |
| $\Phi$ | specularity coefficient (-) |
| $\phi$ | phase (rad) |
| $\phi_d$ | phase delay (rad) |
| $\theta$ | angle of internal friction ($^o$) |
| $\mu$ | bubble velocity coefficient |
| $\mu_g$ | gas viscosity (Pa s) |
| $\rho$ | density ($kg/m^3$) |
| $\sigma$ | standard deviation |
| $\omega$ | angular velocity (rad/s) |

*Subscripts*

| | |
|---|---|
| *exp* | experiment |
| *g* | gas phase |
| *i* | frame index |

| | |
|---|---|
| $p$ | particle (solid) phase |
| $sim$ | simulation |

# References

Acosta-Iborra, A., Hernández-Jiménez, F., de Vega, M. & Briongos, J.V. 2012 A novel metodology for simulating vibrated fluidized beds using two-fluid models. *Chem. Eng. J.* 198-199, 261–274.

Baird, M.H.I. 1963 Resonant bubbles in a vertically vibrating column. *Can. J. Chem. Eng.* 41, 52–55.

Barletta, D., Donsi, G., Ferrari, G., Poletto, M. & Russo, P. 2008 The effect of mechanical vibration on gas fluidization of a fine aeratable powder. *Chem. Eng. Res. Des.* 86, 359–369.

Barletta, D. & Poletto, M. 2012 Aggregation phenomena in fluidization of cohesive powders assisted by mechanical vibrations. *Powder Technol.* 2012, 93–100.

Barletta, D., Russo, P. & Poletto, M. 2013 Dynamic response of a vibrated fluidized bed of fine and cohesive powders. *Powder Technol.* 237, 276–285.

Cano-Pleite, E., Gómez-Hernández, J., Sánchez-Prieto, J. & Acosta-Iborra, A. 2013 Characterization of the bubble behavior in vibrated fluidized beds by means of two-fluid CFD simulations coupled with accelerometry data. In *The 14th International Conference on Fluidization - From Fundamentals to Products, ECI Symposium Series.*

Davidson, J.F. & Harrison, D. 1963 *Fluidised Particles.* Cambridge University Press, Cambridge.

Eccles, E.R.A. & Mujumdar, A.S. 1997 Bubble phenomena in aerated vibrated beds of small particles. *Drying Technol.* 15:1, 95–116.

Ellenberg, J. & Krishna, R. 2007*a* Levitation of air bubbles and slugs in liquids under low-frequency vibration excitement. *Chem. Eng. Sci.* 62, 7548–7553.

Ellenberg, J. & Krishna, R. 2007*b* Levitation of air bubbles in liquid under low frequency vibration excitement. *Chem. Eng. Sci.* 62, 5669–5673.

Hernández-Jiménez, F., Sánchez-Delgado, S., Gómez-García, A. & Acosta-Iborra, A. 2011 Comparison between two-fluid model simulations and particle image

analysis & velocimetry (PIV) results for a two-dimensional gas-solid fluidized bed. *Chem. Eng. Sci.* 66, 3753–3772.

Hernández-Jiménez, F., Sánchez-Prieto, J., Soria-Verdugo, A. & Acosta-Iborra, A. 2013 Experimental quantification of the particle-wall frictional forces in pseudo-2D gas fluidised beds. *Chem. Eng. Sci.* 102, 257–267.

Jameson, G.J. & Davidson, J.F. 1966 The motion of a bubble in a vertically oscillating liquid: theory for an inviscid liquid, and experimental results. *Chem. Eng. Sci.* 21, 29–34.

Johnson, P.C. & Jackson, R. 1987 Frictional-collisional constitutive relations for granular materials, with application to plane shearing. *J. Fluid Mech.* 176, 67–93.

Li, T., Grace, J.R. & Bi, X. 2010 Study of wall boundary condition in numerical simulations of bubbling fluidized beds. *Powder Technol.* 203, 447–457.

Limtrakul, S., Rotjanavijit, W. & Vatanatham, T. 2007 Lagrangian modeling and simulation of effect of vibration on cohesive particle movement in a fluidized bed. *Chem. Eng. Sci.* 62, 232–245.

Mawatari, Y., Koide, T., Tatemoto, Y., Takeshita, T. & Noda, K. 2001 Comparison of three vibrational modes (twist, vertical and horizontal) for fluidization of fine particles. *Adv. Powder Technol.* 2, 157–168.

Mawatari, Y., Tagawa, K., Tatemoto, Y. & Noda, K. 2005 Bubbling characteristics under vertical vibration in a two-dimensional fluidized bed. *Chem. Eng. Jpn.* 38, 18–23.

Musmarra, D., Poletto, M., Vaccaro, S. & Clift, R. 1995 Dynamic waves in fluidized beds. *Powder Technol.* 82, 255–268.

O'Hern, T., Shelden, B., Torczynsky, J. & Romero, L. 2012 Bubble oscillations and motion under vibration. *Phys. Fluids.* 24, 091108.

Raffel, M., Willert, C. & Kompenhans, J. 1967 The rising velocity of bubbles in two-dimensional fluidized beds. *Chem. Eng. Sci.* 22, 531–53.

Roy, R., Davidson, J.F. & Tuponogov, V.G. 1990 The velocity of sound in fluidised beds. *Chem. Eng. Sci.* 45, 3233–3245.

Rubin, E. 1968 Behavior of gas bubbles in vertically vibrating liquid columns. *Can. J. Chem. Eng.* 46, 145–149.

van der Schaaf, J., Schouten, J.C. & van den Bleek, C.M. 1998 Origin, propagation and attenuation of pressure waves in gas-solid fluidized beds. *Powder Technol.* 95, 220–233.

Wang, T.J., Jin, Y., Tsutsumi, A., Wang, Z. & Cui, Z. 2000 Energy transfer mechanism in a vibrating fluidized bed. *Chem. Eng. J.* 78, 115–123.

Xiang, L., Shuyan, W., Huilin, L., Goudong, L., Juhui, C. & Yikun, L. 2010 Numerical simulation of particle motion in vibrated fluidized beds. *Powder Technol.* 197, 25–35.

Zeilstra, C., van der Hoef, M.A. & Kuipers, J.A.M. 2013 Experimental and numerical study of solids circulation in gas-vibro fluidized beds. *Powder Technol.* 248, 153–160.

Zhou, T., Kage, H., Funaoka, S., Ogura, H. & Matsuno, Y. 2001 Fluidization behaviour of glass beads under different vibration modules. *Adv. Powder Technol.* 12, 559–575.

Zhou, T., Kage, H. & Li, H. 2005 Bubble characteristics in a two-dimensional vertically vibro-fluidized bed. *China Partic.* 3, 224–228.

Zhou, T., Ogura, H., Yamamura, M. & Kage, H. 2004 Bubble motion pattern and rise velocity in two-dimensional horizontal and vertical vibro-fluidized beds. *Can. J. Chem. Eng.* 82, 236–242.

CHAPTER
**FIVE**

# The solids motion and pressure distribution around an isolated bubble in a vibrated fluidized bed

**Contents**



## 5.1 Introduction

The cyclic compression and expansion of the bed bulk and the effect of vibration on the shape and motion of bubbles rising alone in the bed was studied in the previous chapters. However, it is not clear how the bed bulk oscillation interacts with the bubble and how the resulting solids velocity in the bed bulk distributes around the rising bubble. Knowledge of the solids motion around bubbles can be crucial to understand the solids mixing and fuel transport in a vibrated bed reactor.

Many experimental and numerical works available in the literature have tested the capabilities of the potential flow theory developed in the early 1960s by Davidson &

Harrison (1963). Müller *et al.* (2007) studied the eruption of a bubble in a fluidized bed by means of PIV. They observed that, even after eruption, the potential flow theory was capable of predicting the velocity of the particles on the roof of the bubble. Hernández-Jiménez *et al.* (2011*b*) carried out two-fluid model simulations of the system used in (Müller *et al.*, 2007). The results of the simulations indicated that the potential flow theory provides a more accurate prediction for the particle velocities in erupting bubbles than other semi-empirical relations available in the literature. Experimental and numerical works being compared with Davidson & Harrison (1963) model are also focused on the gas pressure distribution around bubbles in fluidized beds. Croxford & Gilbertson (2011) successfully applied a model, based on Davidson & Harrison (1963) potential theory, to describe the dynamics of bubbling fluidized beds. Patil *et al.* (2003) used both experiments and two-fluid model simulations to characterize the gas dispersion in a single bubble rising in a fluidized bed. Again, their results were in agreement to those predicted by the Davidson & Harrison (1963) model. Good agreement between Davidson & Harrison (1963) potential flow model and numerical simulations was also found by Hernández-Jiménez *et al.* (2013) in terms of the pressure distribution and the gas interchange coefficient for isolated bubbles rising in the bed.

The characterization of the solids motion in a vibrated bed provide clear and valuable information on the impact of vibration on the oscillatory behavior of a bubble and the bed bulk and their mutual interaction. Previous works (e.g. Barletta *et al.* (2013)) have confirmed that the pseudo-homogeneous approach for the wave propagation proposed by Roy *et al.* (1990) could be satisfactorily extended to vibrated beds. This approach of wave propagation was also used to estimate the velocities of propagation of solids velocity waves in Chapters 3 and of bubble characteristics in Chapter 4. Nevertheless, it would be desirable to analyze whether the propagation of bubble characteristics is caused by a wave in the dense phase that affects the motion of solids around the bubble, including the wake region. Besides, from a practical point of view in the development of models, it would be also of great interest to check whether the potential flow model proposed by Davidson & Harrison (1963) is still applicable to describe the particle motion around a bubble rising in a fluidized bed subjected to vibration.

The aim of the present chapter is to experimentally study the oscillatory motion of particles in the bed bulk and the vicinity of an isolated bubble rising in a vibrated fluidized bed. These novel results are presented using a bubble averaging method, which averages the bubble contour and the velocity of solids in the proximity of different bubbles. Also, as far as the author is concerned, the motion of particles and the volume of the wake region of a bubble rising in a vibrated bed is characterized for the first time as a function of the vibration phase for different vibration amplitudes and frequencies. Additionally, a combination of DIA and PIV techniques is used to determine the validity of the

potential model of Davidson & Harrison (1963) for the estimation of the particle motion and the pressure distribution around a bubble rising in a vibrated fluidized bed. As mentioned before, these results can be useful to clarify the essential mechanisms affecting the oscillatory motion of bubbles in a vibrated bed, the effect of the compression-expansion waves traveling inside the bed bulk and the ability of bubbles to drag solids in VFBs.

## 5.2 Experimental setup

The experimental facility used in the present chapter is the pseudo-2D vibrated bed of dimensions 0.3 x 0.6 x 0.01 m (width W, height H and thickness K, respectively) described in Section 2.1.1. The bed material was ballotini glass beads with a size range between 425-600 $\mu$m and a density of 2500 kg/m$^3$ (Geldart's classification type B (Geldart, 1973)). Approximately 5% of the particles were painted in black to enhance the cross-correlation of the bed images during their processing by Particle Image Velocimetry (PIV). The minimum fluidization velocity of the particles at static conditions was measured using the mean value method and resulted in $U_{mf} = 0.28$ m/s.

As in Chapter 4, two independent air supply lines were employed to fluidize the bed and inject bubbles in the system. In particular, an air supply line was used to reach minimum fluidization conditions in the bed. A secondary air supply was used to inject bubbles in the bed through a hole drilled in the rear wall of the vessel at 5 cm above the distributor. To obtain bubbles of approximately the same size, air was preloaded in the volume of a tube placed between two valves (valve 1 and valve 2 in Figure 2.1). The mass injected could be controlled by setting the volume (i.e. the length of the tube) and the pressure of the air between the two valves.

A high speed camera (Redlake Motion pro X3) was employed to record images of the front view of the bed at a frame rate of 250 images per second during an acquisition time of around 14 seconds, which corresponded to the injection of, approximately, 10 bubbles along an experiment. The images started to be acquired about 10 seconds after turning on the vibro-motors to avoid the recording of start-up effects. Once the bed was started to be recorded by the camera, bubbles commenced to be sequentially injected in the bed.

An accelerometer and two pressure probes situated at $y_{p1} = 0.15$ m and $y_{p2} = 0.25$ m from the distributor were used to measure the instantaneous acceleration and the pressure fluctuations of the bed at an acquisition rate of 2000 Hz. More details about the pressure and acceleration acquisition can be found in Section 2.1.1.

The set of experiments carried out in the present chapter are listed in Table 5.1. Exp. 1 was selected as the nominal experiment. The effects of the vibration frequency and amplitude were investigated by independently increasing or decreasing $A$ or $f$ around the values chosen for Exp. 1, which are $A = 4.2$ mm and $f = 14.2$ Hz. In all the experiments,

**Table 5.1:** Experimental conditions.

| Exp. | Vibration frequency $f$ (Hz) | Vibration amplitude $A$ (mm) |
|---|---|---|
| 1 | 14.2 | 4.2 |
| 2 | 14.2 | 2.8 |
| 3 | 14.2 | 5.6 |
| 4 | 15.6 | 4.1 |
| 5 | 17.1 | 4 |
| 6 | No vibration | |

the static bed height was $H_0 = 0.375$ m ($H_0/W = 1.25$), which was considered large enough to characterize the motion of isolated bubbles along the bed height. It was observed that larger static bed heights (e.g. $H_0/W = 1.5$) increased the particle rain inside the bubbles, which complicated the determination of the bubble contour and the measurement of the solids velocity on top of the injected bubbles.

## 5.3 Theory

### 5.3.1 Potential flow description of the solids velocity around a bubble

The solids velocities obtained from the experiments are compared in this chapter with those resulting from the potential flow model around a bubble proposed by Davidson & Harrison (1963). Figure 5.1 shows a schematic drawing of the solids motion and the pressure distribution around a bubble rising in a conventional fluidized bed.

Davidson & Harrison (1963) used the potential flow theory around a cylinder or a sphere to predict the motion of particles around a bubble in a conventional fluidized bed. The velocity potential, $\Phi$, is governed by the Laplace equation:

$$\nabla^2 \Phi = 0 \tag{5.1}$$

As a first approximation, the bubble in a two-dimensional domain is assumed to be cylindrical with velocities in the horizontal, $x$, and vertical, $y$, directions defined with:

$$u = \frac{\partial \Phi}{\partial x} \tag{5.2}$$

$$v = \frac{\partial \Phi}{\partial y} \tag{5.3}$$

where $x$ and $y$ are the horizontal and vertical coordinates with origin in the center of the circle defining the bubble contour. In Equations (5.2) and (5.3) $u$ and $v$ are the solids velocities in a system of reference attached to the bubble center ($x = 0$, $y = 0$). The velocity potential around a rising bubble in a 2D fluidized bed was defined by Davidson & Harrison (1963) as:

$$\Phi_{xy} = -V_b \left( \frac{R_b^2}{x^2 + y^2} \right) (y \cos(\theta_b) + x \sin(\theta_b)) \tag{5.4}$$

where $R_b$ is the bubble radius, $V_b$ is the bubble velocity and $\theta_b$ is the rising angle of the bubble with respect to the vertical direction.

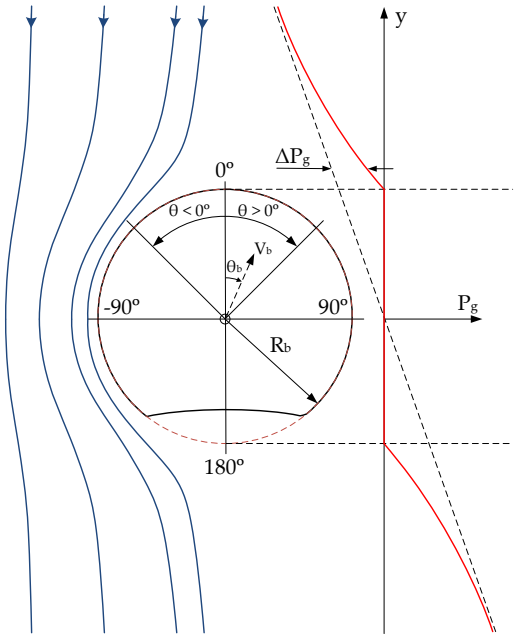


**Figure 5.1:** Schematic drawing of the potential flow theory of Davidson & Harrison (1963) showing the theoretical particle tracks (blue lines, on the left of the bubble) and the theoretical pressure distribution on the axis above the bubble (red lines, on the right of the bubble).

Following Hernández-Jiménez *et al.* (2011*a*), the solids velocity in the horizontal and vertical directions as a function of the distance to the bubble centroid can be calculated in cartesian coordinates using Equations (5.5) and (5.6).

$$u(x, y) = \left( \frac{V_b R_b^2}{x^2 + y^2} \right) \left( \frac{2x(y \cos(\theta_b) + x \sin(\theta_b))}{x^2 + y^2} - \sin(\theta_b) \right) \tag{5.5}$$

$$v(x,y) = \left(\frac{V_b R_b^2}{x^2+y^2}\right)\left(\frac{2y(y\cos(\theta_b)+x\sin(\theta_b))}{x^2+y^2} - \cos(\theta_b)\right) \tag{5.6}$$

If a bubble rises in the bed in the vertical direction (i.e. $\theta_b = 0$), the solids velocity described through Equations (5.5) and (5.6) can be simplified to yield:

$$u(x,y) = 2V_b xy\left(\frac{R_b}{x^2+y^2}\right)^2 \tag{5.7}$$

$$v(x,y) = V_b(y^2-x^2)\left(\frac{R_b}{x^2+y^2}\right)^2 \tag{5.8}$$

### 5.3.2 Pressure distribution around a bubble

The potential flow model described in the previous section can also be used to predict the pressure distribution in the vicinity of a bubble, as deduced in Davidson & Harrison (1963):

$$\frac{\Delta P_g}{\rho_d} = \left\{ \begin{array}{ll} -g\left(y - \dfrac{R_b^2}{y}\right) & \text{if } |y| \geq R_b \\ 0 & \text{if } |y| < R_b \end{array} \right\} \tag{5.9}$$

where $\Delta P_g$ is the gas pressure relative to the weight of the particles, $\rho_d = (1-\varepsilon)\rho_s + \varepsilon\rho_g$ is the density of the bed bulk, $\varepsilon$ is the void fraction of the bed bulk and $\rho_s$ and $\rho_g$ are the density of the particles material and the fluidizing gas, respectively. In the present chapter, the following values are used: $\rho_g = 1.2$ kg/m$^3$, $\rho_s = 2500$ kg/m$^3$ and $\varepsilon = 0.4$.

## 5.4 Results and discussion

The results presented in this chapter are divided into four main sections. In the first section, the signals obtained by the pressure probes connected to the rear wall of the bed are analyzed and compared to the prediction of the gas pressure distribution around an isolated bubble provided by Davidson & Harrison (1963). In the second section, the interaction of the bubbles with the oscillating velocity of the bed bulk in a vertically vibrated fluidized bed is examined. These results serve as a basis to understand the effect of vibration on the solids motion around the bubble, which is also compared with the Davidson & Harrison (1963) classical potential flow model. Lastly, the PIV measurements are additionally used to investigate the behavior of particles in the wake of bubbles rising in the vibrated bed.

### 5.4.1 Pressure signal analysis

A common way of characterizing the dynamics of the bed bulk and the rise of bubbles is the analysis of gas pressure signals. This has been also done for VFBs (Wang *et al.*, 1997, 2000). Figure 5.2 shows an example of the signals obtained from the accelerometer and the pressure sensors connected to experimental the bed, as described in Section 2.1.1. Due to the characteristics of the pressure sensors, the relative pressure $\Delta P = P - P_{ref}$ is measured, where $P_{ref}$ is a reference pressure. In this case, $P_{ref}$ corresponds to the pressure in the bed without any vibration nor gas injection. In the figure, a smoothing spline was applied to the accelerometry signal in order to reduce noise. It can be observed in Figure 5.2 that the pressure signals oscillate with the same frequency as the bed vessel (i.e. the accelerometry signal). The injection of bubbles into the system promotes a sudden increase of the pressure of the bed, which occurs at $t \simeq 5$ s and $t \simeq 6.5$ s in Figure 5.2. The mean value and the amplitude of the pressure signal also changes when the bubble volume passes next to the pressure sensors, as in $t \simeq 5.1 - 5.3$ s for the sensor placed at the vertical distance $y_{p1} = 0.15$ m from the distributor, and $t \simeq 5.4 - 5.7$ s for the sensor at $y_{p2} = 0.25$ m. A similar trend was observed for the rest of bubbles tested in the experiments.

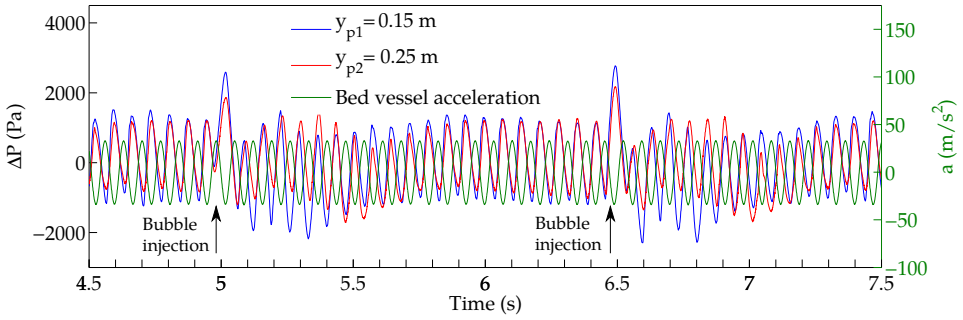


**Figure 5.2:** Example of pressure signals at 0.15 m and 0.25 m from the distributor and filtered accelerometry signal. Exp. 1.

In Figure 5.2 the two pressure signals present a slight temporal delay when no bubble is present in the system, which corroborates the presence of the traveling pressure waves created by vibration found in Chapter 3. To see this effect, Figure 5.3(a) shows a detail of the pressure and accelerometry signals just after the bubble injected at $t \simeq 5$ s has already erupted at the surface of the bed (i.e. there is no bubble in the system). In Figure 5.3(a), the pressure commences to increase when the bed vessel acceleration starts to decrease (i.e. the bed bulk starts to move upwards), which corresponds to the fraction of the cycle

in which the pressure and solids compression waves are generated and travel upwards the bed (see Chapter 3). It can be also observed in Figure 5.3(a) that the pressure signal at $y_{p1} = 0.15$ m is ahead of the signal at $y_{p2} = 0.25$ m for the same fluctuating value of the local pressure.

In addition, the rise of the bubble creates another delay in the pressure signal, as the bubble first passes through the sensor at $y_{p1}$ and then through the sensor at $y_{p2}$. In order to discriminate the pressure fluctuation caused by the vibration of the bed vessel from the one attributed to the bubble passing next to the sensor, a moving average filter is applied to the original pressure signals. This filter averages the values of the pressure signal in an interval $[-T/2, T/2]$, where $T$ is the vibration period, so that the cyclic oscillation of the pressure signal directly caused by vibration is eliminated. Figure 5.3(b) shows the filtered pressure signals. In this case, it can be clearly observed that the injection of the bubble promotes a pressure pulse in the bed. Firstly, the injection of the bubble generates a perturbation on the pressure signal, which is nearly synchronized in both pressure probes (i.e. $t \simeq 5$ s and $t \simeq 6.5$ s in Figure 5.3(b)). The passage of the bubble through the pressure probes can be clearly discriminated in Figure 5.3(b) and is manifested by a nearly linear decrease of the pressure. Once all the bubble volume has passed through the sensor, the pressure augments and returns to its original value.

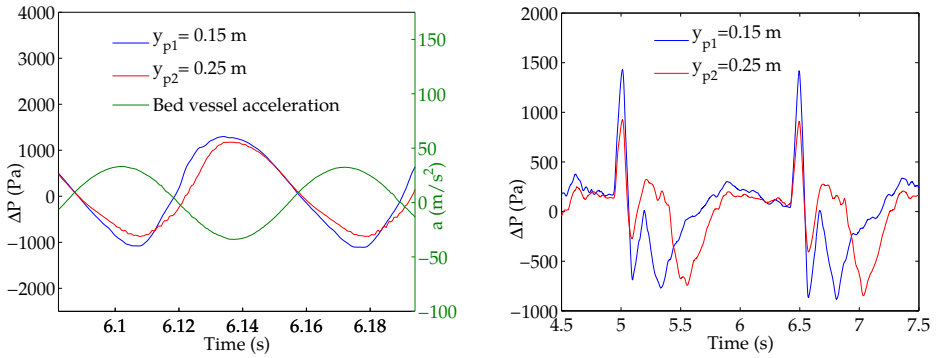


(a) (b)

**Figure 5.3:** (a) Detail of the pressure signals at 0.15 m and 0.25 m from the distributor and the filtered accelerometry signal. (b) Filtered pressure signals. Exp. 1.

Figure 5.4 shows a comparison between the passing of two bubbles through the sensors when the system is vibrating and when no vibration is applied to the bed. The behavior of the pressure signal is similar in both cases. It happened in the experiments that bubbles in the non-vibrated bed tended to be split by particle rain, specially in the upper section of the bed $y_b = 0.2 - 0.3$ m, which also reduced significantly their velocity while rising in

the bed. This explains the smaller decreasing rate of the pressure signals at $y_{p1}$ and $y_{p2}$ during the passage of a bubble, and the larger phase delay between the pressure signals, when the system is not vibrated in Figure 5.4(a).

The validity of Davidson & Harrison (1963) model for VFBs can be accounted for in terms of the pressure distribution close to an isolated bubble. To do so, the spatial distribution of the pressure in the vicinity of an isolated bubble in a fluidized bed, Equation (5.9) (Section 5.3.2), is transformed into a temporal evolution of the pressure at a specified height by substituting $y$ and $R_b$ by the instantaneous position $y_b(t)$ and radius $D_b(t)/2$ of a bubble rising in the bed. Here $y_b(t)$ and $D_b(t)$ were obtained by means of DIA from the images of the bubbles analyzed (see Section 2.3.1). With this transformation, the gas pressure signals obtained at $y_{p1}$ and $y_{p2}$ from the Davidson & Harrison (1963) model for a bubble rising in the vibrated fluidized bed are shown in Figure 5.4(b) superimposed and synchronized to the experimentally measured pressure. As a reference, the figure also includes the instantaneous position of the bubble inside the bed, $y_b(t)$ and the time instants, $t_1$ and $t_2$, at which the bubble centroid is in the same vertical position, $y_{p1}$ and $y_{p2}$, as the pressure sensors. As the pressure sensors measure the relative pressure, $\Delta P$, the pressure signal obtained by means Davidson & Harrison (1963) model of Equation (5.9), is vertically translated in Figure 5.4(b) so that its mean value matches the mean value of the experimental pressure signals. The Davidson & Harrison (1963) model for the pressure distribution around the bubble clearly matches with the experimental results both in the amplitude and the slope of the decrease of the pressure caused by the bubble passage for the two pressure signals analyzed. These results seem to confirm the validity of the pressure distribution of the Davidson & Harrison (1963) model for an isolated bubble rising the vibrated fluidized bed tested. This finding suggests that the pressure waves produced by vibration do not interfere coherently with the perturbation produced by a bubble on the gas. That is, both sources, vibration and bubbles, perturb the gas pressure linearly for the conditions here studied.

### 5.4.2 Bulk behavior

The previous section showed that the gas pressure distribution around an isolated bubble rising in the vibrated fluidized bed tested can be predicted by means of the Davidson & Harrison (1963) model. Thus, it could be of interest to check whether the motion of solids around the bubble can be also estimated using this model. Besides, the vibration of the bed vessel promotes a cyclic compression and expansion of the bed bulk and creates compression and expansion waves that travel through the bed, as seen in previous chapters. The presence of the bubble in the system may change the motion of the surrounding bed bulk and vice versa. Thus, a characterization of the motion of the

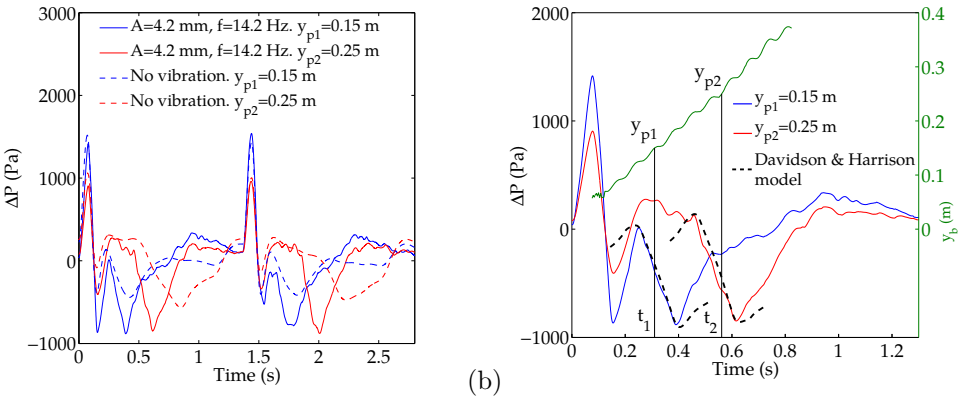


**Figure 5.4:** (a) Example of filtered pressure signals at $y_{p1} = 0.15$ and $y_{p2} = 0.25$ m from the distributor for a bubble rising in the fluidized bed with vibration (Exp. 1) and no vibration (Exp. 6). (b) Pressure signals, bubble position and Davidson & Harrison (1963) model for a bubble rising in the vibrating fluidized bed. Exp. 1.

particles in the bed bulk with bubbles is a necessary step before attempting to study the motion of solids around the bubble.

To analyze the bed bulk motion and the behavior of the solids velocity waves in the bed, Figure 5.5 compares the phase evolution of the absolute vertical velocity of solids along the vertical direction with and without a bubble rising in the bed. This phase evolution was obtained by using the averaging of cycles method on the solids velocity, which was calculated by means of PIV (see Section 2.3.3). The solids velocity has been sampled in two vertical stripes of width of $\Delta x \simeq 0.02$ m (three PIV windows) symmetrically placed at an approximate distance of $x_s = W/8$ from the bed left and right walls. This position of the vertical stripes was chosen so that the volume of the injected bubbles did not cross the vertical stripes. The solids velocity has been also sampled in a vertical fringe of the same width situated in the central section of the bed (i.e. $x_s = W/2$). In Figure 5.5, every curve represents the horizontal average of the solids velocities in the two lateral stripes along the whole bed height. In the figure, the solids velocity was normalized with the bed vessel velocity $V_{bed}$. Results are separated in $M = 16$ consecutive phase intervals of $\Delta\phi = 2\pi/M$. As in Chapter 3, the standard deviation of the velocity with regard to the mean values represented in Figure 5.5 has been checked. Thus, for $\Delta\phi = \pi/8$ rad and every height interval, the resulting standard deviation of $V/V_{bed}$ is in the range of 0.06-0.15 in Figure 5.5(a), 0.05-0.18 in Figure 5.5(b) and 0.06-0.17 in Figure 5.5(c). This indicates that the uncertainty of the PIV profiles in Figure 5.5 is relatively low.

In Figure 5.5(a) no bubbles are present in the system and hence the bed bulk cyclically

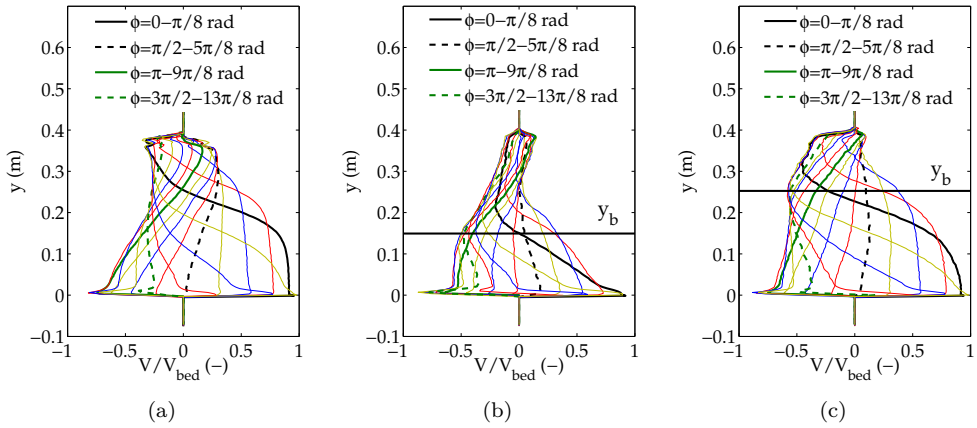


**Figure 5.5:** Vertical evolution of the normalized absolute vertical velocity of the solids in the bed for different phase intervals: (a) No bubble present in the system, (b) bubble in the height interval $y_b = 0.1 - 0.2$ m, and (c) bubble in the height interval $y_b = 0.2 - 0.3$ m. The red, blue and yellow lines represent intermediate phase intervals of $\Delta\phi = \pi/8$ rad placed between the phase intervals defined in the legend of the figures. The horizontal black line indicates the average position of the bubble in each figure. Exp. 1.

expands and compresses without being perturbed by bubbles. For $\phi = 3\pi/2$ rad, the bed vessel commences to move upwards and impacts the bed bulk, which creates a compression wave of solids that travels upwards in the bed bulk. As in Chapter 3, the compression wave front divides the bed into two regions with different relative velocities: upward velocity below the wave front and downward velocity above the wave front. Similarly, when the bed vessel starts to move downwards at $\phi = \pi/2$ rad, an expansion wave traveling upwards the bed appears. The expansion wave front also separates the bed in two regions of solids velocity moving downwards below the wave front and upwards above the wave front. In general, the front of the expansion wave is less pronounced and produces a softer change in the velocity of solid than the front of the compression wave.

Figure 5.5(b,c), shows the average solids velocity in the vertical stripes when a bubble is situated at $y_b = 0.1 - 0.2$ m (Figure 5.5(b)) and $y_b = 0.2 - 0.3$ m (Figure 5.5(c)) from the distributor. Note that these figures are the result of the averaging of cycles of the isolated bubbles sequentially injected in the experiment. The injection of bubbles was produced at random phases in the vibration cycle. In Figure 5.5(b,c), the motion of the solids belonging to the bed bulk is modified when a bubble is present in the system. During the compression stage of the bed bulk, the opposite velocities of the bed bulk regions (i.e. positive velocity of solids in the lower section of the bed and negative in the upper section of the bed) also appear. However, contrary to the case without bubble in

Figure 5.5(a), the maximum negative velocity of particles during the expansion stage of the bed bulk (i.e. $\phi = \pi - 2\pi$ rad) takes place at the average bubble height ($y \simeq 0.15$ m in Figure 5.5(b) and $y \simeq 0.25$ m in Figure 5.5(c)). This can be explained as follows. The presence of the bubble reduces the section volume through which the bulk of particles descends at the lateral sides of the bubble. This may promote a larger downward velocity of particles at the vicinity of the bubble and the reduction of the upwards solids velocity in the region above the bubble. Both effects lead to the commented minimum velocity of particles.

The position and velocity of the compression and expansion wave fronts were calculated using the vertical coordinate, in the vertical stripe, at the point at which the absolute vertical velocity of the particles is equal to a threshold value. As in Chapter 3, this threshold is taken equal to half the maximum absolute value of the vertical velocity of solids in the vertical stripe. As the bed bulk impacts the bed vessel in a phase $\phi \simeq 3\pi/2$ rad, the compression wave position is calculated in an interval starting at $\phi = 3\pi/2$ rad and ending at $\phi = 7\pi/2$ rad (i.e. $\phi = \pi/2$ rad of the next cycle), which corresponds to the ascending stroke of the bed vessel. Equivalently, the expansion wave position is calculated in a phase interval $\phi = \pi/2 - 3\pi/2$ rad.

Figure 5.6(a) shows the position of the compression and expansion wave fronts as a function of the vibration phase and for the lateral ($x_s = W/8$) and central ($x_s = W/2$) vertical stripes. The position of the compression and expansion wave fronts close to the lateral walls of the bed is higher than that in the central stripe for the same phase. This is due to the presence of the lateral walls, as in Chapter 3. This makes that the particles close to the corners of the bed impact the base of the bed earlier than the particles on the distributor center and they can easily follow the upward motion of the distributor, which slightly increases the velocity of propagation of the wave front. This same phenomena is observed for the expansion wave in Figure 5.6(a).

In Figure 5.6(b), the position of the fronts of compression and expansion waves is modified when a bubble is present in the bed. Here, the wave fronts were calculated at $x_s = W/8$ whereas the bubble centroid is at $x_s = W/2$.

The propagation velocity of both the compression and expansion wave fronts can be calculated as in Section 3.4.1:

$$V_{prop} = 2\pi f \frac{\Delta y_f}{\Delta \phi} \tag{5.10}$$

where $y_f$ is the vertical position of the wave front shown in Figure 5.6 and $\Delta\phi$ is the phase variation between two consecutive positions of the wave fronts.

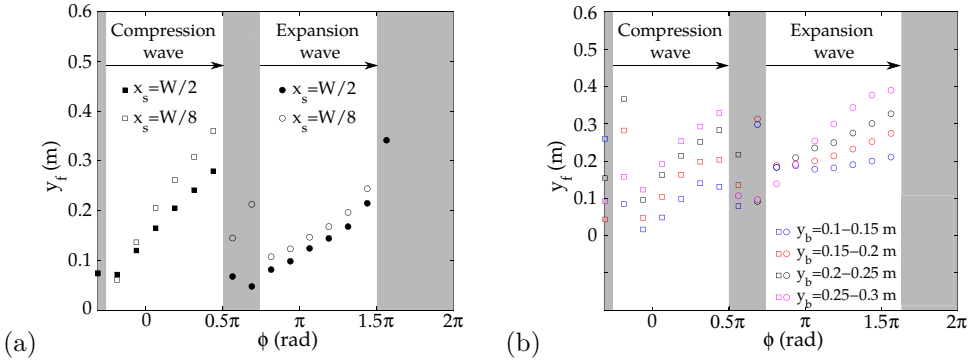


**Figure 5.6:** Vertical positions of the compression and expansion wave fronts as a function of the vibration phase. (a) No bubble in the bed and (b) Bubble rising within different height intervals. Exp. 1.

In addition, Table 5.2 contains the results obtained for the mean velocity of the compression ($V_{prop,c}$) and expansion ($V_{prop,e}$) wave fronts for the conditions shown in Figure 5.6. When a bubble is located close to the distributor, $y_b = 0.1 - 0.15$ m, both the compression and the expansion wave fronts are closer to the distributor than when the bubble is higher (e.g. $y_b = 0.25 - 0.3$ m) for the same vibration phase. This suggests that the bed bulk impacts the distributor progressively earlier in phase as the bubble rises in the bed. Note that the wave front velocity at $x_s = W/2$ with bubbles cannot be calculated because the presence of the bubble perturbs the solids velocity along the vertical stripe. When the compression wave is originated, it travels upwards in the bed at a similar velocity regardless of the bubble vertical position in the bed. Due to the low number of phase intervals used to characterize the wave front position, no significant changes in the velocity of the wave front are observed in Figure 5.6. When no bubble is present in the system, the velocity of the compression wave is greater in the lateral section of the bed, $x_s = W/8$, than at the sides of the bed, $x_s = W/2$. Furthermore, values of $V_{prop,c}$ remain practically unchanged when a bubble is present in the system regardless the vertical position of the bubble in the bed. However, as seen in Figure 5.5 and Table 5.2 the behavior of the expansion wave is largely affected by the presence of the bubble. Also, the velocity of the expansion wave progressively increases when the bubble is present in a higher vertical coordinate in the bed.

**Table 5.2:** Mean velocity of propagation of the compression and expansion wave fronts.

| $y_b$ (m) | $x_s$ (m) | $V_{prop,c}$ (m/s) | $V_{prop,e}$ (m/s) |
|---|---|---|---|
| No bubble | $W/2$ | 9.45 | 6.32 |
| No bubble | $W/8$ | 14.03 | 6.22 |
| 0.1-0.15 | $W/8$ | 9.37 | 1.04 |
| 0.15-0.2 | $W/8$ | 11.38 | 3.54 |
| 0.2-0.25 | $W/8$ | 10.61 | 5.43 |
| 0.25-0.3 | $W/8$ | 11.65 | 9.51 |

### 5.4.3 Isolated bubble behavior

It was evidenced in the previous sections that the presence of the bubble in the system changes the motion of solids in regions far from the bubble and the behavior of the compression and expansion waves of solids traveling through the bed bulk. Thus, the motion of solids just around the bubble is presumably affected by these compression and expansion waves. The present section analyzes the motion of solids around the bubble.

Figure 5.7 shows an example of four consecutive snapshots of a bubble rising in the vibrated fluidized bed. The snapshots belong to different instants within the same oscillation period of the bed vessel oscillation, as indicated in the top part of the figure. Figure 5.7(b) shows the instantaneous vectors of the absolute solids velocity superimposed to each of the snapshots. Note that the absolute system of coordinates $(x, y)$ in Figure 5.7(a) is referred to the bottom left corner of the bed ans has been changed in Figure 5.7(b) to a new system of coordinates $(X, Y)$ when computing the solids velocity vectors, so that the bubble is centered at the origin of the new system, as indicated in Section 2.3.3.

It can be observed in Figure 5.7(b) that, regardless of the vibration phase of the bed vessel, there is a region around the bubble in which the solids motion is strongly influenced by the presence of the bubble. The solids present an upward absolute velocity on top of the bubble, as the bed particles are pushed upwards due to the bubble ascending motion. The solids move around the bubble following the bubble contour, as in an isolated bubble rising in a conventional fluidized bed without vibration (Davidson & Harrison, 1963; Müller *et al.*, 2007; Hernández-Jiménez *et al.*, 2011*b*). Also, in the figure, between $\phi = 0.7\pi$ rad and $\phi = 1.4\pi$ rad ($\phi = 2.22 - 4.35$ rad), the contour of the bubble close to its wake is deformed because part of the wake penetrates into the bubble changing the shape of the bubble. This wavy shaped contour is characteristic of vibrated fluidized beds (see, for example, Figure 4.2) and its behavior will be analyzed in a subsequent subsection.

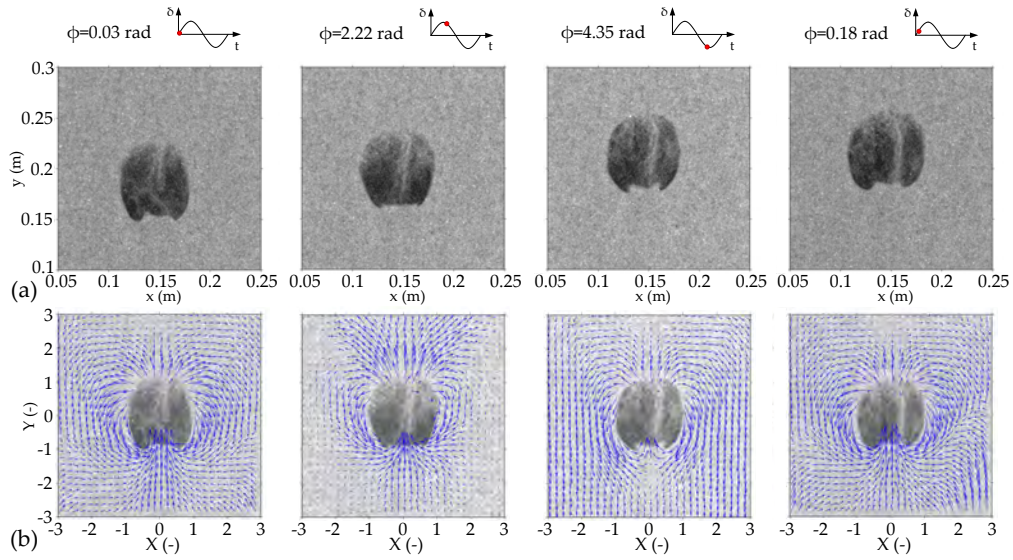


**Figure 5.7:** Grayscale digital images of an isolated bubble rising in the vibrated fluidized bed and captured at different vibration phases. (a) Original images in an absolute system of coordinates. (b) Instantaneous absolute solids velocity superimposed to the captured images in the normalized coordinate system $(X, Y)$. Exp. 1.

Figure 5.8 represents the streamlines and the module of the normalized absolute solids velocity around the average contour of bubbles rising in the vibrated fluidized bed and situated within the vertical interval $y = 0.1 - 0.3$ m. To characterize the solids motion as a function of the oscillatory displacement of the bed vessel, the solids velocities are averaged within phase intervals of size $\Delta\phi = 0.25\pi$ rad, as explained in Section 2.3.3. As can be seen in Figure 5.8, the solids motion close to the bubble contour and in the surroundings of the bubble varies significantly with the vibration phase.

In the phase interval $\phi = 0 - 0.25\pi$ rad of Figure 5.8(a), there exists a high ascending velocity of particles below the bubble contour, which is caused by the front of the compression wave of solids that is generated at the bottom of the bed. However, the presence of the bubble in the system perturbs this ascending motion of solids, as they are dragged upwards by the bubble wake. This behavior is also observed in the phase interval $\phi = 0.25\pi - 0.5\pi$ rad (Figure 5.8(c)). Nonetheless, when the bed vessel commences to descend in the phase interval $\phi = 0.5\pi - 0.75\pi$ rad (Figure 5.8(c)) the velocity of the solids below the bubble decreases significantly, as solids begin to move downwards following the bed vessel oscillatory motion. The expansion of the bed bulk commences in this phase interval, as manifested in Section 5.4.2, and a region of low solids velocity appears in the vicinity of the bubble. However, the region of particles that are in direct contact with the bubble contour are strongly affected by the presence of the bubble and

move around it following its contour. This happens regardless the vibration phase and the behavior of the bed bulk around the bubble. During the subsequent phase intervals (i.e. $\phi = 0.75\pi - 1.5\pi$ rad in Figure 5.8(d-f)) the solids present a descending absolute velocity produced by the descending motion of the bed bulk, which causes the formation of a solids expansion wave front that travels upwards in the bed. This promotes a descending flow of solids in the whole bed except in the regions directly affected by the presence of the bubble. The bed bulk impacts again the distributor in a phase close to $\phi = 1.5\pi$ rad and the behavior described in the above lines is cyclically repeated.

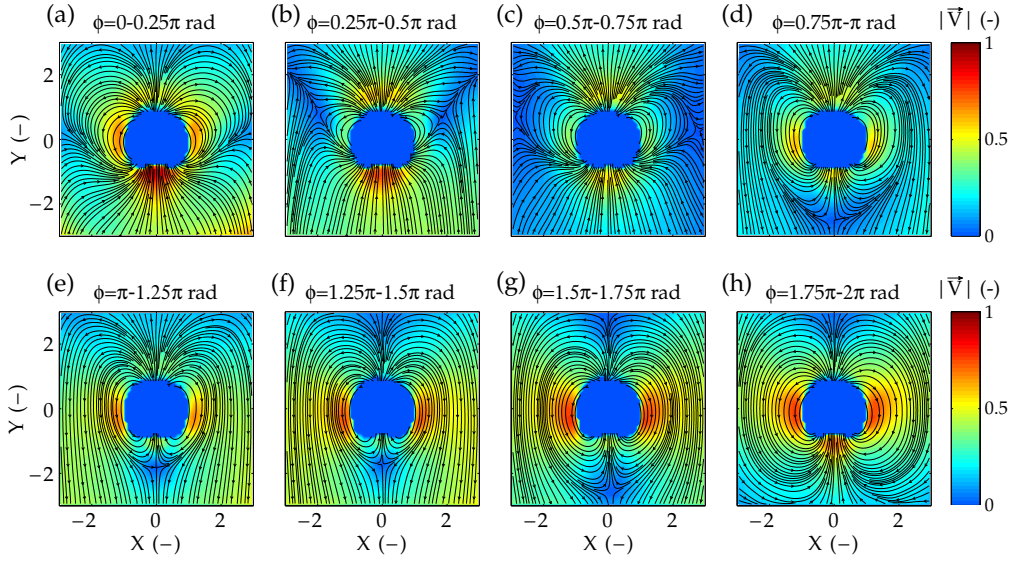


**Figure 5.8:** Streamlines of the normalized absolute solids velocity around the equivalent bubble contour resulting from the bubble averaging method in the vertically vibrated fluidized bed. Results are presented for eight different phase intervals of size $\Delta\phi = 0.25\pi$ rad over a total interval of $\phi = 0 - 2\pi$ rad. The solid streamlines are shown superimposed to the velocity magnitude maps. Exp. 1.

To obtain the solids motion relative to the bubble displacement in the bed, Figure 5.9 illustrates the solid streamlines and velocity magnitude around an isolated bubble in a system of coordinates that moves at the same vertical velocity as the bubble front, which is defined as the vertical velocity of the solids at the fitting circle $(X, Y)_n^{(F)}$ (see Section 2.3.3) and within an angle $\theta \in [-10°, 10°]$. Here $\theta$ is the angle between a given point and the vertical line passing through the bubble center. Thus, for each absolute normalized solids vertical velocity value $V(X, Y)$, in Figure 5.8, a new normalized velocity of solids is computed following (5.11):

$$\vec{V}_r(X,Y) = \vec{V}(X,Y) - \int_{\theta_i=-10°}^{\theta_f=10°} \frac{\vec{V}(R(\theta)_n)d\theta}{\theta_f - \theta_i} \tag{5.11}$$

For all the phase intervals shown in Figure 5.9, the motion of solids around the average bubble resembles that of a potential flow around a bubble in a conventional fluidized bed (Equations (5.2) and (5.3), Davidson & Harrison (1963)). Nevertheless, the solids behavior around the bubble is partially modified by the cyclic expansion and compression of the bed bulk. This is specially noticeable in the region below the bubble, in which the bubble is affected by the interaction of the bubble wake with both the compression and the expansion wave fronts of solids traveling in the bed. A more detailed description of the bubble wake behavior is carried out in Section 5.4.4.

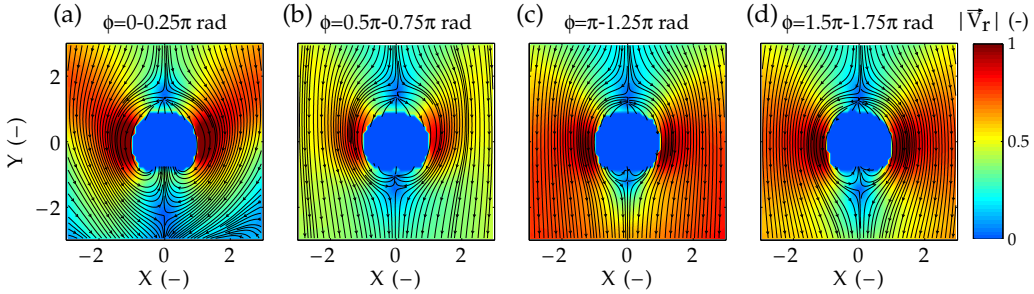


**Figure 5.9:** Streamlines of the normalized relative solids velocity around the equivalent bubble contour resulting from the bubble averaging method in the vertically vibrated fluidized bed. Results are presented for four different phase intervals of size $\Delta\phi = 0.25\pi$ rad over a total interval of $\phi = 0 - 2\pi$ rad. The solid streamlines are shown superimposed to the velocity magnitude maps. Exp. 1.

It was observed in the previous paragraph that the motion of particles around an isolated bubble, even if the system is vibrated, looks alike that of the potential flow model (Davidson & Harrison, 1963). In order to quantitatively characterize the velocity of particles around the bubble as a function of the vibration phase of the bed, a direct comparison between the solids velocity and the potential flow model is carried out in Figure 5.10. For each of the phase intervals in which the cyclic behavior is discretized, Figure 5.10 shows the relative horizontal velocity ($U_r(X,Y)$) and the relative vertical velocity ($V_r(X,Y)$), as defined in Equation (5.11) in the fitting circle $(X,Y)_n^{(F)}$. The experimental results are compared with the potential flow model described in Section 5.3.1 for $(x/R_b, y/R_b)$ at a radius, $R^*$, equal to the radius of the fitting circle $(X,Y)_n^{(F)}$, as detailed in Section 2.3.3. Note that different values of $R^*$ (e.g. ranging between 1.4 and 1.6) among the different vibration phase intervals in which the solids are averaged may promote changes in the velocity of solids predicted by the potential flow theory. Here, $\theta_b \simeq 0$ and Equations (5.7) and (5.8) are used because the horizontal component of the bubble velocity of each individual bubble is very reduced compared to the vertical component. Also, the averaging of different bubbles compensates the inaccuracies arising from considering $\theta_b = 0$.

In Figure 5.10, the potential flow model provides a very good prediction in terms of the behavior of the solids velocity as a function of the angle, $\theta$, of their position. Specifically, in the phase interval $\phi = 0.25\pi - 1.5\pi$ rad, the magnitude of the horizontal solids velocity in the experiments is smaller than in the rest of phase intervals. In this phase interval, the particles around the bubble are dragged downwards affected by the downwards bed bulk motion in the proximity of the bubble, as evidenced in Figures 5.8 and 5.9, which reduces the horizontal component of the solids velocity around the bubble.

Besides, a reduction of the magnitude of the vertical velocity of solids is found at $\theta = \pm 90°$ in the phase interval $\phi = 0.25\pi - 0.5\pi$ rad. This behavior was also observed in Figures 5.8 and 5.9 and is attributed to the decrease of the solids velocity in the regions close to the bubble. In that phase interval, the bed bulk compression is maximum, which reduces both the solids and the bubble velocity. The reduction of the solids velocity in the regions close to the bubble could be also observed in Figure 5.8(b,c) for the absolute velocity of solids. Additionally, the largest velocity of the particles in the wake region of the bubble ($\theta \simeq \pm 180°$), when they are affected by the compression wave front of particles caused by bed vessel ascending stroke, is manifested in Figure 5.10 in a phase range $\phi = 1.75\pi - 0.25\pi$ rad at an angle of $\theta \pm 180°$.

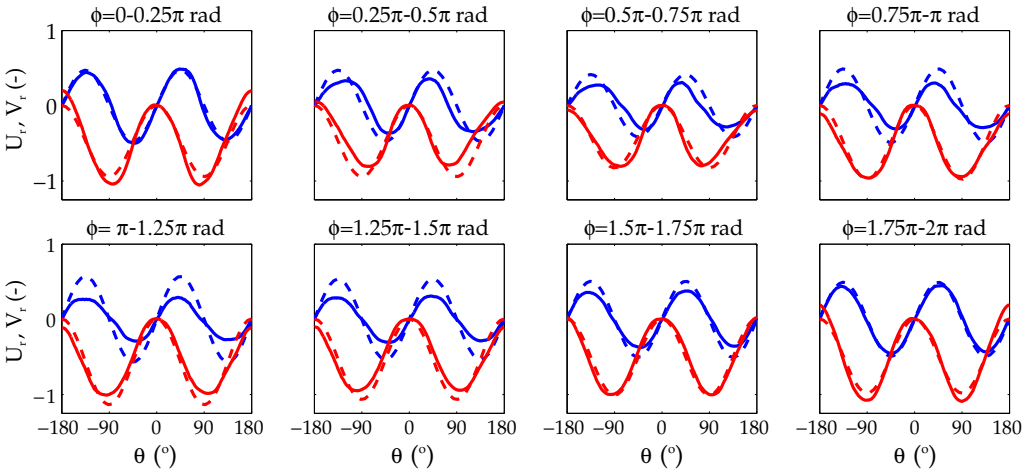


**Figure 5.10:** Normalized relative solids velocity at the fitting circle of the bubble contour for eight different phase intervals of size $\Delta\phi = 0.25\pi$ rad over a total interval $\phi = 0 - 2\pi$ rad. The blue, red and dashed lines correspond, respectively, to the horizontal and vertical solids velocity and to the potential flow theory. Exp. 1.

The results shown in Figures 5.8 to 5.10 correspond to bubbles whose centroids were situated at a height interval of $y_b = 0.1 - 0.3$ m from the distributor. However, as stated in Chapter 4, the behavior of bubbles changes as they rise in a vibrated bed. Thus, the solids velocity may also vary as a function of the bubble position in the bed. To quantify

the dependence of the solids behavior around the bubble with the vertical position of the bubble, Figure 5.11 shows the standard deviations, $\sigma_U$, and $\sigma_V$, of the normalized horizontal and vertical solids velocity at the fitting circle $(X,Y)_n^{(F)}$ (i.e. the standard deviation with $\theta$ of the curves shown in Figure 5.10). $\sigma_U$ and $\sigma_V$ are calculated for two different vertical intervals $y_b = 0.1 - 0.2$ m and $y_b = 0.2 - 0.3$ m, which will be referred hereafter as the upper and lower sections of the bed, respectively. Analysis of the results, not included here for brevity, showed that the curves in Figure 5.10 preserved a sinusoidal shape regardless the averaging is done for bubbles that are in the upper or in the lower section of the bed. Hence, the standard deviation of the curves in Figure 5.10 is considered a valid method to measure and compare the magnitude of the oscillation of solids velocities around the bubble.

The results are compared in Figure 5.11 with the standard deviation of the solids velocity at $(X,Y)_n^{(F)}$, for $y_b = 0.1 - 0.3$ m, obtained by means of the Davidson & Harrison (1963) model. In addition, the relative discrepancy between the experimental results and the values predicted by the Davidson & Harrison (1963) model are included in Table 5.3. The relative discrepancy is calculated as:

$$Dr_{\sigma_{U,V}} = \frac{|\sigma_{U,V,exp} - \sigma_{U,V,Davidson}|}{\sigma_{U,V,Davidson}} \tag{5.12}$$

where $\sigma_{U,V,exp}$ and $\sigma_{U,V,Davidson}$ are, respectively, the standard deviation of the experimental results and that of the results of the Davidson & Harrison's potential model shown in Figure 5.11.

It can be noted in Figure 5.11(a) that the magnitude of the normalized horizontal solids velocity (proportional to $\sigma_U$) is weakly affected by the vertical position of the bubble in the bed. The more remarkable differences are observed in a phase interval $\phi = 1.5\pi - 2\pi$ rad, where the propagation of the compression wave in the bed has a larger effect on the vertical velocity of bubbles situated in the lower section of the bed. It is expected that the kinetic energy of the compression wave generated at the bottom of the bed is dissipated while it travels upwards the bed, which may explain, in Figure 5.11(a), the smaller values of the normalized horizontal solids velocity as the bubble rises in the bed. As depicted in Figure 5.10, for all the phase intervals shown in Figure 5.11, $\sigma_U$ in the experiments presents a standard deviation smaller than in the Davidson & Harrison (1963) model. Large differences are observed between the experimental results and the Davidson & Harrison (1963) model in the phase interval $\phi = 0.25\pi - 1.75\pi$ rad both in Figure 5.11 and in Table 5.3, which may reflect the significant effect of the bed bulk cyclic oscillation on the normalized horizontal solids velocity around the bubble.

The normalized vertical solids velocity varies more noticeably with the vertical posi-

tion of the bubble in the bed in Figure 5.11(b). Here, the standard deviation (i.e. the magnitude) of the normalized vertical solids velocity is maximum in a phase interval $\phi = 1.5\pi - 0.25\pi$ rad (of the next cycle), as the bubble is strongly affected by the compression wave front generated at the bottom of the bed, as shown in Figure 5.8. The normalized vertical velocity of solids decreases in the later phases due to the deceleration of the bed vessel and increases again in Figure 5.11(b) in an interval $\phi = 0.6\pi - 1.3\pi$ rad owing to the expansion of the bed bulk, which increases the vertical velocity of the solids as they move around the bubble, as in Figure 5.8. The values obtained for $\sigma_V$ for bubbles situated at $y_b = 0.1 - 0.3$ m are slightly underestimated in the phase interval $\phi = 0.3\pi - 1.6\pi$ rad by the Davidson & Harrison (1963) model. Differences smaller than 20% are typically found between the experimental results and the Davidson & Harrison (1963) model, as shown in Table 5.3, whereas larger differences appear in the horizontal velocity. These differences in $U$ probably resort from the interaction of the bed bulk cyclic oscillation with the solids velocity around the bubble. As also evidenced in Figure 5.10, for the first and last phase intervals in Figure 5.11(b), the experimental $\sigma_V$ is around a 15% above the Davidson & Harrison (1963) model results. Besides, the magnitude of the normalized solids velocity is larger in the lower section of the bed. This may occur because the bed bulk and the bubble motion are affected by the compression and expansion solids waves, which are progressively damped as they travel upwards the bed, as seen in Chapter 3 and in Section 5.4.2 of the present chapter.

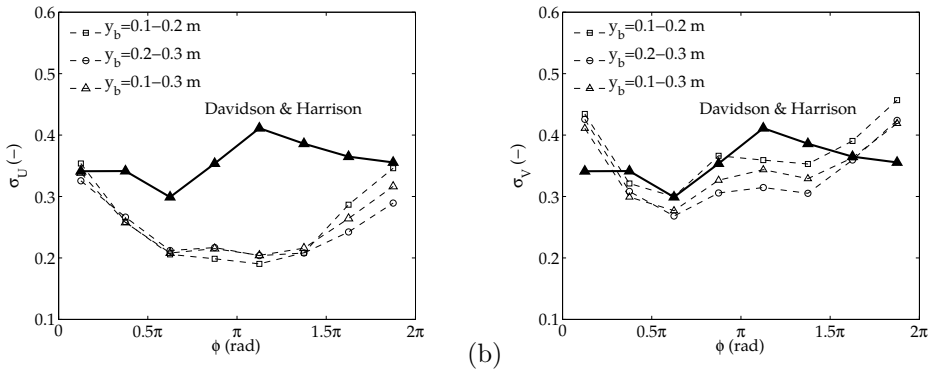


**Figure 5.11:** Standard deviation of the normalized solids velocity at the fitting circle for eight different phase intervals of size $\Delta\phi = 0.25\pi$ rad and for bubbles situated in the upper and lower sections of the bed: (a) horizontal component and (b) vertical component of the solids velocity. The solid line indicates the standard deviation predicted by Davidson & Harrison (1963) for bubbles situated at $y_b = 0.1 - 0.3$ m. Exp. 1.

Despite the cyclic variation of the amplitude of the solids motion that can be observed

**Table 5.3:** Relative discrepancy of the standard deviation of the normalized solids velocity found between the experimental results and the Davidson & Harrison (1963) model. Exp. 1, $y_b = 0.1 - 0.3$ m.

| $\phi$ (rad) | $Dr_{\sigma_U}$ (-) | $Dr_{\sigma_V}$ (-) |
|---|---|---|
| $0 - 0.25\pi$ | 0.01 | 0.2 |
| $0.25\pi - 0.5\pi$ | 0.25 | 0.12 |
| $0.5\pi - 0.75\pi$ | 0.3 | 0.08 |
| $0.75\pi - \pi$ | 0.4 | 0.08 |
| $\pi - 1.25\pi$ | 0.5 | 0.16 |
| $1.25\pi - 1.5\pi$ | 0.44 | 0.15 |
| $1.5\pi - 1.75\pi$ | 0.28 | 0.01 |
| $1.75\pi - 2\pi$ | 0.11 | 0.18 |

in the vicinity of the bubble, Figure 5.10, all the results shown above confirm the qualitative validity of the Davidson & Harrison (1963) model for the solids velocity around an isolated bubble rising in a vertically vibrated fluidized bed.

### Effect of the vibration amplitude and frequency

Qualitatively similar results to the ones shown in Figures 5.8, 5.9 and 5.10 were obtained for all the frequencies and amplitudes of vibration tested in the experiments (Table 5.1). However, quantitative differences regarding the magnitude of the particles velocity around an isolated bubble were found. Figure 5.12 provides a picture of these differences through the calculation of the standard deviation of the vertical and horizontal velocities along the fitting circle $(X, Y)_n^{(F)}$ for the different vibration conditions. Note that the results shown in Figure 5.12 are calculated at $R^*$, which may vary from one experiment to another and can affect the trend of the data in the figure.

The decrease of the amplitude of the normalized horizontal solids velocity in the phase interval $\phi = 0.25\pi - 1.5\pi$ rad observed in Figures 5.10 and 5.11 is manifested for all the vibration conditions tested, as shown in Figure 5.12. In Figure 5.12(a), the magnitude of the normalized solids horizontal velocity decreases dramatically when reducing the vibration amplitude from $A = 4.2$ mm to $A = 2.8$ mm. This decrease of the standard deviation of the normalized solids velocity is also manifested in the vertical velocity of particles (Figure 5.12(c)). As a reference, Figure 5.12 also includes $\sigma_U$ and $\sigma_V$ at $(X, Y)_n^{(F)}$ when the bed is not vibrated and for a height interval of $y = 0.1 - 0.2$ m to avoid capturing bubbles affected by splitting or particle rain. For the case of low vibration amplitudes ($A = 2.8$ mm), the results in the phase interval $\phi = 0.6\pi - 1.4\pi$ rad are closer to those obtained when no vibration is added to the system. This suggests that, in that phase interval and for low vibration amplitudes, the normalized horizontal velocity of solids around the bubble is not strongly affected by vibration.

A decrease of $\sigma_U$ and $\sigma_V$ is also observed when increasing the vibration frequency in Figures 5.12(b,d). Vibration at low $A$ and/or high $f$ may promote the homogenization of the particles velocity in the bed, which might reduce the effect of the bubble on the motion of solids around it. However, care should be taken when interpreting Figure 5.12(b,d). During the processing of the results it was found that the vibration frequency also increases $R^*$, and that contributes to the reduction of $\sigma_U$ and $\sigma_V$.

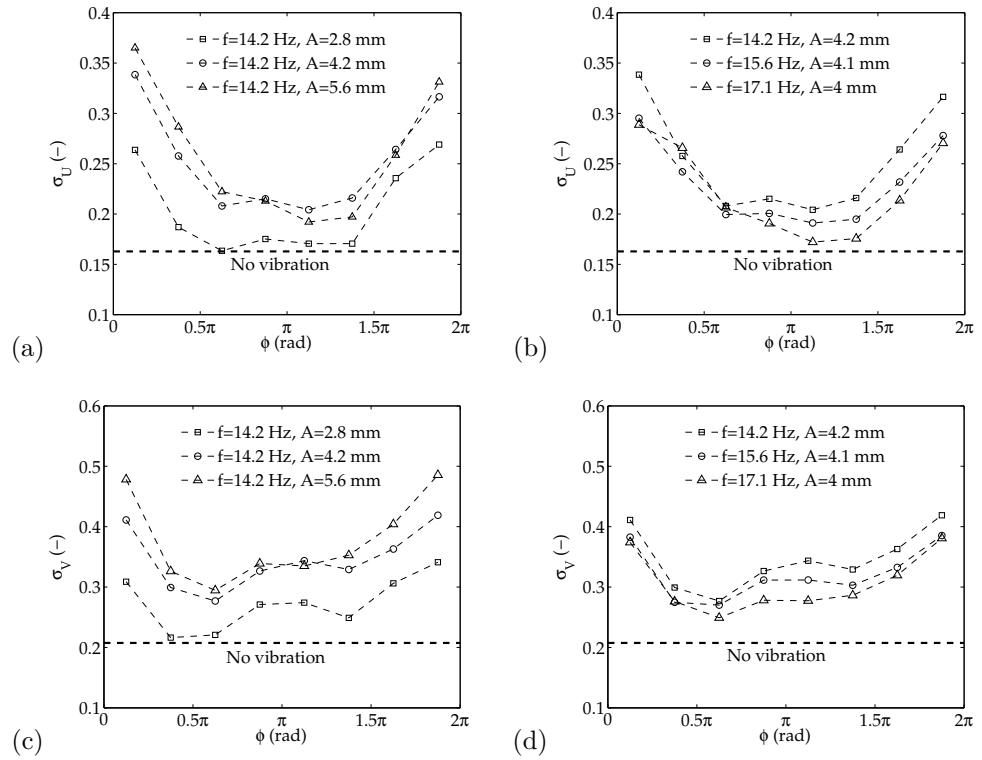


**Figure 5.12:** Standard deviation of the (a,b) horizontal and (c,d) vertical normalized solids velocity at the fitting circle for eight different phase intervals of size $\Delta\phi = 0.25\pi$ rad and for bubbles situated in the upper and lower sections of the bed. (a,c) Variation of the vibration amplitude (Exp. 1, 2 and 3) (b,d) Variation of the vibration frequency (Exp. 1, 4 and 5).

### 5.4.4 Wake behavior

From a practical point of view, it is of interest to analyze the ability of the bubble wake to drag particles upwards in a vibrated fluidized bed as a function of the vibration phase and the bed vessel vibration amplitude and frequency. This dragging ability may have an impact on the rate of solids mixing in vibrated fluidized bed reactors.

Figure 5.13 shows five consecutive snapshots of a bubble rising in the studied vibrated

fluidized bed at a bed height $y_b \simeq 0.2$ m. The figure allows to analyze the interaction of solids with the bubble. For the bubbles and the conditions of the present chapter, it was observed that the wake generally penetrates the bubble during the descending stroke of the bed vessel ($\phi = 0.5\pi - 1.5\pi$ rad).

The bed vessel commences to descend in Figure 5.13(a). Below the bubble, the particles move upwards because the bed bulk maintains the inertial motion of the upwards displacement of the bed vessel, as shown in Figure 5.5. The presence of the bubble perturbs this upward motion of particles, causing the regions of low solids velocities observed in Figure 5.13(a,e).

In the snapshots shown in Figure 5.13(b,c) the bed vessel descends and the bed bulk expands according to Figure 5.5. In this phase range, the bubble velocity decreases and, also, a negative velocity of the solids of the bed bulk to the right and left sides of the bubble appears due to the expansion of the bed bulk. However, the particles belonging to the bubble wake are not affected by this downward solids velocity and maintain their inertial upward displacement. This causes the penetration of the bubble wake in the interior of the bubble contour, producing the characteristic wavy contour of bubbles in a vibrated fluidized bed, which was also observed in Chapter 4. Also, below the bubble, in Figure 5.13(b,c), the volume of solids that is dragged by the bubble wake has positive vertical velocity and can be discriminated from the solids moving downwards outside the wake of the bubble. This leads to the appearance of an inflexion point (i.e. null solids velocity) and a region of low solids velocities below the bubble.

As indicated in Section 5.4.3, the bed vessel impacts the bed bulk in a phase close to $\phi = 1.5\pi$ rad. This promotes an upward velocity of particles below the bubble, as reflected in Figure 5.13(d). Also in Figure 5.13(d), the volume of particles that penetrate the bubble decreases (see Figure 5.8(a)) due to the increase of the bubble velocity and the collapse of the waves formed in the bubble wake in the previous phases of the cycle.

Quantitatively, the wake behavior described in the previous lines can be analyzed by means of the volume of particles dragged upwards in the bubble wake. The volume of particles dragged by the bubble was analyzed as a function of the vibration phase for the different vibration conditions tested. This volume is arbitrarily calculated in Equation (5.13) as the volume of the dense phase under the bubble where the solids velocity is larger than the velocity of the bubble front. The volume belonging to the bubble wake can be graphically seen in Figure 5.9 as the volume of particles below the bubble center (i.e. $Y < 0$) with upwards relative solids velocity.

In order to increase the resolution of the results, a subgrid interpolation of the normalized solid velocity vectors, $\vec{V}_r$, was carried out. Thus, the number of windows in which the velocity vectors are averaged (see Section 2.3.3) is increased to $N_w = 3N_{bins}$. It was observed that further increasing the number of analysis windows did not yield an appre-

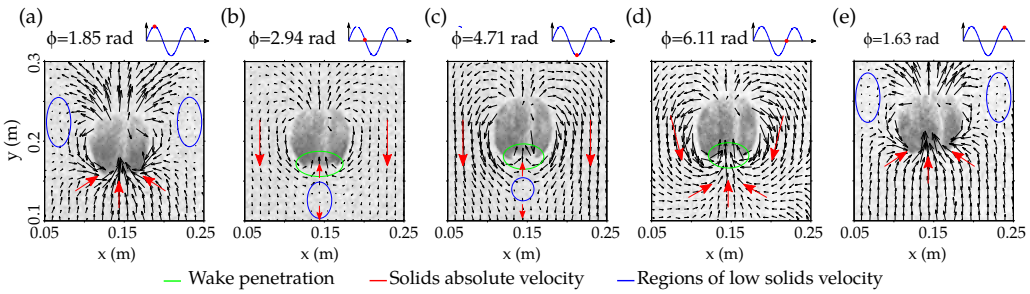


**Figure 5.13:** Snapshots of a bubble rising in the vibrated fluidized bed and schematic behavior of the solids absolute velocities and the wake penetration phenomena. The velocity vectors and the system of coordinates are not normalized. The red arrows indicate the solids absolute velocity and the green and red circles mark, respectively, the wake penetration into the bubble contour and the regions of low solids velocity module. Exp. 1.

ciable change on the obtained results. Then, neglecting velocity gradients perpendicular to the PIV plane, the wake volume is defined as:

$$VOL_w = \sum_{n=1}^{N_w} X_w Y_w K \gamma_n \tag{5.13}$$

with

$$\gamma_n = \begin{cases} 1 & \text{if } V_n \geq 0 \text{ and } Y_n < 0 \\ 0 & \text{otherwise} \end{cases} \tag{5.14}$$

where $K$ is the bed thickness and $X_w$ and $Y_w$ are, respectively, the horizontal and vertical dimensions of the $N_w$ analysis windows. To obtain results independent of the bubble diameter, the wake volume was normalized dividing it by the volume of the average bubble in each phase interval of analysis:

$$\overline{VOL}_w = \frac{VOL_w}{A_{b,avg} K} \tag{5.15}$$

where $A_{b,avg}$ is the visible area of the normalized average bubble.

Figure 5.14 shows maps of the vertical normalized relative velocity magnitude, $V_r$, together with the volume of particles dragged by the bubble wake for four different phase intervals of size $\Delta\phi = 0.25\pi$ rad. From Figure 5.14 it is clear that the volume of particles dragged by the wake is directly affected by the oscillatory motion of the bed bulk. The compression wave front directly affects the volume of the wake, as it collaborates with the bubble dragging ability, making the bubble to more easily drag the particles below it. This can be observed in the phase interval $\phi = 0 - 0.25\pi$ rad in Figure 5.14. Equivalently,

the larger downward velocity of solids in the vicinity of the bubble in the phase interval $\phi = 0.5\pi - 1.25\pi$ rad decreases the wake volume, as shown in Figure 5.14 and also in Figure 5.9.

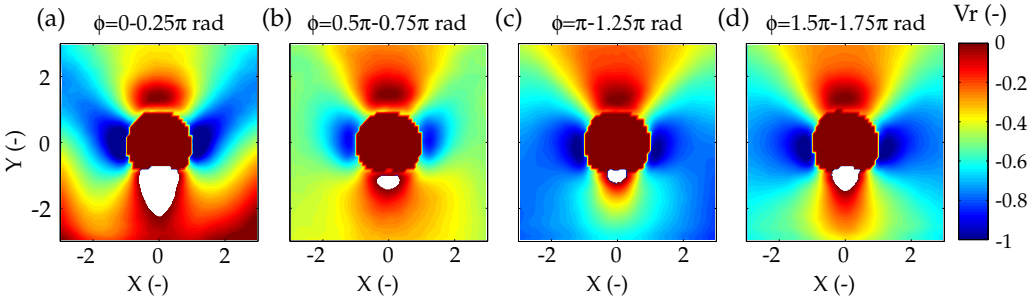


**Figure 5.14:** Contours of the normalized relative vertical velocity for four different phase intervals of size $\Delta\phi = 0.25\pi$ rad over a total interval of $\phi = 0 - 2\pi$ rad. The white regions correspond to the bubble wake volume. Exp. 1.

Figure 5.15 shows the normalized volume of the bubble wake in Exp. 1 for different intervals of the bubble vertical position and 8 phase intervals. Figure 5.15 also shows the volume of particles dragged by a bubble in the case the bed is not vibrated (Exp. 6). In Figure 5.15, the increase of the wake volume with an increase of $\phi$, as a consequence of the compression wave, can be clearly observed in the phase interval $\phi \simeq 1.45\pi - 2\pi$ rad. Similarly to the observation done in Figure 5.14, during the phase interval $\phi = 0 - 0.6\pi$ rad, the volume of particles dragged upwards by the bubble decreases with $\phi$ due to the commencement of the bed expansion (see Figures 5.13 and 5.14). Also, in the phase range $\phi = 0.6\pi - 1.4\pi$ rad, when the bubble is in the lower section of the bed, the volume of solids dragged by the wake of the bubble is nearly similar to that of the case in which the bed is not vibrated. Noticeably, the phase range $\phi = 0.6\pi - 1.4\pi$ rad corresponds to the phase interval in which the wake penetrates the bubble, as commented in Figure 5.13. In that phase range, in addition to the smaller volume of particles dragged below the bubble (Figure 5.14), the particles that penetrated the bubble contour are not affected by the bulk motion around the bubble and present a smaller upward velocity than the bubble front. The same qualitative behavior of the wake volume with the vibration phase described in Figure 5.15 is followed for all the vibration conditions tested (i.e. the wake volume is minimum in the range $\phi = 0.6\pi - 1.4\pi$ rad)

The effects of the vibration amplitude and frequency on the normalized wake volume are investigated in Figure 5.16. This figure also includes the normalized volume of particles dragged upwards by the average bubble when the bed is not vibrated. The normalized volume of the dragged particles increases when increasing both the vibration amplitude and frequency of the vibration of the bed vessel. When increasing $f$ or $A$,

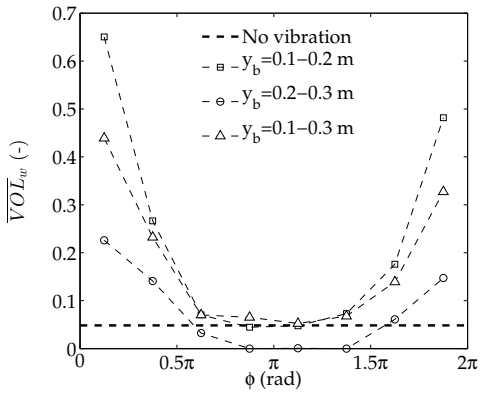


**Figure 5.15:** Normalized wake volume for eight phase intervals of size $\Delta\phi = 0.25\pi$ rad and for bubbles situated in different sections of the bed. Exp. 1.

the vibration strength $\Lambda = A(2\pi f)^2/g$ increases and a larger amount of momentum is introduced in the system, which might favor the dragging of a larger amount of particles by the bubble in the phase interval $\phi = 1.4\pi - 0.6\pi$ rad (of the next cycle). In particular, vibration of the bed vessel at the lower amplitude ($A = 2.8$ mm), reduced the volume of the bubble wake to zero in the phase range $\phi = 0.6\pi - 1.4\pi$ rad. That is, in that phase interval the particles in the front of the bubble move faster than the particles below the bubble. This implies that, for low vibration amplitudes, the bubble drags less wake in $\phi = 0.6\pi - 1.4\pi$ rad than a bubble in a non-vibrated bed. Besides, increasing the vibration amplitude in the phase range $\phi = 0.6\pi - 1.4\pi$ rad clearly increases the normalized wake volume. For the highest vibration frequency ($f = 17.1$ Hz) and the phase interval $\phi = 0 - 0.25\pi$ rad, the wake volume is sufficiently large to interact with the compression wave front below it. This front also travels at a velocity larger than the position of the bubble front and that makes difficult to differentiate between the volume of solids below the bubble directly dragged by the bubble wake and the solids pushed upwards by the compression wave front.

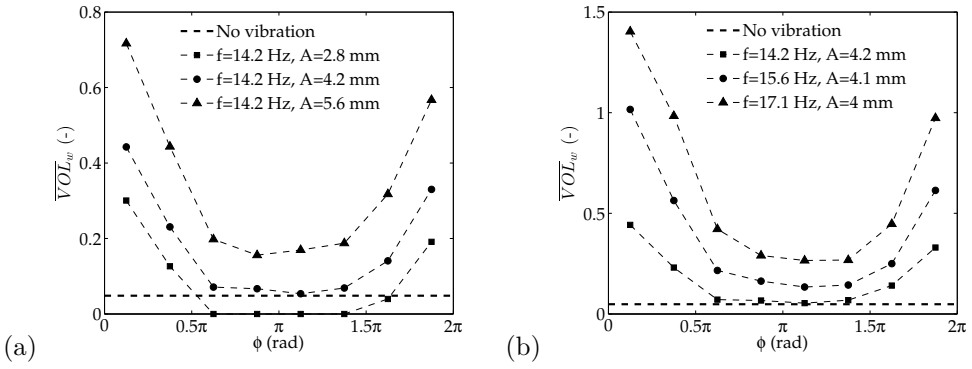


**Figure 5.16:** Normalized wake volume for eight different phase intervals of size $\Delta\phi = 0.25\pi$ rad. (a) Variation of the vibration amplitude (Exp. 1, 2 and 3) (b) Variation of the vibration frequency (Exp. 1, 4 and 5).

## 5.5 Conclusions

The pressure distribution and the motion of solids around isolated bubbles in a pseudo-2D fluidized bed subjected to vertical vibration were experimentally studied in the present chapter by means of DIA, PIV and pressure signal analysis. The bed was filled with Geldart B particles and vibrated at different amplitudes and frequencies. A bubble averaging methodology was used to analyze the mean solids velocity around isolated bubbles as a function of the vibration phase. This methodology also allowed the determination of the behavior of the wake of bubbles affected by vibration.

In the first section of this chapter, local pressure signals were used to understand the pressure fluctuations in the bed induced by vibration and by the presence of the bubble in the bed. The pressure signals were filtered, which allowed to distinguish between the pressure fluctuations caused by vibration and by the passage of the bubble void next to the pressure probes. The perturbation produced by a bubble in the pressure signal was found similar to that expected for a bubble rising in a bed without vibration. This suggests that the gas pressure fluctuations produced by vibration of the bed do not interfere coherently with the pressure perturbation produced by the bubble, which may be of great utility when monitoring of the bubble behavior in beds without optical access.

As observed in Chapter 3, vibration of the bed vessel promotes the appearance of compression and expansion wave fronts of solids that are generated by the interaction of the bed bulk with the distributor and travel upwards in the bed. The PIV results shown in the present chapter reveal that the presence of the bubble in the system modifies the way the compression and expansion wave fronts propagate in the bed. Reciprocally, the

motion of solids around the bubble is strongly affected by the cyclic compression and expansion of the bed bulk. The velocity of the compression wave front seems to remain unaffected as the bubble rises in the bed. However, the velocity of the expansion wave increases as the bubble rises in the bed.

Besides, direct comparisons of the experimental results with the classical Davidson & Harrison (1963) potential flow model confirmed the validity of this simple model to qualitatively describe the solids motion around the bubbles rising the vibrated fluidized bed studied in this chapter.

The oscillatory motion of the bed bulk has also a strong effect on the behavior of the bubble wake. The PIV results of solids velocity were also used to give an explanation to the characteristic wavy shape of bubbles in vibrated beds, which is not present in bubbles rising in conventional fluidized beds. The volume of particles dragged by the wake increases when increasing the vibration amplitude and frequency, as it is also strongly affected by the oscillatory motion of the bed vessel.

Overall, the results of pressure and velocity presented in this chapter can help to understand the complex mutual interaction of the bubbles and the bed bulk in this kind of vibrated systems. This interaction, in turn, affects the shape of bubbles and the volume of solids that they drag, which are aspects of great relevance in reactors and chemical conversion processes.

## Nomenclature

| | |
|---|---|
| $A$ | bed vibration amplitude (mm) |
| $a$ | bed acceleration (m/s$^2$) |
| $D_b$ | bubble diameter (m) |
| $Dr$ | relative dispersion (-) |
| $f$ | vibration frequency (Hz) |
| $g$ | gravity acceleration constant (m/s$^2$) |
| $H$ | bed height (m) |
| $H_0$ | static bed height (m) |
| $K$ | bed thickness (m) |
| $M$ | number of phase intervals for averaging of cycles (-) |
| $(X,Y)_n^{(F)}$ | new fitting circle normalized coordinates (-) |
| $N_{bins}$ | number of windows for velocity averaging (-) |
| $N_w$ | number of wake analysis windows (-) |
| $P$ | pressure (Pa) |
| $R_b$ | bubble radius (m) |
| $R^*$ | bubble extended radius (-) |

| | |
|---|---|
| $t$ | time (s) |
| $T$ | period of vibration (s) |
| $U$ | solids horizontal velocity (m/s) |
| $\overline{U}$ | normalized horizontal velocity (-) |
| $U_{mf}$ | minimum fluidization velocity (m/s) |
| $u$ | solids horizontal velocity (m/s) |
| $\vec{V}$ | normalized solids velocity vector (-) |
| $V$ | normalized vertical velocity (-) |
| $V_b$ | bubble velocity (m/s) |
| $V_r$ | normalized relative velocity (-) |
| $\overline{V}$ | normalized vertical velocity (-) |
| $\overline{VOL}$ | normalized volume (-) |
| $v$ | solids vertical velocity (m/s) |
| $W$ | bed width (m) |
| $X$ | normalized horizontal coordinate (-) |
| $x$ | horizontal coordinate (m) |
| $Y$ | normalized vertical coordinate (-) |
| $y$ | vertical coordinate (m) |

*Greek letters*

| | |
|---|---|
| $\delta(t)$ | instantaneous vibration displacement (m) |
| $\varepsilon$ | gas void fraction (-) |
| $\theta$ | angle from the vertical direction (°) |
| $\theta_b$ | bubble rising angle (°) |
| $\Lambda$ | vibration strength (-) |
| $\rho$ | density (kg/m$^3$) |
| $\phi$ | bed vessel vibration phase (rad) |
| $\sigma$ | standard deviation (-) |
| $\Phi$ | velocity potential (m$^2$/s) |

*Subscripts*

| | |
|---|---|
| $avg$ | average |
| $b$ | bubble |
| $bed$ | bed vessel |
| $c$ | compression |
| $d$ | bed bulk |
| $e$ | expansion |
| $f$ | wave front |

| | |
|---|---|
| $g$ | gas |
| $prop$ | propagation |
| $r$ | relative |
| $s$ | stripe |
| $w$ | wake |

## References

Barletta, D., Russo, P. & Poletto, M. 2013 Dynamic response of a vibrated fluidized bed of fine and cohesive powders. *Powder Technol.* 237, 276–285.

Croxford, A.J. & Gilbertson, M.A. 2011 Pressure fluctuations in bubbling gas-fluidized beds. *Chem. Eng. Sci.* 66(16), 3569–3578.

Davidson, J.F. & Harrison, D. 1963 *Fluidised Particles*. Cambridge University Press, Cambridge.

Geldart, D. 1973 Types of gas fluidization. *Powder Technol.* 7, 285.

Hernández-Jiménez, F., Gómez-García, A., Santana, D. & Acosta-Iborra, A. 2013 Gas interchange between bubble and emulsion phases in a 2D fluidized bed as revealed by two-fluid model simulations. *Chem. Eng. J.* 215-216, 479–490.

Hernández-Jiménez, F., Sánchez-Delgado, S., Gómez-García, A. & Acosta-Iborra, A. 2011*a* Comparison between two-fluid model simulations and particle image analysis & velocimetry (PIV) results for a two-dimensional gas-solid fluidized bed. *Chem. Eng. Sci.* 66, 3753–3772.

Hernández-Jiménez, F., Third, J.R., Acosta-Iborra, A. & Müller, C.R. 2011*b* Comparison of bubble eruption models with two-fluid simulations in a 2D gas-fluidized bed. *Chem. Eng. J.* 171, 328–339.

Müller, C.R., Davidson, J.F., Dennis, J.S. & Hayhurst, A.N. 2007 A study of the motion and eruption of a bubble at the surface of a two-dimensional fluidized bed using particle image velocimetry (PIV). *Ind. Eng. Chem. Res.* 46, 1642–1652.

Patil, D.J., van Sint Annaland, M. & Kuipers, J.A.M. 2003 Gas dispersion and bubble-to-emulsion phase mass exchange in a gas-solid bubbling fluidized bed: a computational and experimental study. *Int. J. Chem. React. Eng.* 1, 1–20.

Roy, R., Davidson, J.F. & Tuponogov, V.G. 1990 The velocity of sound in fluidised beds. *Chem. Eng. Sci.* 45, 3233–3245.

Wang, T.J., Jin, Y., Tsutsumi, A., Wang, Z. & Cui, Z. 2000 Energy transfer mechanism in a vibrating fluidized bed. *Chem. Eng. J.* 78, 115–123.

Wang, T., Jin, Y., Wang, Z. & Yu, Z. 1997 The characteristics of wave propagation in a vibrating fluidized bed. *Chem. Eng. Technol.* 20, 606–611.

CHAPTER
**SIX**

# Mean and oscillatory bubbling behavior of a vibrated fluidized bed in freely bubbling regime

## Contents



## 6.1 Introduction

The motion of both the bed bulk and isolated bubbles in a vibrated fluidized bed were studied by means of DIA and PIV in the previous chapters. However, from a practical point of view, it is of great interest to analyze how vibration affects both the mean bubble characteristics and the oscillation of the bubble behavior when the bed is operated in freely bubbling regime and bubbles mutually interact.

As commented in Chapter 1, there exist numerous works studying the bed behavior and the bubble characteristics in a vertically vibrated fluidized bed. However, in all the works mentioned for bubbling regime in which the bubble characteristics (i.e. the bubble diameter and velocity) are analyzed the area in which the bubble behavior was quantified comprises only a fraction of the bed. For example, Mawatari *et al.* (2005) studied bubbles located in a horizontal stripe of 5 cm height in a pseudo-2D bed, Zhou *et al.* (2005) in two stripes of 2 cm height and Eccles & Mujumdar (1997) in a stripe of 6 cm height. This precludes from the extraction of spatially resolved results and the determination of

the variation of the bubble properties along the vertical direction. Spatially resolving the bubble behavior may shed light onto the different phenomena affecting bubble behavior and may explain in a comprehensive way the apparently contradictory trends reported in the literature (Eccles & Mujumdar, 1997; Mawatari *et al.*, 2005; Zhou *et al.*, 2005).

Besides, as commented in Chapter 1, the number of works analyzing the oscillatory behavior of the bed bulk and bubbles in a vertically vibrated fluidized bed are comparatively scarce (Wang *et al.*, 2000; Barletta *et al.*, 2013). Wang *et al.* (2000) studied the energy transfer mechanism in a vertically vibrated cylindrical bed where they observed that in a VFB there exists a propagation of pressure waves originated at the base plate of the bed. Barletta *et al.* (2013) studied the dynamic response of a vibrated fluidized bed of cohesive powders of Geldart A and C classification. They found a wide range of vibration frequencies that caused an opposition in phase between the bed height and the bed vessel, which revealed a cyclic compression and expansion of the bed bulk. In Chapters 4 and 5 the oscillatory behavior of the bed bulk in a vertically vibrated fluidized bed was studied both experimental and numerically. Isolated bubbles were injected, so that bubble interaction was negligible. These works (Barletta *et al.*, 2013) and Chapter 4 were carried out for beds at, or close to, minimum fluidization conditions and with the presence of isolated bubbles. However, the oscillatory motion of bubbles and their interaction with the bulk motion in a vertically vibrated fluidized bed operating in freely bubbling regime still remains unexplored in these studies.

The present chapter aims at systematically analyze both the mean and oscillatory behavior of the bed bulk and bubble characteristics in a vertically vibrated pseudo-2D bed operated in bubbling regime so that the interaction between multiple bubbles is not negligible. Four different types of bed powders, belonging to Geldart groups A, A/B and B, are studied. The bed is fluidized with different superficial gas velocities in combination with several vibration amplitudes and frequencies. This aims at clarifying the effect of vibration on the local bubble characteristics as a function of the distance to the distributor and the resulting overall bubble behavior (i.e. averaged over the whole bed). In addition, the general bed dynamics is studied by means of the bubble hold-up distribution as well as the oscillation of the bed bulk center of mass and the surface of the bed. A bubble tracking methodology is developed to individually study the oscillatory behavior of bubbles inside the bed. The results presented in this chapter reveal that vibration of the bed vessel promotes a confinement of the bubbles to the central part of the bed, especially for the bed of smaller particles. This confinement affects the way bubbles behave along the bed. Also, this chapter analyzes the oscillation of multiple interacting bubbles in a vibrated bed, its relation with the oscillation of the bed bulk, and the influence of the frequency and amplitude of vibration on the oscillation of bubble characteristics.

## 6.2 Experimental setup

The facility used in this chapter is the vibrated fluidized bed described in Section 2.1.2 of Chapter 2. Particles of four different diameters were used in order to investigate the effect of the particle diameter on the bubble and bed dynamics in vibrated beds. The particles were ballotini glass beads, and their mean diameter, standard deviation and density are included in Table 6.1. According to Geldart's classification of particles, the particles of 46.5 $\mu$m and 60 $\mu$m are of type A, those of 90.5 $\mu$m are type A/B and 120 $\mu$m particles correspond to type B. For all the experiments conducted, the bed was filled with 1.1 kg of glass beads. This corresponded to an approximate settled bed height of 0.39 m. The minimum fluidization velocity of each particle type under static conditions was measured with a pressure probe connected to the plenum. Table 6.1 lists the experimental values obtained for the minimum fluidization velocity, $U_{mf}$, together with the theoretical values provided by Ergun's equation (Ergun, 1952) with a void fraction of $\varepsilon = 0.4$, $U_{mf,th}$, and the gas velocity ratios, $U/U_{mf}$, used in the experiments.

**Table 6.1:** Particle properties

| $d_p$ ($\mu$m) | $\rho_p$ (kg/m$^3$) | $U_{mf}$ (mm/s) | $U_{mf,th}$ (mm/s) | $U/U_{mf}$ (-) | Geldart classification |
|---|---|---|---|---|---|
| 46.5±6.5 | 2500 | 2.4 | 2.1 | 4, 8, 12, 16, 20 | A |
| 60±15 | 2500 | 3.3 | 3.5 | 4, 6, 8, 10 ,12 | A |
| 90.5±14.5 | 2500 | 9.9 | 7.9 | 2, 3, 4, 5, 6 | A/B |
| 120±15 | 2500 | 14.3 | 13.8 | 2, 2.5, 3, 3.5, 4 | B |

The vibration conditions indicated in Table 6.2 were tested for each of the four particles sizes under study in order to independently investigate the influence of the vessel vibration amplitude and frequency on the bed. For each kind of particle, experiments comprised three different vibration frequencies (i.e. 10, 15 and 20 Hz) keeping constant the vibration amplitude, $A_{pp}$ (peak-to-peak amplitude). This was carried out for several vibration amplitudes, including no vibration ($A_{pp} = 0$), as indicated in Table 6.2. When the frequency of vibration of the bed vessel was changed from one experiment to another (i.e. $f$ =10, 15 and 20 Hz for the same row in Table 6.2), it was difficult to exactly preserve the value of the amplitude of vibration $A_{pp}$. This created a slight modification of $A_{pp}$ with the vibration frequency. To quantify this effect, Table 6.2 includes the mean and standard deviation of the vibration amplitude measured by means of DIA corresponding to the three vibration frequencies tested. Also, Table 6.2 shows the resulting intervals for the vibration strength parameter, $\Lambda$.

In the present chapter, the vibration strength parameter $\Lambda$, ranges from small values to values slightly larger than $\Lambda = 1$, in order to study the effect of small strength

vibrations on the bubble behavior and its dependence with the particle diameter.

**Table 6.2:** Vibrating conditions of the experiments

| $d_p$ ($\mu$m) | $f$ (Hz) | $A_{pp}$ (mm) | $\Lambda$ (-) |
|---|---|---|---|
| | | 0 | 0 |
| 46.5 | 10, 15, 20 | 0.8±0.1 | 0.2-0.6 |
| | | 1.9±0.2 | 0.4-1.5 |
| | | 0 | 0 |
| | | 0.6±0.1 | 0.1-0.5 |
| 60 | 10, 15, 20 | 1±0.1 | 0.2-0.8 |
| | | 1.4±0.1 | 0.3-1.1 |
| | | 1.9±0.3 | 0.4-1.5 |
| | | 0 | 0 |
| | | 0.5±0.1 | 0.1-0.4 |
| 90.5 | 10, 15, 20 | 0.9±0.1 | 0.3-0.7 |
| | | 1.2±0.1 | 0.2-2 |
| | | 1.9±0.1 | 0.4-1.5 |
| | | 0 | 0 |
| | | 0.6±0.1 | 0.1-0.5 |
| 120 | 10, 15, 20 | 1±0.1 | 0.2-0.8 |
| | | 1.4±0.1 | 0.3-1.1 |
| | | 2±0.2 | 0.4-1.6 |

The bed was recorded by a CCD camera with a frame rate of 125 fps (for the particles of 60, 90.5 and 120 $\mu$m) and 60 fps (particles of 46.5 $\mu$m). Each of the conducted experiments comprised a recording time of 51 seconds. Sensitivity analysis of the recording time, carried out by comparing the bubble behavior during the first and last 25 seconds of the experiments, showed no significant variation on bubble characteristics, which ensures a statistically stationary behavior of bubbles in the bed.

The experimental results are affected by two sources of errors. Firstly, the error related to the image analysis is caused by the discrimination of the bubble and dense phases, and is directly related to the spatial resolution and graylevel resolution of the image. The spatial resolution of the image is given by the size of a pixel, which is around $4{\cdot}10^{-4}$ m. The grayscale resolution is determined by the grayscale level, which ranges from 0 to 255, the grayscale resolution being 1. Secondly, the mean values of variables (e.g. mean bubble diameter) have an uncertainty error due to the finite size of the mean. According to the standard theory of statistics, this uncertainty of the mean of a variable is given by the standard deviation of the variable divided by the number of samples of the mean. An order of magnitude estimation of these sources of error led to values two orders of magnitude smaller than the variable being measured.

## 6.3 Results and discussion

The results presented in this chapter are divided into three main sections. Firstly, the effect of vibration on the bubble hold-up distribution and on the mean bubble characteristics (i.e. bubble fraction, number density, diameter and velocity) is studied. Secondly, the oscillatory behavior of the bed bulk and the bubbles is studied by means of the averaging of cycles and the bubble tracking methods presented in Chapter 2. This is paramount to understand the global oscillatory behavior of the bed and, in particular, the effect of the oscillation of the bed bulk on the bubble characteristics. The oscillatory behavior of the bubble diameter, position and velocity is studied for different superficial gas velocities, vibration amplitudes and frequencies. Lastly, the phase delay of bubble characteristics along the bed is calculated and discussed.

### 6.3.1 Bubble hold-up distribution

#### Solids hold-up

An important effect that vibration of the bed vessel promotes in the dynamics of the bed is the modification of the bubbles preferred paths in the bed (Mawatari *et al.*, 2005), which has an impact on the bubble behavior. As a way to qualitatively report the effect of vibration on the bubble path, Figure 6.1 shows the normalized mean solids hold-up (see Section 2.3.1) of the experiments carried out for a bed with particles of 60 $\mu$m subject to different vibration amplitudes and frequencies, and two different gas velocity ratios ($U/U_{mf}$). Note that $U_{mf}$ refers to the minimum fluidization velocity under static conditions, which is relatively easy to measure or to calculate using well-known correlations (see Table 6.1).

It can be observed in Figure 6.1 that there exist regions in which the normalized mean grayscale image is larger than in the central section of the bed and close to the bed lateral walls. These regions typically form two easily discernible tracks that are caused because, for the bed analyzed in this chapter, bubbles close to the distributor follow two preferred paths that merge into a single one far from the distributor. A net upward displacement of the bed particles is induced by bubbles in the bubble path, whereas close to the walls bubbles are scarce and particles move downwards at a relatively low velocity. As can be seen in Figure 6.1, this downward motion region is larger if the amplitude and frequency of vibration is increased because more kinetic energy is introduced in the system and that seems to favor the flowability of the solids. Here, the bubble path is confined to the center of the bed due to the enhancement of particle circulation promoted by vibration. Also, it could be observed in the experiments that vibration promotes a larger oscillation of bubbles and a decrease of the effective $U_{mf}$, which contribute to the

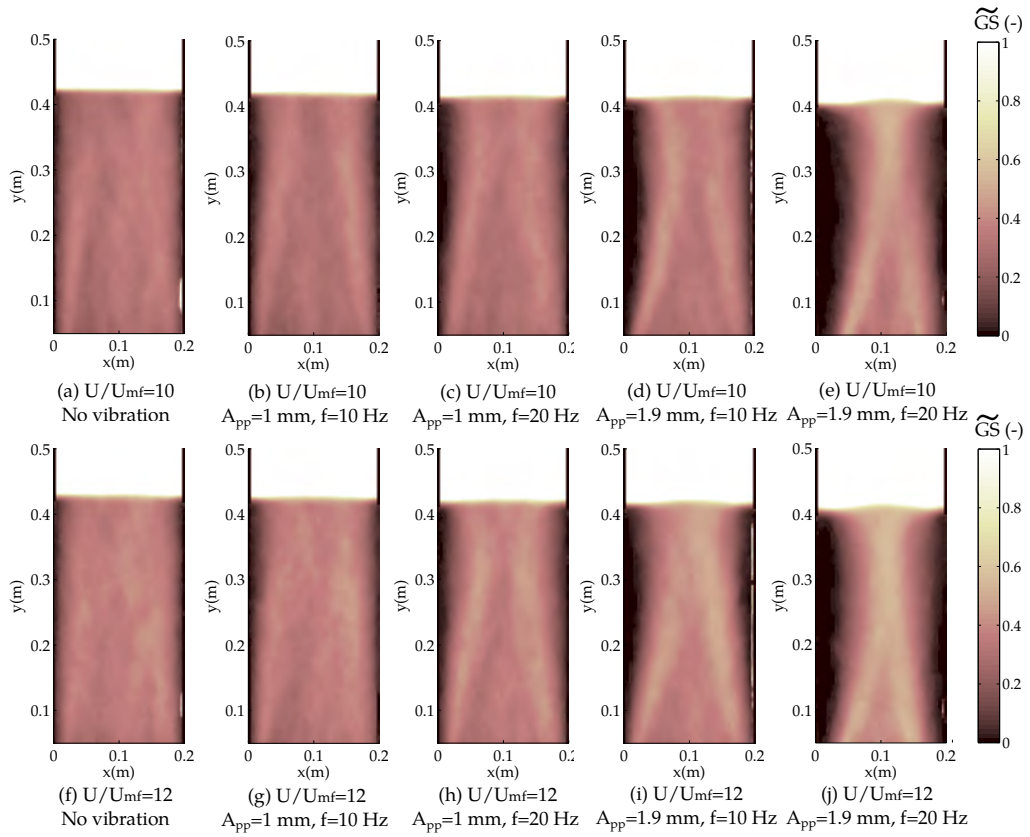


**Figure 6.1:** Normalized mean grayscale images of the bed for different vibration conditions. $d_p$=60 $\mu$m.

coalescence and the formation of larger bubbles in the bed. Larger bubbles present in the system due to the increase of $U/U_{mf}$ drift up a greater amount of particles through the center of the bed, and that requires a larger zone for particles to descend near to the bed walls. Confinement of the bubble path promotes the coalescence of bubbles and, as a consequence, has a significant impact on bubble characteristics such as bubble diameter and velocity.

Pairwise comparison of the normalized images in Figure 6.1 (e.g. Figure 6.1(b-c)) shows that increasing the amplitude or the frequency of vibration has a strong impact on the confinement of the bubble path. The preferred point at which bubbles coalesce can be inferred from Figure 6.1 as the vertical coordinate in which the two main bubble paths join in the center of the bed. This coalescence point gets closer to the distributor as the frequency and amplitude of vibration increase. It can be also observed in Figure 6.1 that a variation of the superficial gas velocity modifies the bubble hold-up. An increase of $U/U_{mf}$ promotes the formation of bigger bubbles and increases the width of the bubble

path. Since the increase of the superficial gas velocity promotes the formation of bigger bubbles, this also decreases the lowering of the vertical position where the two initial paths of bubbles join.

Figure 6.2 compares the normalized mean grayscale images for different particle sizes. Results without vibration as well as with the maximum vibration strength tested ($A_{pp} = 1.9 - 2$ mm, $f = 20$ Hz, $\Lambda = 1.5 - 1.6$) are presented. For each particle size, the superficial velocity is chosen so that the gas excess velocity, $U - U_{mf}$, is similar for all the particle sizes in Figures 6.2(a) to (h). Note that $U - U_{mf}$ is closely related to the bubble size, which has a direct impact on the normalized mean grayscale images shown in Figures 6.1 and 6.2. On the contrary, keeping constant $U/U_{mf}$ in Figure 6.2 would lead to very uneven bubble sizes among the different particles being compared. As for the particles of 60 $\mu$m in Figure 6.1, it can be observed in Figure 6.2 that bubbles tend to separate from the walls when introducing vibration in the fluidized bed regardless the particle size. From Figure 6.2 it seems that the impact of the vibration on the bubble path becomes more important as the particle diameter decreases. This effect is observed in Figure 6.2, and it can be attributed to the gulf stream circulation of particles that is promoted by vibration. The circulation of particles in the bed seems to be more intense for the smallest particles. This is attributed to their less inertia and to the smaller proportion of particles colliding with the vibrating front and rear walls, whose oscillatory displacement may promote an increase of wall friction. As observed previously, an increase of the gulf stream circulation produces a larger descending flow of particles close to the walls, which tends to confine the bubble path towards the bed center, as observed previously.

### Bubble distribution index

Figure 6.3 shows the distribution index of bubbles in the bed (see Section 2.3.1) for all the particle sizes analyzed and for different vibration conditions. In Figure 6.3, when bubbles are uniformly distributed across the bed width, large values of the distribution index appear because bubbles induce similar values of the mean gray level in the bed along the horizontal axis and that reduces the denominator of Equation (2.11). Generally, excepting for the largest particles, the best distribution of bubbles along all the bed, (i.e. high distribution index) is found to be the case in which the bed is not vibrating. When introducing vibration in the system, the distribution of bubbles is less uniform and the distribution index decreases. For all the cases under study, it can be seen in Figure 6.3 that the distribution index decreases with the distance to the distributor. This is so because a less uniform distribution of bubbles is found due to the progressive bubble confinement to the center of the bed. For the particles of 46.5 $\mu$m and 60 $\mu$m

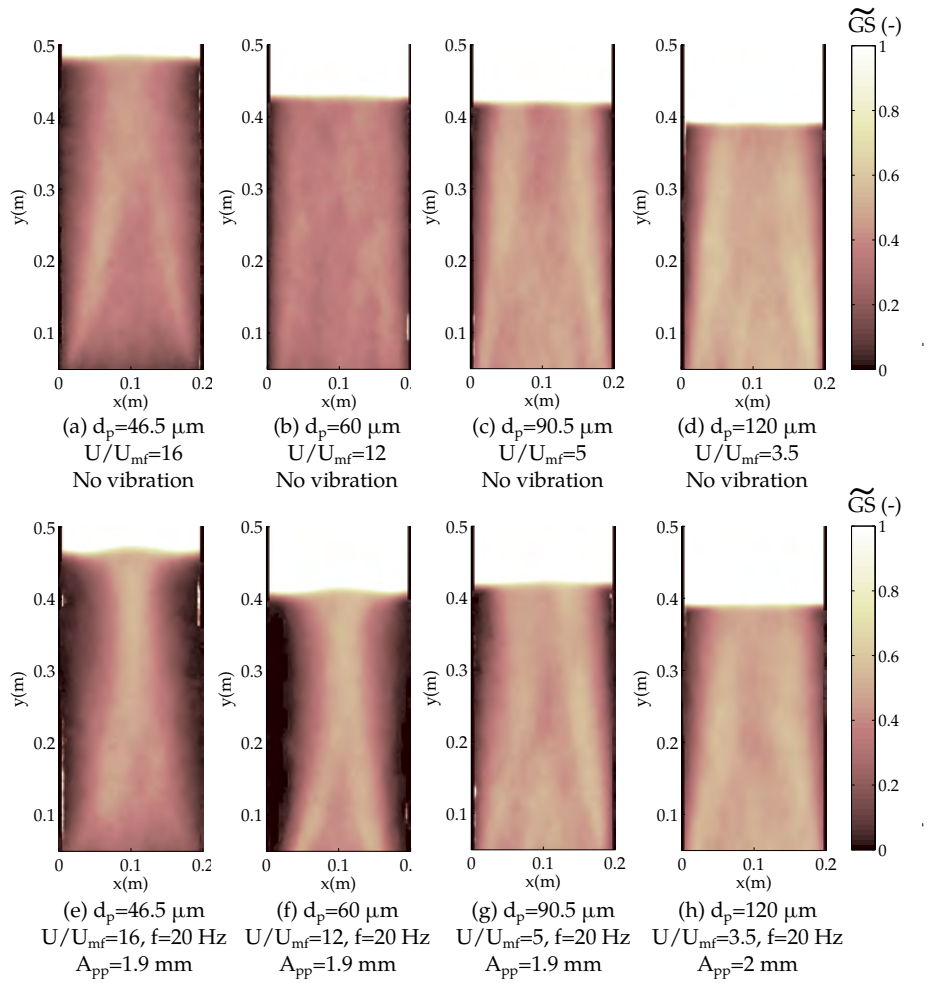


**Figure 6.2:** Normalized mean grayscale images of the bed for particles of 46.5 $\mu$m, 90.5 $\mu$m and 120 $\mu$m mean diameters: (a-d) cases without vibration and (e-h) with vibration of $A_{pp} = 1.9 - 2$ mm and $f = 20$ Hz.

mean diameter the variation of $DI$ with the distance to the distributor is reduced with $\Lambda$, as bubble coalescence and the confinement of the bubble path is promoted in the lower section of the bed.

The effect of the vibration of the bed vessel on the distribution index for the particles of 46.5 $\mu$m and 60 $\mu$m (Figure 6.3(a) and (b)) is more significant than for the particles of 90.5 $\mu$m and 120 $\mu$m (Figure 6.3(c) and (d)). This was also qualitatively observed in Figure 6.2 where the vibration-induced confinement of the bubbles to the central part of the bed with particles of 46.5 and 60 $\mu$m mean diameters (Figure 6.2(a,b,e,f)) was superior to the one found for particles of 90.5 and 120 $\mu$m (Figure 6.2(c,d,g,h)). This

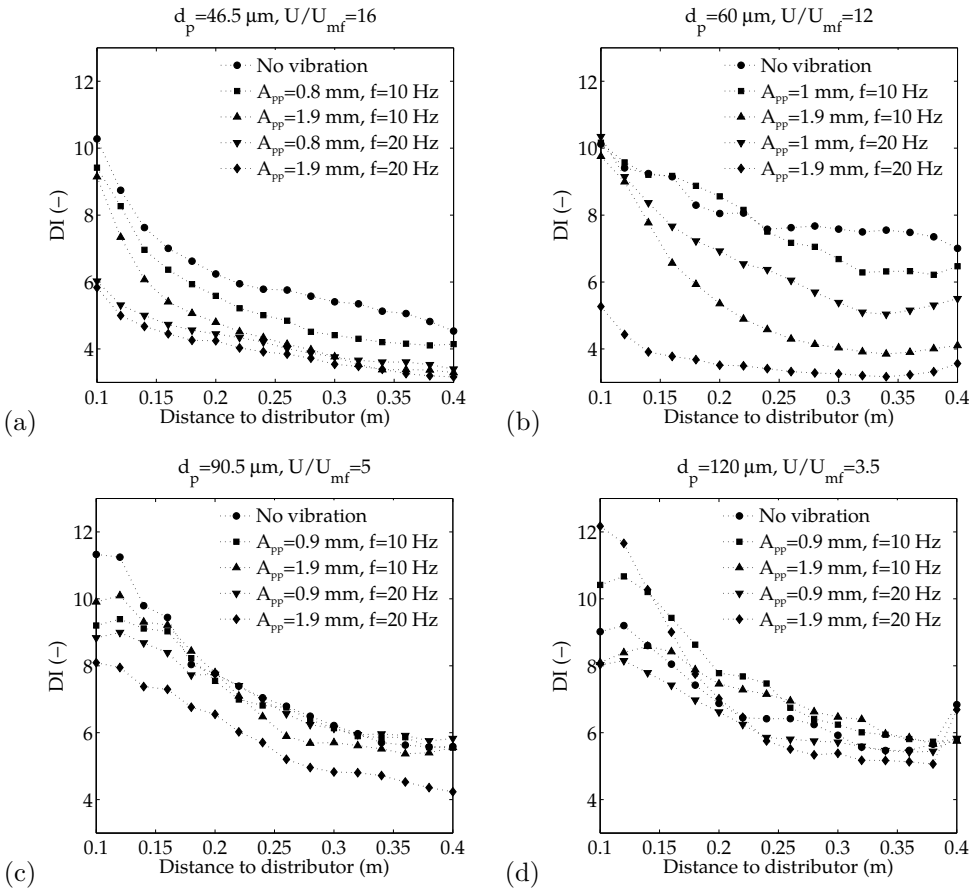


**Figure 6.3:** Distribution index as a function of the vertical distance to the distributor for different vibration strengths and mean particle diameters: (a) $d_p = 46.5$ $\mu$m, (b) $d_p = 60$ $\mu$m, (c) $d_p = 90.5$ $\mu$m and (d) $d_p = 120$ $\mu$m.

is attributed (see Section 6.3.1) to the larger mobility of the smallest particles in the vibrated bed, which enhances a more intense convective circulation of particles. Particles with diameter 60 $\mu$m seem to lead to a distribution index more sensitive to $\Lambda$ than the other particles. This might be related to the existence of an optimum particle size and vibration strength for which the gas drag and particle inertia combine in such a way that the $DI$ seen in Figure 6.3 is enhanced. More experiments would be required to give an exact answer to this phenomenon. It can be observed in Figure 6.3 that, in general, the distribution index decreases with the vibration strength $\Lambda$, due to the larger confinement of bubbles to the central section of the bed. According to Figure 6.3, an increase of both the amplitude and frequency of vibration of the bed vessel accentuates the progressive confinement of the bubble path with the distance to the distributor due

to the enhancement of convective circulation of particles in the bed. Thus, in all the particles tested, the least uniform distribution of bubbles (i.e. minimum distribution index) appears in Figure 6.3 for the conditions of maximum vibration amplitude and frequency, $A_{pp} = 1.9 - 2$ mm and $f = 20$ Hz.

### 6.3.2 Mean bubble characteristics

Bubble characteristics are studied in this section for beds with particles of 60, 90.5 and 120 $\mu$m mean diameters. Beds with particles of 46.5 $\mu$m mean diameter will not be considered because they produced an intense particle rain inside bubbles which prevented their correct visualization and subsequent analysis. To analyze the effect of the bubble characteristics as a function of the distance to the distributor, a fixed frequency of 20 Hz (i.e. the highest vibration strengths, $\Lambda$) together with an intermediate gas excess ratio (i.e. $U/U_{mf}$=8, 4 and 3 for the particles of 60, 90.5 and 120 $\mu$m, respectively) were chosen as base cases for the analysis of these values. As explained in Chapter 2, spatial averaging of the bubble characteristics was performed by vertically dividing the bed in stripes of 2 cm.

#### Bubble fraction and bubble number density

Figure 6.4 shows the bubble fraction (Equation (2.8)) and the bubble number density (Equation (2.9)) as a function of the distance to the distributor. It can be observed in Figure 6.4(a-c) that the bubble fraction increases close to the distributor and, after reaching a maximum value around $y > 0.2$ m, decreases with the vertical position. Increasing the vibration amplitude, $A_{pp}$, produces an increase of visible flow when the bubbles are well separated, which generally happens in the lower half of the bed ($y < 0.2$ m). This tendency is reversed when bubbles are closer to each other, which occurs sufficiently far from the distributor (i.e. upper half of the bed, $y > 0.2$ m). For the particles of 60 $\mu$m, the rain of particles in bubbles may hinder the smallest bubbles located close to the distributor. Although this effect is largely reduced by means of the double thresholding methodology (see Section 6.2), when small particles are used, the number of particles in the thickness direction is so large that their rain of particles makes difficult to capture bubbles by the high speed camera. Note that particle rain inside bubbles is always present in these kind of pseudo-2D systems (Shen *et al.*, 2004; Busciglio *et al.*, 2008; Cano-Pleite *et al.*, 2014). The bubbles hindered by the rain of particles grow inside the bed until they reach a diameter big enough to be captured by the camera with accuracy, $A_b > 1$ cm$^2$, and that causes a growth of the bubble number density with the distance to the distributor in the lower half of the bed. Besides, the greater excess of gas (i.e. the effective $U_{mf}$ is reduced by vibration) produced by increasing the vibration amplitude

leads to bubbles big enough to be sampled, which increases the bubble number density in the lower half of the bed for high vibration amplitudes and particles of 60 $\mu$m mean diameter. However, this is not applicable for particles of 90.5 and 120 $\mu$m since bubbles are initially big enough to be sampled.

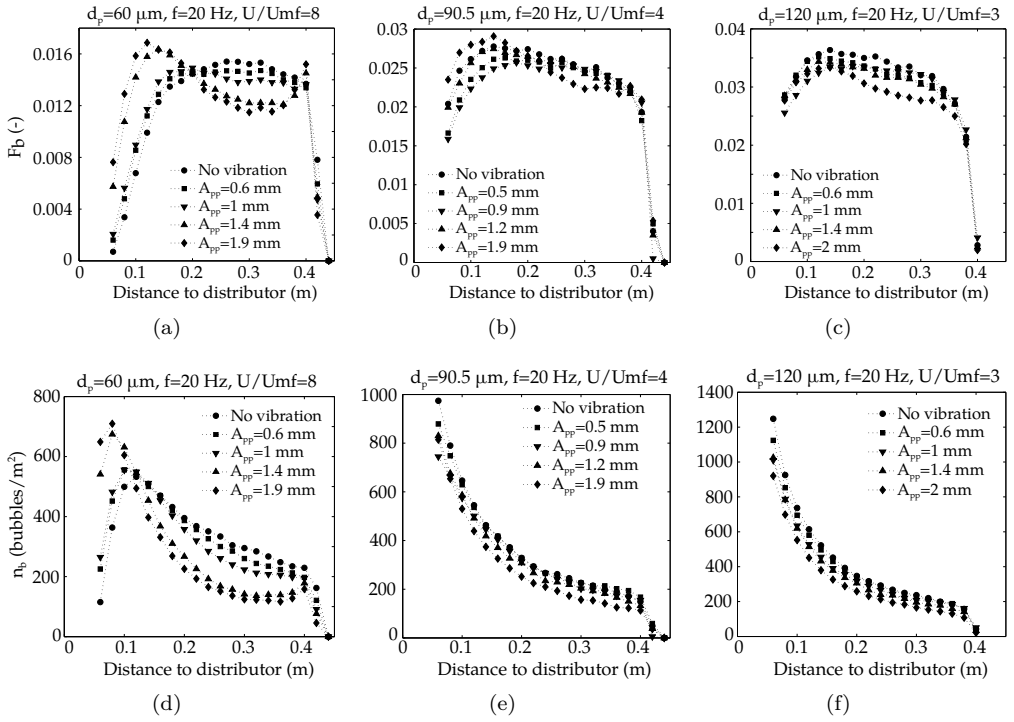


**Figure 6.4:** (a-c) Mean bubble fraction and (d-f) mean bubble number density as a function of the vertical distance to the distributor for different mean particle diameters: (a, d) $d_p = 60$ $\mu$m, (b, e) $d_p = 90.5$ $\mu$m and (c, f) $d_p = 120$ $\mu$m.

All these results suggest that there are two counteracting effects in vibration. Firstly, an increase of the vibration amplitude of the bed vessel makes bubbles bigger both by the decrease of the effective $U_{mf}$ and by the enhancement of bubble coalescence, which promotes an increase of the number of sampled bubbles in the lower half of the bed (see Figure 6.4(d)) with the vibration amplitude. This is especially important for the bed of small particles, since bubbles can be more easily hindered by a curtain of particles. Secondly, vibration also promotes coalescence of bubbles when they are far enough from the distributor and that tends to increase the throughflow of gas between bubbles, which may produce a decrease of the total visible flow and the bubble number density in favor of the non-visible throughflow. In the lower half of the bed, since bubbles are more sep-

arated, the increase of bubble diameter with vibration may be the dominant mechanism affecting the visible flow. In the upper half of the bed, vibration-induced coalescence is the main effect because bubbles are bigger and closer, and thus are more prone to coalesce. All these phenomena seem to be affecting the three types of particles in Figure 6.4, but their separate effect is most noticeable for the smallest particles (Figure 6.4 (a,d)) because this bed has smaller bubbles.

Figure 6.5 shows the bed fraction covered by bubbles in the whole bed ($y = 0.05 - 0.4$ m) as a function of the vibration amplitude for different gas velocities and vibration frequencies. In Figure 6.5, the bubble fraction increases with $U/U_{mf}$, as expected. According to the results, the bubble fraction is not very sensitive to either the vibration amplitude, $A_{pp}$, or the frequency, $f$, as can be inferred from integration of Figures 6.5(a-c) along the bed height. In general, when introducing vibration in the system, the mean bubble diameter increases (Figure 6.8). At the same time, the number of bubbles is reduced as coalescence is promoted by vibration (see Figure 6.6). These two effects compensate and lead to small variations of the bubble fraction with the vibration amplitude and frequency. The bubble fraction increases with the particle diameter for constant values of $U/U_{mf}$ due to the presence of bigger bubbles.

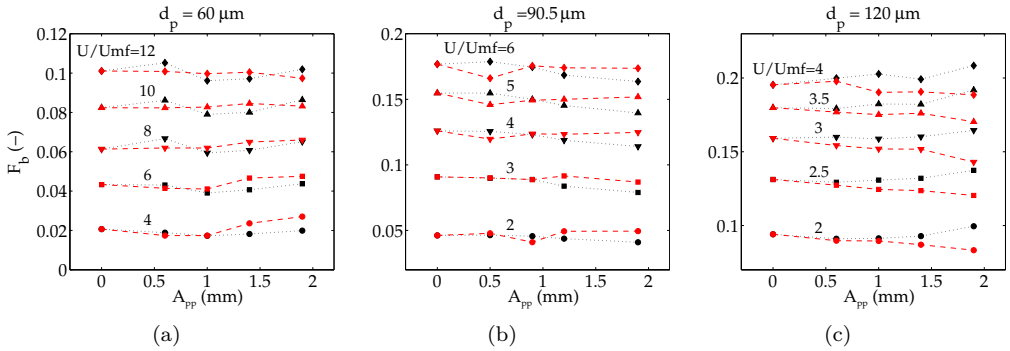


**Figure 6.5:** Mean bubble fraction as a function of the vibration amplitude for different mean particle diameters and superficial gas velocities: (a) $d_p = 60$ $\mu$m, (b) $d_p = 90.5$ $\mu$m, (c) $d_p = 120$ $\mu$m. Black symbols $f = 10$ Hz and red symbols $f = 20$ Hz.

Figure 6.6 presents the bubble number density in the whole bed as a function of the vibration amplitude for different vibration frequencies and superficial gas velocities. Counteracting effects are observed affecting both the bubble fraction and bubble density depending on the particle diameter. If the particles are small (60 $\mu$m), the number of bubbles increases when increasing the superficial gas velocity, because bubbles become more easily observable, as commented before. For the mean particle diameters of 90.5 and 120 $\mu$m (Figures 6.6(b, c, e, f)), bubbles are initially big enough to be captured

and, in consequence, both an increase of $U/U_{mf}$ and the introduction of vibration in the system promote the formation of bigger bubbles that are more prone to coalesce and that makes the mean bubble density decrease. This decrease of the mean bubble density is more pronounced at higher vibration frequencies of the bed because frequency has a strong impact on the confinement of the bubble path to the central section of the bed, as commented in Section 6.3.1.

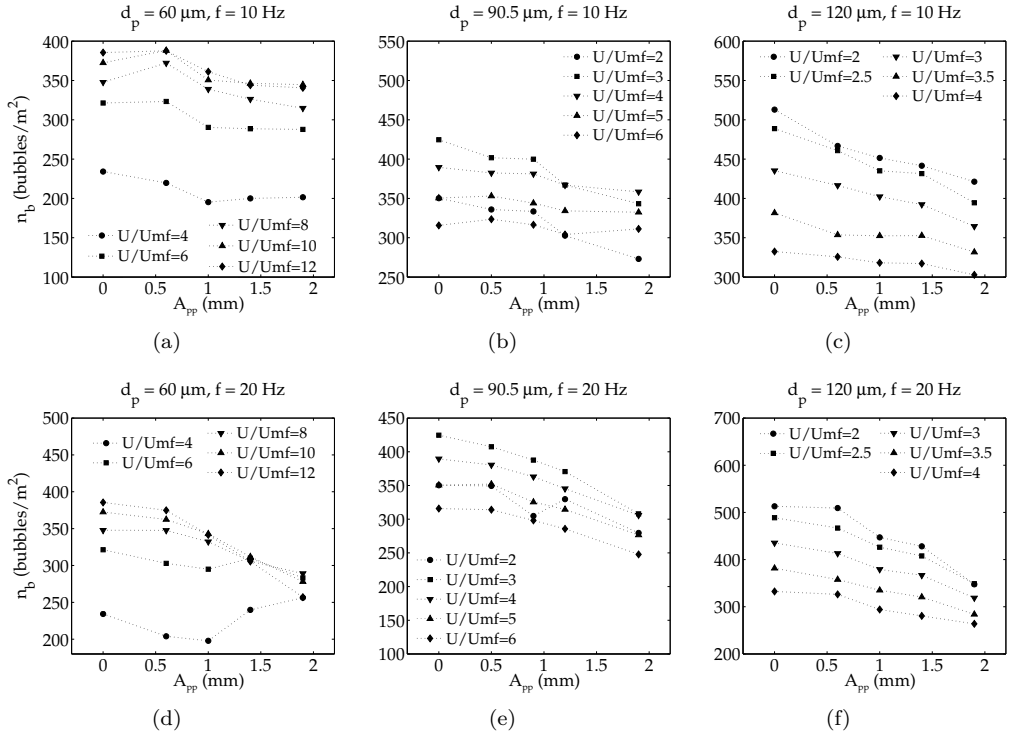


**Figure 6.6:** Mean bubble number density as a function of the vibration amplitude for different mean particle diameters and superficial gas velocities: (a, d) $d_p = 60$ $\mu$m, (b, e) $d_p = 90.5$ $\mu$m, (c, f) $d_p = 120$ $\mu$m, (a-c) $f = 10$ Hz and (d-f) $f = 20$ Hz.

### Bubble diameter and velocity

Figure 6.7 shows the mean bubble diameter and vertical velocity, in an absolute system of reference, as a function of the distance to the distributor. The mean bubble diameter at any distance to the distributor, Figure 6.7 (a-c), increases when increasing the vibration amplitude, regardless of the effects involved (i.e. increase of isolated-like bubbles or increase due to coalescence). The mean bubble diameter decreases close to the freeboard of the bed since large bubbles are skipped from the data averaging when they are erupting

at the bed surface.

The behavior of the mean bubble velocity as a function of the distance to the distributor and for different vibration amplitudes is also depicted in Figure 6.7(d-f). The bubble absolute velocity tends to decrease with the vibration amplitude in the lower half of the bed in consonance with reported numerical predictions (Acosta-Iborra *et al.*, 2012). This decrease of bubble velocity can be explained as follows. In the lower half of the bed, bubbles are small and far enough from other bubbles so that they behave like if they were isolated bubbles (see Section 6.3.2). According to Chapter 4, the velocity of isolated bubbles decreases when the amplitude of vibration increases, which is in harmony with the behavior of the isolated-like bubbles found in Figure 6.7(d-f) in the lower half of the bed. On the contrary, at a sufficient distance from the distributor (i.e. the upper half of the bed) the bubble velocity tends to increase with the vibration amplitude as reported in (Zhou *et al.*, 2004, 2005; Mawatari *et al.*, 2005). This result can be understood by taking into account the confinement of the bubble path due to vibration (Figure 6.1). In this part of the bed, bubbles are bigger and closer to each other, and, in consequence, they tend to coalesce and their velocity becomes higher due to both the acceleration of the trailing bubble prior to coalescence with the leading bubble (Kunii & Levenspiel, 1991) and the larger diameter of the bubble produced after coalescence. Therefore, there is a certain distance from the distributor (about 20 cm in Figure 6.7) at which the dependence of the bubble velocity with vibration amplitude is reversed. For $f = 20$ Hz in Figure 6.7(d) the height at which the reversal of tendency occurs is clearly seen. These point of inversion could be attributed to the cyclic compression and expansion of the bed bulk caused by vibration (as in Chapters 3 to 5). This may cause the bubbles in the bed to behave differently as a function of their distance to the distributor, being $y \simeq 20$ cm the region in which the trend of the bubble velocity is changed due to the confluence of these two regions, however, more experiments with different static bed heights would be needed to confirm this fact. In Figures 6.7(e) and 6.7(f) this reversal of the tendency of the bubble velocity is partially hidden and is attributed to the greater buoyancy of the big bubbles present on the bed filled with particles of 90.5 $\mu$m and 120 $\mu$m, which makes them to be less affected by the vertical vibration and, in consequence, less influenced by this reversal tendency of the bubble velocity.

Figure 6.8 shows the mean bubble diameter in the whole bed for the particles of 60, 90.5 and 120 $\mu$m as a function of the vibration amplitude for different vibration frequencies and superficial gas velocities. Firstly, in Figure 6.8, the mean bubble diameter increases with $U/U_{mf}$. In the figure, generally, the bubble diameter tends to increase with the vibration amplitude due to an enhancement of coalescence. However, this is not true for the particles of 90.5 $\mu$m and a vibration frequency of 10 Hz. Two main effects may be causing this decrease of the bubble diameter. Firstly, the bubble diameter

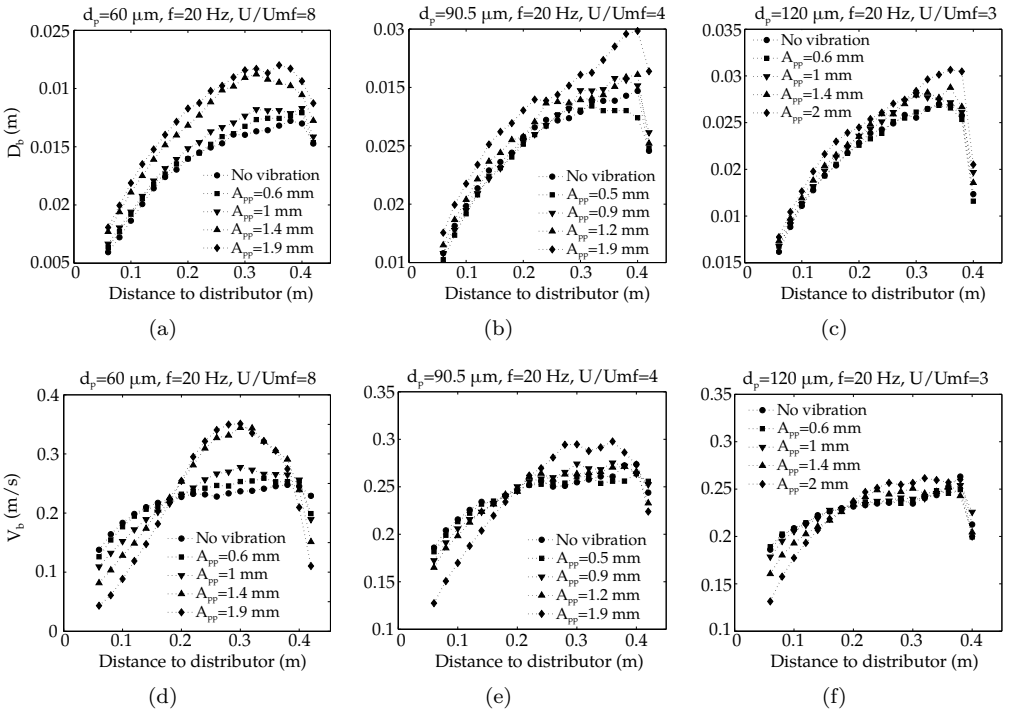


**Figure 6.7:** (a-c) Mean bubble diameter and (d-f) mean bubble absolute velocity as a function of the distance to the distributor and for different particle diameters: (a, d) $d_p = 60$ $\mu$m, (b, e) $d_p = 90.5$ $\mu$m and (c, f) $d_p = 120$ $\mu$m.

decreases due to the intense particle rain inside the bubble and the penetration of the bubble wake in the interior of the bubble, which promotes the reduction of the bubble diameter. In contrast, under the same vibration conditions, the bubbles rising in the bed of particles of 60 $\mu$m tend to drift to the central section of the bed, and that promotes bubble coalescence and, hence, tends to increase the bubble diameter. For these particles of 60 $\mu$m, the increase of bubble diameter due to coalescence seems to be predominant over the decrease due to the penetration of the wake in the bubble. Finally, the bed with particles of 120 $\mu$m yields bubbles with less wake penetration and rain of particles and that seems (in view of Figure 6.8) to be unable to hidden the effect of the bubble growth promoted by coalescence that occurs owing to the increase of the bed shaking when the vibration amplitude is augmented.

The increase of the mean bubble diameter with the vibration amplitude is particularly clear for the cases of high vibration frequencies combined with high $U/U_{mf}$, in which the mean bubble diameter grows with the amplitude of vibration while the bubble fraction remains nearly constant (Figure 6.5) and the mean bubble density decreases (Figure 6.6).

This effect is more intense at high gas velocities because the resulting bubbles are bigger and closer so that bubbles are more prone to coalesce. The closeness of bubbles is also promoted by the confinement of bubbles to the central part of the bed for higher vibration strengths, as indicated in Section 6.3.1.

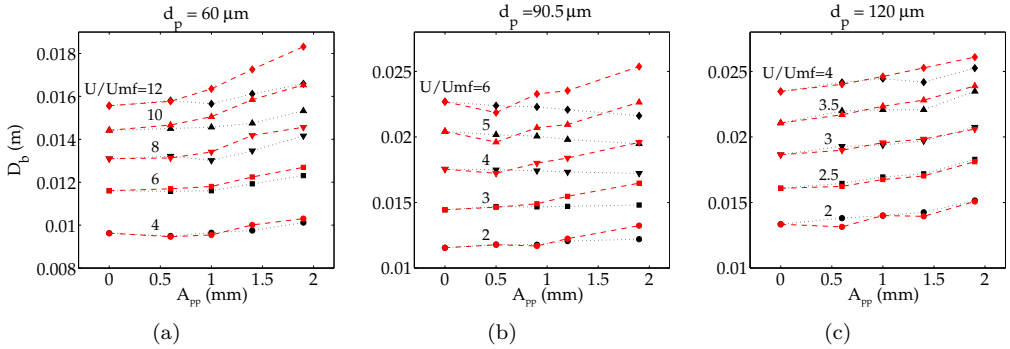


**Figure 6.8:** Mean bubble diameter as a function of the vibration amplitude for different mean particle diameters and superficial gas velocities: (a) $d_p = 60$ $\mu$m, (b) $d_p = 90.5$ $\mu$m, (c) $d_p = 120$ $\mu$m. Black symbols $f = 10$ Hz and red symbols $f = 20$ Hz.

Figure 6.9 shows the vertical velocity of bubbles averaged over the whole bed (i.e. bubbles within 5 to 40 cm above the distributor). In general, the average vertical velocity of bubbles decreases for $f = 20$ Hz (Figure 6.9(d-f), whereas for $f = 10$ Hz it only decreases for the particles of $d_p = 60$ $\mu$m (Figure6.9(a)). For the particles of 60 $\mu$m and at sufficiently high $U/U_{mf}$ and small vibration frequencies (Figure 6.9(a-c)) bubble absolute velocity increases with $A_{pp}$ as a consequence of the growth of the bubble diameter (Figure 6.8) due to both the larger excess of gas, produced by the decrease of the effective $U_{mf}$ caused by vibration (Mawatari *et al.*, 2003), and the coalescence of bubbles (Figure 6.6). However, in this case, the vibration strength is not enough to reduce the velocity of the bubbles except for the case $U/U_{mf} = 4$, in which the bubbles are sufficiently small to be affected by vibration as if they were an isolated bubble. Also, at small vibration frequencies, the gulf stream motion of particles drifts upwards the bubbles in the middle of the bed so that their velocity increases with the vibration amplitude. This increase of the bubble velocity with the vibration amplitude is not observed in Figure 6.9(b, c) for the particles of 90.5 and 120 $\mu$m since their fluidization leads to bigger bubbles that are generally less affected by vibration than those in the bed with particles of 60 $\mu$m mean diameter.

Besides, in Figure 6.9 there is a critical value of $U/U_{mf}$ (function of the particle size and the frequency of vibration) below which the bubble velocity decreases with the amplitude of vibration because bubbles are sufficiently small to scarcely interact with

other bubbles and they behave most of the time like if it were isolated bubbles. In that case, the mean velocity of bubbles decreases with amplitude, as was justified before in Figure 6.7. This can be clearly observed in Figures 6.9(d-f). However, at higher gas velocities and vibration amplitudes, the coalescence of bubbles due to their confinement to the central section of the bed increases the velocity of bubbles and that partially counteracts the decrease of bubble velocity commented above. This results in a less significant decrease of the mean bubble velocity compared to the cases of lower gas velocities. For low vibration frequencies ($f = 10$ Hz) and particles of 90.5 and 120 $\mu$m (Figure 6.9(b,c)), the change of the vibration amplitude does not greatly affect the mean velocity of the bubbles.

To sum up, it can be observed in Figures 6.8 and 6.9 that both the mean bubble diameter and velocity are more sensitive to changes in the vibration amplitude for vibration frequencies of $f = 20$ Hz than for $f = 10$ Hz. Which suggests that the effect of vibration on the bed and bubble dynamics is enhanced at high vibration strengths.

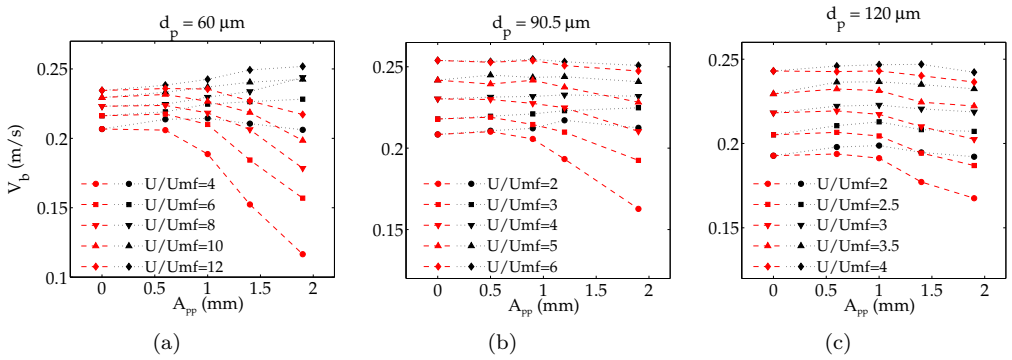


**Figure 6.9:** Mean bubble absolute velocity as a function of the vibration amplitude for different mean particle diameters and superficial gas velocities: (a) $d_p = 60$ $\mu$m, (b) $d_p = 90.5$ $\mu$m, (c) $d_p = 120$ $\mu$m. Black symbols $f = 10$ Hz and red symbols $f = 20$ Hz.

Figure 6.10 shows the relation between the bubble absolute velocity and diameter in the bed operated at the highest frequency tested ($f = 20$ Hz) and at an intermediate value of $U/U_{mf}$ for the particles of 60, 90.5 and 120 $\mu$m mean diameters. Figure 6.10 is obtained by dividing in 20 intervals the total range of bubble diameters found in the bed and assigning the bubbles to any of the intervals depending of their diameter. Each point in Figure 6.10 represents the average value of the bubble diameter and velocity in each interval. A clear increasing trend of the bubble velocity with the bubble diameter is observed in Figure 6.10 for the three types of particles under study and the vibration amplitudes tested. Accordingly with previous reports (Kunii & Levenspiel, 1991), for

conventional fluidized beds, the bubble velocity is proportional to the square root of the bubble diameter. This is true for the cases of no vibration in Figure 6.10. However, this trend changes when introducing vibration in the system and a nearly linear trend of bubble velocity with bubble diameter is observed in Figure 6.10 in the lower half of the bed.

Also, Figure 6.10 clearly shows that, for small bubbles, the bubble velocity decreases with the amplitude of vibration for a given diameter of bubble and keeping constant the superficial gas velocity. Generally, large bubbles (i.e. $D_b > 0.03$ m) are much less affected by the bed vessel vibration than small bubbles and present velocities that are even similar to those obtained without vibrating the bed. Also, these large bubbles are typically located in the upper half of the bed, where bubbles tend to coalesce and are deformed prior to their eruption, which explains why bubble velocity is more disperse in Figure 6.10 for $D_b \gtrsim 0.05$ m.

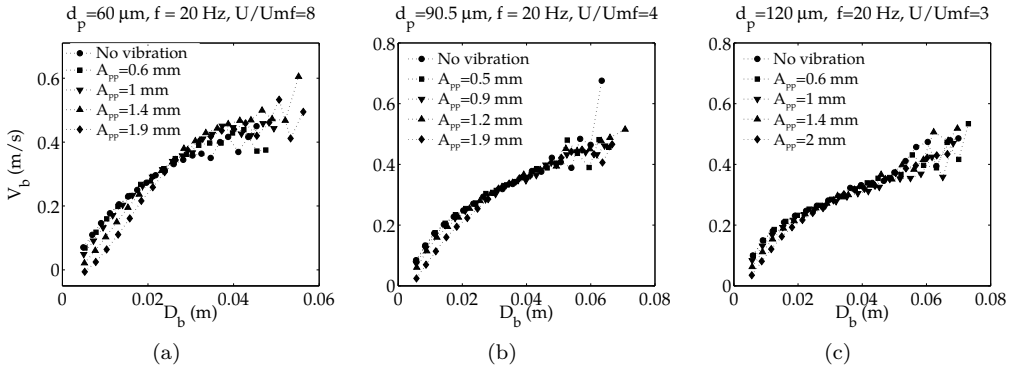


**Figure 6.10:** Mean bubble absolute velocity as a function of the mean bubble diameter for a vibration frequency $f = 20$ Hz and different vibration amplitudes and particle diameters: (a) $d_p = 60$ $\mu$m, (b) $d_p = 90.5$ $\mu$m, (c) $d_p = 120$ $\mu$m.

Alternatively, Figure 6.11 depicts the relation between the absolute velocity and diameter of bubbles averaged in all the bed (i.e. $y = 0.05 - 0.4$ m). Each curve in Figure 6.11 contains 5 points that are taken from Figures 6.8 and 6.9 at a given vibration amplitude, $A_{pp}$, for 5 different values of $U/U_{mf}$. Figure 6.11 also includes results for low and intermediate vibration frequencies ($f = 10$ Hz and $f = 15$ Hz). The solid lines in Figure 6.11 connect data points with the same vibration amplitude, whereas the dotted lines are obtained after fitting of the points having the same superficial velocity and are included to facilitate the visual inspection of the results. Therefore, the increase of bubble size in Figure 6.11 from left to right is principally caused by the increase of $U/U_{mf}$ and not by bubble coalescence as a function of the distance to the distributor. That explains why

the slope of the curves does not decay for large bubble diameters as in Figure 6.10. Thus, the results depicted in Figure 6.11 reflect the global behavior of bubbles in the bed, and each point corresponds to an individual experiment.

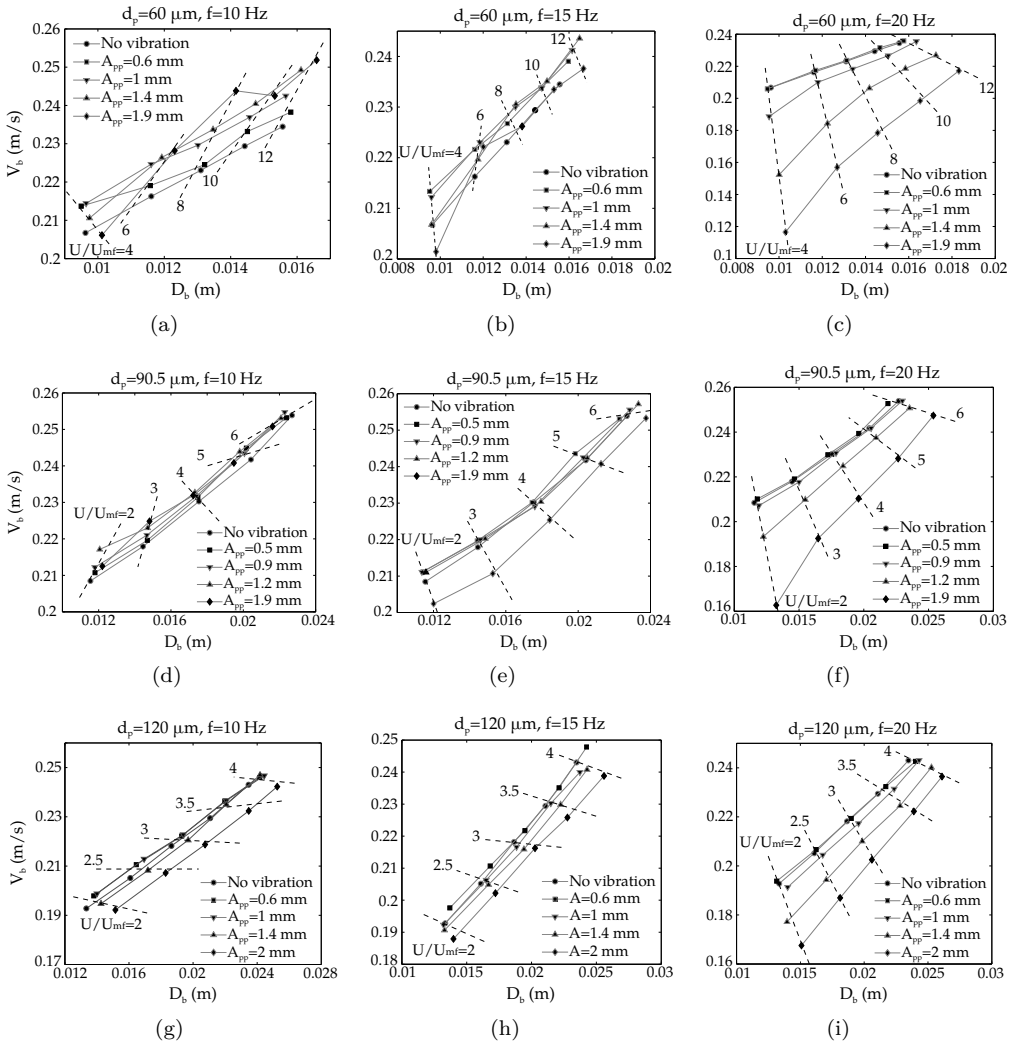


**Figure 6.11:** Mean bubble velocity as a function of the mean bubble diameter for different vibration amplitudes and frequencies. The superficial gas velocity increases from left to right in each curve. (a-c) $d_p$ =60 $\mu$m, (d-f) $d_p$ = 90.5 $\mu$m, (g-i) $d_p$ = 120 $\mu$m.

There are three effects affecting the bubble velocity in vibration that have been observed in previous figures and can be used to understand Figure 6.11. Firstly, if the bubble is sufficiently separated from other bubbles and the vibration strength is high (i.e. higher frequency of vibration) it behaves as if it was an isolated bubble due to the

scarce interaction with the surrounding bubbles. In this situation, an increase of vibration amplitude produces a decrease of bubble velocity, for a given bubble size, as commented before when Figure 6.10 was analyzed and in Chapter 4. This effect causes that at high vibration frequencies, e.g. Figure 6.11(c,f,i), the mean bubble velocity in the bed clearly decreases when increasing the vibration amplitude for a given superficial velocity ratio $U/U_{mf}$, this promotes a negative slope of the dashed lines in Figure 6.11 (c,f,i). This slope decreases when increasing the superficial gas velocity, which indicates that the velocity of larger bubbles (due to the higher $U/U_{mf}$) is less affected by the vibration amplitude than for smaller bubbles. The bubble velocity decrease with vibration amplitude is still observed, to a lesser extent, at intermediate frequencies on all the particle sizes (i.e. $f = 15$ Hz, Figures 6.11(b,e,h)), and at low frequencies and the larger particle diameter ($d_p = 120$ $\mu$m). As can be seen on the left hand side of Figure 6.11, the decrease of bubble velocity with $A_{pp}$ is more significant for lower superficial velocities, for which bubbles are smaller and interaction between bubbles is still reduced.

Secondly, on passing from no vibration to vibration, the mean bubble diameter grows due to a decrease of the effective $U_{mf}$ (as seen in Figure 6.8). This effect is also observed in Figure 6.11 in which $D_b$ decreases with $A_{pp}$ for a given $U/U_{mf}$. Exception of this is Figure 6.11(d) for large values of $U/U_{mf}$ where the experimental points are very close and the effect of $A_{pp}$ is unclear. Thirdly, as seen in Section 6.3.1, vibration of the bed vessel produces recirculation of particles in the bed, creating a net upward motion of particles in the center of the bed whereas by the lateral walls the motion of particles is downwards. This upward motion of particles is higher if superficial gas velocities or the amplitude of vibration are increased because more kinetic energy is introduced in the system (Zeilstra *et al.*, 2013). Owing to the upward motion of particles, bubbles tend to be faster because they are normally confined to the central section of the bed and they interact more with each other (Zhou *et al.*, 2004, 2005; Mawatari *et al.*, 2005), and, in consequence, bubbles cease to behave as if they were isolated. The increase of the interaction of bubbles, together with the growth of bubbles due to coalescence tends to increase the bubble velocity, as seen in Section 6.3.2, and this occurs when bubbles are sufficiently far from the distributor. For example, in Figure 6.11(a) an increase of vibration amplitude promotes a growth of the bubble velocity due to the presence of bigger bubbles and the confinement of the bubble path to the central section of the bed (see also Figure 6.9(a)). In this situation the velocity of bubbles is mainly affected by confinement, coalescence and diameter growth because the vibration frequency is small in contrast to Figure 6.11(c,f,g) where the vibration frequency is high. In the case of particles of intermediate diameter, $d_p = 90.5$ $\mu$m, and low vibration frequency, $f = 10$ Hz, no clear trend is found for bubble velocity because probably the confinement of the bubble path and bubble coalescence are competing against the commented effect of the amplitude of

vibration. It is clear from Figure 6.11 that adequate selection of vibration amplitude and frequency can be used to influence and have some control on the bubble behavior for a given particle size and superficial gas velocity.

### 6.3.3 Oscillatory behavior of bubbles

#### Center of mass of the bed

Figure 6.12 shows the normalized oscillation of the center of mass of the bed for different superficial gas velocities and for each of the particle types employed. Fixed vibration conditions of $A_{pp} = 2$ mm and $f = 20$ Hz were chosen when varying the superficial gas velocity as they provide the maximum vibration strength studied, as seen in Table 6.2. Normalization of the variables shown in Figure 6.12 is carried out with the semiamplitude ($A_{pp}/2$) of the bed vessel displacement. Note that the results regarding the oscillation of the center of mass of the bed are computed in an absolute system of reference. Oscillations relative to the bed vessel position can be obtained by subtracting the bed normalized displacement from the curves shown in Figure 6.12.

Figure 6.12 shows that the normalized amplitude of the oscillation of the center of mass decreases as the superficial velocity increases. This tendency is followed by the three types of particles employed. Besides, the amplitude of the oscillation of the center of mass decreases when increasing the particle size from Figure 6.12(a) to Figure 6.12(c). In general, for the range of $U/U_{mf}$ used in this work, the mean bubble size and the bubble fraction increase for the larger particles used (see Chapter 4). Also, when increasing $U/U_{mf}$ the mean bubble size increases. An explanation for this is that the effect of the vibration of the bed vessel on the oscillation of the center of mass of the bed is damped by the presence of larger bubbles in the system, which explains the low amplitude oscillation of the center of mass for the particles of 120 $\mu$m (see Figure 6.12(c)) and for larger $U/U_{mf}$ in Figure 6.12.

In Figure 6.12 the oscillation of the center of mass position is nearly opposed in phase to the oscillation of the bed vessel (i.e. $\phi_d = \pi$ rad). This indicates that the bed volume is cyclically compressed and expanded, i.e. when the bed vessel moves upwards, the bed volume tends to contract and vice versa, as it has been also reported in (Barletta *et al.*, 2013) and in Chapters 3 to 5. As a reference, Figure 6.12 also includes the oscillation of the free surface of the bed, normalized with $A_{pp}/2$, for the case of $A_{pp} = 1.9 - 2$ mm, $f = 20$ Hz and relative superficial velocities of $U/U_{mf} = 4, 2$ and 2 for the particles of $d_p = 60$, 90.5 and 120 $\mu$m, respectively, as these superficial velocities show the greatest oscillation of the center of mass position in Figure 6.12. The surface of the bed presents a phase similar to that of the center of mass of the bed for the three types of particles

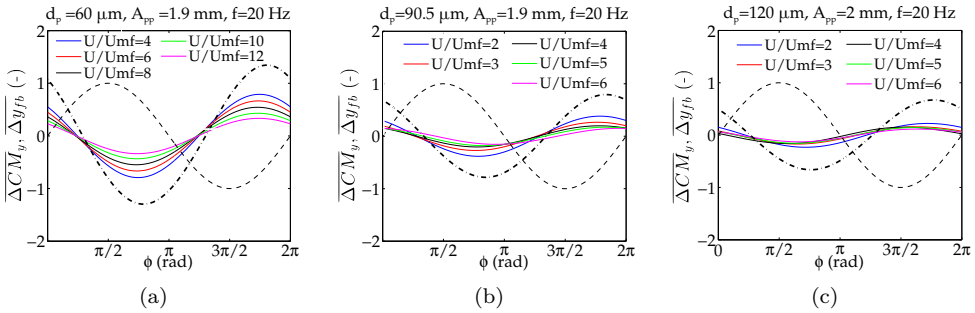


**Figure 6.12:** Oscillation of the vertical position of the center of mass of the bed bulk. Variation with the superficial gas velocity for three different particle diameters: (a) $d_p = 60$ $\mu$m, (b) $d_p = 90.5$ $\mu$m and (c) $d_p = 120$ $\mu$m. The dashed and dashed-dotted lines indicate, respectively, the normalized oscillations of the bed vessel and the free surface of the bed.

under study, which confirms that there is a cyclic compression and expansion of the bed bulk. This suggests that the lower and the upper sections of the bed present opposed displacements between them. That is, when the particles belonging to the upper section of the bed are moving downwards, the lower section of the bed bulk is moving up as it is being pushed by the upward displacement of the bed vessel ($\phi$ between $3\pi/2$ rad and $\pi/2$ rad of the next cycle). On the contrary, when the bed vessel commences to move downwards, the particles belonging to the upper section of the bed maintain their upward inertial motion and, at the same time, the lower section of the bed commences to move downwards ($\phi$ between $\pi/2$ rad and $3\pi/2$ rad), which promotes the expansion of the bed bulk. As the mean particle size decreases, the oscillation of the surface of the bed is larger due, probably, to the smallest bubbles present in the system and also to the less inertia of the smaller particles. In Figure 6.12, an increase of the superficial gas velocity and, thus, of the mean diameter of the bubbles in the system, does not greatly affect the phase $\phi_d$ of the oscillations of the center of mass, which are mainly driven by the cyclic expansion and compression of the bed volume.

Figure 6.13 shows the effect of varying the vibration amplitude, $A_{pp}$, on the normalized oscillation of the center of mass of the bed for a given vibration frequency ($f = 20$ Hz). As in Figure 6.12 for the normalized oscillation of the free surface of the bed, in Figures 6.13(a-c) the relative superficial velocities of $U/U_{mf} = 4, 2$ and 2 were selected. In Figure 6.13, an increase of the vibration amplitude barely affects the normalized oscillation amplitude of the center of mass of the bed, since the oscillation of the center of mass is normalized with $A_{pp}/2$. This reveals a linear increase of the amplitude of the actual oscillation of the center of mass with $A_{pp}$ ($\Delta CM_y = \overline{\Delta CM}_y \cdot A/2$). As in Figure 6.12, the effect of vibration on the oscillation of the center of mass becomes weaker as the particle size is increased, leading to smaller amplitudes of the oscillation

of the bed bulk. This is again attributed to the presence of larger bubbles in the system, which damp the oscillation of the center of mass of the bed. In addition, the bed filled with the smaller particles seems to be more affected by vibration. In this case, as seen in Section 6.3.1, the convective circulation of particles in the bed is more intense, which is attributed to their less inertia and to the smaller proportion of particles colliding with the bed walls, which reduces wall friction (Hernández-Jiménez *et al.*, 2013). This may also cause a larger oscillation of the center of mass of the bed bulk.

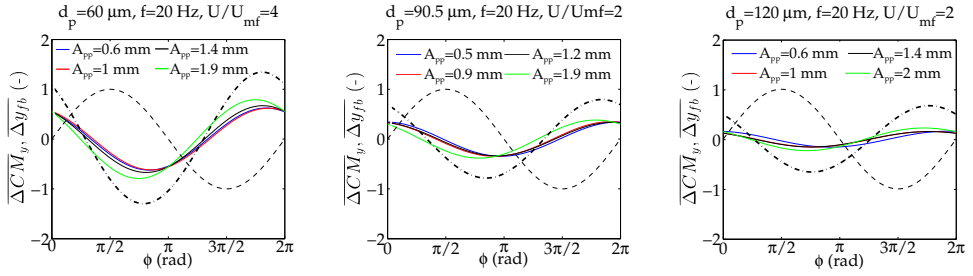


(a) (b) (c)

**Figure 6.13:** Oscillation of the vertical position of the center of mass of the bed bulk. Variation with vibration amplitude for three different particle diameters: (a) $d_p = 60$ $\mu$m, (b) $d_p = 90.5$ $\mu$m and (c) $d_p = 120$ $\mu$m. The dashed and dashed-dotted lines indicate, respectively, the normalized oscillations of the bed vessel and the free surface.

Similarly to Figure 6.13, in Figure 6.14 the effect of the vibration frequency is investigated for a vibration amplitude of $A_{pp} = 1.9 - 2$ mm. The phase delay $\phi_d$ of the oscillation of both the center of mass and the surface of the bed increases when increasing the vibration frequency in Figure 6.14 ($f = 15 - 20$ Hz), indicating that the bed follows more easily low frequency vibrations than high frequency ones, probably due to the inertial displacement of the bed bulk. For vibration at low frequencies, $f = 10$ Hz, the lower section of the bed follows the displacement of the bed base because the gravity acceleration is greater than the acceleration of the displacement of the bed vessel ($\Lambda < 1$). The phase at which the compression of the bed bulk volume commences, which can be associated to the downward displacement oscillation of the center of mass of the bed bulk, is delayed with regard to the phase at which the bed vessel starts to move upwards (which corresponds to $\phi = 3\pi/2$ rad). In the phase $\phi = 3\pi/2$ rad, the bed center of mass moves downwards and the bed bulk is compressed because the particles in the upper section of the bed maintain their downward displacement due to their inertia. Generally, the amplitude of the oscillation of the center of mass of the bed in Figure 6.14 is damped when the oscillation of the center of mass of the bed is in opposition in phase (i.e. $f = 15$ Hz) with the oscillation of the bed vessel. In this situation, the rise (fall) of the

center of mass position caused by the upward (downward) displacement of the bed vessel is partially counteracted by the compression (expansion) of the bed bulk volume, so that the net amplitude of the oscillation of the center of mass of the bed is comparatively low.

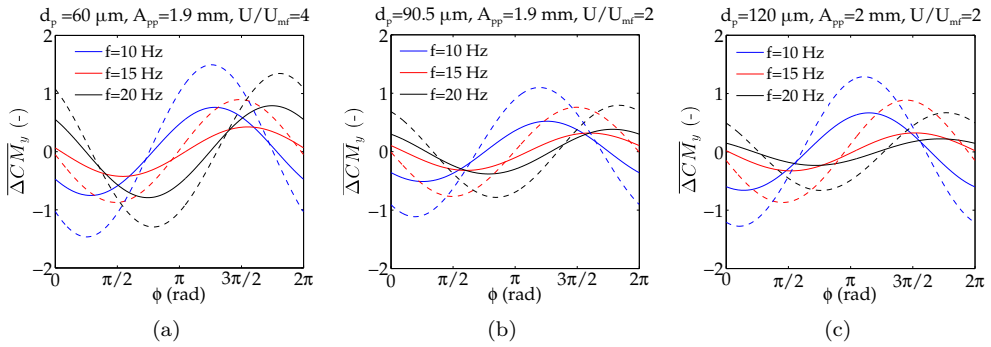


**Figure 6.14:** Oscillation of the vertical position of the center of mass and the surface of the bed bulk. Variation with vibration frequency for three different particle diameters: (a) $d_p = 60$ $\mu$m, (b) $d_p = 90.5$ $\mu$m and (c) $d_p = 120$ $\mu$m. The straight and the dashed lines indicate, respectively, the normalized displacement of the bed center of mass and the bed surface.

### Bubble diameter

From a qualitative point of view, it was observed in the experiments of this work that there are three effects mainly affecting the oscillation of the bubble diameter in the bed. These effects are schematized in Figure 6.15 for a bubble placed in the lower and upper sections of the bed (see Chapter 2). Firstly, for a bubble situated in the upper section of the bed (Figure 6.15(a)) when the bed phase is between $\phi = 0 - \pi$ rad, the bubble diameter is decreased due both to the compression of the bed bulk in the upper section of the bed and the wake penetration inside the bubble. For a phase $\phi = \pi - 2\pi$ rad, the bubble diameter in the upper section of the bed increases due to the expansion of the bed volume. An opposed behavior was found for a bubble located in the lower section of the bed 6.15(b). In this case, when the phase of the bed vessel is between $\phi = 0 - \pi$ rad, the bubble diameter of the bubble tends to decrease due to the compression of the bed bulk in that region. If the phase is $\phi = \pi - 2\pi$ rad, there is a growth of the bubble size caused by the bed expansion. This growth may be damped or reversed by the wake penetration and the particle rain inside the bubble. The different impacts on the oscillation of the bubble diameter shown in Figure 6.15 are quantitatively analyzed by means of the oscillation of the bubble diameter in Figures 6.16, 6.17 and 6.18 for particle diameters of 60, 90.5 and 120 $\mu$m, respectively.

In Figure 6.16, different superficial velocities are tested at the maximum vibration

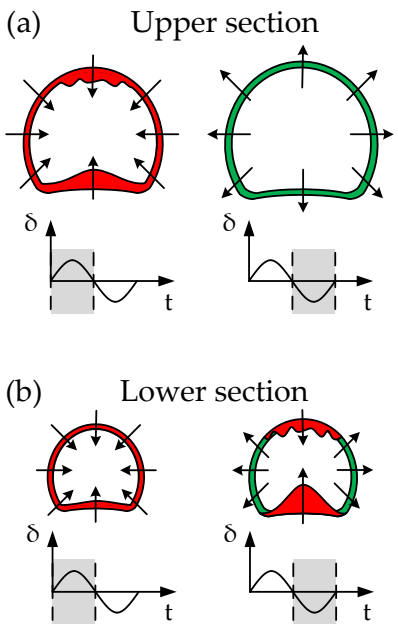


**Figure 6.15:** Schematic behavior of the oscillation of the bubble diameter in the lower and upper sections of the bed as a function of the vibration phase. The green contours represent the growth of the bubble diameter due to the oscillation of the bed bulk. The red contours schematize the oscillation of the bubble diameter caused by the compression of the bed bulk (left figures) and the penetration of the wake and the rain of particles inside the bubble (lower right figure).

strength (i.e. $A_{pp} = 1.9 - 2$ mm and $f = 20$ Hz). Different vibration amplitudes (Figure 6.17) and frequencies (Figure 6.18) are analyzed at an intermediate $U/U_{mf}$ for each type of particle (i.e. $U/U_{mf} = 8$ for the particles of 60 $\mu$m, $U/U_{mf} = 4$ for the particles of 90.5 $\mu$m and $U/U_{mf} = 3$ for the particles of 120 $\mu$m). As in the previous chapters, the bubble diameter oscillation is normalized with the moving average of the bubble diameter in an interval $[-T/2, T/2]$ in order to obtain results independent of the size of each bubble in the experiment:

$$\overline{\Delta D}_{bi} = \frac{D_{bi} - \widehat{D}_{bi}}{\widehat{D}_{bi}} \tag{6.1}$$

where $D_{bi}$ is the instantaneous bubble diameter and $\overline{D}_{bi}$ is the moving average of $D_{bi}$ calculated from $-T/2$ to $T/2$ as defined in Chapter 2.

As mentioned in Section 6.3.3, vibration of the bed vessel promotes the expansion and compression of the bed bulk. In agreement with previous Chapters 4 and 5, devoted to isolated bubbles, when the bed is expanded, the higher bed voidage probably allows

the bubble diameter to grow more easily than when the bed is compressed. This causes the bubble diameter to decrease when the bed vessel is moving up and the bed bulk is compressing ($\phi = 3\pi/2 - \pi/2$ rad) and to increase when the bed vessel is moving down and the bed bulk is expanding ($\phi = \pi/2 - 3\pi/2$ rad).

It can be observed in Figure 6.16 that the bubble diameter oscillates more vigorously for the particles of 60 $\mu$m than for the particles of 90.5 and 120 $\mu$m. For the particles of 60 $\mu$m in Figure 6.16(a), the bubbles in the upper section of the bed present a phase delay close to $\phi_d = \pi$ rad, whereas the bubbles in the lower section of the bed oscillate with a phase close to that of the bed vessel, $\phi_d = 0$ rad. In Figure 6.16(c), the amplitude of the oscillations of bubble diameter remains around the same values with variations of $U/U_{mf}$. This indicates that the oscillations of the bubbles present in the bed with particle diameter $d_p = 120$ $\mu$m are mainly affected by the overall oscillation of the bed bulk volume (i.e. the bubble diameter presents a larger oscillation when the bed volume is expanded and vice versa) and depend linearly on the size of the bubble.

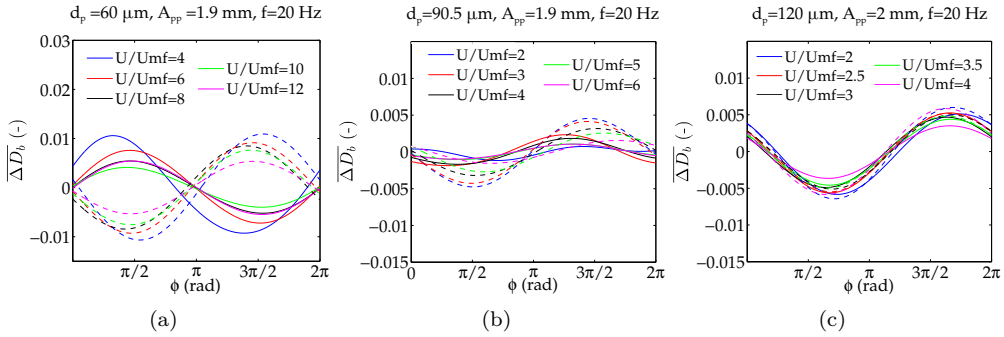


**Figure 6.16:** Oscillation of the normalized bubble diameter: variation with the superficial gas velocity. Results are obtained for three different particle diameters: (a) $d_p = 60$ $\mu$m, (b) $d_p = 90.5$ $\mu$m and (c) $d_p = 120$ $\mu$m. The solid lines correspond to bubbles in the lower section of the bed ($y = 0.1 - 0.2$ m) and dashed lines to bubbles in the upper section of the bed ($y = 0.3 - 0.4$ m).

As mentioned in Figure 6.15, inspection of the instantaneous images of the vibrated bed (e.g. Figure 2.7(a)) showed that the bubble diameter is also affected by the penetration of the bubble wake in the interior of the bubble. This observation was also reported for isolated bubbles Chapter 4. As can be seen in Figure 2.7(a), the wake of the bubble penetrates into the bubble reducing the bubble visible area and the bubble equivalent diameter. This wake penetration phenomenon is not simultaneous for all the bubbles but propagates upwards; that is, bubbles in the lower section of the bed are penetrated by their wake in an earlier phase than bubbles in the upper section with a relative phase delay between the upper and the lower sections of the bed of approximately $\Delta\phi = \pi$ rad.

This effect is schematized in Figure 6.15, where the wake penetrates the bubbles in the lower section of the bed in the phase interval $\phi = 3\pi/2 - 2\pi$ rad and in the upper section of the bed in the phase interval $\phi = 0 - \pi/2$ rad. Also, wake penetration affects the oscillation of the bubble diameter of the particles of 60 $\mu$m in Figure 6.16(a) more vigorously than the diameters of the particles of 90.5 $\mu$m and 120 $\mu$m. This is probably due to the less inertia of the 60 $\mu$m particles and the presence of smaller bubbles (in average) in the bed with these particles. It was also observed that the volume of the particles dragged by the wake is not directly proportional to the bubble diameter but the bubble size has negligible influence on it. This causes that the normalized value of the oscillation of bubble diameter caused by the wake is more pronounced for smaller bubbles. In the lower section of the bed, where bubbles are small and, hence, the effect of the wake penetration is more pronounced, the oscillation of the bubble diameter reaches a maximum when the bed vessel position is at its maximum height and starts moving downwards ($\phi = \pi/2$ rad in Figure 6.16(a)). In this case, the cyclic wake penetration in the bubble interior is predominant over the bubble growth caused by the bed bulk expansion. In the upper section of the bed, owing to the presence of larger bubbles, the effect of the wake penetration on the oscillation of the bubble diameter is smaller, which causes the bubble diameter to grow mainly by the expansion of the bed bulk. Thus, as in Figure 6.16(c) for the particles of 120 $\mu$m, the phase delay of the diameter oscillations in Figure 6.16(a) is $\phi_d = 3\pi/2$ rad (i.e. opposition in phase between the oscillation of bubble diameter and the bed vessel displacement). The smaller wake penetration with $D_b$ may also explain the decrease of the bubble diameter oscillation with an increase of the superficial gas velocity in Figure 6.16(a).

The third effect affecting bubble diameter is the rain of particles in their interior. During the experiments, it was observed that this effect was of relative importance for small bubbles in cases in which the frequency of vibration was high and the vibration amplitude was small. Although this effect is reduced by the use of an adaptive threshold, for small vibration amplitudes the rain of particles tends to cyclically hinder or increase the bubble visible area, which respectively decreases or increases the bubble equivalent diameter. In particular, an increase of the particle rain in the lower section of the bed seems to appear in a phase close to $\phi = 3\pi/2 - \pi/2$ rad (i.e. the bed bulk is compressing) although its impact on the bubble diameter is difficult to separate from the reduction of the bubble diameter caused by the penetration of the bubble wake. The presence of these combined effects on the oscillation of the bubble diameter may explain the higher amplitude of the oscillations of the bubble diameter when decreasing the vibration amplitude to $A_{pp} = 1$ mm in Figure 6.17(a). In contrast, larger bubbles in the upper section of the bed in Figure 6.17(a) are less affected by the particles rain and are mainly affected by the oscillation of the volume of the bed bulk close to the free surface

of the bed. The effect of particle rain is less significant as the particle diameter increases because gradients in the thickness direction are more constrained. In view of Figures 6.16(c), 6.17(c) and 6.18(c) when the particle diameter increases ($d_p = 120$ $\mu$m), the main effect on the oscillation of bubble diameter is the cyclic compression and expansion of the bed bulk because, in this case, bubbles oscillate with approximately the same phase ($\phi_d = \pi$ rad) regardless they are located in the lower or upper section of the bed. Thus, little variation of $\overline{\Delta D}_b$ is observed with $A_{pp}$ in Figure 6.17. In consequence, for the 120 $\mu$m particles, the magnitude of the oscillation of the bubble diameter, $\overline{\Delta D}_b D_b$, increases when increasing the amplitude of the oscillation, as $D_b$ increases with $A_{pp}$ (see Figure 6.8.

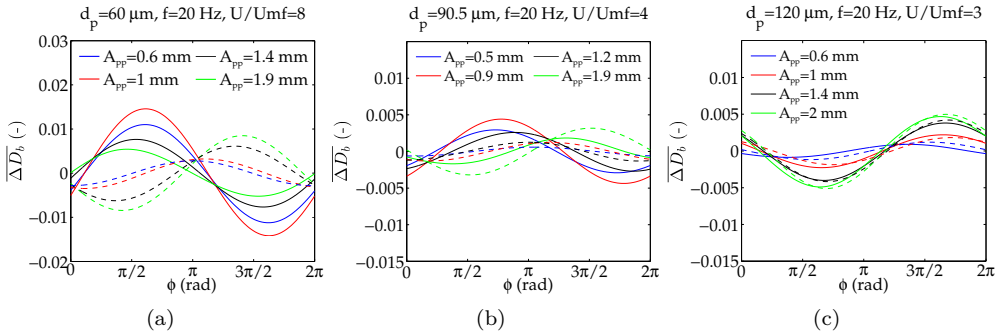


(a) (b) (c)

**Figure 6.17:** Oscillation of the normalized bubble diameter: variation with the vibration amplitude. Results are obtained for three different particle diameters: (a) $d_p = 60$ $\mu$m, (b) $d_p = 90.5$ $\mu$m and (c) $d_p = 120$ $\mu$m. The solid lines correspond to bubbles in the lower section of the bed ($y = 0.1 - 0.2$ m) and dashed lines to bubbles in the upper section of the bed ($y = 0.3 - 0.4$ m).

Regarding the effect of vibration frequency on the amplitude of the oscillation of bubble diameter, it can be observed in Figure 6.18 that $f$ has generally a stronger effect in the lower section than in the upper section of the bed. This is probably due to the fact that the previously commented effects that modify the bubble diameter are more noticeable for smaller bubbles situated in the lower section of the bed. Besides, when the vibration frequency is increased, bubble coalescence is promoted by the confinement of the bubble path to the central section of the bed, which is especially noticeable for the particles of 60 $\mu$m, as in Section 6.3.2. Confinement leads to larger bubble interaction and this may reduce the effect of vibration on the oscillation of bubble diameter. The combination of all these effects can be complex, producing an apparent lack of tendency in the variation of the oscillation amplitude of $\overline{\Delta D}_b$ with the vibration frequency in the lower section of the bed for the particles of 60 $\mu$m in Figure 6.18(a) and 90.5 $\mu$m in Figure 6.18(b). For the particles of 120 $\mu$m in Figure 6.18(c), the amplitude of oscillation of bubble diameter

in the lower section of the bed decreases with the vibration frequency. Note that for the isolated bubbles rising in a bed reported in Chapter 4, when the frequency of oscillation is increased, the amplitude of bubble oscillation tends to increase in the lower section of the bed, whereas it slightly decreases in the upper section of the bed. The lack of bubble confinement and interaction when bubbles rise isolated may explain the differences between the observations in Chapter 4 and the present experiments.

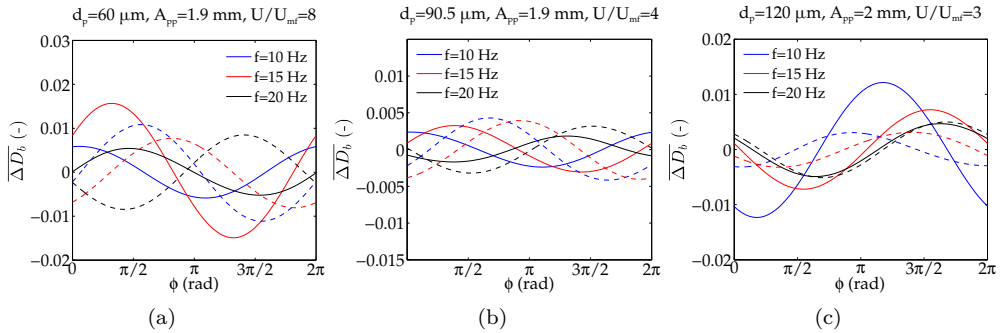


**Figure 6.18:** Oscillation of the normalized bubble diameter: variation with the vibration frequency. Results are obtained for three different particle diameters: (a) $d_p = 60$ $\mu$m, (b) $d_p = 90.5$ $\mu$m and (c) $d_p = 120$ $\mu$m. The solid lines correspond to bubbles in the lower section of the bed ($y = 0.1 - 0.2$ m) and dashed lines to bubbles in the upper section of the bed ($y = 0.3 - 0.4$ m).

An interesting result arising from Figure 6.18 is that the phase delay $\phi_d$ of the mean bubble diameter oscillation is strongly affected by the frequency of vibration, as in Figure 6.14 for the oscillation of the center of mass of the bed. Higher frequencies of vibration yield a higher delay between the bed vessel displacement and the oscillations of the mean bubble diameter (see Section 6.3.3). This effect is clear for small particle diameters ($d_p = 60$ $\mu$m), since the smaller bubbles present in the bed with these particles are more sensitive to vibration, as commented before. Also, in Figure 6.18(a), there exists a positive phase delay between particles situated in the lower and the upper sections of the bed.

For the three types of particles tested, there exists a clear upward trend of the phase delay of the oscillation of the bubble diameter in the upper section of the bed in Figure 6.18. When the vibration frequency increases, the period of vibration decreases. If the time delay of the information to reach the upper section of the bed is similar within the range of frequencies tested, the phase delay for low vibration frequencies increases, as the fraction of period for the information to reach the top of the bed is smaller. A similar trend on the phase delay of the oscillation of bubble diameter is observed for bubbles situated in the lower section of the bed in Figure 6.18, which implies that the bubble

diameter oscillation is strongly affected by a wave propagation mechanism originated at the bottom of the bed and that modifies the way the bubble diameter oscillates in the bed. In Figure 6.18(c), it can be observed that the phase of the oscillation of bubble diameter in the upper section of the bed is similar to that of the center of mass of the bed, which suggests that, for the larger particles tested, the bubble diameter oscillation is mainly affected by the cyclic oscillation of the bed bulk.

### Bubble position and velocity

The effect of the superficial gas velocity and the vibration amplitude on the oscillation of the bubble position and velocity is studied in this section, whereas the effect of the vibration frequency will be studied in terms of the phase delay of the position and velocity oscillations (Section 6.3.3). In this case, to link bubble positions and velocities with the motion of the bed vessel, the oscillation of the bubble displacement is normalized with the semiamplitude of the vessel displacement $A_{pp}/2$. In addition, the amplitude of the oscillation of the bubble velocity is normalized with, $A_{pp}\omega/2$, where $\omega = 2\pi f$ is the angular frequency of the vessel vibration.

Figure 6.19 shows the oscillation of the bubble position and the bubble velocity for different superficial gas velocities and for all the particles under study. Figure 6.19 also includes the normalized oscillation of the bed surface and the bed center of mass (see Figure 6.12). It can be observed that the oscillation of the normalized bubble position is similar to that of the bubble velocity but with a phase delay close to $\phi = \pi/2$ rad because the oscillation is sinusoidal (i.e. for a bubble located in the lower section of the bed the bubble position oscillates proportionally to $\sin(\omega t - \phi_{d,y_b})$ with a phase $\phi_{d,y_b}$ close to $\pi/2$ rad whereas the bubble velocity oscillates with the derivative of the position oscillation, $\omega\cos(\omega t - \phi_{d,y_b}) = \omega\sin(\omega t - \phi_{d,V_b})$, with a phase $\phi_{d,V_b}$ close to $3\pi/2$ rad). Thus, to avoid redundancy of the results, only figures concerning bubble velocity are presented in the subsequent paragraphs.

In Figure 6.19, the amplitude of the normalized oscillation of the bubble velocity in the lower section of the bed is barely affected by the superficial gas velocity. The same behavior is observed for the oscillation of the bubble velocity as a function of the vibration amplitude shown in Figure 6.20. This indicates that the oscillation of the bubble velocity in the lower section of the bed is mainly affected by the oscillation of the bed vessel and increases linearly with $A_{pp}$. In the lower section of the bed, the presence of larger bubbles, caused by an increase of $U/U_{mf}$, seems to have a negligible effect on the normalized amplitude of the oscillations, especially for the case of large particles (Figure 6.19(c) and 6.19(f)). Besides, in Figure 6.19, the amplitude of the oscillations of the bubbles position and the velocity of bubbles situated in the upper section of the bed

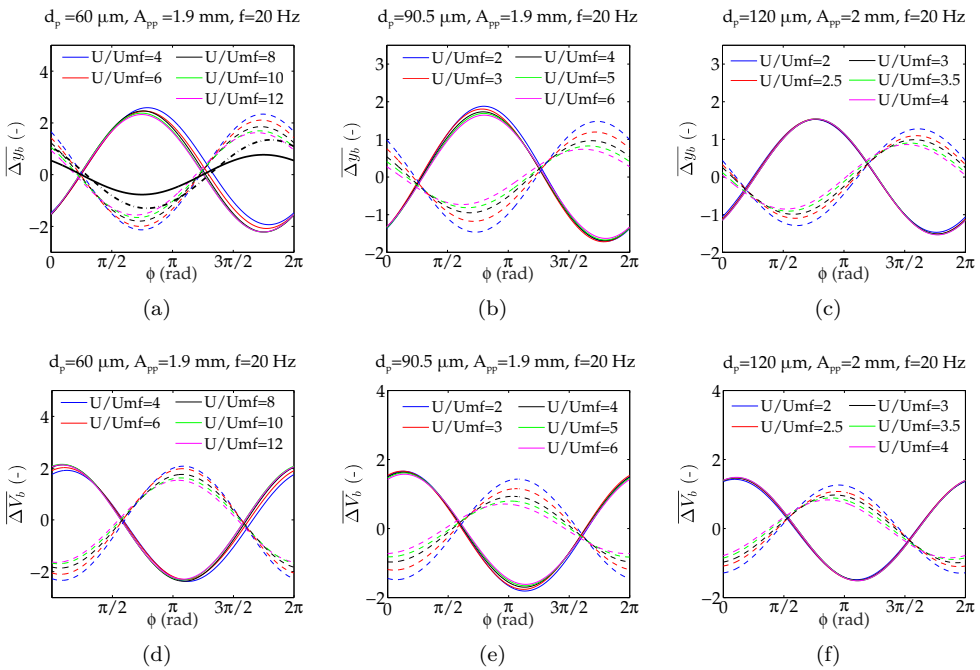


**Figure 6.19:** Oscillation of the bubble vertical position (a-c) and absolute velocity (d-f). Variation with superficial gas velocity for three different particle diameters: (a,d) $d_p = 60$ $\mu$m, (b,e) $d_p = 90.5$ $\mu$m and (c,f) $d_p = 120$ $\mu$m. The solid lines correspond to bubbles in the lower section of the bed ($y = 0.1 - 0.2$ m) and dashed lines correspond to bubbles in the upper section of the bed ($y = 0.3 - 0.4$ m). The black solid and dashed lines in (a) represent, respectively, the oscillation of the bed center of mass and the bed surface.

decreases when increasing the superficial gas velocity, as larger bubbles are less affected by the oscillatory displacement of the bed bulk and also the bed oscillates with less amplitude when $U/U_{mf}$ is increased, as commented in Section 6.3.3.

All these results suggest that the bubble centroid oscillation in a bubbling bed is directly affected by the oscillation of the bed bulk (see Figure 6.19(a)). If a bubble is situated in the lower section of the bed, the bed bulk moves in close phase with the bed base and that makes $\overline{\Delta y_b}$ nearly insensitive to variations in $U/U_{mf}$ (see solid lines in Figure 6.19). If a bubble is located in the upper section of the bed, $\overline{\Delta y_b}$ is sensitive to variations of $U/U_{mf}$ because the oscillation of the bed bulk is affected by $U/U_{mf}$, as was seen in Section 6.3.3. The bubble oscillation in the upper section of the bed decreases with $U/U_{mf}$, as the bulk reduces its oscillation amplitude when increasing the superficial gas velocity (see Figure 6.12). Also, in Figure 6.12 the amplitude of the oscillation of the bed bulk is more reduced when increasing the particle size. This may explain the smaller amplitude of the oscillation of the bubble position when increasing the particle

size in Figure 6.19.

The phase delay of the bubble velocity oscillation of both the lower and the upper sections of the bed is weakly affected by the variation of the superficial gas velocity and the vibration amplitude. In Figures 6.19 and 6.20 when the bed vessel moves downwards ($\phi = \pi/2 - 3\pi/2$ rad), the bed bulk expands and the particles in the upper section of the bed move upwards (see Section 6.3.3). This causes the bubbles situated in this upper region of the bed to move upwards following the local bed bulk oscillation. Equivalently, when the bed vessel moves downwards, the lower section of the bed tends to follow the displacement of the bed base and that tends to promote a downwards oscillation of the bubbles in the lower section of the bed, as they are drifted downwards by the local bed bulk motion. The opposite behavior is encountered when the bed bulk is compressing, facilitating the rise of bubbles situated in the lower section of the bed (as the bed bulk in that region is moving upwards) and impeding that of bubbles in the upper section of the bed. This promotes a phase delay of the oscillation of the bubble position and velocity in Figures 6.19 and 6.20 slightly larger than $\phi_{y_b} = 0$ rad and $\phi_{y_b} = \pi$ rad in the lower and upper sections of the bed, respectively.

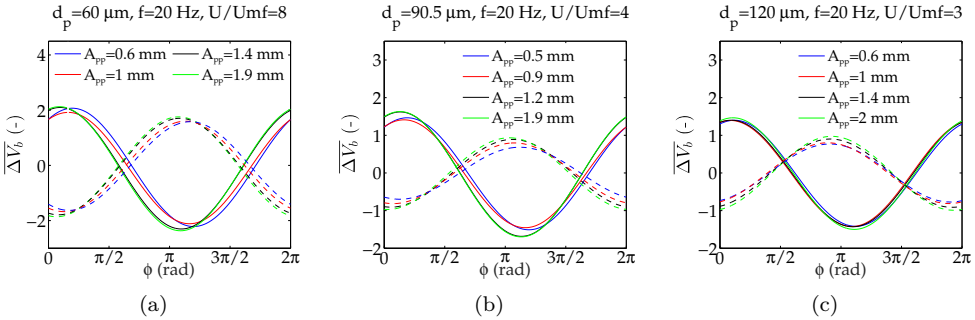


**Figure 6.20:** Oscillation of the normalized bubble absolute velocity. Variation with the vibration amplitude for three different particle diameters: (a) $d_p = 60$ $\mu$m, (b) $d_p = 90.5$ $\mu$m and (c) $d_p = 120$ $\mu$m. The solid lines correspond to bubbles in the lower section of the bed ($y = 0.1 - 0.2$ m) and dashed lines correspond to bubbles in the upper section of the bed ($y = 0.3 - 0.4$ m).

The previously described effect of the bed bulk cyclic compression and expansion on the bubble position oscillation is schematized in Figure 6.21. In Figure 6.21, the bed bulk compression takes place in the phase interval $\phi = 3\pi/2 - \pi/2$ rad (of the next cycle), that is, when the bed vessel is moving upwards, and the bed bulk expansion takes place in a phase $\phi = \pi/2 - 3\pi/2$ rad (i.e. the bed vessel is moving downwards).

Figure 6.22 shows the oscillation of the bubble velocity as a function of the phase and the distance to the distributor. The results are calculated in horizontal fringes of 2 cm

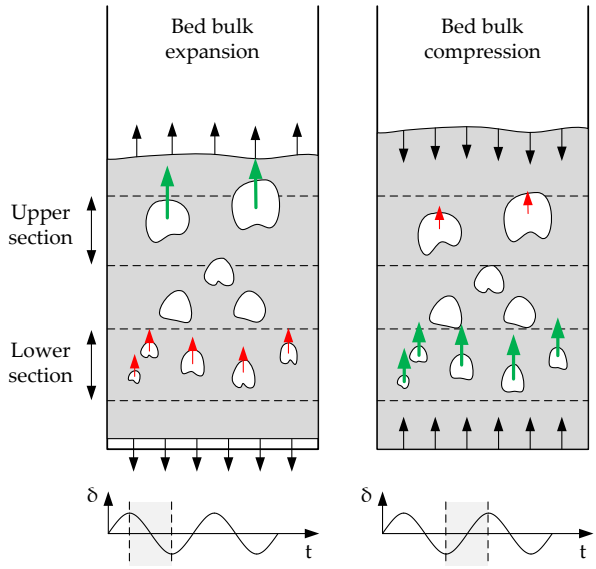


**Figure 6.21:** Schematic behavior of the motion of bubbles coupled with the cyclic compression and expansion of the bed bulk as a function of the vibration phase. The black arrows indicate the motion of the bed bulk whereas the red and green arrows schematize the absolute velocity of the bubble centroids inside the lower and upper sections of the bed.

spanning all the bed height ($y = 0.05 - 0.4$ m). Therefore, this figure provides a spatially resolved view of the oscillation of the bubble velocity as a function of its vertical position in the bed. For all the particles under study, the maximum oscillation amplitude of the bubble velocity is obtained in the regions close to the distributor ($y = 0.1 - 0.2$ m) and close to the surface of the bed ($y = 0.35 - 0.4$ m), as the bubbles in these regions are greatly affected by the motion of the bed distributor and the oscillatory motion of the bed surface of the bed (see Figure 6.21). Interestingly, the phase delay of the oscillation of the bubble velocity progressively increases along the bed height, which confirms the presence of a propagation mechanism in a form of a wave that travels upwards the bed that modifies the bubble position and velocity. Thus, this propagation mechanism is, quite probably, the compression-expansion waves of solids that were previously found and studied in Chapters 3 and 4. In addition, for a height around $y \simeq 0.3$ m, the magnitude of the bubble velocity oscillation is minimal, as the effects of the bed cyclic compression and expansion on the bubble velocity shown in Figure 6.21 are simultaneously affecting the bubble oscillation and counterbalance each other.

In summary, the above results suggest that the bed vessel vibration amplitude linearly affects the amplitude of the oscillations of the bubble position and velocity and has a weak impact on the phase delay of these oscillations because the bubble motion is mainly

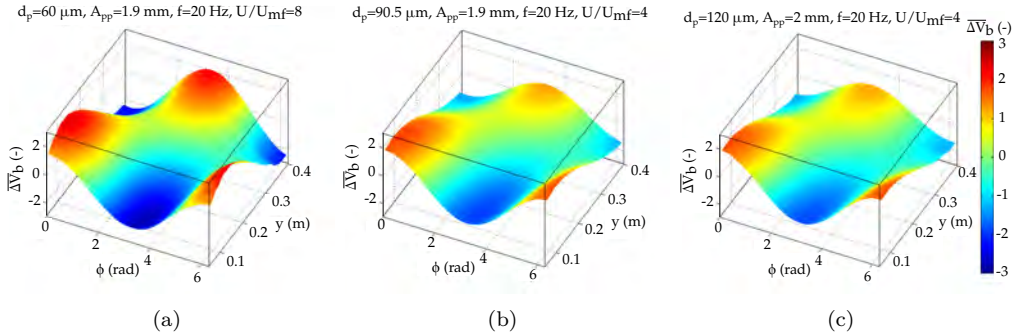


**Figure 6.22:** Oscillation of the normalized bubble absolute velocity as a function of the phase of the bed vessel and the vertical position of the bubble in the bed. (a) $d_p = 60$ $\mu$m, (b) $d_p = 90.5$ $\mu$m and (c) $d_p = 120$ $\mu$m.

affected by the local oscillation of the bed bulk. Also, the different phase delays observed for the bubble position and velocity are similar to those for isolated bubbles rising in a VFB at minimum fluidization conditions in Chapter 4. Concerning the oscillations of bubble position and velocity, the presence of a phase delay between bubbles in the lower and upper sections of the bed, despite the bed is operated in bubbling regime with multiple interacting bubbles, suggests the existence of a strong wave propagation mechanism of bubble characteristics, similarly to the one encountered for isolated bubbles in Chapter 4. This propagation mechanism affecting the bubble position and velocity is, most likely, due to the compression and expansion waves of solids velocity (Chapter 3).

### Phase delay of bubble characteristics

As indicated in the previous sections, the results have revealed the existence of a phase delay of bubble characteristics between the upper and lower sections of the vibrated bubbling bed. The phase delay is attributed to the propagation of waves through the bed volume that are generated at the bottom of the bed vessel. This wave propagation was also found for an isolated bubble rising in a bed at minimum fluidization (Chapter 4), modifying the way the bubble behaves along the bed height. Figures 6.23 and 6.24 show the phase delays of bubble diameter and velocity (calculated following the methodology described in Chapter 2) in the upper and lower sections of the bed as a function of the superficial gas velocity and the vibration frequency. Due to the weak influence that the vibration amplitude possesses on the phase delay of the bubble position and velocity (see Section 6.3.3) the dependence of the phase delay on the vibration amplitude is indirectly presented in Figures 6.23 and 6.24 by means of error bars accounting for the standard deviation of the values at the different vibration conditions. In particular, each point

and error bar in Figures 6.23 and 6.24 represents, respectively, the mean and standard deviation of the phase delay calculated from a sample of different vibration amplitudes at the same vibration frequency and superficial gas velocity. It can be observed in Figure 6.24 that the standard deviation due to the dispersion of the phase delay with the variation of the vibration amplitude is very reduced when it refers to the oscillation of the bubble velocity. As seen in Figures 6.17 and 6.20 the variation of the phase delay with the vibration amplitude is greater for the case of the bubble diameter than for the bubble position and velocity, causing large error bars in Figures 6.23 compared to Figure 6.24.

Note that, in some cases, negative phase delays appear in Figures 6.23 and 6.24. For a better understanding of the results and depending on the trend of the data, phase delays close to $\phi_d \sim 2\pi$ rad are associated in Figures 6.23 and 6.24 to a new phase delay $\phi_{n,d} = \phi_d - 2\pi$ rad. This change preserves, in most of the data presented in the figures, the general trend that the phase delay in the upper section of the bed is greater than in the lower section. The new phase delay $\phi_{n,d}$ is also used for the calculation of the propagation velocity in the bed.

In both the lower and the upper sections of the bed for the three different types of particles in Figure 6.23, the phase delay of the oscillations of bubble diameter increases when increasing the vibration frequency. Also, the phase delay of the bubble diameter in the lower section of the bed is always smaller than in the upper section of the bed. This suggests that, although the oscillation of the bubble diameter is subjected to numerous effects (i.e. bulk cyclic expansion and compression, wake penetration, rain of particles and interaction between bubbles) as commented in Section 6.3.3, there exists a clear wave mechanism that propagates a perturbation in the bed in upward direction. In particular, for the particles of 60 $\mu$m and $f = 20$ Hz in the lower section of the bed the bubble diameter oscillation has a phase delay close to $\phi_d = 0$ rad (Figure 6.16(a)) as they are mainly affected by wake penetration. It was observed in the experiments that the oscillation of the bubble diameter in the upper section of the bed is mainly caused by the cyclic compression and expansion of the bed bulk (Figure 6.15). This implies a phase delay of the diameter oscillation in the upper section of the bed close to $\phi_{\overline{\Delta D}_b} = \pi$ rad, as shown in Figure 6.23(a). However, for the particles of 120 $\mu$m, in Figure 6.23(c), bubbles are larger and the diameter oscillation is mainly affected by the cyclic compression and expansion of the bed bulk along the bed, so that $\phi_{\overline{\Delta D}_b}$ matches the phase of the oscillation of the center of mass of the bed bulk, $\phi_{\overline{\Delta D}_b} \simeq \pi$ rad (see Section 6.3.3).

Regarding the phase delay of the oscillations of bubble position and velocity in Figure 6.24, the three sizes of particles studied present a similar behavior. In this case, the oscillation of the bubble centroid position and velocity is mainly affected by the oscillation of the bed bulk. It can be observed in Figure 6.24, that the bubbles in the lower

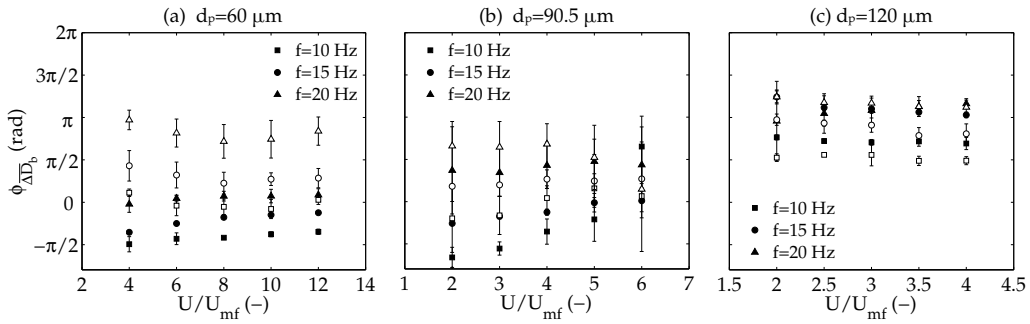


**Figure 6.23:** Phase delay of the bubble diameter in the lower section of the bed (filled symbols) and the upper section of the bed (empty symbols). (a) $d_p = 60$ $\mu$m, (b) $d_p = 90.5$ $\mu$m, (c) $d_p = 120$ $\mu$m.

section of the bed at the smaller frequency ($f = 10$ Hz) behave differently to bubbles in beds vibrated at larger frequencies ($f = 15 - 20$ Hz). For the case of $f = 10$ Hz, the bed bulk can easily follow the displacement of the bed vessel ($\Lambda < 1$). That may make the position of the bubbles in the bed to tend to move upwards when the bed is expanded, so that their phase delay is similar to that of the bed surface (see Figure 6.14). This is especially noticeable when the superficial gas velocity is small as bubbles are smaller and they are more subjected to the bed cyclic expansion and compression. However, when increasing the superficial gas velocity for $f = 10$ Hz, the phase delay of the oscillation of the bubble position and velocity decreases, which may be attributed to the larger buoyancy of large bubbles. These large bubbles reduce the effect of the cyclic expansion and compression of the bed bulk (see Section 6.3.3) and tends to cause a bubble oscillation with a phase similar to that of the bed vessel. However, more experiments at intermediate frequencies of vibration would be needed to find an exact explanation to this behavior at low frequencies. In the case of higher vibration frequencies, $f = 15 - 20$ Hz, the bed bulk seems to be unable to follow the high frequency oscillation of the bed and cyclically compresses and expands in close to opposition in phase with the bed vessel displacement, as in Chapter 4. As justified in Section 6.3.3, when this cyclic compression and expansion occurs, the upper section of the bed bulk follows an oscillatory displacement that is different to that of the lower section of the bed (Figure 6.21). As the bubble position oscillates accordingly to the bed bulk oscillation, this promotes a phase delay of the bubble position and velocity between the lower and upper sections of the bed of $\Delta\phi_{D_b,V_b} \simeq \pi$ rad.

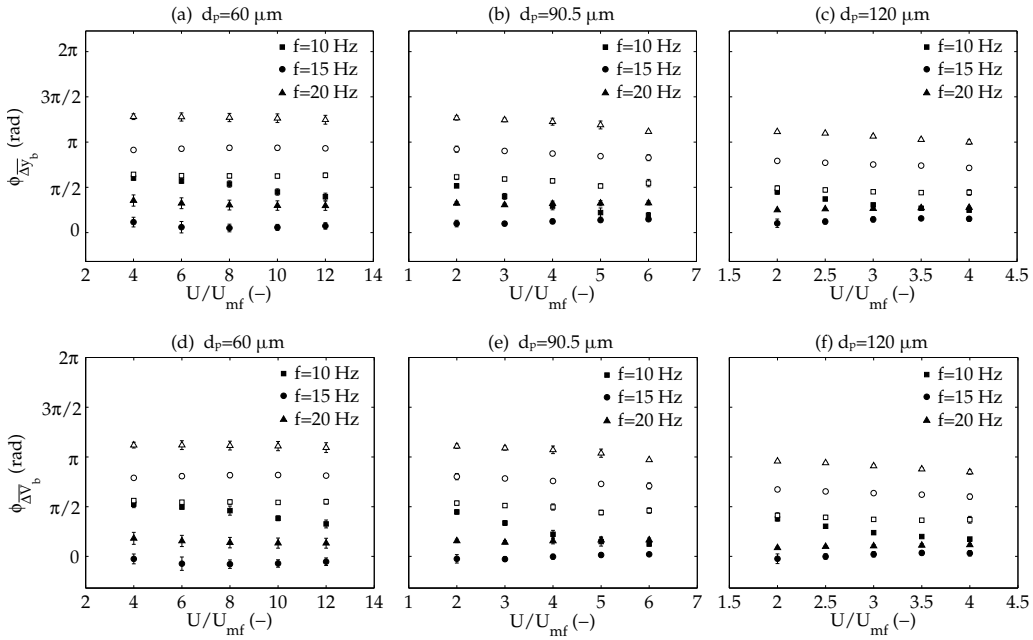


**Figure 6.24:** Phase delay of the bubble vertical position and velocity in the lower section of the bed (filled symbols) and the upper section of the bed (empty symbols). (a,d) $d_p = 60$ $\mu$m, (b,e) $d_p = 90.5$ $\mu$m, (c,f) $d_p = 120$ $\mu$m.

Equation (6.2) can be used to determine the velocity of the propagation of the bubble characteristics in the bed:

$$V_{prop} = 2\pi f \frac{\Delta y}{\Delta \phi} \tag{6.2}$$

where $f$ is the vibration frequency, $\Delta y$ is the distance between the center of the upper and the lower sections of the bed (i.e. $\Delta y = 0.15$ m, see Figure 2.1.2) and $\Delta\phi$ is the retardation in phase of a variable $\phi$ in the upper section of the bed with respect to the phase of the variable in the lower section of the bed ($\Delta\phi = \phi_2 - \phi_1$).

For each of the mean particle diameters and vibration frequencies depicted in Figures 6.23 and 6.24, Table 6.3 shows the mean velocity of propagation of bubble characteristics. This mean velocity has been calculated by averaging all the velocities obtained for each $U/U_{mf}$ at a given frequency. Table 6.3 also includes the range of vibration strengths of the set of experiments used in the calculation of the mean velocity. Equivalently to Figures 6.23 and 6.24, Table 6.3 includes the standard deviation of the mean propagation velocity, for different $U/U_{mf}$, as affected by the variation of the vibration amplitude. As

**Table 6.3:** Velocity of propagation of bubble characteristics.

| $d_p$ ($\mu$m) | $f$ (Hz) | $V_{prop,y_b}$ (m/s) | $V_{prop,V_b}$ (m/s) | $\Lambda$ (-) |
|---|---|---|---|---|
| 60 | 10 | 49.9±33.4 | 56.5±39.9 | 0.1-0.4 |
| | 15 | 7±0.3 | 6.9±0.3 | 0.3-0.9 |
| | 20 | 8.4±0.1 | 8.3±0.1 | 0.5-1.5 |
| 90.5 | 10 | 20.1±11.8 | 21.6±13.8 | 0.1-0.4 |
| | 15 | 8±0.6 | 7.9±0.6 | 0.2-0.9 |
| | 20 | 9.1±0.7 | 8.9±0.6 | 0.4-1.5 |
| 120 | 10 | 41.4±31.4 | 48.2±42.1 | 0.1-0.4 |
| | 15 | 9.8±0.8 | 9.7±0.8 | 0.3-0.9 |
| | 20 | 10.1±0.8 | 10±0.7 | 0.5-1.6 |

commented in Section 6.3.3, the oscillation of bubble diameter is subjected to multiple effects such as the bed bulk compression and expansion, the wake penetration, the rain of particles in the bubbles and the interaction between bubbles, which may perturb the way the size of bubbles oscillates and may lead to unrealistic values of $V_{prop,D_b}$. Thus, results of the velocity of propagation of the bubble diameter are not included in Table 6.3. The results of the velocity of propagation of the bubble position and velocity shown in Table 6.3 are in agreement with the effective sound propagation in a fluidized bed, which can be calculated following Roy *et al.* (1990):

$$u_s = u_{s0}\sqrt{\frac{\rho_g}{\gamma\varepsilon\left[\rho_p(1-\varepsilon)+\rho_g\varepsilon\right]}} \tag{6.3}$$

where $u_{s0} = \sqrt{\gamma R_g T_g}$ is the velocity of sound in the gas, $\rho_g = 1.165$ kg/m$^3$ is the density of the gas, $\varepsilon = 0.44$ is the bed voidage, calculated as a function of the static bed height and the mass of particles and $\gamma = 1.4$ is the heat capacity ratio. For these experimental conditions, Equation 6.3 yields an effective velocity of sound of 12.9 m/s, which is of the same order of magnitude of the values in Table 6.3 for frequencies of vibration of 15 and 20 Hz. However, this is not true for small vibration frequencies (i.e. $f = 10$ Hz), which exhibit higher propagation velocities. The cause of this discrepancy is not clear and may be due to the high uncertainty of the measurement because the standard deviation of the mean in Table 6.3 is relatively high at $f = 10$ Hz. The previous results imply that the main phenomenon affecting the propagation of oscillations of bubble characteristics, even if the bed is operated in bubbling regime, is the presence of compression-expansion waves in the bulk of the bed that are generated by vibration. These waves seem to be linked with the gas compressibility in accordance to the similitude of their propagation velocity and the sound velocity of the gas in a fluidized bed, as seen in (Wang *et al.*, 2000) and Chapters 3 and 4.

## 6.4 Conclusions

The solids hold-up and mean bubble behaviors in a vertically vibrated fluidized bed were experimentally studied in the present work by means of DIA. Experiments with four different sizes of particles at several vibration strengths were carried out in order to obtain a wide range of results regarding bubble and bed dynamics. A bubble tracking methodology was developed to follow the diameter and position of all the individual bubbles in the bed along the time period of the experiments. The bed displacement and the bubble diameter, position and velocity, were dynamically characterized by means of an averaging of oscillation cycles methodology. The analysis of results covered different aspects to show, and help to understand, the multiple effects of vibration on the bed and bubble dynamics.

Firstly, mean characteristics of the bed were studied by averaging over time and space the solids hold-up. The mean solids hold-up allowed the characterization of the bubble distribution inside the bed. The experiments revealed that, when introducing vibration in the system, the bubble path tends to be confined to the center of the studied bed, making the distribution of bubbles less uniform. The confinement of the bubble path is more significant when increasing the vibration strength. The bubble number density in the bed decreases with an increase of vibration amplitude due to bubble coalescence whereas the bubble fraction remains nearly constant. In general, the vibration amplitude has an impact on the mean diameter and velocity of bubbles that is greater at high vibration frequencies. In the bubbling bed tested, increasing the vibration amplitude produces an increase of the mean bubble diameter, specially at high vibration frequencies. Two regimes of bubble dynamics were detected in the bed, depending on the vibration characteristics, the particles employed and the bed morphology. Small bubbles close to the distributor (i.e. lower half of the bed) were found to behave more similarly to isolated bubbles, so that their velocity decreased when increasing the vibration amplitude. In contrast, the bubble velocity increased with the vibration amplitude for bubbles in the upper half of the bed, as they were more influenced by bubble coalescence and gulf stream drifting of particles. In summary, all the previous results show that careful selection of the vibration amplitude and frequency, altogether with the gas velocities and type of particles, may be used to modify the bed behavior, including the number, size and velocity of bubbles in the bed. Also, bubbles behave differently depending on their spatial location in the bed and this may explain the different, and apparently contradictory, trends found in the literature concerning the bubble behavior in vibrated fluidized beds.

The results devoted to the oscillatory behavior of the bed bulk and the bubbles indicated that both the bed bulk and the bubble characteristics in a bubbling bed oscillate

with a frequency equal to the frequency of vibration of the bed vessel but with different phases. The frequency at which the bed vessel is vibrated has a strong influence on both the amplitude and the phase delays of the oscillations of bubble characteristics. In contrast, the vibration amplitude and the superficial gas velocity mainly affect the amplitude of the oscillations of bubble characteristics. For all the particles employed in this work, the presence of a phase delay of bubble characteristics between the lower and upper sections of the bubbling bed, similar to that encountered for an isolated bubble (Chapter 4), indicates the presence of compression-expansion waves generated at the bottom of the bed that propagate upwards thorough the bed. These waves modify the way the bubbles behave along the bed height, despite the fact the bed is operated under bubbling regime and bubbles interact continuously with each other.

The effect of vibration on the mean and oscillatory behavior of both the bed bulk and the bubbles has been found to be more pronounced for beds of small particles (i.e. Geldart A). All the previous results show that the selection of the superficial gas velocity, together with the vibration amplitude and frequency has an impact, not only in the mean characteristics of bubbles and the bed bulk, but on their oscillatory behavior, which changes the way bubbles behave depending on their vertical position in the bed. The presence of compression-expansion waves in the bed affecting the oscillation of the bubble position and diameter may perturb heat and mass transfer between the bed and the bubbles, which may have an impact on reactions and transfer operations within the particles and the gas. Thus, the fundamental results here encountered could be employed to improve the understanding and design of vibrated fluidized bed reactors operated in bubbling regime.

# Nomenclature

| | |
|---|---|
| $A_{pp}$ | vibration amplitude, peak-to-peak (mm) |
| $A_b$ | bubble area ($m^2$) |
| $CM_y$ | center of mass vertical coordinate (m) |
| $D_b$ | bubble equivalent diameter (m) |
| $DI$ | distribution index (-) |
| $d_p$ | particle diameter ($\mu$m) |
| $f$ | vibration frequency (Hz) |
| $F_b$ | bubble fraction (-) |
| $GS$ | grayscale level (-) |
| $g$ | gravity acceleration constant ($m/s^2$) |
| $n_b$ | bubble number density (bubbles/$m^2$) |
| $R_g$ | ideal gas constant for air (J/kg K) |
| $T_g$ | gas temperature (K) |
| $t$ | time (s) |
| $U$ | superficial gas velocity (m/s) |
| $U_{mf}$ | minimum fluidization velocity (m/s) |
| $U_{mf,th}$ | theoretical minimum fluidization velocity (m/s) |
| $u_s$ | equivalent sound velocity in the bed (m/s) |
| $u_{s0}$ | gas velocity of sound (m/s) |
| $V_b$ | bubble velocity (m/s) |
| $V_{prop}$ | propagation velocity (m/s) |
| $x$ | horizontal coordinate (m) |
| $y$ | vertical coordinate (m) |
| $y_b$ | bubble centroid vertical coordinate (m) |
| $z(t)$ | instantaneous variable value |
| $\widehat{z}$ | moving average of $z$ |
| $\Delta z$ | oscillation of $z$ |

*Greek letters*

| | |
|---|---|
| $\gamma$ | heat capacity ratio (-) |
| $\delta(t)$ | bed vessel vertical displacement (m) |
| $\varepsilon$ | bed void fraction (-) |
| $\Lambda$ | vibration strength parameter (-) |
| $\rho_g$ | gas density ($kg/m^3$) |
| $\rho_p$ | particle density ($kg/m^3$) |
| $\phi$ | phase (rad) |

| | |
|---|---|
| $\phi_d$ | phase delay (rad) |
| $\omega$ | angular velocity (rad/s) |

## References

Acosta-Iborra, A., Hernández-Jiménez, F., de Vega, M. & Briongos, J.V. 2012 A novel metodology for simulating vibrated fluidized beds using two-fluid models. *Chem. Eng. J.* 198-199, 261–274.

Barletta, D., Russo, P. & Poletto, M. 2013 Dynamic response of a vibrated fluidized bed of fine and cohesive powders. *Powder Technol.* 237, 276–285.

Busciglio, A., Vella, G., Micale, G. & Rizzuti, L. 2008 Analysis of the bubbling behaviour of 2D gas solid fluidized beds: Part I. digital image analysis technique. *Chem. Eng. J.* 140, 398–413.

Cano-Pleite, E., Hernández-Jiménez, F., de Vega, M. & Acosta-Iborra, A. 2014 Experimental study on the motion of isolated bubbles in a vertically vibrated fluidized bed. *Chem. Eng. J.* 255, 287–299.

Eccles, E.R.A. & Mujumdar, A.S. 1997 Bubble phenomena in aerated vibrated beds of small particles. *Drying Technol.* 15:1, 95–116.

Ergun, S. 1952 Fluid flow through packed columns. *Chem. Eng. Prog.* 48, 89–94.

Hernández-Jiménez, F., Sánchez-Prieto, J., Soria-Verdugo, A. & Acosta-Iborra, A. 2013 Experimental quantification of the particle-wall frictional forces in pseudo-2D gas fluidised beds. *Chem. Eng. Sci.* 102, 257–267.

Kunii, D. & Levenspiel, O. 1991 *Fluidization Engineering*. Butterworth-Heinemann, Newton, MA.

Mawatari, Y., Tagawa, K., Tatemoto, Y. & Noda, K. 2005 Bubbling characteristics under vertical vibration in a two-dimensional fluidized bed. *Chem. Eng. Jpn.* 38, 18–23.

Mawatari, Y., Tatemoto, Y. & Noda, K. 2003 Prediction of minimum fluidization velocity for vibrated fluidized bed. *Powder Technol.* 131, 66–70.

Roy, R., Davidson, J.F. & Tuponogov, V.G. 1990 The velocity of sound in fluidised beds. *Chem. Eng. Sci.* 45, 3233–3245.

Shen, L., Johnsson, F. & Leckner, B. 2004 Digital image analysis of hydrodynamics two-dimensional bubbling fluidized beds. *Chem. Eng. Sci.* 59, 2607–2617.

Wang, T.J., Jin, Y., Tsutsumi, A., Wang, Z. & Cui, Z. 2000 Energy transfer mechanism in a vibrating fluidized bed. *Chem. Eng. J.* 78, 115–123.

Zeilstra, C., van der Hoef, M.A. & Kuipers, J.A.M. 2013 Experimental and numerical study of solids circulation in gas-vibro fluidized beds. *Powder Technol.* 248, 153–160.

Zhou, T., Kage, H. & Li, H. 2005 Bubble characteristics in a two-dimensional vertically vibro-fluidized bed. *China Partic.* 3, 224–228.

Zhou, T., Ogura, H., Yamamura, M. & Kage, H. 2004 Bubble motion pattern and rise velocity in two-dimensional horizontal and vertical vibro-fluidized beds. *Can. J. Chem. Eng.* 82, 236–242.

CHAPTER

**SEVEN**

# Applications of vibrated fluidized beds: density segregation in a rectangular bed and pattern formation in a triangular bed

## Contents



Two different applications of vibrated fluidized beds are experimentally studied in this chapter from a fundamental point of view. In the first section, the effect of vibration on the density segregation of equally-sized particles is studied. The second section experimentally analyzes the effect that vibration has on the patterns of solids motion formed in a triangular vibrated fluidized bed.

# 7.1 Density segregation in a vertically vibrated fluidized bed

## 7.1.1 Introduction

Many operations in the chemical, energy-conversion and processing industries rely on the fluidization of heterogeneous materials. During fluidization, particles of different densities can segregate even if they are of the same size (Rowe & Nienow, 1976). Segregation can be used to separate granular materials, but it should be avoided in processes requiring well mixed particles and a uniform distribution of the fluidizing gas (Kunii & Levenspiel, 1991). Thus, an understanding of segregation on a fundamental level is paramount to identify effective measures to control it. One approach to control segregation is mechanical vibration of the bed vessel. In mechanically vibrated fluidized beds, the oscillation movement of the bed vessel is transmitted to the interior of the bed and affects the dynamics of its dense and bubble phases as shown in (Zhou *et al.*, 2001; Mawatari *et al.*, 2005) and in Chapters 3 to 6. This can be used to modify (i.e. increase or decrease) the rate and extent of particle segregation in a fluidized bed.

As mentioned in Chapter 1, several works have made use of vibrated fluidized beds in processes involving particle segregation such as coal beneficiation (Luo *et al.*, 2008; He *et al.*, 2015), fine coal cleaning (Yang *et al.*, 2013) and lignite cleaning (Zhao *et al.*, 2015). However, in these experimental works, the segregation phenomenon was simultaneously induced by differences on the size and the density of non-spherical particles, making difficult to elucidate the actual role of the particle density on the observed segregation. Also, due to the nature of the experiments, the temporal evolution of particle segregation was estimated by taking the ensemble average of independent experiments under the same operating conditions. Thus, the results of the segregation index were limited to a reduced number of time instants, which are insufficient to obtain a detailed time evolution of the segregation phenomenon. In addition, there is little literature available concerning the effect of vibration on density-induced segregation with equally sized particles in a fluidized bed.

To the author's best knowledge, experimental works studying segregation (i.e. variation with time and final value) in a vibrated fluidized bed filled with spherical particles with approximately the same particle diameter and different particle densities are currently lacking. These experiments could be very useful for understanding segregation in vibrated fluidized beds, developing new models and validating numerical simulation. Thus, the present chapter aims to characterize experimentally density driven segregation in a vertically vibrated fluidized bed comprising a mixture of spherical particles of two different densities and similar diameters.

### 7.1.2 Experimental setup

The segregation experiments were conducted in the pseudo-2D bed of dimensions 0.2 m width, 0.5 m height and 0.01 m thickness described in Section 2.1.3. The bed material was glass particles of density $\rho_L = 2500$ kg/m$^3$ mixed with the same volume of white ceramic particles of either $\rho_D = 6000$ kg/m$^3$ (Mixture 1) or $\rho_D = 4100$ kg/m$^3$ (Mixture 2). Spherical particles were used. To obtain an equal volume mixture of light and dense particles, the bed was first filled with a layer (0.055 m) of ceramic particles. Subsequently, an additional layer (0.055 m) of glass particles was added on top of the previous bed. Thus, the total static bed height was $H_0 = 0.11$ m. Table 7.1 shows the properties of each of the mixtures employed in the experiments.

**Table 7.1:** Properties of the mixtures of light (L) and dense (D) particles.

| | $d_{p,L}$ (mm) | $\rho_L$ (kg/m$^3$) | $U_{mf,L}$ (m/s) | $d_{p,D}$ (mm) | $\rho_D$ (kg/m$^3$) | $U_{mf,D}$ (m/s) |
|---|---|---|---|---|---|---|
| Mixture 1 | 1-1.3 | 2500 | 0.63 | 1-1.2 | 6000 | 1.08 |
| Mixture 2 | 1-1.3 | 2500 | 0.63 | 1-1.2 | 4100 | 0.85 |

In Table 7.1, $U_{mf,L}$ and $U_{mf,D}$ are, respectively, the minimum fluidization velocity of the light and dense particles in the mixture. The minimum fluidization of each type of particles was determined experimentally. In the present chapter, the superficial gas velocity, $U_0$, will be normalized with the minimum fluidization velocity, $U_{mf,D}$, of the denser particles in the mixture, i.e. particles of $\rho_D = 6000$ kg/m$^3$ in Mixture 1 and particles of $\rho_D = 4100$ kg/m$^3$ in Mixture 2, since dense particles determine the onset of complete fluidization of the mixture.

Each experiment started with the light (black) and dense (white) particles randomly mixed, and the air valve was opened synchronously with the onset of vibration ($t = 0$). A high speed CCD camera (Optronics CL 600 x2/M) was used to record images of the bed through its front wall at a frame rate of 50 images per second. Digital Image Analysis (DIA) of the captured images was used to characterize the rate and extent of particle segregation with time. The experiments were stopped when no variation on the distribution of the black and white particles was identified.

In order to study separately the influence of the amplitude and frequency of the vibrations and the superficial gas velocity on the segregation of the mixtures, several conditions were tested in the experiments. For each of the mixtures, a reference case with $f = 15$ Hz and $A = 4$ mm and a relative superficial velocity of $U_0/U_{mf,D} = 0.91$ for the Mixture 1 and $U_0/U_{mf,D} = 1.16$ for the Mixture 2 was selected (see bold numbers in Table 7.2). These experimental velocities corresponded to conditions in which segregation could be clearly identified in the mixture when the bed vessel was vibrated. Note that

for Mixture 1, the superficial gas velocity of the reference case is below $U_{mf,D}$ whereas for Mixture 2, the gas velocity of the reference case exceeds the minimum fluidization velocity of the denser particles. Thus, the reference cases in the two mixtures investigate the effect of vibration with two different flow conditions. In each of the experiments, only one parameter was changed at a time. Table 7.2 shows the different vibration frequencies, amplitudes and superficial gas velocities of the experiments conducted. The table also contains the vibration strength.

**Table 7.2:** Experimental conditions. The bold numbers correspond to the reference cases.

| $f$ (Hz) | $A$ (mm) | $\Lambda$ (-) | **Mixture 1** | **Mixture 2** |
|---|---|---|---|---|
| | | | $U_0/U_{mf,D}$ (-) | $U_0/U_{mf,D}$ (-) |
| 10 | 4 | 1.6 | 0.91 | 1.16 |
| **15** | **4** | **3.6** | 0.74, 0.81, 0.86, **0.91**<br>0.96, 1.01, 1.07, 1.12 | 0.79, 1.05, 1.1<br>**1.16**, 1.22, 1.29 |
| 20 | 4 | 6.4 | 0.91 | 1.16 |
| 15 | 3 | 2.7 | 0.91 | 1.16 |
| 15 | 5 | 4.5 | 0.91 | 1.16 |
| No vibration | | | 1.01, 1.07, 1.12 | 1.05, 1.1, 1.16, 1.22, 1.29 |

### 7.1.3 Results and Discussion

#### General bed behavior and segregation regimes

Figure 7.1 shows four examples of how density induced segregation of particles evolves with time once the fluidization air and vibration have been switched on simultaneously ($t = 0$). The figure contains snapshots of the bed every 10 seconds showing the distribution of light and dense particles. The normalized mean concentration of heavier (white) particles, $c_k$, horizontally averaged along the bed width, is also presented at the right side of each snapshot.

For the case of $f = 15$ Hz and $A = 4$ mm in Figure 7.1(a), a clear progression of segregation of light and dense particles with time can be observed. The increase of segregation with time (viz. segregation rate) is higher at the beginning of the experiment, reaching a segregation pattern in which the light particles can be found in the upper half of the bed and the denser particles are in the lower half of the bed. As segregation progresses, the thickness of the layer of light particles in the upper half of the bed increases with time. Note that segregation at $t = 30$ s in Figure 7.1(a) is not yet completed and slowly increases due to the fact that some light (black) particles remain trapped among the dense (white) particles and they progressively ascend to the upper half of the bed.

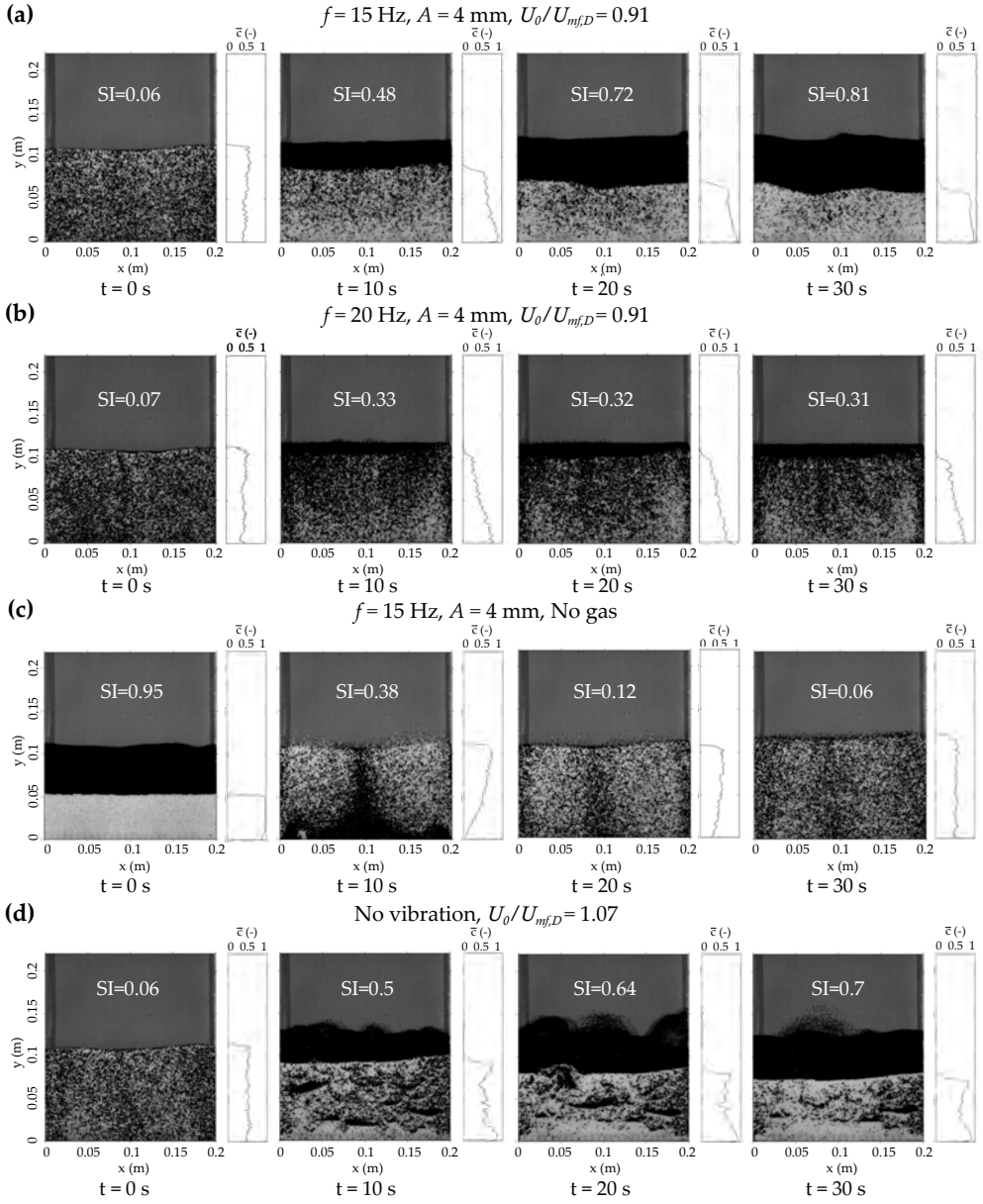


**Figure 7.1:** Images showing the evolution of particle segregation in a vibrated fluidized bed at different instants of time: (a) $f = 15$ Hz, $A = 4$ mm and $U_0/U_{mf,D} = 0.91$ and (b) $f = 20$ Hz, $A = 4$ mm and $U_0/U_{mf,D} = 0.91$ (c) $f = 15$ Hz, $A = 4$ mm and no superficial gas velocity (d) No vibration and $U_0/U_{mf,D} = 1.07$. White particles have $\rho_D = 6000$ kg/m$^3$ and black particles $\rho_L = 2500$ kg/m$^3$.

For the case of $f = 20$ Hz and $A = 4$ mm, Figure 7.1(b) shows that the progression of segregation is very reduced and reaches a stable value around $SI = 0.31$. In this case, it was observed in the experiment that the particle mixture presented a downward movement close to the front and rear walls of the bed and ascended through the central section of the bed. However, the full three dimensional movement of particles is restricted by the limited transverse thickness of the bed. Thus, the thickness of the bed may influence the segregation index when three dimensional movement of particles occurs. The upwards motion of particles in the central section of the bed was observed visually from a lateral perspective while carrying out the experiments. Segregation can be reversed towards complete mixing if only vibration is applied to the bed without introducing gas through the distributor. This is shown in Figure 7.1(c) for $f = 15$ Hz and $A = 4$ mm and an initially segregated distribution with light particles in the upper half of the bed and the dense particles in the lower half. In this experiment, a three dimensional recirculation movement appeared, similarly to Figure 7.1(b) but stronger. This reveals that by switching on gas fluidization at velocities close to $U_{mf,D}$ in a vibrated bed, density segregation is induced.

In the experiments without vibration for $U/U_{mf,D} = 0.91$, gas alone was unable to segregate the mixture. Figure 7.1(d) shows the evolution of particle segregation for a larger superficial gas velocity ($U_0/U_{mf,D} = 1.07$) in which gas alone is able to segregate the mixture, but with a reduced rate. This indicates that the fluidization with gas, when coupled to vibration, is the main driving factor that leads to segregation in these experiments.

A qualitative study using sequences of images as shown in Figure 7.1 was undertaken for different vibration conditions to identify the phenomena involved in density induced segregation. The results are sketched in Figure 7.2, which shows the effect of increasing the vibration strength, for the same superficial gas velocity, in the segregation of light and dense particles observed in the experiments of the vibrated fluidized bed. Three different regimes of density-induced segregation of particles were detected, which are described below.

**Vibration-enhanced segregation** At low vibration strengths, Figure 7.2(a), vibration enhances segregation as it cooperates with the segregation caused by the superficial gas velocity for $U_0/U_{mf,D} \sim 1$, creating larger voids between the particles in the bed. In this vibration-enhanced segregation, which is the situation also described in Figure 7.1(a), dense particles percolate easier through these voids due to their larger weight and move downwards as the light particles move upwards. In this case, if the superficial gas velocity is sufficiently large, bubbles appear. Due to the smaller minimum fluidization velocity of the lighter particles, the bubbles are larger in the region in which these particles are

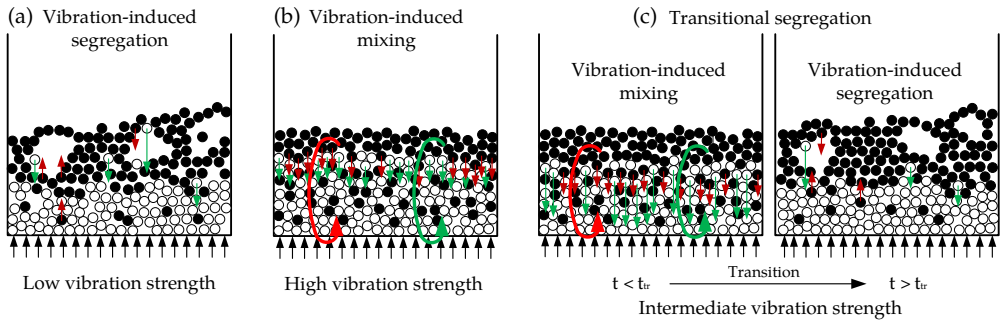


**Figure 7.2:** Schematic behavior of the particle movement observed in the experiments for different vibration strengths. (a) Vibration-induced mixing, (b) vibration-induced segregation, (c) transitional segregation. The red and green arrows represent, respectively, the motion of the light and dense particles in the bed.

present. For example, in Figure 7.1(a), bubbles only appear in the upper black layer of the bed. However, they cannot be recognized easily in the figure due to the low contrast between the black particles and the background color of the bed vessel. Bubbles also promote segregation because dense particles rain inside the bubble at a higher velocity than the light particles. A further increase of the superficial gas velocity may decrease the final segregation extent as dense particles can be dragged up by bubbles to the upper half of the bed.

**Vibration-induced mixing** When the vibration strength is large enough, the transport of particles is dominated by the convective movement of the bed bulk induced by vibration of the bed vessel, as in vibrated beds without gas (Aoki *et al.*, 1996, 1997; Akiyama *et al.*, 1998), similar to the behavior encountered in Figure 7.1(c) when no gas is injected in the bed. This effect is sketched in Figure 7.2(b). Here, both the impact of the bed with the distributor and the interaction of the particles with the front and rear walls of the bed feed energy into the system that is not counterbalanced by the gas phase. A three dimensional convective motion with the light and dense particles descending at a similar velocity close to the front and rear walls, and ascending through the central section of the bed, was observed. This vibration-induced mixing precludes the formation of bubbles for the range of superficial gas velocities tested in the experiments. The segregation of the mixture was quite reduced and only a small layer of light particles become segregated at the top of the bed (e.g. Figure 7.1(b) at 30 s).

**Transitional segregation** Interestingly, for intermediate values of the vibration strength, the behaviors in Figures 7.2(a) and 7.2(b) can be observed in the same experiment before and after a transition time, $t_{tr}$, as indicated in Figure 7.2(c). During

the first seconds of the experiment, vibration-induced mixing, with downward movement of the particles close to the front and rear walls of the bed appeared ($t < t_{tr}$ in Figure 7.2). Here, the particle behavior is similar to that shown in Figure 7.2(b). However, dense particles move downward slightly faster than light particles, which promotes a gradual segregation of the bed that slowly creates a layer of light particles at the top of the bed. This increases the average density of the remaining mixture placed below. That seems to stop the convective motion that is enhanced by vibration and the front and rear walls that are in close proximity. In turn, the vibration-enhanced segregation mechanism described in Figure 7.2(a) is triggered, causing the separation of the light and dense particles after this transition ($t > t_{tr}$ in Figure 7.2(b)). From that moment on, the bed behavior is similar to that shown in Figure 7.1(a). The segregation index in this transitional segregation mode presents two clearly distinguishable regions, as will be shown later in Figure 7.4(b,c).

**Segregation index**

Figure 7.3 shows the time evolution of the segregation index of Mixture 1 ($\rho_D = 6000$ kg/m$^3$) for different vibration conditions and superficial gas velocities. Firstly, Figures 7.3(a) and 7.3(b) show the effect of vibration on segregation as a function of the superficial gas velocity. Curves of the segregation index are smoothed out with a moving average to eliminate the perturbation on the segregation index caused by bubbling and the oscillation of the bed surface. It can be clearly observed in Figure 7.3(a) that vibration of a gas fluidized bed improves the segregation of the mixture by increasing the final segregation index (i.e. steady value for large $t$) and decreasing the time required to reach it. Gas without vibration of the bed vessel was unable to segregate appreciably the mixture for the superficial gas velocities, $U_0$, below 1.01 $U_{mf,D}$, and these results are not presented in Figure 7.3(a). The introduction of vibration produces the separation of the mixture even for $U_0/U_{mf,D} < 1$ as a result of the effects commented in the previous section for the regime of vibration-enhanced segregation (Figure 7.2(a)). In particular, according to Figure 7.3(b), the qualitative evolution of segregation with time is the same for $U_0/U_{mf,D} \geq 0.91$. At the beginning of the experiment the rate of segregation is high because vibration-induced segregation is the driving mechanism. Once high $SI$ values have been reached, the rate of segregation progressively decreases as the bed approaches the maximum $SI$. These observations made are similar to the results reported by Sun *et al.* (2014), in which density segregation is modeled using DEM simulations (see Chapter 1). Generally, for $U_0/U_{mf,D} \geq 0.91$ in Figure 7.3(b), at the beginning of the experiment the rate of segregation increases when increasing the superficial gas velocity. However, for superficial gas velocities smaller than $U_0/U_{mf,D} < 0.91$ the gas velocity

together with the vibration were unable to completely segregate the mixture ($SI < 0.8$). Also in Figure 7.3(b), the final index of particle segregation reached at the end of the experiment increases with the superficial gas velocity.

Figures 7.3(c) and 7.3(d) show, respectively, the effect of the vibration frequency and amplitude on the segregation index for a case in which the gas alone is unable to segregate the mixture (i.e. $U_0/U_{mf,D} = 0.91$). It can be observed that an increase of either the vibration amplitude or frequency promotes a decrease of the segregation rate ($d(SI)/dt$) after the first 10 s of the experiment. The final segregation index decreases significantly for high vibration amplitudes ($A = 5$ mm) and, especially, for high vibration frequencies ($f$ =20 Hz), as observed in Figure 7.1(b). In this case, the final segregation index diminishes due to the effect of vibration-induced mixing described in the previous section (Figure 7.2(b)).

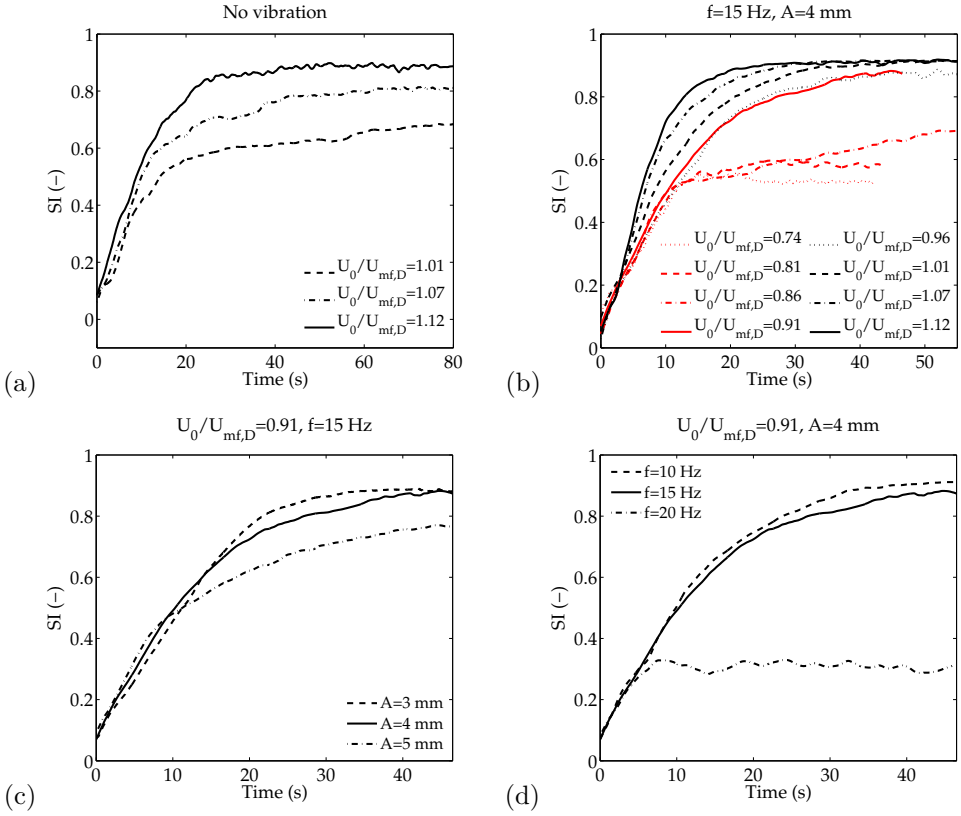


**Figure 7.3:** Evolution of the segregation index with time for the mixture of particles of density 2500 kg/m$^3$ and 6000 kg/m$^3$ (Mixture 1). Effect of (a) superficial gas velocity without vibration, (b) superficial gas velocity with vibration, (c) vibration amplitude and (d) vibration frequency.

Figure 7.4 shows the evolution of segregation with time for the Mixture 2 ($\rho_D = 4100$ kg/m$^3$). Similarly to Figure 7.3, both increasing the superficial gas velocity and adding vibration to the system increase the segregation of the mixture (the last effect due to vibration-enhanced segregation). The rate of segregation of particles in Mixture 2 shows a similar behavior as the one plotted in Figure 7.3. That is, the rate of segregation increases when increasing the superficial velocity of the fluidizing gas. However, for high superficial gas velocities the rate of segregation between the different experiments changes only slightly and the final value of the segregation index decreases when increasing $U_0/U_{mf,D}$ (see Figure 7.4(a,b)). In these cases, the bubbles rising in the upper half of the bed are able to drag upwards white (dense) particles, and that counteracts the density segregation. This behavior was also observed when increasing the superficial gas velocity in Mixture 1 beyond $U_0/U_{mf,D} > 1.12$.

The transitional segregation regime qualitatively described in Figure 7.2(c) is observed in Figure 7.4(b) for the superficial gas velocity equal to $U_0/U_{mf,D} = 1.1$ and in Figure 7.4(c) for a vibration amplitude of $A = 5$ mm. If the superficial gas velocity is large enough, the segregation effect induced by the gas is able to overcome the vibration-induced mixing and the mixture is segregated. However, either by decreasing the superficial gas velocity or by increasing the vibration strength, vibration-induced mixing becomes the dominant mechanism in the bed. Thus, the transitional segregation mode appears as an intermediate state between vibration-induced mixing, observed for $U_0/U_{mf,D} < 1.1$ in Figure 7.4(b), and vibration-induced segregation, observed for $U_0/U_{mf,D} > 1.1$ and for $A < 5$ mm in Figures 7.4(b) and (c), respectively. Figure 7.4 shows that the range of $U_0/U_{mf,D}$ in which the transitional segregation region occurs is relatively narrow. In the transitional segregation regime, vibration-induced mixing is counteracting density induced segregation. During the beginning of the experiment ($10$ s $< t < 40$ s), there is a convective movement of the bed bulk and, hence, vibration-induced mixing is the prevalent mechanism affecting particle behavior in the bed. In this situation, the segregation index grows slowly following a nearly linear slope. Around $t_{tr} = 45$ s in Figure 7.4(b) and $t = 35$ s in Figure 7.4(c), the increased weight of the mixture in the lower half of the bed is enough to stop the three dimensional convective movement of the bed bulk and promote a change of the segregation mechanism to vibration-enhanced segregation (see Figure 7.2(c)). From this instant on, the segregation rate increases and approaches an asymptotic value similar to that encountered at higher superficial gas velocities or low vibration strengths.

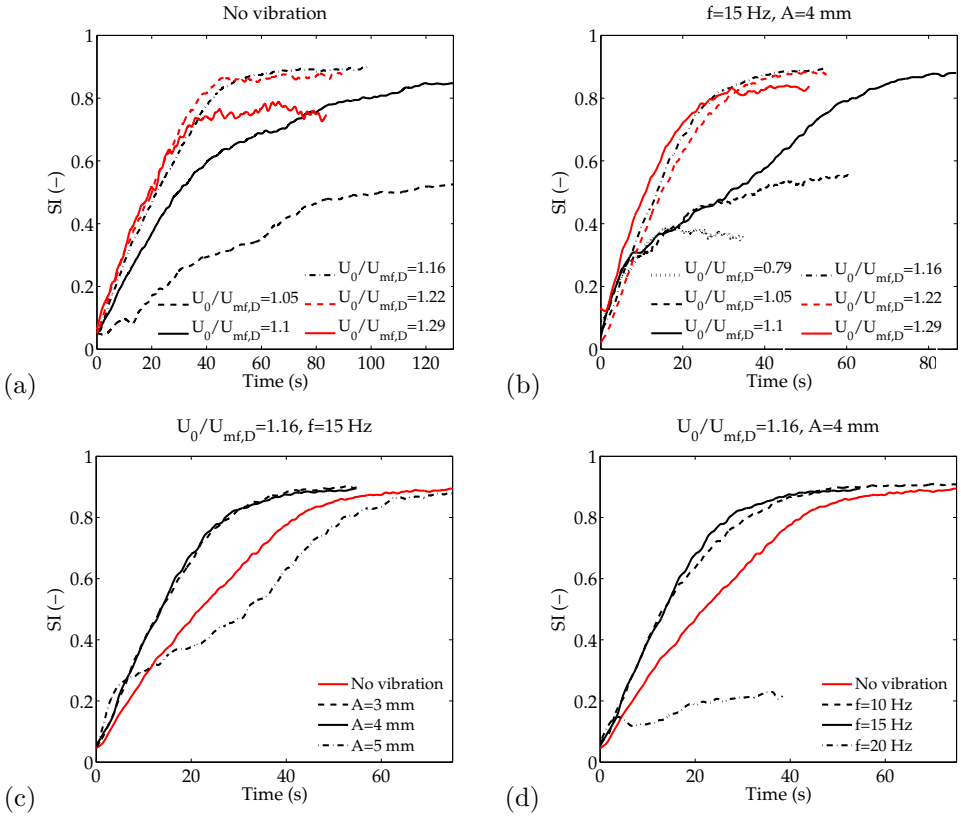


**Figure 7.4:** Evolution of the segregation index with time for the mixture of particles of density 2500 kg/m$^3$ and 4100 kg/m$^3$ (Mixture 2). Effect of (a) superficial gas velocity without vibration, (b) superficial gas velocity with vibration, (c) vibration amplitude and (d) vibration frequency.

Figure 7.5 shows the time evolution of the segregation index as a function of the vibration strength, $\Lambda$, by separately varying the vibration amplitude and frequency (see Table 7.2), for 6 different time instants and an example of superficial gas velocity chosen for the reference case, i.e. $U_0/U_{mf,D} = 0.91$ (Mixture 1) and $U_0/U_{mf,D} = 1.16$ (Mixture 2). The data correspond to the experiments of Figures 7.3(c,d) and Figures 7.4(c,d). It can be observed in Figure 7.5 that the segregation index is strongly influenced by the vibration strength. As mentioned previously, vibration and the superficial gas velocity can exhibit counteracting effects on segregation. The segregation index increases when introducing vibrational energy into the system (i.e. $\Lambda$ is increased), this effect has been also observed in other experimental (Zhao *et al.*, 2015) and numerical (Sun *et al.*, 2014) studies. This can be seen clearly in Figure 7.5(b) for Mixture 2 and $0 \leq \Lambda \leq 3$. At low vibration intensities, vibration promotes a decrease of the effective $U_{mf}$, which increases the void fraction of the bed and enhances segregation similarly as

an increase of the superficial gas velocity. For Mixture 1 (Figure 7.5(a)), values at $\Lambda = 0$ have not been included because the introduction of only gas was unable to segregate the mixture for $U_0/U_{mf,D} = 0.91$. However, at higher vibrational intensities, the vibration induced a convective motion of particles in the bed leading to vibration-induced mixing, which in turn, decreased the segregation index. This is evidenced in Figure 7.5(a,b), showing a dramatic decrease of the segregation index for $\Lambda \geq 6$. Note that different combinations of $A$ and $f$ can yield the same vibration strength $\Lambda$. Previous works concerned with segregation in vibrated fluidized beds (Zhao *et al.*, 2015), evidenced different values of the segregation index for the same $\Lambda$ and different combinations of $A$ and $f$. However, the superficial gas velocity at which the segregation index reaches a maximum is very similar in these combinations of $f$ and $A$. Hence, for the system studied, $\Lambda$ is a key parameter controlling segregation.

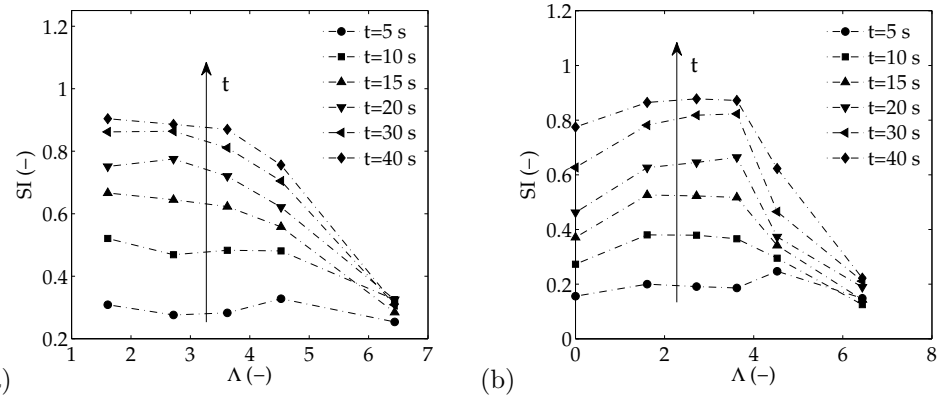


**Figure 7.5:** Segregation index as a function of the vibration strength at different time instants. (a) Mixture 1 with $U_0/U_{mf,D} = 0.91$, (b) Mixture 2 with $U_0/U_{mf,D} = 1.16$.

Figure 7.6 presents the final value of the segregation index, viz. the $SI$ reached at large $t$ (i.e. when the rate of segregation is very small) as a function of the superficial gas velocity and the vibration strength for the two mixtures. As observed before in Figures 7.3 and 7.4, Figure 7.6(a) shows that vibration extends the range of superficial gas velocities for which the final segregation of the mixture is relatively high ($SI > 0.8$). For Mixture 2, the segregation index reaches a maximum value for a superficial velocity slightly above the minimum fluidization velocity ($U_0/U_{mf,D} = 1.15$). This observation is in agreement with previous studies (Yang *et al.*, 2013; Sun *et al.*, 2014; Zhao *et al.*, 2015). Only for superficial velocities higher than $U_0/U_{mf,D} = 1.15$ the segregation index of Mixture 2 decreased with increasing superficial gas velocity. Figure 7.6(b) shows that, for the vibrated fluidized bed studied here, the maximum value of the $SI$ remained

unchanged regardless of the vibration strength. Only for $\Lambda \gtrsim 3.6$, the final segregation index decreases dramatically for Mixture 1. In Mixture 2, the critical value was higher, i.e. $\Lambda \sim 4.5$. This difference in the critical values obtained may be attributed to the higher velocity ratio, $U_0/U_{mf,D}$, used for Mixture 2. This requires a greater vibration strength to counteract vibration-induced segregation by the vibration-induced mixing effect.

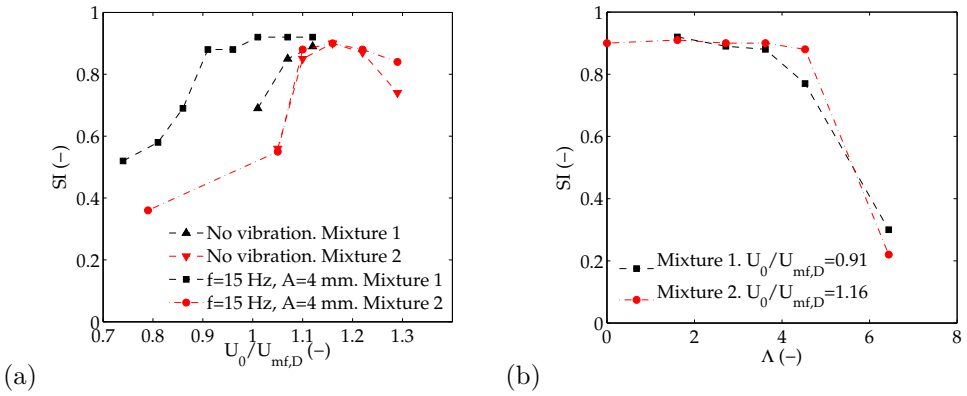


**Figure 7.6:** Final segregation index as a function of (a) the superficial gas velocity and (b) the vibration strength.

Figure 7.7 plots the time required to reach 90% of the final segregation index for each of the experiments conducted. Figure 7.7 only includes experiments in which the mixture attains a final segregation index $SI > 0.6$. From Figure 7.7(a) it can be observed that by passing from no vibration to vibration conditions, the time employed to segregate the particles is reduced in both mixtures. The difference between the segregation times of the experiments with no vibration and vibration decreases when $U_0/U_{mf,D}$ is increased. This is because at large superficial gas velocities, the effect of vibration on segregation is comparatively smaller than the effect of the gas. Also, for similar gas velocity ratios, $U_0/U_{mf,D}$, the segregation time of Mixture 1 is considerably shorter than Mixture 2 due to the higher density ratio ($\rho_D/\rho_L$) of the former.

The effect of the vibration strength on the segregation time is depicted in Figure 7.7(b). There exists a value of the vibration strength above which the introduction of vibration increases the time needed to segregate the mixture. In Mixture 1, the minimum segregation time occurs for $\Lambda = 2.7$ and progressively increases when increasing the vibration strength. The increase of the segregation time at large $\Lambda$ occurs despite the fact that the final segregation index decreases with $\Lambda$ (see Figure 7.6(b)). For Mixture 2 the trend is clearer. The segregation time decreased for increasing vibration strengths. However,

the segregation time shows a sudden increase for $\Lambda = 4.5$ since, for that experiment, a transitional-segregation regime occurs and that increases the segregation time (see Figures 7.2 and 7.4).

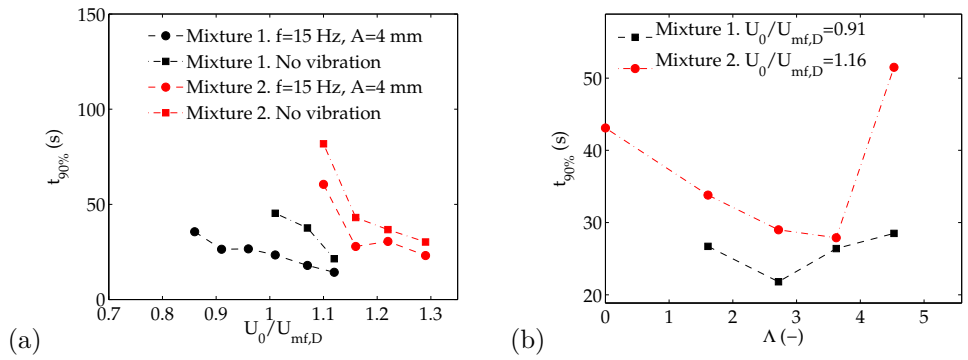


**Figure 7.7:** Time to reach 90% of the final segregation index observed for different (a) superficial gas velocities and the cases of no vibration and vibration with $f = 15$ Hz and $A = 4$ mm, (b) vibration strengths.

### 7.1.4 Conclusions

The effect of vibration and superficial gas velocity on density-induced particle segregation in a vertically vibrated fluidized bed was studied experimentally. A segregation index was developed to quantify segregation from DIA data. The results show that vibration enhances segregation in a gas fluidized bed in cases when the gas alone is unable to separate the particles of different density. The experiments revealed further that the temporal evolution and final extent of segregation is directly influenced by the vibration strength. It was observed that the superficial gas velocity and the vibration of the bed vessel possess counteracting effects on segregation. An increase of the superficial gas velocity increases segregation and facilitates dense particle percolation through light particles. This increased the extent of segregation as long as there is no vigorous bubbling in the bed. Low vibration strengths increase the excess of fluidization gas, enhancing in turn segregation (vibration-enhanced segregation). The introduction of strong vibrations in the system promotes convective movements of the bed promoting particle mixing (vibration-induced mixing) and counteracting the segregating effect of the superficial gas velocity. This decreases the final extent of the particle segregation. At intermediate vibration strengths, a transitional segregation regime occurs in which an initial vibration-induced mixing transitions to vibration-enhanced segregation. Generally, it was observed that a mixture with a higher density ratio decreases the time required for segregation.

The experiments indicate that, for each mixture, there is an optimum combination of vibration strength and superficial gas velocity to maximize segregation. In this optimum combination regime, vibration does not counteract gas-induced effects and allows the percolation (segregation) of the denser particles while limiting re-mixing effects.

## 7.2 Reversal of gulf stream circulation in a vibrated triangular fluidized bed

### 7.2.1 Introduction

When vibration energy is introduced in a granular assembly, a great variety of phenomena can appear (Jaeger *et al.*, 1996). These phenomena include heaping (Faraday, 1831), convection (Laroche *et al.*, 1989; Gallas *et al.*, 1992; Taguchi, 1992; Aoki *et al.*, 1996, 1997; Akiyama *et al.*, 1998; Zhang *et al.*, 2014) and subharmonic instabilities such as surface waves (Miles & Henderson, 1990; Pak & Behringer, 1993; Melo *et al.*, 1995; Clement *et al.*, 1997) and arching (Douady *et al.*, 1989; Wassgren *et al.*, 1996; Hsiau & Wu, 1998; Sano, 2005). They appear for different vibration strengths, commonly denoted as $\Gamma$ in these works. Among the different phenomena associated to vibration of the granular bed, convection of particles is one of the most important and has been deeply studied (Laroche *et al.*, 1989; Gallas *et al.*, 1992; Taguchi, 1992; Aoki *et al.*, 1996, 1997; Akiyama *et al.*, 1998; Zhang *et al.*, 2014). The appearance of granular patterns in vibrated beds is not only restricted to square-shaped beds. Recently, Lu *et al.* (2012*a*), studied the formation of polygon shaped patterns in a pseudo-2D vibrated bed of circular section. In their work, they identified a variety of granular patterns such as Faraday tilting, surface waves having 1/2 and 1/4 the frequency of vibration of the bed vessel, convection and polygonal structures. They proposed that the polygon-shaped patterns are the geometrical transformation of the arching structures typically encountered in vibrated beds of rectangular vertical section. Knight *et al.* (1993), studied the vibration-induced size separation in a vibrated granular media in both a rectangular and a conical bed filled with spherical particles of 2 mm of diameter. They observed that convection drives size segregation and, to confirm their hypothesis, they designed a conical container. In that container they observed that vibration promoted a convective motion of particles upwards along the walls and downwards in the middle of the container. The same convective pattern of particles was observed by Wassgren *et al.* (2002) in a vibrated pseudo-2D hopper of wedge shape (triangular) closed at its bottom exit and filled with soda lime particles of 1.3 mm of mean diameter. They also detected the formation of $f/2$ waves in the surface of the vibrated hopper, similar to those observed in vibrated rectangular

beds.

Although convection patterns have been studied in conical hoppers, the effect of injecting gas through the inclined lateral walls on the overall convection patterns is currently unexplored. It is conceivable that the injection of gas may alter the convection pattern and hence, in turn, also the particle recirculation and residence times in such systems. The potential use of this triangular geometry with background gas injection can be similar to that of either aerated hoppers (Papazoglou & Pyle, 1970; Ouwerkerk *et al.*, 1992; Chen *et al.*, 2011; Lu *et al.*, 2012*b*,*c*, 2015) or spout-fluidized beds with inclined walls, namely cylindrical spout-fluidized beds (Zhong *et al.*, 2006*a*,*b*, 2008; Sutkar *et al.*, 2013). The injection of gas through the inclined walls of this kind of beds, even if the bed walls are not vibrated, has been demonstrated to improve their performance.

Aerated hoppers are often used to avoid undesirable phenomena such as arching and funnel-flow in hoppers operating with fine particles. In these hoppers, the discharge rate can be increased when aerating the bed until a critical gas flow is reached, after which the discharge rate becomes constant (Papazoglou & Pyle, 1970; Ouwerkerk *et al.*, 1992). Different regimes may appear in the hopper depending on the aeration rate (Lu *et al.*, 2012*b*,*c*, 2015).

In spout-fluidized beds, in addition of the spouting gas, background gas is injected through the base or the inclined walls of the bed. Thus, this type of beds combines the favorable properties of both spouted and fluidized beds and have received great interest in the last decades in applications such as granulation, coating and drying (Mathur & Gishler, 1955; Marmo, 2007; Zielinska & Markowski, 2007; Sutkar *et al.*, 2013). Previous works on cylindrical spout-fluidized beds (Zhong *et al.*, 2006*a*,*b*, 2008), studied the hydrodynamic and spout characteristics in this type of beds without vibration.

The addition of vibration in aerated hoppers and spout-fluidized beds appears as a promising alternative to be considered in the near future because vibration can reduce the gas minimum fluidization velocity and increase the homogeneity of the granular material. However, the introduction of vibration may promote the appearance of different patterns which may cause large heterogeneities in the bed.

Additionally, the fact that the bed is of triangular shape may lead to interaction of the solids compression waves (observed in Chapters 3 and 5 for rectangular beds) caused by the collision of the bed bulk with each of the distributor inclined walls. This may help to better understand the dynamics of vibrated systems with complex geometries. Thus, a fundamental characterization of the combined effects of vibration and aeration in triangular or conical shaped beds is crucial to understand and further design these systems.

The present section aims at clarifying the dynamics of granular systems subjected to vibration in a bed of triangular geometry (i.e. pseudo-2D conical bed) and the influence

of gas injection through the inclined walls of the bed on the surface waves and convective patterns observed in the granular material. Different granular patterns are identified as a function of the vibration frequency, vibration strength and the superficial gas velocity. The results here presented may serve as a fundamental basis for elucidation of optimal combinations of vibration and gas injection in beds of triangular or conical geometry with implications to the spout-fluidized beds and aerated hoppers.

### 7.2.2 Experimental setup

The bed was filled up to the top of the inclined walls with ballotini glass beads with a mean diameter of $d_p = 1.15$ mm and density $\rho_p = 2500$ kg/m$^3$. Approximately a 5% of the particles were black to enhance the correlation during the processing of results with Particle Image Velocimetry (PIV). The minimum fluidization velocity of the particles under static conditions was measured by means of a pressure sensor located in the first plenum and resulted to be $U_{mf} = 0.41$ m/s. A high speed camera (Optronics CL 600 x2/M) was used to record images through the front wall of the bed at a frame rate of 200 images per second during 20 seconds.

The effect of vertical vibration on the dynamics of the vibrated triangular fluidized bed was studied in a twofold way. Firstly, a qualitative observation of the granular patterns of the bed was carried out. The different transitions in the flow regimes for a variety of vibration strengths, $\Gamma = A(2\pi f)^2/g$, were qualitatively identified as a function of the vibration frequency, $f$, and for different superficial gas velocities under, equal and above the minimum fluidization velocity, including the case of no gas injection (i.e. $U_0/U_{mf}$ =0, 0.7, 1 and 1.2). Secondly, once the flow regimes were identified, PIV measurements were undertaken in order to study the motion of particles in the triangular bed for the experimental conditions depicted in Table 7.3.

**Table 7.3:** Experimental conditions.

| $f$ (Hz) | $\Gamma$ (-) | $A$ (mm) | $U_0/U_{mf}$ (-) |
|---|---|---|---|
| 14 | 3.5 | 4.4 | 1.2 |
| 15 | 1.5 | 1.7 | 1.2 |
| 15 | 2 | 2.2 | 1.2 |
| 15 | 2.5 | 2.8 | 1.2 |
| 15 | 3 | 3.3 | 1.2 |
| 15 | 3.5 | 3.9 | 0.7, 0.9, 1, 1.1, 1.2 |
| 16 | 3.5 | 3.4 | 1.2 |

### 7.2.3 Results and discussion

The following sections study the dynamics of the particles in the vibrated fluidized bed. Firstly, the general bed behavior is described and different granular patterns are detected. Then, the convective motion (viz. gulf stream circulation) of particles in the bed is characterized using the time-averaged velocity of particles. Finally, to further explain the origin of the gulf stream motion and the occurrence of a reversal in its direction, the cyclic particle motion is analyzed as a function of the phase in a period of vibration.

#### General bed behavior

Under conventional fluidization conditions, i.e. the air is introduced through the inclined walls and the bed is not vibrated, there is no particle motion for $U_0 < U_{mf}$ and bubbles appear for $U_0 > U_{mf}$, which rise close to the inclined walls.

It was observed that the combination of vibration of the bed and gas injection through the inclined walls of the bed drastically changed the way particles behave in the bed, promoting the formation of granular patterns in the bed. In the case the bed vessel is not vibrated, the particles presented a behavior similar to that of a conventional fluidized bed. That is, the bed is fixed for superficial gas velocities below $U_{mf}$, whereas bubbles, which tended to rise close to the lateral walls of the bed, commence to appear for superficial gas velocities above $U_{mf}$. Figure 7.8 shows the different granular patterns observed in the triangular bed when the bed is vibrated with different combinations of the vibration frequency, vibration strength and superficial gas velocity. In Figure 7.8(a), Faraday tilting is the dominant behavior (Lu *et al.*, 2012*a*). Here, the bed is lifted by vibration ($\Gamma > 1$) and the particles roll down in the inclined surface of the bed and move up through the bulk of the bed. In Figures 7.8(b) and 7.8(c), surface waves with formation frequencies $f/4$ and $f/2$ (i.e. the frequency of the surface waves is one quarter or one half of the vibration frequency, respectively), are observed. These surface waves are similar to those produced in rectangular and circular beds (Pak & Behringer, 1993; Lu *et al.*, 2012*a*). Figures 7.8(d-f) schematize the different convective patterns observed in the triangular bed for the range of vibration conditions tested. In Figure 7.8, vibration conditions and gas fluidization velocities have been selected to exemplify the most characteristic surface waves and convective patterns detected in the experiments.

In Figure 7.8(d), a convective motion with a downflow of particles at the center of the bed takes place. Interestingly, if the gas injection through the lateral walls is large enough, the gulf-stream motion of particles in the bed could be reversed, as depicted in Figure 7.8(e,f). During this convective motion, the particles at the extreme sides of bed barely mix, despite the fact the particles move upwards and downwards at the center of the bed. This may induce the presence of large heterogeneities in the bed in

chemical conversion processes. Figure 7.8(f) represents a case in which an inflexion point in the central section of the bed, with upward and downward motion above and below it, respectively, could be observed. A net downward displacement of particles could be observed close to the front and rear walls of the bed and the particles are transported to the top of the bed inside the bulk between these walls. Also, in Figure 7.8(f), vibration causes the whole bed to cyclically detach from the inclined walls, which probably have and influence in making the side walls convection observed in Figure 7.8(e) to disappear. In particular, in Figure 7.8(e) an upward vertical motion of particles is observed in the center of the bed, whereas the convection cells are very small and are situated close to the side walls.

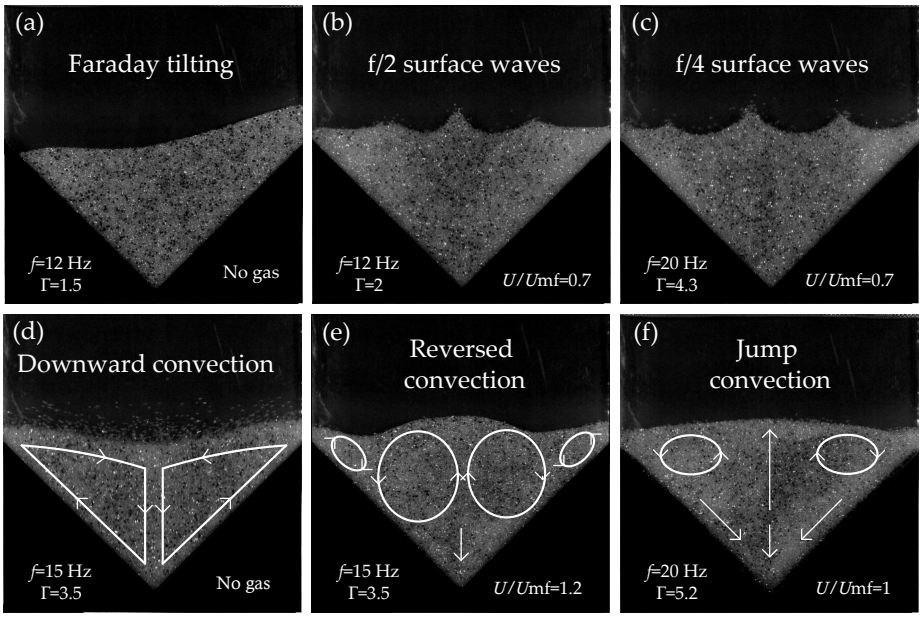


**Figure 7.8:** Snapshots of the granular patterns observed in the triangular fluidized bed. (a) Faraday tilting ($f = 12$ Hz, $\Gamma = 1.5$, No gas), (b) $f/4$ surface waves ($f = 20$ Hz, $\Gamma = 4.3$, $U_0/U_{mf} = 0.7$), (c) $f/2$ surface waves ($f = 12$ Hz, $\Gamma = 2$, $U_0/U_{mf} = 0.7$), (d) normal convective motion ($f = 15$ Hz, $\Gamma = 3.5$, No gas), (e) reversed convective motion ($f = 15$ Hz, $\Gamma = 3.5$, $U_0/U_{mf} = 1.2$), (f) jump convective motion ($f = 20$ Hz, $\Gamma = 5.2$, $U_0/U_{mf} = 1$).

Figure 7.9 shows the time-averaged solids relative velocity obtained with PIV in the vibrated triangular fluidized bed for different combinations of the vibration amplitude, vibration frequency and superficial gas velocity. In general, for the case with no gas injection through the lateral walls of the bed, the only convective motion observed is similar to the one shown in Figure 7.9(a) for $f = 15$ Hz and $\Gamma = 3.5$ with a downward displacement of particles in the central part of the bed and downward close to the inclined

walls of the vessel. The result is a convective motion of the bed particles (i.e. gulf stream circulation). Here, the bed bulk is cyclically lifted from the inclined walls with a frequency equal to the frequency of vibration of the bed. The convective motion observed in Figure 7.9(a), will be denominated hereafter as 'downward convection'.

When increasing the superficial gas velocity while keeping the same $\Gamma$ and $f$, different convective patterns were observed. Figure 7.9(b,c,e,f,g) represents the velocity vectors for the example case of $f = 15$ Hz, $\Gamma = 3.5$ and superficial gas velocities of $U_0/U_{mf} = 0.7, 0.9, 1, 1.1$ and $1.2$, respectively. For a superficial gas velocity of $U_0/U_{mf} = 0.7$ in Figure 7.9(b), the whole bed bulk separates from the lateral walls of the bed with a period $T_o = 2/f$, i.e. the particles in the bed repeat the same pattern every 2 cycles of the vessel vibration. In Figure 7.9(b), the downward motion of particles found in Figure 7.9(a) in the center of the bed is still present. Increasing the superficial gas velocity from $U_0/U_{mf} = 0.7$ (Figure 7.9(b)) to $U_0/U_{mf} = 0.9$ (Figure 7.9(c)) does not promote a significant change on particle average velocity in the bed. In these cases of $U < U_{mf}$ it was visually observed that a three dimensional convective motion of particles appears, which is induced by the interaction of the particles with the front and rear walls of the bed. In general, when air is introduced through the distributor of the bed, particles move down close to the front and back walls of the bed and move up through the middle section between these walls. These 3D effects are manifested in Figures 7.9(b,c) through a uniform field of descending velocity vectors on the transparent front wall of the bed.

Noticeably, for $f = 15$ Hz and $\Gamma = 3.5$, when the superficial gas velocity is equal or above $U_{mf}$ ($U_0/U_{mf} \geq 1$), (see Figure 7.9(e-g)), a reversal of the previously described downward convection of the bed particles is observed. Particles ascend now in the central section of the bed and descend in the regions closer to the inclined walls (see Figure 7.9(e)). For the sake of simplicity, this pattern of upward convection of particles in the central region of the bed will be referred in the present chapter as 'reverse convection' since it has opposite direction to the pattern found in Figure 7.9(a). Figure 7.9(h) schematically shows the behavior of particles in the bed when this reverse convection occurs. The region in which the particles ascend is delimited by the presence of two inflexion points (i.e. locations with null average velocity) in the central section of the bed at different heights, which separate the ascending or descending average displacement of particles. Another two inflexion points are symmetrically located at the same height at both sides of the bed. These last inflexion points are centers of the two main convective cells formed in the bed. In Figure 7.9(e-g), two regions with different convective motions can be clearly distinguished in the triangular bed: the central part of the bed (from around $x = 0.04$ m to $x = 0.16$ m in Figure 7.9(g)) and the two regions close to the side walls. These two regions behave similarly to the arching structures in rectangular granular beds (see Aoki *et al.* (1996)) in which arches alternatively detach from the bottom of

the bed and present an upward convective motion of particles on their central section and downwards in the boundary between the two arches (see Figure 7.9(h)). The size of the arch formed on the region close to the bed lateral walls increases with the gas velocity in Figures 7.9(e-g). Further increase of the superficial gas velocity under the same vibration conditions leads to the formation of bubbles close to the sidewalls of the bed and, again, to a downward convection of particles in the central section of the bed. If the vibration strength $\Gamma$ is large enough, for $U_0/U_{mf} = 1$ (Figure 7.9(d)), the size of the zone in which the arching structures appear is very reduced and the bed bulk completely detaches from the inclined bed. The period of oscillation of the bed bulk in this case is $T_o = 3/f$.

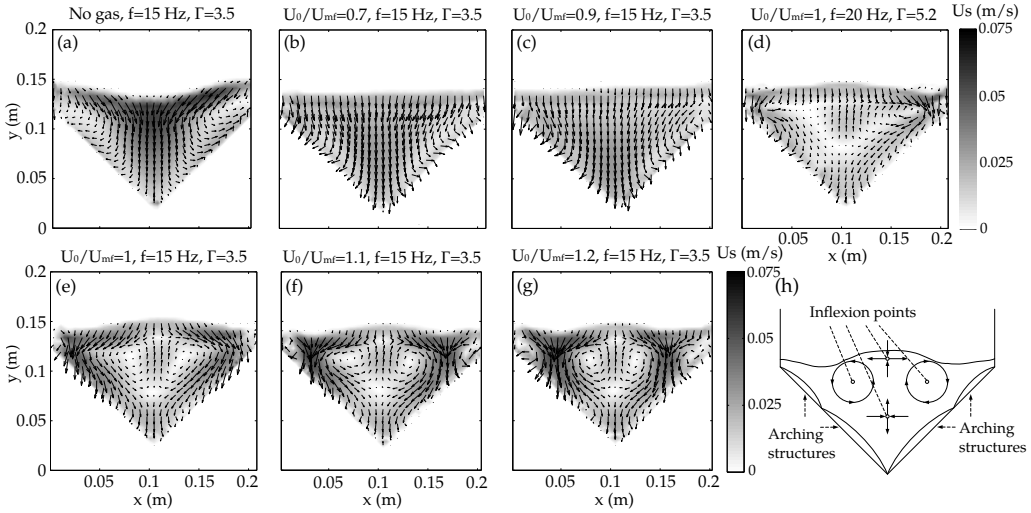


**Figure 7.9:** Time-averaged particle velocity in the triangular vibrated fluidized bed for (a) No gas injection, (b) $U_0 = 0.7U_{mf}$, (c) $U_0 = 0.9U_{mf}$, (d) $U_0/U_{mf} = 1$, (e) $U_0/U_{mf} = 1$, (f) $U_0 = 1.1U_{mf}$ and (g) $U_0 = 1.2U_{mf}$. Results correspond to $f = 15$ Hz and $\Gamma = 3.5$ (a-c, e-g) and $f = 20$ Hz and $\Gamma = 5.2$ (d). The velocity vectors are shown superimposed to the particle velocity magnitude. (h) Schematic behavior of particles in the reversed convection mode.

In order to characterize the vibration and gas conditions that lead to the different granular patterns encountered in Figures 7.8 and 7.9, Figure 7.10 depicts the transition maps resulting from varying $\Gamma$ and frequency $f$ for four different superficial gas velocities. For the case of no gas injection, the particles started to appreciable show convective motions for ($\Gamma > 1$). For $1.2 < \Gamma < 1.8$ Faraday tilting (see Figure 7.8(a)) prevails. The convective pattern described in Figure 7.9(a) was observed in the experiments for values of the vibration strength between 1.8 and 3.75. Further increase of the vibration amplitude to values $\Gamma = 3.5 - 4$ promoted the formation of surface waves of period $T_o = 4/f$ (see Figure 7.8(b)). As mentioned above, the dependence of the particle behavior on the vibration frequency and amplitude changed dramatically when gas was injected through

the inclined walls. This may be attributed to an increase in bed voidage with increasing gas flow, affecting critically the interaction between particles and the walls and, in turn, the propagation of the vibration inside the bed bulk. The effect of $U_0/U_{mf}$ on the particles flow pattern can be seen in Figure 7.10(b-d), which shows the transition maps for superficial gas velocities under, equal to, and above the minimum fluidization velocity. For a superficial gas velocity of $U_0/U_{mf} = 0.7$, an intricate transition map was obtained, in which surface waves of frequency $f/2$, $f/4$ and reversed convection were obtained for narrow ranges of $\Gamma$ (i.e. operative windows). For the same vibration frequency, up to seven different motions could be observed when progressively increasing $\Gamma$: no motion of particles, motion of particles in an unordered fashion, $f/2$ surface waves, jump mode in which the bed bulk fully detached from the inclined walls, $f/4$ surface waves and an unstable mode in which particles did not find a stable granular pattern. In general, the value of $\Gamma$ required to a specific bulk motion to appear decreases with $f$. The operative window for reverse convection observed in Figure 7.10(b) broadened when increasing the superficial gas velocity to $U_0/U_{mf} = 1$ in Figure 7.10(c). In this case, four different particle behaviors were encountered when increasing $\Gamma$. For low vibration amplitudes, the particles appreciably moved in the bed without following an ordered pattern. Increasing the vibration amplitude promoted the formation of the so called reversed convection. An unstable mode, serving as a transition between the reversed convection and jump modes depicted, respectively, in Figures 7.9(e,f) was observed when further increasing $\Gamma$. Finally, when increasing the superficial gas velocity beyond $U_{mf}$, as shown in Figure 7.10(d), only two modes were observed. In this case, for a fixed $f$, if the vibration strength was small enough, a convective motion with particles moving downwards in the center of the bed was observed. However, when increasing the vibration amplitude, there was a value of $\Gamma$ beyond which the reversed convection of particles was found, with a behavior similar to that described in Figure 7.8(e). The vibrational strength at which the convective motion is reversed increases with $f$. This implies that for a sufficiently high superficial gas velocity, the reversal of the gulf stream is suppressed by increasing the vibration frequency.

**Particle gulf stream motion in the bed**

Figure 7.11 shows the effect of the vibration strength on the reversed convection pattern of the time-averaged particle velocity described in Section 7.2.3. The superficial gas velocity of the experiments was $U_0/U_{mf} = 1.2$ and the vibration conditions were $f = 15$ Hz and $\Gamma = 1.5 - 3.5$. According to Figure 7.10(d), these operative conditions ensure the presence of cases in which downward convection ($\Gamma = 1.5$ and 2) and reversed convection ($\Gamma = 2.5, 3$ and 3.5) are observed.

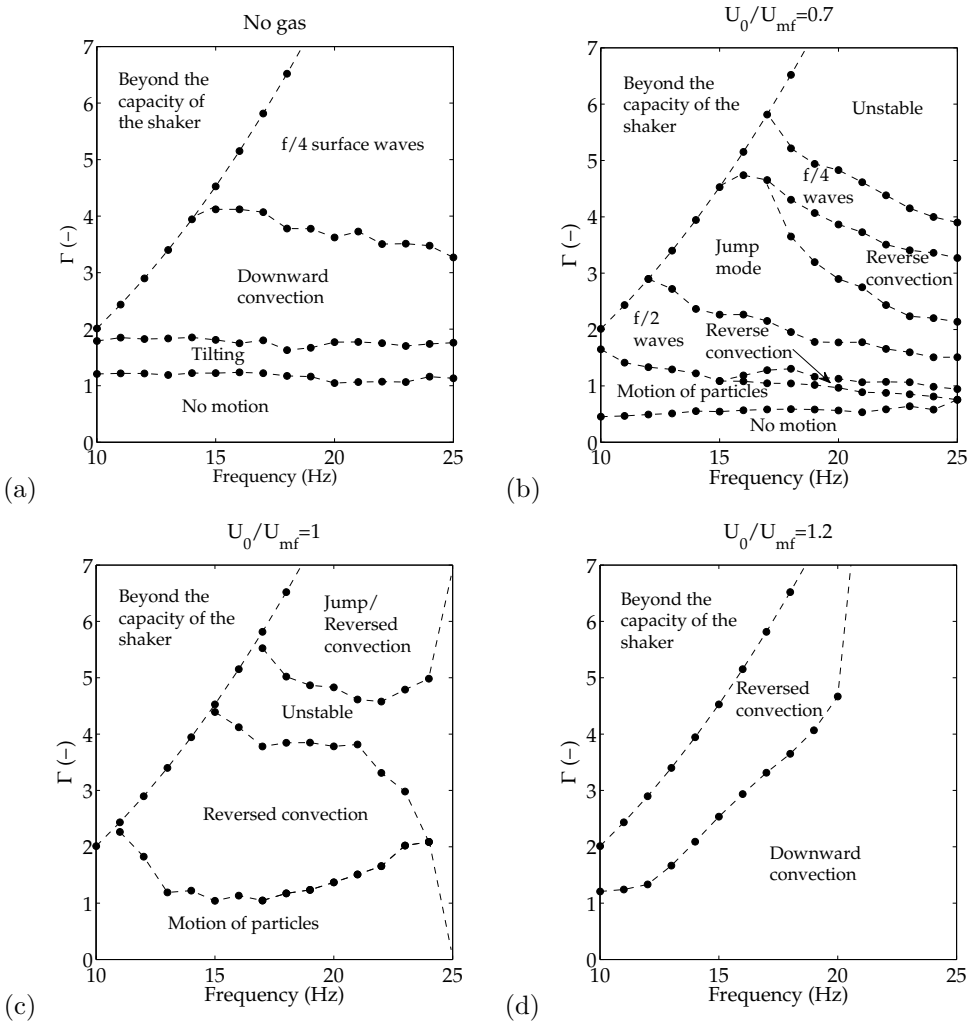


**Figure 7.10:** Phase map of the different regimes observed in the vibrated fluidized triangular bed at different superficial gas velocities: (a) No gas injection, (b) $U_0 = 0.7\ U_{mf}$, (c) $U_0 = U_{mf}$ and (d) $U_0 = 1.2\ U_{mf}$.

Figures 7.11(a,b) confirm the regimes defined in Figure 7.10(d) (i.e. for $\Gamma \lesssim 2.4$). A downward convection pattern is observed with particles moving downwards in the central section of the bed and upwards close to the inclined walls. Two recirculation vortexes are formed close to the inclined walls of the bed due to the change from ascending to descending motion of the particles in that region of the bed.

An increase of the vibration strength to values $\Gamma \gtrsim 2.4$ promotes the reversion of the gulf stream motion of the bed. For $\Gamma = 2.5$ (Figure 7.11(c)), the area with upward velocities of particles (viz. reversed gulf stream motion) is smaller than for $\Gamma = 3$ and

$\Gamma = 3.5$ in Figure 7.11(d,e), due to its closeness to the transition between the downward convection and the reverse convection. Also, for $\Gamma = 2.5$, the period of the bed bulk oscillation is $T_o = 2/f$, i.e. the bed bulk repeats the same granular motion every two oscillations of the bed vessel. An increase of the $\Gamma$ within the range of operation tested does not seem to promote significant changes in the position of the arching structures formed close to the lateral walls of the bed. However, the period of oscillation of the bed bulk motion in the cases of $\Gamma = 3$ and 3.5 is $T_o = 4/f$, which implies that the bed bulk repeats the same oscillatory behavior every four vibration cycles of the bed vessel. Besides, the average velocity of particles in the boundary between two arches ($x = 0.04$ m and $x = 0.16$ m in Figure 7.11(c-e)) increases when increasing the vibration strength due to the more vigorous oscillation of the bed bulk. This manifests that the velocity of the convective rolls formed in the bed is sensitive to the vibration amplitude. However, the velocity of the reversed gulf stream circulation in the central region of the bed does not greatly change when increasing $\Gamma$.

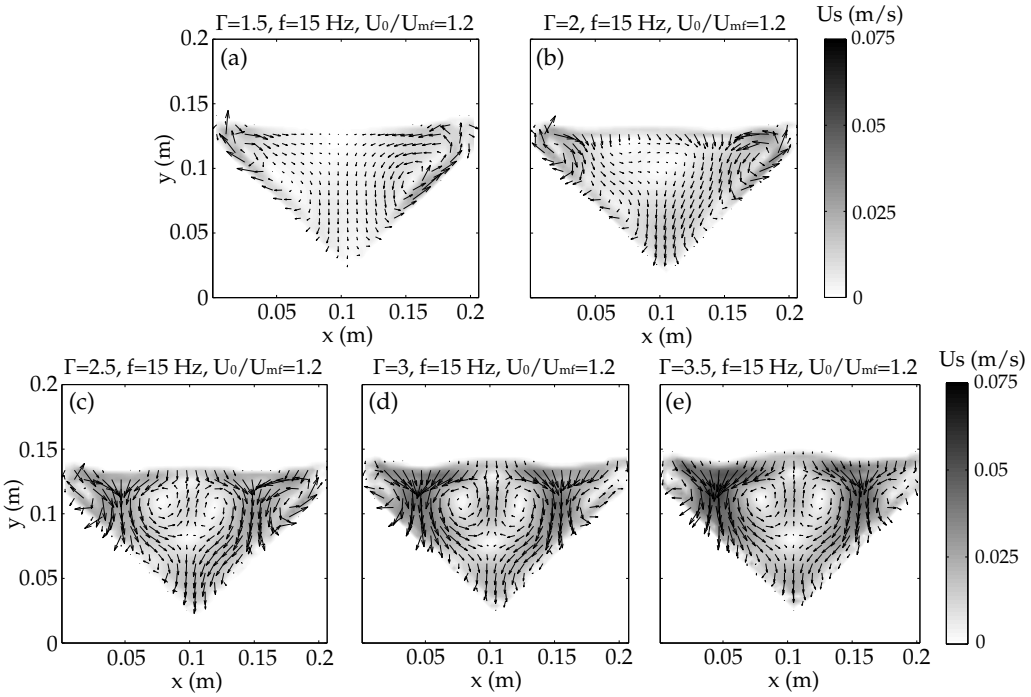


**Figure 7.11:** Effect of the vibration strength on the time-averaged particle velocity in the triangular vibrated fluidized bed for $f = 15$ Hz and $U_0 = 1.2\ U_{mf}$: (a) $\Gamma = 1.5$, (b) $\Gamma = 2$, (c) $\Gamma = 2.5$, (d) $\Gamma = 3$ and (e) $\Gamma = 3.5$. The velocity vectors are shown superimposed to the particle velocity magnitude.

Figure 7.12 shows the average velocity vectors superimposed to the average velocity magnitude for experiments conducted for the same superficial gas velocity ($U_0/U_{mf} = 1.2$) and vibration strength ($\Gamma = 3.5$) and different vibration frequencies $f$ =14, 15 and 16 Hz. In Figure 7.12, the average velocity of the particles in the bed slightly decreases as the frequency of vibration of the bed vessel increases. This can be clearly appreciated in the velocity magnitude between the arching regions formed in the bed. Note that the vibration amplitude decreases when increasing the vibration frequency for the same $\Gamma$ (4.4 mm for 14 Hz, 3.8 mm for 15 Hz and 3.4 mm for 16 Hz). The results depicted in Figure 7.12 reveal that the downward velocity of particles between the arching regions is slightly higher for the cases with bigger vibration amplitudes. Thus, it can be deduced that the velocity of the particles is mainly affected by the vibration amplitude and not by the vibration strength (see also Figure 7.11). However, as in Figure 7.11, the upward velocity of particles in the central section of the bed is not strongly affected by the change in the vibration frequency. Besides, from a qualitative point of view, a slight change of position and a loss of symmetry of the four inflexion points in the bed that can be observed in Figure 7.12 for the cases of $f = 14$ Hz and $f = 16$ Hz. This can be explained taking into account that the reversal of the gulf stream motion and the appearance of inflexion points in the bed (Figure 7.9(h)) is induced by vibration that is transmitted to the bed by the collision of the bed bulk with the inclined walls. If the bed bulk detaches (at least partially) from the bed in a non perfectly symmetrical way, particles would impact one of the inclined walls earlier than the other, and this promotes the asymmetry of the inflexion points.

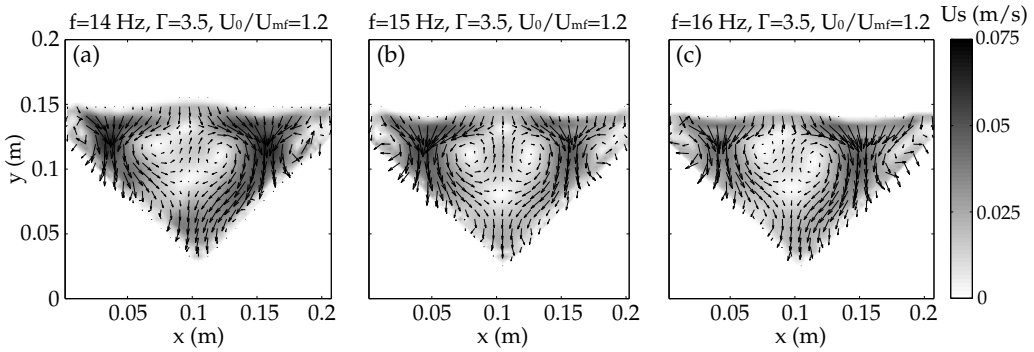


**Figure 7.12:** Effect of the vibration frequency on the time-averaged particle velocity in the triangular vibrated fluidized bed for $U_0 = 1.2\ U_{mf}$ and $\Gamma = 3.5$ (a) $f = 14$ Hz, (b) $f = 15$ Hz, (c) $f = 16$ Hz. The velocity vectors are shown superimposed to the particle velocity magnitude.

**Particle motion as a function of the vibrating phase**

It has been seen in the previous sections that mean values of particle velocity define recirculations that can be reversed for certain conditions. Also, when the reversed motion occurs, inflexion points appear. In order to study the origin of the reversed recirculations and inflexion points, this section analyzes the behavior of the particle velocity in the triangular bed as a function of the phase in the vibration period (see Section 2.3.3). This type of analysis helps to understand the average motion of solids in the bed, for example the downward convective motion or the propagation of the wave of solids velocity.

Figure 7.13 presents the results of the phase averaged velocity vectors for the case of $f = 15$ Hz, $\Gamma = 3.5$ and no gas injection through the bed inclined walls. This combination of $f$ and $\Gamma$ has been selected to ensure the presence of recirculation patterns of particles for the case of no gas injection through the inclined walls of the bed and for the case of $U_0/U_{mf} = 1.2$ shown in Figure 7.14 (see Figure 7.9(a,g)). Here, $\phi$ represents the phase of the bed vessel displacement, with $\phi = 0 - 0.5\pi$ rad corresponding to the bed vessel moving upwards from the central to the highest vertical position. In the interval $\phi = 0.5\pi - 1.5\pi$ rad the bed bulk detaches from the inclined walls due to the inertia of the particles, i.e. the bed vessel starts to move downwards but the bed bulk keeps on moving upwards because $\Gamma > 1$. Due to this, the average particle motion in Figure 7.13 in the intervals $\phi = 0.5\pi - \pi$ rad and $\phi = \pi - 1.5\pi$ rad presents a net upward displacement (relative to the bed vessel). Note that the slightly higher velocity magnitude of particles in the top region of the bed, close to the freeboard of the bed, for the interval $\phi = \pi - 1.5\pi$ rad reflects the expansion of the bed bulk. The particles in the upper section of the bed, as they support a smaller mass of particles above them, move more freely than the particles in the lower layers and present a larger upward velocity. The contact between the bed inclined walls and the bed bulk takes place in the phase interval $\phi = 1.5\pi - 2\pi$ rad when the ascending bed vessel impacts the descending bulk of the bed. This can be deduced in Figure 7.13(a) as a result of the decrease of the average particle velocity in a reduced region close to the walls in that phase interval. In order to further describe the effect of the impact of the bed vessel on the bulk motion, Figure 7.13(b) details the averaged velocity vectors presented in Figure 7.13(a) for a phase interval $\phi = 1.75\pi$ rad to $\phi = 0.06\pi$ rad of the next cycle. In that phase interval, the bed impacts the inclined walls of the bed at around $\phi = 1.75\pi$ rad. From that phase instant on, the velocity maps of the bed present, in Figure 7.13(b), two distinguishable regions in the intervals $\phi = 1.94\pi - 2\pi$ rad and $\phi = 0 - 0.06\pi$ rad: one central region ($\alpha$ in Figure 7.13(b)) that maintains the downward velocity of the particles relative to the walls due to gravity, and a progressively growing region in which particles are slowed down by the collision of particles with the inclined walls ($\beta, \eta$), similar to that encountered

in Wassgren *et al.* (2002). In Figure 7.13(b), the red and blue lines delimit the solids' velocity magnitude $U_s = 0.2$ m/s and $U_s = 0.5$ m/s, respectively. These two velocities have been selected as they can define the progression of the solids velocity wave inside the bed. The displacement of these curves to the central region of the bed reveals the presence of a mechanism of wave propagation inside the bed caused by the impact of the bed bulk with the inclined walls, similarly as the observations of a rectangular bed in Chapter 3. The velocity of propagation of this velocity perturbation can be calculated as the distance employed by the $U_s = 0.2$ m/s and $U_s = 0.5$ m/s velocity contours presented in Figure 7.13(b) to cover the propagation distance parallel to the inclined bed walls divided by the time needed to cover that distance. The mean propagation velocities calculated for the red and blue contours between $\phi = 1.75\pi$ rad and $0.06\pi$ rad in Figure 7.13(b) are $V_{prop,0.2} = 5.8$ m/s and $V_{prop,0.5} = 5.5$ m/s, respectively. The relative displacement of particles in the central section of the bed ($\alpha$) with regard to the displacement in the regions close to the inclined walls ($\beta, \eta$) shown in Figure 7.13(b), promotes the formation of the convection cells observed in Figure 7.9 when no gas is injected through the lateral walls of the bed.

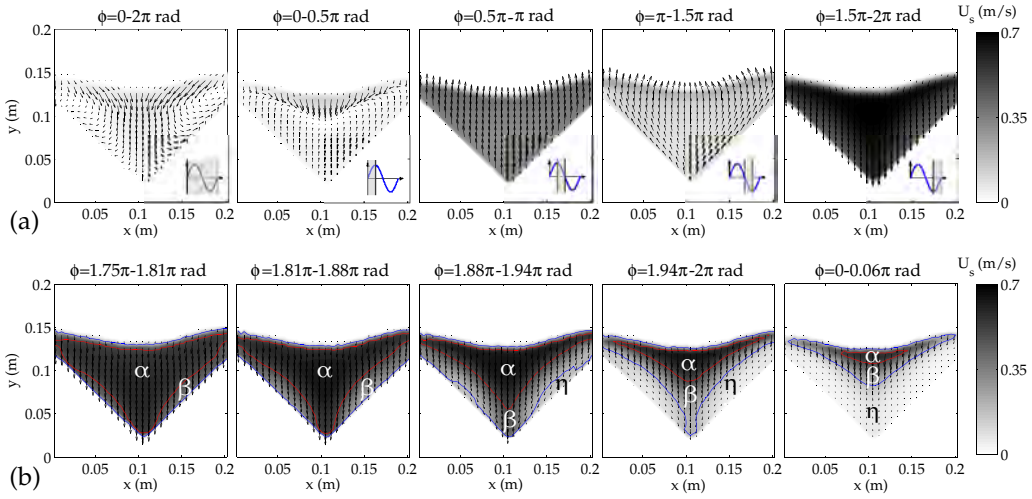


**Figure 7.13:** Phase averaged particle velocity in the vertically vibrated triangular bed with $f = 15$ Hz, $\Gamma = 3.5$ and no gas injection. (a) Average oscillation over the complete vibration cycle and for four different phase intervals. (b) Detail of the particle behavior on the interval $\phi = 1.75\pi - 0.06\pi$ rad (of the next cycle): the blue lines indicate the contours of $U_s = 0.2$ m/s and the red line the contours of $U_s = 0.5$ m/s. The shadowed zone in the cycle represented in the lower right corner of each figure represents the phase interval in which the particle velocity was averaged. The velocity vectors are shown superimposed to the particle velocity magnitude.

Figure 7.14 shows the solids phase averaged velocity in the bed for the case of $f = 15$ Hz, $\Gamma = 3.5$ and a superficial gas velocity of $U_0/U_{mf} = 1.2$. In addition to the reversal motion of particles in the bed, it was observed in the recorded images that the main frequency of oscillation of the bed bulk was equal to the vibration frequency of the bed vessel, $f$. However, injection of gas through the bed inclined walls made these oscillations of the bed bulk not totally similar to each other and the bed required four consecutive vibration cycles of the vessel to repeat the same granular pattern. Therefore, gas injection at $U_0/U_{mf} = 1.2$ through the bed inclined walls increased the overall period of oscillation of the bed bulk to $T_o = 4/f$. In consequence, an overall cycle of the bed bulk oscillation were composed of four consecutive subcycles (subcycles 1 to 4 in Figure 7.14). Each subcycle covers a time period equal to the vibration period of the bed vessel, $T$. In Figure 7.14, each row (e.g. Figures 7.14(a) to 7.14(b)) comprises a subcycle. The first column of Figure 7.14 contains the velocity vectors in the triangular bed time averaged over a subcycle. Thus, the average of the velocity vectors in the first column of Figure 7.14 corresponds to the overall time averaged particle velocity, which is shown in Figure 7.9(g). The next columns of Figure 7.14 represents the phase averaged particle velocity (see Section 2.3.3) resulting from averaging the velocity vectors over a vibration phase intervals of size $\Delta\phi = \pi/2$ rad.

In Figure 7.14 there are two clearly distinguishable regions in the bed, i.e. the central section of the bed, close to $x = 0.1$ m, and the lateral region, close to the bed lateral corners. These two regions present opposite vertical particle average velocities in each of the subcycles studied in the figure. When the particles in the central section of the bed have an average ascending velocity, the ones belonging to the region close to the lateral corners present a descending velocity and vice versa. The bed bulk impacts the bed vessel close to the vertex of the triangle just before the first subcycle (Figure 7.14(a)) and a compression wave of particles propagates upwards inside the central region of the bed between Figure 7.14(d5) and (a2), which decreases the velocity of the particles in that region. Once the bed vessel commences its descending motion ($\phi = \pi/2$ rad in Figure 7.14(a3)), the particles in the bed bulk ascend (relatively to the bed vessel) due to their inertia. However, the phase averaged velocity of particles in the phase interval $\phi = \pi/2 - \pi$ rad in each of the subcycles (Figures 7.14(a3,b3,c3,d3)) are different from each other because in the previous phase interval the collision points of the particles with the inclined walls occurred at different locations. This causes the particles in the central and lateral regions of the bed to move with a different relative velocity. In the next phase interval, $\phi = \pi - 3\pi/2$ rad, the difference in the relative velocity of the central and lateral regions is more noticeable. Finally, during the phase $\phi = 3\pi/2 - 2\pi$ rad, the bed bulk presents a net relative downward motion as the bed vessel is moving upwards.

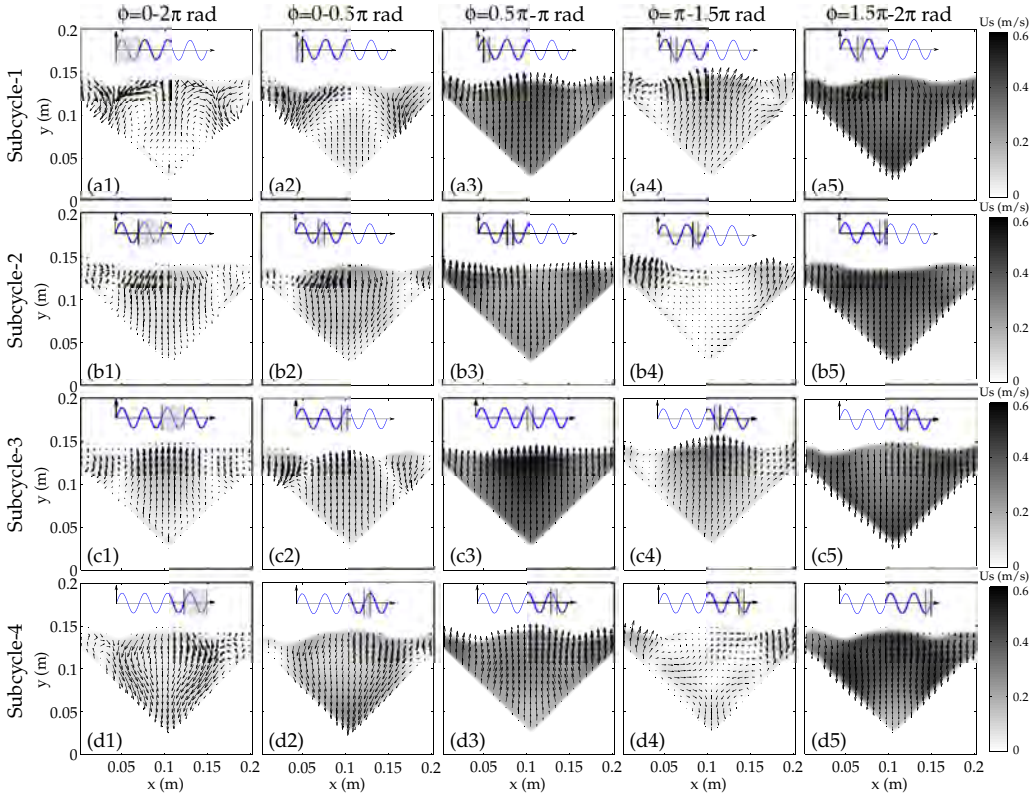


**Figure 7.14:** Phase averaged particle velocity in the vertically vibrated triangular bed, $f = 15$ Hz, $\Gamma = 3.5$ and $U_0/U_{mf} = 1.2$ for the four consecutive subcycles of oscillation observed (a-d). The velocity vectors in the first column in the figure represents the particle averaged velocity over a complete subcycle, which corresponds to a vessel vibration cycle $\phi = 0 - 2\pi$ rad. The next four columns show the decomposition of the averaged velocities of particles in phase intervals of $\Delta\phi = \pi/2$ rad. The shadowed zone in the vessel displacement included in the lower right corner of each figure represents the phase interval in which the particle velocity was averaged. The velocity vectors are shown superimposed to the particle velocity magnitude.

In the second subcycle of oscillation of the bed (Figure 7.14(b)), the impact of the particles with the vessel takes place in a region of the inclined walls close to the bed lateral walls. Thus, the interval $\phi = 0 - \pi/2$ rad (Figure 7.14(b2)) presents a descending motion of particles in the central region of the bed while particles are still unaffected by the presence of the inclined walls. Besides, the particle motion in the lateral region is impeded due to the presence of the inclined walls. In the next two fractions of the cycle, $\phi = \pi/2 - 3\pi/2$ rad, Figures 7.14(b3, b4), the region close to the lateral walls present a larger upward velocity and the particles in the central region of the bed are compacted. This eventually promotes the earlier impact of the central region of the bed bulk with the inclined walls of the bed in a region close to the bed vessel vertex. However, differently

to the first subcycle (Figure 7.14(a)), when the impact of particles with the bed vessel takes place between the second and the third subcycle (Figure 7.14(a3,a4)), the central region of the bed impacts the bed inclined walls over a wider surface, which promotes a different behavior of the particles in the bed along the third and fourth subcyles of vibration (Figure 7.14(c,d)). All the phenomena previously described and the differences in the relative velocity of particles in the two distinguishable regions in the bed promote the formation of the time-averaged recirculation patterns shown in Section 7.2.3. This indicates that the four inflexion points found when averaging the velocity vectors along an experiment are points of average velocity equal to zero caused by the composition of opposed relative velocities resulting from each subcycle of bed bulk oscillation.

If the amplitude of the bed vessel vibration is sufficiently small, for example $f = 15$ Hz, $U_0/U_{mf} = 1.2$ and $\Gamma = 2.5$ in Figure 7.11(c), the period of oscillation of the bed bulk was found to be $T_o = 2/f$. In this case, only two subcycles of the bed bulk oscillation appear and the reversal of the gulf stream motion is promoted by a particle behavior similar to that observed in the first two subcycles of Figure 7.14 (a,b).

### 7.2.4 Conclusions

This section experimentally studied the effect of the vibration frequency, the vibration strength and the superficial gas velocity in a triangular fluidized bed that was vertically vibrated. In this novel configuration, the gas was injected through the inclined walls of the bed. When no gas was injected, different granular patterns could be observed. These patterns were similar to those reported for rectangular and circular beds, e.g. Faraday tilting, $f/2$ and $f/4$ surface waves and a gulf stream circulation (i.e. convective motion of particles) due to particles descending through the central section of the bed and ascending close to the inclined walls. However, gas injection through the inclined walls of the bed changed the way particles behave in the bed. Under some vibration conditions, specially if the superficial gas velocity is above, but close, to the minimum fluidization velocity, the gulf stream circulation of particles in the triangular bed could be reversed, leading to particles ascending through the central section of the bed and descending next to the inclined walls. Also, arching structures, which alternatively detach from the inclined distributor of the triangular bed, were formed in a similar way to the arching structures reported for vibrated rectangular beds.

PIV measurements of the particle motion in the bed were employed to identify the cause of the gulf stream reversal and the effects of the vibration frequency and vibration strength on the particle motion in the bed. The results revealed that an increase of the vibration amplitude promotes a higher average velocity of particles close to the inclined walls of the bed. However, the vertical ascending velocity of particles in the central section of the bed was not strongly affected by the vibration amplitude or frequency.

Lastly, the PIV results were decomposed into different phase intervals of oscillation in order to understand the behavior of the particles of the bed during a complete oscillation cycle of the bed bulk. For the case of no gas injection through the inclined walls of the bed, the downstream motion of particles through the central section of the bed is produced by differences in the extent of the perturbation on the particle velocity caused by the impact with the inclined walls of the bed. A more intricate phase behavior of particles was observed when gas was injected through the lateral walls. In this situation, several subcycles of vibration appeared depending on the vibration conditions. Particles alternatively ascended and descended in two regions in the bed bulk, similarly to the arching structures in vibrated rectangular beds. The average particle motion after a whole cycle of the bed bulk leads to a net upward motion of particles in the center of the bed and the presence of four inflexion points in the mean particle motion.

The results here presented can serve as a basis for the understanding of granular dynamics in triangular or conical-shaped vibrated beds when gas is injected through the inclined walls. This kind of geometry is commonly used in aerated hoppers and spout-fluidized beds. Thus, the results here presented provides fundamental knowledge on the granular dynamics in the case vibration energy is introduced in this type of systems.

# Nomenclature

| | |
|---|---|
| $A$ | vertical vibration amplitude (m) |
| $c_k$ | normalized concentration of white particles (-) |
| $\overline{c}$ | horizontally averaged normalized concentration (-) |
| $d_p$ | particle diameter (mm) |
| $f$ | vibration frequency (Hz) |
| $g$ | gravity acceleration constant (m/s$^2$) |
| $H_0$ | static bed height (m) |
| $K$ | bed thickness (m) |
| $SI$ | segregation index (-) |
| $T$ | period of vibration (s) |
| $T_o$ | period of oscillation of the bed bulk (s) |
| $t$ | time (s) |
| $t_{tr}$ | transition time (s) |
| $U_0$ | superficial gas velocity (m/s) |
| $U_{mf}$ | minimum fluidization velocity (m/s) |
| $U_s$ | solids velocity (m/s) |
| $V_{prop}$ | propagation velocity (m/s) |
| $W$ | bed width (m) |

| | |
|---|---|
| $x$ | horizontal coordinate (m) |
| $y$ | vertical coordinate (m) |

*Greek letters*

| | |
|---|---|
| $\delta$ | vibration displacement (-) |
| $\Gamma$ | vibration strength (triangular bed) (-) |
| $\Lambda$ | vibration strength (segregation) (-) |
| $\rho$ | solids density (kg/m$^3$) |
| $\phi$ | bed vessel vibration phase (rad) |

*Subscripts*

| | |
|---|---|
| $D$ | dense particles |
| $L$ | light particles |

## References

Akiyama, T., Aoki, K.M., Yamamoto, K. & Yoshikawa, T. 1998 Experimental study on vibration-induced convection and heaping in granular beds. *Granul. Matter* 1, 15–20.

Aoki, K.M., Akiyama, T., Maki, Y. & Watanabe, T. 1996 Convective roll patterns in vertically vibrated beds of granules. *Phys. Rev. E* 54, 874–883.

Aoki, K.M., Akiyama, T., Yamamoto, K. & Yoshikawa, T. 1997 Experimental study on the mechanism of convection modes in vibrated granular beds. *Europhys. Lett.* 40, 159–164.

Chen, P., Yuan, Z., Chyang, C.S. & Zhuan, F.X. 2011 Sawdust discharge rate from aerated hoppers. *Particuology* 9, 306–313.

Clement, E., Vanel, L., Rajchenbach, J. & Duran, J. 1997 Pattern formation in a vibrated granular layer. *Int. J. Numer. Meth.* 23, 927–944.

Douady, S., Fauve, S. & Laroche, C. 1989 Subharmonic instabilities and defect in a granular layer under vertical vibrations. *Europhys. Lett.* 8, 621–627.

Faraday, M. 1831 On a peculiar class of acoustical figures; and on certain forms assumed by groups of particles upon vibrating elastic surfaces. *Philos. Trans. R. Soc. Lond.* 52, 299–340.

Gallas, J.A.C., Herrmann, H.J. & Sokolowski, S. 1992 Convection cells in vibrating granular media. *Phys. Rev. Lett.* 69, 1371–1374.

He, J., Zhao, Y., Zhao, J., Luo, Z., Duan, C. & He, Y. 2015 Separation performance of fine low-rank coal by vibrated gas-solid fluidized bed for dry coal beneficiation. *Particuol.* 23, 200–108.

Hsiau, S.S. & Wu, M.S. 1998 Arching phenomena in a vibrated granular bed. *Adv. Powder Technol.* 99, 185–193.

Jaeger, H.M., Nagel, S.R. & Behrimger, R.P. 1996 Granular solids, liquids, and gases. *Rev. Modern Phys.* 68, 1259–1273.

Knight, J.B., Jaeger, H.M. & Nagel, S.R. 1993 Vibration-induced size separation in granular media: the convection connection. *Phys. Rev. Lett.* 70:24, 3728–3731.

Kunii, D. & Levenspiel, O. 1991 *Fluidization Engineering*. Butterworth-Heinemann, Newton, MA.

Laroche, C., Douady, S. & Fauve, S. 1989 Convective flow of granular mass under vertical vibrations. *J. Phys. (Paris)* 51, 699–706.

Lu, G., Third, J.R., Köhl, M.H. & Müller, C.R. 2012*a* On the occurrence of polygon-shaped patterns in vibrated cylindrical granular beds. *Eur. Phys. J. E* 35, 90.

Lu, H., Guo, X., Gong, X., Barletta, D. & Poletto, M. 2015 Prediction of solid discharge rates of pulverized coal from an aerated hopper. *Powder Technol.* 286, 645–653.

Lu, H., Guo, X., Gong, X., Cong, X., Dong, W. & Huang, W. 2012*b* Effect of gas type on the fluidization and discharge characteristics of the pulverized coal. *Powder Technol.* 217, 347–355.

Lu, H., Guo, X., Gong, X., Cong, X., Liu, K. & Qi, H. 2012*c* Experimental study on aerated discharge of the pulverized coal. *Chem. Eng. Sci.* 71, 438–448.

Luo, Z.F., Fan, M.M., Zhao, Y.M., Tao, X.X., Chen, Q.R. & Chen, Z.Q. 2008 Density-dependent separation of dry fine coal in a vibrated fluidized bed. *Powder Technol.* 187, 119–123.

Marmo, L. 2007 Low temperature drying of pomace in spout and spout-fluid beds. *J. Food Eng.* 79, 1179–1190.

Mathur, K. & Gishler, P. 1955 A study of the application of the spouted bed technique to wheat drying. *J. Appl. Chem.* 5, 624–636.

Mawatari, Y., Tagawa, K., Tatemoto, Y. & Noda, K. 2005 Bubbling characteristics under vertical vibration in a two-dimensional fluidized bed. *Chem. Eng. Jpn.* 38, 18–23.

Melo, F., Umbanhower, P.B. & Swinney, H.L. 1995 Hexagons, kinks, and disorder in oscillated granular layers. *Phys. Rev. Lett.* 75, 3838.

Miles, J. & Henderson, D. 1990 Parametrically forced surface waves. *Rev. Fluid Mech.* 22, 143.

Ouwerkerk, C.E.D., Molenaar, H.J. & Frank, M.J.W. 1992 Aerated bunker discharge of fine dilating powders. *Powder Technol.* 72, 241–253.

Pak, H.K. & Behringer, R.P. 1993 Surface waves in vertically vibrated granular materials. *Phys. Rev. Lett.* 71, 1832–1835.

Papazoglou, C.S. & Pyle, D.L. 1970 Air-assisted flow from a bed of particles. *Powder Technol.* 4, 9–18.

Rowe, P.N. & Nienow, A.W. 1976 Particle mixing segregation in gas fluidised beds. a review. *Powder. Technol.* 15(2), 141–147.

Sano, O. 2005 Dilatancy, buckling, and undulations on a vertically vibrating granular layer. *Phys. Rev. E.* 72, 051302.

Sun, L., Zhao, F., Zhang, Q., Li, D. & Lu, H. 2014 Numerical simulation of particle segregation in vibration fluidized bed. *Chem. Eng. Technol.* 37(12), 2109–2115.

Sutkar, V.S., Deen, N.G. & Kuipers, J.A.M. 2013 Spout fluidized beds: Recend advances in experimental and numerical studies. *Chem. Eng. Sci.* 86, 124–136.

Taguchi, Y. 1992 New origin of a convective motion: elastically induced convection in granular materials. *Phys. Rev. Lett.* 69, 1367–1370.

Wassgren, C.R., Brennen, C.E. & Hunt, M.L. 1996 Vertical vibration of a deep bed of granular material in a container. *J. Appl. Mech.* 63, 712–719.

Wassgren, C.R., Hunt, M.L., Freese, P.J., Palarma, J. & Brennen, C.E. 2002 Effects of vertical vibration on hopper flows of granular material. *Phys. Fluids* 14, 10.

Yang, X., Zhao, Y., Luo, Z., Song, S., Duan, C. & Dong, L. 2013 Fine coal dry cleaning using a vibrated gas-fluidized bed. *Fuel Process. Technol.* 106, 338–343.

Zhang, F., Wang, L., Liu, C., Wu, P. & Zhan, S. 2014 Patterns of convective flow in a vertically vibrated granular bed. *Phys. Lett. A* 378(18-19), 1303–1308.

Zhao, P., Zhao, Y., Chen, Z. & Luo, Z. 2015 Dry cleaning of fine lignite in a vibrated gas-fluidized bed: Segregation characteristics. *Fuel* 142, 274–282.

Zhong, W., Chen, X. & Zhang, M. 2006*a* Hydrodynamic characteristics of spout-fluid bed: Pressure drop and minimum spouting/spout-fluidizing velocity. *Chem. Eng. J.* 118, 37–46.

Zhong, W., Li, Q., Zhang, M., Jin, B., Xiao, R., Huang, Y. & Shi, A. 2008 Spout characteristics of a cylindrical spout-fluid bed with elevated pressure. *Chem. Eng. J.* 139, 42–47.

Zhong, W., Zhang, M. & Jin, B. 2006*b* Maximum spoutable bed height of spout-fluid bed. *Chem. Eng. J.* 124, 55–62.

Zhou, T., Kage, H., Funaoka, S., Ogura, H. & Matsuno, Y. 2001 Fluidization behaviour of glass beads under different vibration modules. *Adv. Powder Technol.* 12, 559–575.

Zielinska, M. & Markowski, M. 2007 Drying behavior of carrots dried in a spout-fluidized bed dryer. *Drying Technol.* 25, 261–270.

CHAPTER

# EIGHT

# Concluding remarks

## 8.1 Summary of the results and conclusions

Fluidized beds are widely used in important industry sectors for a large number of operations such as Fluid Catalytic Cracking (FCC), gasification of coal and biomass, coating, drying, adsorption, synthesis reactions, etcetera. Nevertheless, a diversity of factors can affect the fluidization quality, specially when small particles are used. In this regard, fluidized beds subjected to mechanical vibration have been proven to satisfactorily provide the necessary kinetic energy to separate particles and enhance their fluidization. However, if fluidization is intrinsically a complex phenomenon, vibration of the bed complicates even more the understanding of the underlying physics of the fluidized system. Knowledge of the fundamental phenomena arising from vibrating a fluidized bed could be of great value for extending its range of operation to new applications and improving the design and control of existing and new vibrated systems.

The present PhD thesis combined original experimental and numerical analyses to understand the bed bulk and the bubble behaviors in a vertically vibrated fluidized bed of small thickness (viz. pseudo-2D bed). For that, four different experimental setups were used: three rectangular pseudo-2D beds and a triangular pseudo-2D bed. The measurement techniques employed in this dissertation include Digital Image Analysis (DIA), Particle Image Velocimetry (PIV) and pressure signal analysis. Additionally, a simplified one-dimensional (1-D) model was developed and Two-Fluid Model (TFM) simulations were carried out to better understand the bed bulk and the bubble oscillatory behavior observed in the experiments.

The first study presented in this dissertation dealt with the oscillatory motion of the bed bulk. The experimental results, analyzed by means of DIA, revealed that the bed bulk cyclically expands and compresses when it is subjected to vibration. The solids velocity inside the bed bulk was calculated with PIV and averaged by means of an averaging of cycles method, which was developed in this work to account for the intrinsic unsteadiness of the bed bulk. This method allows to analyze the unsteady

dynamics of the bed by presenting the bulk and the particles velocity as a function of the vibration phase of the bed vessel. The results arising from this analysis of the solids velocity revealed the presence of compression and expansion waves traveling in the dense phase of the bed. The compression wave is generated by the periodic impact of the bed bulk with the distributor and travels upwards the dense phase dividing the bed into two regions of different relative velocities: a region with upwards velocity below the wave front and a region with downwards velocity above it. A less intense expansion wave appears in the bed as a consequence of the cyclic downward motion of the bed vessel. Calculations of the velocity of propagation of the compression wave on the dense phase yielded values between 5-30 m/s, which is of the same order as the effective velocity of sound in a conventional fluidized bed. In this context, a simplified 1-D model, which considers the bed as a set of masses and solid-gas volumes, was developed, as commented before. The model was conceived to provide a preliminary explanation of the interaction of the pressure and the solids motion and to discriminate the different forces affecting the cyclic oscillatory movement of the bed bulk. Despite its simplicity, the model was capable of providing a fairly good prediction of the bed bulk cyclic expansion and compression behavior and the cyclic motion of solids in the bed. The results obtained by this model, in combination with the TFM simulations, were used to gain a better understanding on the propagation of the solids waves along the bed height.

The oscillation of the bed bulk and the propagation of velocity waves analyzed in Chapter 3 were used to understand the fundamental mechanisms affecting the bubble dynamics in vibrated fluidized beds. The motion of an isolated bubble rising alone in the bed was studied in Chapters 4 and 5. In Chapter 4, both the experiments and the two-fluid model simulations also revealed a cyclic compression and expansion of the bed bulk despite the fact the bubble in the bed is perturbing the dense phase. The averaging of cycles method was applied in these chapters to average the oscillation of different bubbles rising in the bed as a function of the vibration phase. The experiments showed, again, the presence of compression-expansion waves that propagate the vibration oscillations upwards the bed and that promote a phase delay of the oscillation of the bubble velocity and diameter depending on the distance of the bubble to the distributor. Furthermore, increasing the vibration amplitude seems to decrease the bubble velocity in the bed, whereas changes in the vibration frequency have a larger effect on the phase delay of bubble characteristics. Noticeably, the phase delay on the oscillations of the bubble velocity and diameter that is only predicted by the two-fluid model simulations when the compressibility of the gas phase in the simulation is incorporated in the model equations. Therefore, the compressibility of the gas phase in the bed bulk plays a key role on the generation of waves that propagate the oscillations through the bed. As in Chapter 3, calculation of the propagation velocity yielded values of the same order as the effective

sound propagation velocity in a conventional bed.

A more detailed study in terms of the solids motion and the pressure distribution around a bubble rising in the vibrated bed was carried out in Chapter 5. The results shown in this chapter revealed the strong influence of the bed bulk cyclic compression and expansion on the instantaneous solids motion around an isolated bubble rising in the bed. Reciprocally, the presence of the bubble in the system also modifies the cyclic behavior of the bed bulk manifested in Chapter 3. The propagation of the compression wave through the bed was identified as the source of the wake penetration inside the bed contour and the characteristic wavy shape of bubbles in vibrated fluidized beds. It was found that the volume of the solids dragged by the bubble wake cyclically changes with the vibration phase and increases when increasing the vibration amplitude and frequency. The experimental results were compared to the Davidson & Harrison's potential flow model, revealing that this model is still suitable to qualitatively describe the velocity of solids and the pressure distribution around the bubble despite the system is vertically vibrated.

All the previously mentioned results were employed in Chapter 6 to gain a better understanding of the mean and oscillatory behavior of bubbles rising in a vibrated bed operated in freely bubbling regime. In this chapter, for the first time, spatially and phase resolved results on the average behavior of bubbles rising in a vibrated fluidized bed were presented. According to the observations, vibration of the bed vessel tends to promote coalescence of bubbles and to confine the bubble path to the center of the studied bed, making the distribution of bubbles less uniform. As in the case of isolated bubbles, the mean behavior of bubbles in the bubbling system is different depending on their distance to the distributor. Small bubbles close to the distributor were found to behave more similarly to isolated bubbles, so their velocity decreases when increasing the vibration amplitude. Nevertheless, the interaction of multiple bubbles in the bed hinders this effect when the bubble is in a higher vertical coordinate. Different behaviors were also found in terms of the oscillatory behavior of bubbles depending on their vertical coordinate in the bed. The presence of a phase delay of bubble characteristics between the upper and lower sections of the bed confirmed the prevalence of compression-expansion waves affecting bubble characteristics despite the fact the bed is operated in bubbling regime and bubbles continuously interact with each other. The oscillation of the bubble diameter is affected by the wake penetration, the rain of particles and the cyclic compression-expansion of the bed bulk. In contrast, this cyclic compression-expansion and the local velocity of the bed bulk seems to be the main mechanism affecting the bubble velocity. The frequency at which the bed is vibrated has a profound impact on both the magnitude and phase delays of the bubble characteristics in the bed, whereas the effect of the vibration amplitude has a weaker effect on the phase delay of bubble characteristics.

As evidenced along this PhD thesis, vibration possesses some unique characteristics that influence the way bubbles and particles behave inside the bed. Chapter 7 exemplified the effect of vibration on two potential applications of gas fluidized beds: the segregation of particles of different densities and the generation of diverse solids motion patterns in beds with triangular (or conical-like) shape. The results arising from the density segregation study revealed that, depending on the density ratio of the solids mixture, there is an optimum combination of vibration strength and gas superficial velocity to maximize segregation. In this optimum combination regime, vibration does not counteract gas-induced effects and collaborates with the gas velocity to allow the segregation by percolation of the denser particles while limiting re-mixing effects. Vibration of the triangular fluidized bed presented in Chapter 7 highlighted the complex dynamics of granular media when subjected to vibration and revealed the appearance of different granular patterns depending on the vibration and gas fluidization conditions. Overall, the results presented in Chapter 7 can serve as a basis for the understanding of segregation in rectangular beds and of granular dynamics in triangular or conical-shaped vibrated beds when gas is injected through the inclined walls.

## 8.2 Future work

This dissertation presented a study of some of the fundamental mechanisms affecting the dense phase and bubble behaviors in a pseudo-2D vibrated fluidized bed. However, some new questions arose during its accomplishment and to answer them the following future lines of work are proposed:

- The pressure distribution and the motion of solids around an isolated bubble were investigated in Chapter 5. The extension of this study with DEM and/or two-fluid model simulations could facilitate the understanding of the pressure and velocity fields in the whole bed bulk and in regions close to the bubble. In addition, these simulation results could be used to gain additional valuable information such as the gas velocity and the granular temperature in the whole bed.

- Recent works have pointed out the importance of the front and rear walls in pseudo-2D conventional fluidized beds (Li *et al.*, 2010; Hernández-Jiménez *et al.*, 2013, 2016). Hence, there is a need of characterizing the importance of the wall friction effects in vibrated fluidized systems. This can be done by means of DEM and/or two-fluid model simulations or by developing dedicated analytical models.

- In connection with the previous point, a further improvement of the simplified 1-D model presented in Chapter 3 would allow, not only the characterization of the

frictional forces of the front and rear walls, but also the effect of vibration on large voids (bubbles) within the bed bulk.

- PIV measurements of a vibrated fluidized bed operated in bubbling regime constitute a necessary next step on the comprehension of the bed and bubble dynamics, the solids motion around the bubbles and the dense phase-bubble and bubble-bubble interactions. Two-fluid model and/or DEM simulations can be also used for this purpose.

In addition to the research lines proposed above, future studies should not be only focused on fundamental aspects of pseudo-2D beds, but on the utilization of the results presented along this dissertation in practical applications in either pseudo-2D or three-dimensional vibrated systems. These include mixing, segregation (either by density, size or shape), drying, fluidization of cohesive particles and the motion of objects in the bed, which are among the most attractive applications.

APPENDIX

**A**

# Summary of equations of the two-fluid model

The present appendix lists the governing equations and closure models implemented in the MFIX code for the solution of the fluidized beds (Syamlal *et al.*, 1993). Einstein's compact notation of summation is used when two equal subindexes, $i$ or $j$, appear in a derivative term of the equations.

## A.1 Governing equations

Continuity equation for the solid phase (subindex p):

$$\frac{\partial}{\partial t}(\varepsilon_p \rho_p) + \frac{\partial}{\partial x_i}(\varepsilon_p \rho_p U_{pi}) = 0 \tag{A.1}$$

Continuity equation for the gas phase (subindex g):

$$\frac{\partial}{\partial t}(\varepsilon_g \rho_g) + \frac{\partial}{\partial x_i}(\varepsilon_g \rho_g U_{gi}) = 0 \tag{A.2}$$

Where

$$\varepsilon_g + \varepsilon_p = 1 \tag{A.3}$$

and the subindex $i, j = 1...3$ accounts for the each of the three spatial directions.

Momentum balance equation for the solids phase:

$$\left[\frac{\partial}{\partial t}(\varepsilon_p \rho_p U_{pi}) + \frac{\partial}{\partial x_j}(\varepsilon_p \rho_p U_{pj} U_{pi})\right] = -\varepsilon_p \frac{\partial P_g}{\partial x_i} + \frac{\partial \tau_{pij}}{\partial x_j} + I_{gpi} + \varepsilon_p \rho_p g_i + f_{g,eq} \tag{A.4}$$

Momentum balance equation for the gas phase:

$$\left[\frac{\partial}{\partial t}(\varepsilon_g \rho_g U_{gi}) + \frac{\partial}{\partial x_j}(\varepsilon_g \rho_g U_{gj} U_{gi})\right] = -\varepsilon_g \frac{\partial P_g}{\partial x_i} + \frac{\partial \tau_{gij}}{\partial x_j} - I_{gpi} + \varepsilon_g \rho_g g_i + f_{p,eq} \tag{A.5}$$

Granular temperature equation for solid phase p:

$$\frac{3}{2}\rho_p\left[\frac{\partial\varepsilon_p\Theta_p}{\partial t}+\frac{\partial\varepsilon_p U_{pj}\Theta_p}{\partial x_j}\right]=\frac{\partial}{\partial x_i}\left(\kappa_\Theta\frac{\partial\Theta_p}{\partial x_i}\right)+\tau_{pij}\frac{\partial U_{pi}}{\partial x_j}+\Pi_p-\varepsilon_p\rho_p J_p \tag{A.6}$$

## A.2 Interface Momentum Transfer

Gas-solids momentum interface exchange:

$$I_{gpi}=K_{gp}(u_{gi}-u_{pi}). \tag{A.7}$$

The Gidaspow's drag function is used in this work (Gidaspow, 1994)

$$K_{gp}=\begin{cases}\frac{3}{4}C_D\frac{\rho_g\varepsilon_g\varepsilon_p|\vec{u}_g-\vec{u}_p|}{d_p}\varepsilon_g^{-2.65} & \varepsilon_g\geq 0.8\\ \\ 150\frac{\varepsilon_p^2\mu_g}{\varepsilon_g^2}+1.75\frac{\varepsilon_p\rho_g|\vec{u}_g-\vec{u}_p|}{d_p} & \varepsilon_g<0.8\end{cases} \tag{A.8}$$

where the drag coefficient is defined as

$$C_D=\begin{cases}\frac{24}{Re}(1+0.15Re^{0.687}) & Re<1000\\ \\ 0.44 & Re\geq 1000\end{cases} \tag{A.9}$$

and the local Reynolds number based on a particle is

$$Re=\frac{\rho_g\varepsilon_g|\vec{u}_g-\vec{u}_p|d_p}{\mu_g} \tag{A.10}$$

## A.3 Kinetic theory

The kinetic theory of granular flow (KTGF) is implemented for the closure of the equations (Gidaspow, 1994).

Solids stresses:

$$\tau_{p_{ij}}=\left(-P_p+\eta\mu_b\frac{\partial U_{pi}}{\partial x_i}\right)\delta_{ij}+2\mu_p S_{pij} \tag{A.11}$$

where

$$S_{pij} = \frac{1}{2}\left(\frac{\partial U_{pi}}{\partial x_j} + \frac{\partial U_{pj}}{\partial x_i}\right) - \frac{1}{3}\frac{\partial U_{pi}}{\partial x_i} \tag{A.12}$$

Radial distribution function at contact:

$$g_{0_{pp}} = \frac{1 - 0.5\varepsilon_p}{(1+\varepsilon_p^3)} \tag{A.13}$$

Solids pressure (Lun *et al.*, 1984):

$$P_p = \varepsilon_p \rho_p \Theta_p \left[1 + 4\eta\varepsilon_p g_{0,pp}\right] \tag{A.14}$$

Solids viscosity (Gidaspow, 1994):

$$\mu_p = \left(\frac{2+\alpha}{3}\right)\left[\frac{\mu_p^*}{g_{0,pp}\eta(2-\eta)}\left(1 + \frac{8}{5}\eta\varepsilon_p g_{0,pp}\right)\right.$$
$$\left.\left(1 + \frac{8}{5}\eta(3\eta-2)\varepsilon_p g_{0,pp}\right) + \frac{3}{5}\eta\mu_b\right] \tag{A.15}$$

with

$$\mu_p^* = \frac{\rho_p\varepsilon_p g_{0,pp}\Theta_p\mu}{\rho_p\varepsilon_p g_{0,pp}\Theta_p + \left(\frac{2K_{gp}\mu}{\rho_p\varepsilon_p}\right)} \tag{A.16}$$

$$\mu = \frac{5}{96}\rho_p d_p \sqrt{\pi\Theta_p} \tag{A.17}$$

And the bulk viscosity is:

$$\mu_b = \frac{256}{5\pi}\mu\varepsilon_p^2 g_{0,pp} \tag{A.18}$$

Solids conductivity (Gidaspow, 1994):

$$\kappa_p = \left(\frac{\kappa_p^*}{g_{0,pp}}\right)\left[\left(1 + \frac{12}{5}\eta\varepsilon_p g_{0,pp}\right)\left(1 + \frac{12}{5}\eta^2(4\eta-3)\varepsilon_p g_{0,pp}\right) + \right.$$
$$\left. + \frac{64}{25\pi}(41-33\eta)\eta^2(\varepsilon_p g_{0,pp})^2\right] \tag{A.19}$$

with

$$\kappa_p^* = \frac{\rho_p \varepsilon_p g_{0,pp} \Theta_p \kappa}{\rho_p \varepsilon_p g_{0,pp} \Theta_p + \frac{6 K_{gp} \kappa}{5 \rho_p \varepsilon_p}} \tag{A.20}$$

$$\kappa = \frac{75 \rho_p d_p \sqrt{\pi \Theta_p}}{48 \eta (41 - 33\eta)} \tag{A.21}$$

Collisional dissipation (Lun *et al.*, 1984):

$$J_p = \frac{48}{\sqrt{\pi}} \eta (1-\eta) \frac{\varepsilon_p g_{0,pp}}{d_p} \Theta_p^{3/2} \tag{A.22}$$

$$\eta = \frac{1+e}{2} \tag{A.23}$$

Exchange terms:

$$\Pi_p = -3 K_{gp} \Theta_p + \frac{81 \varepsilon_p \mu_g^2 |\vec{u}_g - \vec{u}_p|^2}{g_{0,pp} d_p^3 \rho_p \sqrt{\pi \Theta_p}} \tag{A.24}$$

## A.4 Frictional stress

To account for the stress due to the interparticle friction forces, the Shaeffer's model is considered (Schaeffer, 1987). This model is used at the critical state when the solids volume fraction exceeds the maximum packing limit $\varepsilon^*$.

$$P_c = \begin{cases} 10^{24} (\varepsilon^* - \varepsilon_g)^{10} & \varepsilon_g < \varepsilon^* \\ 0 & \varepsilon_g \geq \varepsilon^* \end{cases} \tag{A.25}$$

$$\mu_f = \begin{cases} min \left( \frac{P_c \sin(\phi)}{\sqrt{4 I_{2D}}}, \mu_p^{max} \right) & \varepsilon_g < \varepsilon^* \\ 0 & \varepsilon_g \geq \varepsilon^* \end{cases} \tag{A.26}$$

$$\mu_p^{max} = 100 \text{Pa s} \tag{A.27}$$

When the maximum packing limit is exceeded, the bulk viscosity is set to zero:

$$\mu_b = 0 \tag{A.28}$$

The second order deviatory tensor is defined as:

$$I_{2D} = \frac{1}{6}\left[(D_{p,11} - D_{p,22})^2 + (D_{p,22} - D_{p,33})^2 + (D_{p,33} - D_{p,11})^2\right] + \\ + D_{p,12}^2 + D_{p,23}^2 + D_{p,31}^2 \tag{A.29}$$

Where

$$D_{p,ij} = \frac{1}{2}\left(\frac{\partial u_{p,i}}{\partial x_j} + \frac{\partial u_{p,j}}{\partial x_i}\right) \tag{A.30}$$

Gas momentum equation constitutive models.

$$\tau_{gij} = 2\mu_{gt} S_{gij} \tag{A.31}$$

$$S_{gij} = \frac{1}{2}\left(\frac{\partial U_{gi}}{\partial x_j} + \frac{\partial U_{gj}}{\partial x_i}\right) - \frac{1}{3}\frac{\partial U_{gi}}{\partial x_i} \tag{A.32}$$

$$\mu_{gt} = min(\mu_{max}, \mu_g + \mu_e) \tag{A.33}$$

$$\mu_e = 2 l_p^2 \varepsilon_g \rho_g \sqrt{I_{2Dg}} \tag{A.34}$$

And again, the second order deviatory tensor is defined as:

$$I_{2Dg} = \frac{1}{6}\left[(D_{g,11} - D_{g,22})^2 + (D_{g,22} - D_{g,33})^2 + (D_{g,33} - D_{g,11})^2\right] + \\ + D_{g,12}^2 + D_{g,23}^2 + D_{g,31}^2 \tag{A.35}$$

# Nomenclature

| | |
|---|---|
| $C_D$ | drag coefficient (-) |
| $D$ | rate of strain tensor (1/s) |
| $d_p$ | particle diameter (m) |
| $e$ | coefficient of restitution (-) |
| $f_{eq}$ | vibration equivalent force (kg/m$^2$s$^2$) |
| $g_i$ | gravity acceleration (m/s$^2$) |
| $g_{0,pp}$ | radial distribution function (-) |
| $\boldsymbol{I}$ | unit tensor (-) |
| $\boldsymbol{I}_{gp}$ | inter-phase momentum exchange (kg/m$^2$s$^2$) |
| $I_{2Dg}$ | second order deviatory tensor (s$^{-2}$) |
| $J_p$ | collisional dissipation (m$^2$/s$^3$) |
| $K_{gp}$ | gas/solid momentum exchange (-) |
| $l_s$ | turbulence length scale parameter (m) |

| | |
|---|---|
| $P_p$ | solids pressure (-) |
| $Re$ | Reynolds number (-) |
| $t$ | time (s) |
| $U$ | velocity (m/s) |
| $\vec{u}_i$ | velocity vector (m/s) |

*Greek letters*

| | |
|---|---|
| $\delta(t)$ | bed vessel vertical displacement (m) |
| $\varepsilon$ | volume fraction (-) |
| $\varepsilon^*$ | packed bed void fraction (-) |
| $\eta$ | function of restitution coefficient (-) |
| $\Theta_p$ | granular temperature ($m^2/s^2$) |
| $\theta$ | angle of internal friction ($^o$) |
| $\kappa_\Theta$ | granular temperature diffusion coefficient (kg/m s) |
| $\mu$ | viscosity (Pa s) |
| $\mu_b$ | bulk viscosity (Pa s) |
| $\mu_e$ | eddy viscosity of the gas phase (Pa s) |
| $\mu_{gt}$ | turbulent viscosity of the gas phase (Pa s) |
| $\Pi_p$ | exchange terms (kg/m $s^3$) |
| $\rho$ | density ($kg/m^3$) |
| $\boldsymbol{\tau}$ | stress tensor (Pa) |
| $\Phi$ | specularity coefficient (-) |

*Subscripts*

| | |
|---|---|
| $g$ | gas phase |
| $p$ | particle (solid) phase |

# References

Gidaspow, D. 1994 *Multiphase flow and Fluidization*. Academic Press. Boston.

Lun, C.K.K., Savage, S.B., Jeffrey, D.J. & Chepurniy, N. 1984 Kinetic theories for granular flow-inelastic particles in couette-flow and slightly inelastic particles in a general flowfield. *J. Fluid Mech.* 140, 223–256.

Schaeffer, D.G. 1987 Instability in the evolution equations describing incompressible granular flow. *J. Diff. Eqns.* 66, 19–50.

Syamlal, M., Rogers, W. & O'Brien, T.J. 1993 Mfix documentation: Theory guide. *U.S. Department of Energy (DOE), Morgantown Energy Technology Center, Morgantown, West Virginia* .

APPENDIX

**B**

# 1-D model of the vibrated fluidized bed

This appendix summarizes the constitutive equations defining the one-dimensional (1-D) simplified model of the vibrated fluidized bed used to analyze the bed bulk motion in Chapter 3. As commented in Chapter 3, this 1-D model divides the bed bulk into a set of masses that occupy discrete volumes. The motion of each of the masses and its volume is directly affected by vibration and with the gas and the surrounding masses. The model equations here presented were solved using a stiff solver implemented in the Matlab® software.

## B.1 Equation of motion

Firstly, the motion of each of the masses is defined in Equation (B.1).

$$\begin{aligned}\frac{\mathrm{d}^2 x_i}{\mathrm{d}t^2} =& -g + \frac{N_B}{H_0 \rho_b}\varepsilon_{g,i}(P_i - P_{i+1}) + F_{drag,i} \\ &+ \frac{N_B(F_{spring,i} + F_{damper,i})}{\rho_b H_0 A_{bed}} + A\omega^2 \sin(\omega t)\end{aligned} \tag{B.1}$$

where $\omega = 2\pi f$, $x_i$ is the vertical position of the $i^{th}$ mass and $g$ is the gravity acceleration constant ($g = 9.81$ m/s$^2$ by default).

In order of appearance on the right hand side of Equation (B.1), the forces per unit mass used to characterize the motion of each of the masses are: gravity force, force caused by the pressure gradient inside the bed volumes, force caused by the drag of the gas, forces due to the interaction of the solid masses and the apparent acceleration force due to vibration (in a system of reference that moves with the bed vessel).

For the particular case of the upper most mass, which is subjected to the ambient pressure above it, the equation of motion is:

$$\begin{aligned}\frac{\mathrm{d}^2 x_i}{\mathrm{d}t^2} =& -g + \frac{N_B}{H_0 \rho_b}\varepsilon_{g,i}(P_i - P_a) + F_{drag,i} \\ &+ \frac{N_B(F_{spring,i} + F_{damper,i})}{\rho_b H_0 A_{bed}} + A\omega^2 \sin(\omega t)\end{aligned} \tag{B.2}$$

where $N_B$ is the number of masses and bed discrete volumes in which the bed bulk is vertically divided and $P_a = 1.013 \cdot 10^5$ Pa is the pressure outside the bed.

Following (Roy *et al.*, 1990), the whole bed bulk is considered isothermal. Hence, the density $\rho_{g,i}$ and the pressure $P_{g,i}$ inside each of the bed volumes are directly related by the ideal gas law:

$$\rho_{g,i} = \frac{P_{g,i}}{R_g T_g} \tag{B.3}$$

where $R_g = 287$ J/(kg K) is the ideal gas constant, and $T_g = 298$ K is the absolute gas temperature.

The following subsections summarize each of the model parameters and the forces affecting the motion of the masses in which the bed bulk was divided.

### Gas velocity

The superficial gas velocity in each of the bed volumes, $u_{g,i}$ in Figure 3.1, is calculated following Darcy's law for an stationary flow under the hypothesis of quasi-stationary conditions within the volume of a mass. Previous works in vibrated systems (Gutman & Davidson, 1975) have proven the applicability of this law for vibrated systems:

$$u_{g,i} = -\frac{2K_{b,i}}{\mu_g} \frac{(P_{g,i+1} - P_{g,i})}{(x_{i+1} - x_{i-1})} \tag{B.4}$$

where the gas viscosity $\mu_g$ is considered constant along the bed bulk and $K_{b,i}$ is the permeability of each of the bed volumes, which can be calculated using the Ergun equation for low Reynolds numbers (Ergun, 1952):

$$K_{b,i} = \frac{d_p^2 \varepsilon_{g,i}^3}{150\,(1 - \varepsilon_{g,i})^2} \tag{B.5}$$

Equating the buoyant weight of the bed per unit area and the pressure drop over it gives an expression for the minimum fluidization velocity, $u_{mf}$, which is the inflow superficial gas velocity to the model through the bottom of the plenum:

$$u_{in} = \frac{d_p^2 \varepsilon_b^3 \rho_p g}{150(1 - \varepsilon_b)\mu_g} \tag{B.6}$$

where $\varepsilon_b = 0.4$ is the bed bulk void fraction and $d_p$ and $\rho_p$ are, respectively, the diameter and density of the bed particles.

**Drag force**

For the calculation of the interaction of the gas phase with the masses, a drag force exerted by the gas passing through the bed discrete volumes over the bed masses is implemented in the model. The drag model by Gidaspow (1994) was selected. This drag model is a combination of the Wen-Yu drag model (Wen & Yu, 1966) and the Ergun equation (Ergun, 1952). For a voidage in the bed volumes less than 0.8 the Ergun equation is used, whereas for a voidage larger than 0.8 the Wen-Yu drag model is used. Note that in the present model the bed is operated close to minimum fluidization conditions, thus, voidages larger than 0.8 are not expected. The drag force is calculated with:

$$F_{drag,i} = \frac{I_{gs,i}}{\rho_b} \tag{B.7}$$

The gas interstitial velocity is defined as:

$$v_{g,i} = \frac{u_{g,i}}{\varepsilon_{g,i}} \tag{B.8}$$

In Equation (B.7), the gas-solid momentum exchange term is defined as:

$$I_{gs,i} = K_{gs,i}|v_{g,i} - u_i| \tag{B.9}$$

where $v_{g,i} = u_{g,i}/\varepsilon_{g,i}$ is the gas interstitial velocity in the bed volume below the $i^{th}$ mass , $u_i = \frac{\mathrm{d}x_i}{\mathrm{d}t}$ is the vertical velocity of the $i^{th}$ mass and $K_{gs,i}$ is the gas-solid exchange term (Gidaspow, 1994):

$$K_{gs,i} = \begin{cases} \frac{3}{4} C_{D,i} \frac{\frac{P_i}{R_g T_g} \varepsilon_{g,i}(1-\varepsilon_{g,i})|v_{g,i} - u_i|}{d_p} \varepsilon_{g,i}^{-2.65} & \varepsilon_{g,i} \geq 0.8 \\ 150 \frac{(1-\varepsilon_{g,i})^2 \mu_g}{\varepsilon_{g,i} d_p^2} + 1.75 \frac{(1-\varepsilon_{g,i}) \frac{P_i}{R_g T_g} |v_{g,i} - u_i|}{d_p} & \varepsilon_g < 0.8 \end{cases} \tag{B.10}$$

The drag coefficient in $K_{gs,i}$ is:

$$C_{D,i} = \begin{cases} \frac{24}{Re_i}(1 + 0.15 Re_i^{0.687}) & Re_i < 1000 \\ 0.44 & Re_i \geq 1000 \end{cases} \tag{B.11}$$

where the Reynolds number is defined as:

$$Re_i = \frac{\frac{P_i}{R_g T_g}\varepsilon_{g,i}|v_{g,i} - u_i|d_p}{\mu_g} \tag{B.12}$$

**Pressure gradients inside the bed**

Regarding the force exerted on the masses due to the pressure gradients, it is considered that this force is caused by the pressure difference of the bed volumes immediately above and below the masses.

To obtain the pressure in each of the bed volumes, a simple mass balance is proposed:

$$\frac{\mathrm{d}(\rho_{g,i}V_{g,i})}{\mathrm{d}t} = \dot{m}_{i,in} - \dot{m}_{i,out} \tag{B.13}$$

As the air is considered compressible, there is a relative motion between the masses. Both the gas density and the volume of the air gaps between the masses change with time. Air is considered isothermal, as commented in Chapter 3. Thus, the left hand side of Equation (B.13) can be expressed as:

$$\frac{\mathrm{d}(\rho_{g,i}V_{g,i})}{\mathrm{d}t} = \rho_{g,i}\frac{\mathrm{d}V_{g,i}}{\mathrm{d}t} + V_{g,i}\frac{\mathrm{d}\rho_{g,i}}{\mathrm{d}t} = \frac{P_{g,i}}{R_g T_g}\frac{\mathrm{d}V_{g,i}}{\mathrm{d}t} + V_{g,i}\frac{1}{R_g T_g}\frac{\mathrm{d}P_{g,i}}{\mathrm{d}t} \tag{B.14}$$

The volume of air inside each of the volumes depends on their voidage, $\varepsilon_{g,i}$ and the distance between the masses delimiting the volumes:

$$V_{g,i} = \varepsilon_{g,i}(x_i - x_{i-1})A_{bed} \tag{B.15}$$

As a staggered grid is used in the model, half of the first volume is considered to be filled with air and the other half with a mixture of solids and air. The rest of the bed discrete volumes contains only a mixture of solids and air. Thus, the volume of gas in the first bed volume can be defined as:

$$V_{g,1} = (1 + \varepsilon_{g,1})\frac{x_1}{2}A_{bed} \tag{B.16}$$

As a consequence of this, the air gap formed at the bottom of the bed can be estimated with:

$$x_{gap} = \frac{\varepsilon_1 - \varepsilon_{1,eff}}{1 - \varepsilon_{1,eff}}x_1 \tag{B.17}$$

where $\varepsilon_1$ is the void fraction in the first bed volume and $\varepsilon_{1,eff}$ is the effective voidage considering the volume occupied by the mixture (excluding the gap). As a first approximation, it can be considered that the void fraction varies only slightly between the first and the second bed volumes, so that $\varepsilon_{1,eff} = \varepsilon_2$

Therefore, the variation of the air volume in the bed discrete volumes with time can be can be calculated by deriving Equation (B.15):

$$\frac{\mathrm{d}V_{g,i}}{\mathrm{d}t} = A_{bed}\left(\varepsilon_{g,i}\frac{\mathrm{d}(x_i - x_{i-1})}{\mathrm{d}t} + (x_i - x_{i-1})\frac{\mathrm{d}\varepsilon_{g,i}}{\mathrm{d}t}\right) \tag{B.18}$$

In the present model, the volume of particles inside each of the bed volumes is considered constant (i.e. there is no transport of particles from one volume to another). Hence, the voidage in these volumes at any time, $\varepsilon_{g,i}$, can be expressed as a function of the instantaneous position of the masses delimiting the bed volume:

$$\varepsilon_{g,i} = 1 - \frac{(1-\varepsilon_{0,g,i})(x_{0,i} - x_{0,i-1})}{(x_i - x_{i-1})} \tag{B.19}$$

Hence,

$$\frac{\mathrm{d}\varepsilon_{g,i}}{\mathrm{d}t} = (1-\varepsilon_{0,g,i})(x_{0,i} - x_{0,i-1})\frac{1}{(x_i - x_{i-1})^2}\left(\frac{\mathrm{d}x_i}{\mathrm{d}t} - \frac{\mathrm{d}x_{i-1}}{\mathrm{d}t}\right) \tag{B.20}$$

and for the first discrete volume of the bed:

$$\frac{\mathrm{d}\varepsilon_{g,1}}{\mathrm{d}t} = (1-\varepsilon_{0,g,1})x_{0,1}\frac{1}{x_1^2}\left(\frac{\mathrm{d}x_1}{\mathrm{d}t}\right) \tag{B.21}$$

where $\varepsilon_{g,i}$ is the voidage in the $i^{th}$ volume, $\varepsilon_{0,g} = 0.4$ is the initial voidage of all the bed volumes and $x_{0,i}$ is the initial position of the bed masses, which are equally spaced a distance equal to $H_0/N_B$.

In addition, the right hand side of Equation (B.13), which represents the mass flow rates entering and leaving a bed volume, can be expressed as:

$$\dot{m}_{i,in} - \dot{m}_{i,out} = \left(\frac{P_{g,i} + P_{g,i-1}}{2R_gT_g}u_{g,i-1} - \frac{P_{g,i} + P_{g,i+1}}{2R_gT_g}u_{g,i}\right)A_{bed} \tag{B.22}$$

Thus, by combining Equations (B.14) to (B.22), an equation for the variation with time of the pressure in each of the bed volumes as a function of the pressure, the position

and the velocity of the masses is obtained:

$$\frac{\mathrm{d}P_{g,i}}{\mathrm{d}t} = \left[ \frac{P_{g,i} + P_{g,i-1}}{2} u_{g,i-1} - \frac{P_{g,i} + P_{g,i+1}}{2} u_{g,i} + P_{g,i} \left( (x_i - x_{i-1}) \frac{\mathrm{d}\varepsilon_{g,i}}{\mathrm{d}t} + \left( \frac{\mathrm{d}x_i}{\mathrm{d}t} - \frac{\mathrm{d}x_{i-1}}{\mathrm{d}t} \right) \varepsilon_{g,i} \right) \right] \frac{1}{(x_i - x_{i-1})\varepsilon_{g,i}} \quad \text{(B.23)}$$

which can be particularized for the first bed discrete volume:

$$\frac{\mathrm{d}P_{g,1}}{\mathrm{d}t} = \left[ \frac{P_{g,1} + P_p}{2} u_d - \frac{P_{g,1} + P_{g,2}}{2} u_1 + P_{g,1} \left( \frac{x_1}{2} \frac{\mathrm{d}\varepsilon_{g,1}}{\mathrm{d}t} + \frac{1}{2}(1 + \varepsilon_{g,1}) \frac{\mathrm{d}x_1}{\mathrm{d}t} \right) \right] \frac{1}{\frac{x_1}{2}(1 + \varepsilon_{g,1})} \quad \text{(B.24)}$$

where $P_p$ is the pressure in the plenum of the bed, which can be calculated by means of the mass conservation equation in the plenum (Equation (B.25)).

$$\frac{\mathrm{d}P_p}{\mathrm{d}t} = \frac{1}{H_{eq}} \left( P_p u_{in} - \frac{P_p + P_1}{2} u_d \right) \quad \text{(B.25)}$$

In Equation (B.24) $u_d$ is the gas velocity through the distributor:

$$u_d = K_d^{-0.5} |P_p - P_1|^{0.5} \mathrm{sign}(P_p - P_1) \quad \text{(B.26)}$$

where $K_d = 7.6 \cdot 10^4$ kg/m$^3$ is the experimentally determined distributor pressure drop, (i.e. $\Delta P_d = K_d u_d^2$), $u_{in}$ is the inflow gas superficial velocity and $H_{eq}$ is the equivalent height of the plenum, that is, $H_{eq} = V_p / A_{bed}$.

**Spring-dashpot system**

As commented in Section B.1, the interaction between the different masses is modeled considering the bed bulk as a classical spring-damping system. This approach has been used in previous works devoted to vibrated beds without aeration (Matchett & Alsop, 1995; Yanagida *et al.*, 2002). Additionally, as a first approximation, the spring-damping system is only activated when the bed discrete volume presents a void fraction smaller than a prescribed value $\varepsilon_{min,g,i} = 0.4$. This chosen value of $\varepsilon_{min,g,i}$ is similar to the critical value at which the frictional stress model is activated in the two-fluid model.

Following Yanagida *et al.* (2002), the spring force exerted between consecutive masses when they mutually interact can be calculated as:

$$F_{spring,ij} = -K_{s,i}(\delta_{ij} - \delta_{0,ij}) \quad \text{(B.27)}$$

with

$$F_{spring,i} = F_{spring,i,i-1} - F_{spring,i,i} \tag{B.28}$$

where $\delta_{ij}$ and $\delta_{0,ij}$ are, respectively, the instantaneous and initial distances between the $i^{th}$ and the $j^{th}$ masses. That is, $\delta_{ij} = x_i - x_j$. $K_s$ represents the stiffness of the $i^{th}$ spring-damper system, which is only activated if $|\delta_{ij}| < |\delta_{0,ij}|$.

The spring stiffness can be calculated as:

$$K_{s,i} = E_{eff}\frac{N_B A_{bed}}{H_0} \tag{B.29}$$

where $E_{eff}$ is the effective elastic modulus of the bed, that can be estimated following Yanagida *et al.* (2002) as:

$$E_{eff} = \alpha P_s^{1/3} \tag{B.30}$$

where $\alpha = 1.36 \cdot 10^6$ Pa is an empirical constant determined bu Yanagida *et al.* (2002) for particles of similar characteristics (diameter, density and material) as the ones used in Chapter 3 and $P_s = 0.5\rho_b g H_0$ is the mean compressive stress to the powder bed.

In the practice, when the particle layers in the bed bulk collide with each other, only a small amount of particles are in direct contact. Additionally, the use of a constant $K_s$ could lead to a destabilization of the numerical calculation due to the large force discontinuity when $K_s$ is activated at $\varepsilon_{g,i} = 0.4$. To take into consideration these two points, a linear increase of the spring stiffness between $\varepsilon_g = 0.4$ (activation of the spring-damping system) and $\varepsilon_g = 0.36$ (void maximum packing limit for a random packing) is proposed as a first approximation. This increase is such that the effective spring constant $K_s = E_{eff} N_B A_{bed}/H_0$ is obtained at $\varepsilon_g = 0.38$, that is, at the middle of the linear increasing interval.

Analogously to the spring force, the damping force depends on the relative velocity of the $i^{th}$ mass with regard to the neighboring masses:

$$F_{damping,ij} = -D_{d,i}\frac{\mathrm{d}\delta_{ij}}{\mathrm{d}t} \tag{B.31}$$

with

$$F_{damping,ij} = F_{damping,i-1} - F_{damping,i} \tag{B.32}$$

where $D_{d,i}$ is the $i^{th}$ damping coefficient. Accordingly to Yanagida *et al.* (2002), the

damping coefficient can be estimated with:

$$D_{d,i} = \eta\sqrt{m_{bn}K_{s,i}} \tag{B.33}$$

where $\eta = 0.0539$ is an empirical loss factor (Yanagida *et al.*, 2002) and $m_{bn}$ is the mass of each of the masses in which the bed volume was divided. However, in the present dissertation, it was observed that the use of this damping factor was unable to realistically reproduce the interaction of the bed bulk with the bed distributor and a greater $D_{d,i}$ was needed. This may be attributed to the fact that Yanagida *et al.* (2002) employed a cylindrical bed of 78 mm of diameter, and it was vibrated without gas injection. However, the pseudo-2D bed studied here was aerated and has a greater wall-surface to bed volume ratio than a cylindrical bed. Thus, a new damping factor is proposed:

$$D_{d,i} = \chi\eta\sqrt{m_{bn}K_{s,i}} \tag{B.34}$$

where $\chi$ is a damping increasing factor (see Chapter 3). Resulting values of $\chi$ are greater than the unity, which indicates that the effective damping is superior than in Yanagida *et al.* (2002). This suggests that the walls of the pseudo-2D bed have a significative damping effect.

Finally, the differential equations for $x_i$, $V_{g,i}$, $\varepsilon_{g,i}$, $P_{g,i}$ and $P_p$ form a set of ordinary differential equations that must be solved simultaneously to obtain the temporal evolution of these variables.

## Nomenclature

| | |
|---|---|
| $A$ | vibration amplitude (mm) |
| $A_{bed}$ | bed cross sectional area ($m^2$) |
| $C_D$ | drag coefficient (-) |
| $D_d$ | damping coefficient (Ns/m) |
| $d_p$ | particle diameter ($\mu$m) |
| $E$ | elastic modulus (Pa) |
| $F$ | force ($kg/m^3$) |
| $f$ | vibration frequency (Hz) |
| $g$ | gravity acceleration constant ($m/s^2$) |
| $H_0$ | bed bulk static bed height (m) |
| $H_{eq}$ | plenum equivalent height (m) |
| $K_b$ | bed volume permeability ($m^2$) |
| $K_d$ | gas distributor pressure drop ($Pa\ s^2/m^2$) |

| | |
|---|---|
| $K_{gs}$ | gas/solid momentum exchange (-) |
| $K_s$ | spring stiffness (N/m) |
| $N_B$ | number of bed volumes (-) |
| $m$ | mass (kg) |
| $m_{bn}$ | weight of each of the masses (kg) |
| $P$ | pressure (Pa) |
| $P_s$ | compressive stress (Pa) |
| $Re$ | Reynolds number (-) |
| $R_g$ | ideal gas constant (J/kg K) |
| $T_g$ | gas temperature (K) |
| $t$ | time (s) |
| $u_d$ | gas velocity through the distributor (m/s) |
| $u_{in}$ | inflow velocity (m/s) |
| $u_i$ | bed mass velocity (m/s) |
| $u_{g,i}$ | superficial gas velocity (m/s) |
| $V_i$ | volume of the $i^{th}$ discrete volume ($m^3$) |
| $V_p$ | plenum volume ($m^3$) |
| $v_g$ | interstitial gas velocity (m/s) |
| $x_{gap}$ | height of the air gap (m) |
| $x_i$ | bed mass position (m) |

*Greek letters*

| | |
|---|---|
| $\alpha$ | Young's modulus empirical constant (Pa) |
| $\delta_{ij}$ | distance between the masses $i$ and $j$ (m) |
| $\varepsilon_{g,i}$ | bed volume void fraction (-) |
| $\varepsilon_{0,g,i}$ | initial bed volume void fraction (-) |
| $\eta$ | loss factor (-) |
| $\chi$ | damping increasing factor (-) |
| $\omega$ | angular frequency (rad/s) |

*Subscripts*

| | |
|---|---|
| $b$ | bed bulk |
| $g$ | gas phase |
| $i$ | bed volume index |
| 0 | initial conditions |
| $p$ | plenum |

## References

Ergun, S. 1952 Fluid flow through packed columns. *Chem. Eng. Prog.* 48, 89–94.

Gidaspow, D. 1994 *Multiphase flow and Fluidization*. Academic Press. Boston.

Gutman, R.G. & Davidson, J.F. 1975 Darcy's law for oscillatory flow. *Can. J. Chem. Eng.* 30, 89–95.

Matchett, A.J. & Alsop, S. 1995 A two-phase elastic model of vibration in a bed of particulates. *Powder Technol.* 83, 13–28.

Roy, R., Davidson, J.F. & Tuponogov, V.G. 1990 The velocity of sound in fludised beds. *Chem. Eng. Sci.* 45, 3233–3245.

Wen, C.Y. & Yu, Y.H. 1966 Mechanics of fluidization. *Chem. Eng. Prog. Symp. Ser.* 62, 100–111.

Yanagida, T., Matchett, A.J. & Coulthard, J.M. 2002 Damping and elastic properties of binary powder mixtures. *Powder Technol.* 127, 107–115.

# Alphabetical list of references


Acosta-Iborra, A., Hernández-Jiménez, F., de Vega, M. & Briongos, J.V. 2012 A novel metodology for simulating vibrated fluidized beds using two-fluid models. *Chem. Eng. J.* 198-199, 261–274.

Akiyama, T., Aoki, K.M., Yamamoto, K. & Yoshikawa, T. 1998*a* Experimental study on vibration-induced convection and heaping in granular beds. *Granul. Matter* 1, 15–20.

Akiyama, T., Aoki, K.M., Yamamoto, K. & Yoshikawa, T. 1998*b* Experimental study on vibration-induced convection and heaping in granular beds. *Granul. Matter* 1, 15–20.

Almendros-Ibáñez, J.A., Sobrino, C., de Vega, M. & Santana, D. 2006 A new model for ejected particle velocity from erupting bubbles in 2-d fluidized beds. *Chem. Eng. Sci.* 61, 5981–5990.

Aoki, K.M., Akiyama, T., Maki, Y. & Watanabe, T. 1996 Convective roll patterns in vertically vibrated beds of granules. *Phys. Rev. E* 54, 874–883.

Aoki, K.M., Akiyama, T., Yamamoto, K. & Yoshikawa, T. 1997 Experimental study on the mechanism of convection modes in vibrated granular beds. *Europhys. Lett.* 40, 159–164.

Baird, M.H.I. 1963 Resonant bubbles in a vertically vibrating column. *Can. J. Chem. Eng.* 41, 52–55.

Barletta, D., Donsi, G., Ferrari, G., Poletto, M. & Russo, P. 2008 The effect of mechanical vibration on gas fluidization of a fine aeratable powder. *Chem. Eng. Res. Des.* 86, 359–369.

Barletta, D. & Poletto, M. 2012 Aggregation phenomena in fluidization of cohesive powders assisted by mechanical vibrations. *Powder Technol.* 2012, 93–100.

Barletta, D., Russo, P. & Poletto, M. 2013 Dynamic response of a vibrated fluidized bed of fine and cohesive powders. *Powder Technol.* 237, 276–285.

Benyahia, S., Syamlal, M. & O'Brien, T.J. 2012 Summary of MFIX equations 2012-1. In *https://mfix.netl.doe.gov/documentation/MFIXEquations2012-1.pdf*.

Bi, H. 2007 A critical review of the complex pressure fluctuation phenomenon in gas-solids fluidized beds. *Chem. Eng. Sci* 62, 3473–3493.

Boemer, A., Qi, H. & Renz, U. 1997 Eulerian simulation of bubble formation at a jet in a two-dimensional fluidized bed. *Int. J. Numer. Meth.* 23, 927–944.

Bradley, D. & Roth, G. 2007 Adaptive thresholding using the integral image. *Journal of Graphics Tools* 12:2, 13–21.

Briongos, J. V., S anchez Delgado, S., Acosta-Iborra, A. & Santana, D. 2011 A novel approach for modeling bubbling gas-solid fluidized beds. *AIChE Journal* 57(7), 1733– 1750.

Buist, K.A., van der Gaag, A.C., Deen, N.G. & Kuipers, J.A.M. 2014 Improved magnetic particle tracking technique in dense gas fluidized beds. *AIChE J.* 60(9), 3133–3142.

Busciglio, A., Giuseppa, V., Micale, G. & Rizzuti, L 2008*a* Analysis of the bubbling behavior of 2D gas-solid fluidized beds part II: Comparison between experiments and numerical simulations via digital image analysis technique. *Chem. Eng. J.* 148, 145–163.

Busciglio, A., Vella, G., Micale, G. & Rizzuti, L. 2008*b* Analysis of the bubbling behaviour of 2D gas solid fluidized beds: Part I. digital image analysis technique. *Chem. Eng. J.* 140, 398–413.

Cano-Pleite, E., Gómez-Hernández, J., Sánchez-Prieto, J. & Acosta-Iborra, A. 2013 Characterization of the bubble behavior in vibrated fluidized beds by means of two-fluid CFD simulations coupled with accelerometry data. In *The 14th International Conference on Fluidization - From Fundamentals to Products, ECI Symposium Series*.

Cano-Pleite, E., Hernández-Jiménez, F. & Acosta-Iborra, A. 2015 Compressible-gas two-fluid modeling of isolated bubbles in a vertically vibrated fluidized bed and comparison with experiments. *Chem. Eng. J.* 271, 287–299.

Cano-Pleite, E., Hernández-Jiménez, F., Acosta-Iborra, A. & Müller, C. 2016*a* Reversal of gulf stream circulation in a vertically vibrated triangular fluidized bed. In *Fluidization XV, ECI Symposium Series*.

Cano-Pleite, E., Hernández-Jiménez, F., Acosta-Iborra, A., Tsuji, T. & Müller, C. 2016*b* Segregation of equal-sized particles of different densities in a vertically vibrated fluidized bed. In *Fluidization XV, ECI Symposium Series*.

Cano-Pleite, E., Hernández-Jiménez, F., de Vega, M. & Acosta-Iborra, A. 2014 Experimental study on the motion of isolated bubbles in a vertically vibrated fluidized bed. *Chem. Eng. J.* 255, 287–299.

Cano-Pleite, E., Shimizu, Y., Acosta-Iborra, A. & Mawatari, Y. 2016*c* Effect of vertical vibration and particle size on the solids hold-up and mean bubble behavior in a pseudo-2D fluidized bed. *Chem. Eng. J.* 304, 384–398.

Chen, P., Yuan, Z., Chyang, C.S. & Zhuan, F.X. 2011 Sawdust discharge rate from aerated hoppers. *Particuology* 9, 306–313.

Clement, E., Vanel, L., Rajchenbach, J. & Duran, J. 1997 Pattern formation in a vibrated granular layer. *Int. J. Numer. Meth.* 23, 927–944.

Coppens, M.O. & van Ommen, J.R. 2003 Structuring chaotic fluidized beds. *Chem. Eng. J.* 96, 117–124.

Cranfield, R.R. & Geldart, D. 1974 Large particle fluidisation. *Chem. Eng. Sci.* 29, 935–947.

Croxford, A.J. & Gilbertson, M.A. 2011 Pressure fluctuations in bubbling gas-fluidized beds. *Chem. Eng. Sci.* 66(16), 3569–3578.

Cundall, P.A. & Strack, O.D.L. 1979 Discrete numerical-model for granular assemblies. *Geotechnique* 29, 47–65.

Dang, T.Y.N., Kolkman, T., Gallucci, F. & van Sint Annaland M. 2013 Development of a novel infrared technique for instantaneous, whole-field, non invasive gas concentration measurements in gas-solid fluidized beds. *Chem. Eng J.* 219, 545–557.

Davidson, J.F. & Harrison, D. 1963 *Fluidised Particles*. Cambridge University Press, Cambridge.

Deen, N.G., Van Sint Annaland, M., Van der Hoef, M.A. & Kuipers, J.A.M. 2007 Review of discrete particle modeling of fluidized beds. *Chem. Eng. Sci.* 62, 628–44.

Douady, S., Fauve, S. & Laroche, C. 1989 Subharmonic instabilities and defect in a granular layer under vertical vibrations. *Europhys. Lett.* 8, 621–627.

Eccles, E.R.A. & Mujumdar, A.S. 1997 Bubble phenomena in aerated vibrated beds of small particles. *Drying Technol.* 15:1, 95–116.

Ellenberg, J. & Krishna, R. 2007*a* Levitation of air bubbles and slugs in liquids under low-frequency vibration excitement. *Chem. Eng. Sci.* 62, 7548–7553.

Ellenberg, J. & Krishna, R. 2007*b* Levitation of air bubbles in liquid under low frequency vibration excitement. *Chem. Eng. Sci.* 62, 5669–5673.

Erdesz, K. & Ormos, Z. 1983 Hydrodynamic studies on fluidized beds(iv)-bed expansion and pressure drop in vibrofluidized layers. *Hung. J. Ind. Chem.* 11, 21–32.

Ergun, S. 1952 Fluid flow through packed columns. *Chem. Eng. Prog.* 48, 89–94.

Faraday, M. 1831 On a peculiar class of acoustical figures; and on certain forms assumed by groups of particles upon vibrating elastic surfaces. *Philos. Trans. R. Soc. Lond.* 52, 299–340.

Gallas, J.A.C., Herrmann, H.J. & Sokolowski, S. 1992 Convection cells in vibrating granular media. *Phys. Rev. Lett.* 69, 1371–1374.

Geldart, D. 1970 The size and frequency of bubbles in two- and three-dimensional gas fluidised beds. *Powder Technol.* 4, 41–55.

Geldart, D. 1973 Types of gas fluidization. *Powder Technol.* 7, 285.

Gidaspow, D. 1994 *Multiphase flow and Fluidization*. Academic Press. Boston.

Glicksman, L.R., Lord, W.K. & M., Sakagami 1987 Bubble properties in large-particle fluidized beds. *Chem. Eng. Sci.* 42, 479–491.

Goldshtein, A., M., Shapiro, L., Moldavslky & M., Fichman 1995 Mechanics of collisional motion of granular materials. part 2. wave propagation through vibrofluidized granular layers. *J. Fluid Mech.* 287, 349–382.

Gómez-Hernández, J., Soria-Verdugo, A., Villa Briongos, J. & Santana, D. 2012 Fluidized bed with a rotating distributor operated under defluidization conditions. *Chem. Eng. J.* 195-196, 198–207.

Gupta, R. & Mujumdar, A.S. 1980 Aerodynamics of a vibrated fluid bed. *Can. J. Chem. Eng.* 58, 332–338.

Gutman, R.G. & Davidson, J.F. 1975 Darcy's law for oscillatory flow. *Can. J. Chem. Eng.* 30, 89–95.

He, J., Zhao, Y., Zhao, J., Luo, Z., Duan, C. & He, Y. 2015 Separation performance of fine low-rank coal by vibrated gas-solid fluidized bed for dry coal beneficiation. *Particuol.* 23, 200–108.

Hernández-Jiménez, F., Gómez-García, A., Santana, D. & Acosta-Iborra, A. 2013*a* Gas interchange between bubble and emulsion phases in a 2D fluidized bed as revealed by two-fluid model simulations. *Chem. Eng. J.* 215-216, 479–490.

Hernández-Jiménez, F., Sánchez-Delgado, S., Gómez-García, A. & Acosta-Iborra, A. 2011*a* Comparison between two-fluid model simulations and particle image analysis & velocimetry (PIV) results for a two-dimensional gas-solid fluidized bed. *Chem. Eng. Sci.* 66, 3753–3772.

Hernández-Jiménez, F., Sánchez-Prieto, J., Cano-Pleite, E., García-Gutierrez, L.M. & Acosta-Iborra, A. 2016 Development of an empirical wall-friction model for 2D simulations of pseudo-2D bubbling fluidized beds. *Adv. Powder Technol.* 27, 521–530.

Hernández-Jiménez, F., Sánchez-Prieto, J., Soria-Verdugo, A. & Acosta-Iborra, A. 2013*b* Experimental quantification of the particle-wall frictional forces in pseudo-2D gas fluidised beds. *Chem. Eng. Sci.* 102, 257–267.

Hernández-Jiménez, F., Third, J.R., Acosta-Iborra, A. & Müller, C.R. 2011*b* Comparison of bubble eruption models with two-fluid simulations in a 2D gas-fluidized bed. *Chem. Eng. J.* 171, 328–339.

Hernández-Jiménez, F. 2013 Numerical and experimental investigations on pseudo-2D gas fluidized beds. *PhD. Thesis* .

Hsiau, S.S. & Wu, M.S. 1998 Arching phenomena in a vibrated granular bed. *Adv. Powder Technol.* 99, 185–193.

Hulme, I., Clavell, E., van der Lee, L. & Kantzas, A. 2005 Cfd modeling and validation of bubble properties for a bubbling fluidized bed. *Ind. Eng. Chem. Res.* 44, 4254–4266.

Ishida, M. & Shirai, T. 1980 Measurement of the velocity and direction of flow of solid particles in a fluidized bed. *Powder Technol.* 27, 1–6.

Jaeger, H.M., Nagel, S.R. & Behrimger, R.P. 1996 Granular solids, liquids, and gases. *Rev. Modern Phys.* 68, 1259–1273.

Jameson, G.J. & Davidson, J.F. 1966 The motion of a bubble in a vertically oscillating liquid: theory for an inviscid liquid, and experimental results. *Chem. Eng. Sci.* 21, 29–34.

Janssen, L.P.B.M., Marring, E., Hoogerbrugge, J.C. & A.C., Hoffmann 1998 The mechanical behaviour of vibrated beds of glass and starch powders. *Chem. Eng. Sci.* 53, 761–772.

Johnson, P.C. & Jackson, R. 1987 Frictional-collisional constitutive relations for granular materials, with application to plane shearing. *J. Fluid Mech.* 176, 67–93.

Jovanovic, G.N. & Jovanovic, Z.R. 1993 Bubble size and fluidization regimes in magnetically controlled fluidized beds. In *AIChE Annual Meeting, St. Louis, MO, U.S.A.*.

Julián, I., Herguido, J. & Menéndez, M. 2016 Experimental and simulated solids mixing and bubbling behavior in a scaled two-section two-zone fluidized bed reactor. In *Chem. Eng. Sci.*, , vol. 143, pp. 240–255.

Kapur, J.N., Sahoo, P.K. & Wong, A.K. 1985 A new method for gray-level picture thresholding using the entropy of the histogram. *Comput. Graphics Image Process.* 29, 273–285.

Knight, J.B., Jaeger, H.M. & Nagel, S.R. 1993 Vibration-induced size separation in granular media: the convection connection. *Phys. Rev. Lett.* 70:24, 3728–3731.

Kroll, W. 1954 Uber das verhalten von schuttgut in lotrecht schwingenden gefassen. *Forshung* 20, 2–15.

Kuipers, N.J.M., Stamhuis, E.J. & Beenackers, A.A.C.M. 1996 Fluidization of potato starch in a stirred vibrated fluidized bed. *Chem. Eng. Sci.* 51, 2727–2732.

Kunii, D. & Levenspiel, O. 1991 *Fluidization Engineering*. Butterworth-Heinemann, Newton, MA.

Lacey, P.M.C. 1954 Developments in the theory of particle mixing. *J. Appl. Chem.* 4, 257–268.

Ladd, A.J.C. & Verberg, R. 2001 Lattice-boltzmann simulations of particle fluid suspensions. *J. of Statistical Physics* 104, 1191–1251.

Laroche, C., Douady, S. & Fauve, S. 1989 Convective flow of granular mass under vertical vibrations. *J. Phys. (Paris)* 51, 699–706.

Latifi, M., Berruti, F. & Briens, C. 2014 A novel fluidized and induction heated microreactor for catalyst testing. *AIChE J.* 60, 3107–3122.

Laverman, J.A., Roghair, H., van Sint Annaland, M. & Kuipers, H. 2008 Investigation into the hydrodynamics of gas-solid fluidized beds using particle image velocimetry coupled with digital image analysis. *Can. J. Chem. Eng.* 86, 523–535.

Li, Tingwen 2015 Validation of a 2.5d cfd model for cylindrical gas–solids fluidized beds. *Powder Technol.* 286, 817–827.

Li, T., Grace, J.R. & Bi, X. 2010 Study of wall boundary condition in numerical simulations of bubbling fluidized beds. *Powder Technol.* 203, 447–457.

Li, T. & Zhang, Y. 2013 A new model for two-dimensional numerical simulation of pseudo-2D gas–solids fluidized beds. *Chem. Eng. Sci.* 102, 246–256.

Lim, C.N., Gilberston, M.A. & Harrison, A.J.L. 2006 Measurement and simulation of bubbling fluidised beds. *Powder Technol.* 170, 167–177.

Limtrakul, S., Rotjanavijit, W. & Vatanatham, T. 2007 Lagrangian modeling and simulation of effect of vibration on cohesive particle movement in a fluidized bed. *Chem. Eng. Sci.* 62, 232–245.

Lin., J.S., Chen, M.M. & Chao, B.T. 1985 A novel radioactive particle tracking facility for measurement of solids motion in gas fluidized beds. *AIChE Journal* 31(3), 465–473.

Lu, G., Third, J.R., Köhl, M.H. & Müller, C.R. 2012*a* On the occurrence of polygon-shaped patterns in vibrated cylindrical granular beds. *Eur. Phys. J. E* 35, 90.

Lu, H., Guo, X., Gong, X., Barletta, D. & Poletto, M. 2015 Prediction of solid discharge rates of pulverized coal from an aerated hopper. *Powder Technol.* 286, 645–653.

Lu, H., Guo, X., Gong, X., Cong, X., Dong, W. & Huang, W. 2012*b* Effect of gas type on the fluidization and discharge characteristics of the pulverized coal. *Powder Technol.* 217, 347–355.

Lu, H., Guo, X., Gong, X., Cong, X., Liu, K. & Qi, H. 2012*c* Experimental study on aerated discharge of the pulverized coal. *Chem. Eng. Sci.* 71, 438–448.

Lun, C.K.K., Savage, S.B., Jeffrey, D.J. & Chepurniy, N. 1984 Kinetic theories for granular flow-inelastic particles in couette-flow and slightly inelastic particles in a general flowfield. *J. Fluid Mech.* 140, 223–256.

Luo, Z.F., Fan, M.M., Zhao, Y.M., Tao, X.X., Chen, Q.R. & Chen, Z.Q. 2008 Density-dependent separation of dry fine coal in a vibrated fluidized bed. *Powder Technol.* 187, 119–123.

Makkawi, Y.T. & Wright, P.C. 2002 Fluidization regimes in a conventional fluidized bed characterized by means of electrical capacitance tomography. *Chem. Eng. Sci.* 57, 2411–2437.

Marmo, L. 2007 Low temperature drying of pomace in spout and spout-fluid beds. *J. Food Eng.* 79, 1179–1190.

Matchett, A.J. & Alsop, S. 1995 A two-phase elastic model of vibration in a bed of particulates. *Powder Technol.* 83, 13–28.

Mathiesen, V., Solberg, T. & Hjertager, B.H. 2000 An experimental and computational study of multiphase flow behavior in a circulating fluidized bed. *Int. J. Multiphase Flow* 26, 387–419.

Mathur, K. & Gishler, P. 1955 A study of the application of the spouted bed technique to wheat drying. *J. Appl. Chem.* 5, 624–636.

Mawatari, Y., Koide, T., Tatemoto, Y., Takeshita, T. & Noda, K. 2001 Comparison of three vibrational modes (twist, vertical and horizontal) for fluidization of fine particles. *Adv. Powder Technol.* 2, 157–168.

Mawatari, Y., Tagawa, K., Tatemoto, Y. & Noda, K. 2005*a* Bubbling characteristics under vertical vibration in a two-dimensional fluidized bed. *Chem. Eng. Jpn.* 38, 18–23.

Mawatari, Y., Tatemoto, Y. & Noda, K. 2003 Prediction of minimum fluidization velocity for vibrated fluidized bed. *Powder Technol.* 131, 66–70.

Mawatari, Y., Tsunekawa, M., Tatemoto, Y. & Noda, K. 2005*b* Favorable vibrated fluidization conditions for cohesive fine particles. *Powder Technol.* 154, 54–60.

Melo, F., Umbanhower, P.B. & Swinney, H.L. 1995 Hexagons, kinks, and disorder in oscillated granular layers. *Phys. Rev. Lett.* 75, 3838.

Miles, J. & Henderson, D. 1990 Parametrically forced surface waves. *Rev. Fluid Mech.* 22, 143.

Moon, S.J., Kevrekidis, I.G. & Sundaresan, S. 2006 Compaction and dilation rate dependence of stresses in gas-fluidized beds. *Phys. Fluids* 18, 083304.

Mori, S., Yamamoto, A., Iwata, S., Haruta, T., Yamada, I. & Mizutani, E. 1990 Vibro-fluidization of group c particles and its industrial applications. *AlChE Symp. Series.* 86, 88–94.

Morley, D.B. 1991 Evaluation of vibrated fluidized bed techniques in coating hemosorbents. *Int. J. Artif. Organs* 14(6), 371–9.

Mudde, R.F. 2010 Time-resolved x-ray tomography of a fluidized bed. *Powder Technol.* 199(1), 55–59.

Mujumbar, A.S. 1987 *Handbook of Industrial Drying*. Marcel Dekker, New York.

Müller, C.R., Davidson, J.F., Dennis, J.S. & Hayhurst, A.N. 2007 A study of the motion and eruption of a bubble at the surface of a two-dimensional fluidized bed using particle image velocimetry (PIV). *Ind. Eng. Chem. Res.* 46, 1642–1652.

Müller, C.R., Holland, D.J., Sederman, A.J., Scott, S.A., Dennis, J.S. & Gladden, L.F. 2008 Granular temperature: Comparison of magnetic resonance measurements with discrete element model simulations. *Powder Technol.* 203, 241–253.

Musmarra, D., Poletto, M., Vaccaro, S. & Clift, R. 1995 Dynamic waves in fluidized beds. *Powder Technol.* 82, 255–268.

Nahmad−Molinari, Y., Canul−Chay, G. & Ruiz−Suárez, J.C. 2003 Inertia in the brazil nut effect. *Phys. Rev. E* 68, 041301.

Nakamura, H., Kondo, T. & Watano, S. 2013 Improvement of particle mixing and fluidization quality in rotating fluidized bed by inclined injection of fluidizing air. *Chem. Eng. Sci.* 91, 70–78.

Nelson, R.J., Flakker, C.L. & Muggli, D.S. 2007 Photocatalytic oxidation of methanol using titania-based fluidized beds. *Appl Catal B.* 69(3-4), 189–195.

Noda, K., Mawatari, Y. & Uchida, S. 1998 Flow patterns of fine particles in a vibrated fluidized bed under atmospheric or reduce pressure. *Powder Technol.* 99, 11–14.

Nowak, W., Hasatani, M. & Derczynski, M. 1993 Fluidization and heat transfer of fine particles in an acoustic field. *AIChE Symp. Ser.* 89, 137–149.

O'Hern, T., Shelden, B., Torczynsky, J. & Romero, L. 2012 Bubble oscillations and motion under vibration. *Phys. Fluids.* 24, 091108.

van Ommen, J.R. & Mudde, R.F. 2008 Measuring the gas-solids distribution in fluidized beds – a review. *Int. J. Chem. R. Eng.* 6, R1.

van Ommen, J.R., Sasic, S., van der Schaaf, J., Gheorghiu, S., Johnsson, F. & Coppens, M.O. 2011 Time-series analysis of pressure fluctuations in gas-solid fluidized beds - a review. *Int. J. Multiphase Flow* 37, 403–428.

van Ommen, J.R., Valverde, J.M. & Pfeffer, R. 2012 Fluidization of nanopowders: a review. *J. Nanopart. Res.* 314, 737.

Otsu, N. 1979 A threshold selection method from gray-level histograms. *IEEE Trans. Syst. Man. Cybern.* 9, 62–66.

Ouwerkerk, C.E.D., Molenaar, H.J. & Frank, M.J.W. 1992 Aerated bunker discharge of fine dilating powders. *Powder Technol.* 72, 241–253.

Pak, H.K. & Behringer, R.P. 1993 Surface waves in vertically vibrated granular materials. *Phys. Rev. Lett.* 71, 1832–1835.

Pan, X., Ye, S., Zhang, Z., Zhang, L. & Zhu, X. 2009 A study of spray granulation in vibrated fluidized bed with internal heating tubes. *Front. Chem. Eng. China* 3, 78.

Papazoglou, C.S. & Pyle, D.L. 1970 Air-assisted flow from a bed of particles. *Powder Technol.* 4, 9–18.

Patil, D.J., van Sint Annaland, M. & Kuipers, J.A.M. 2003 Gas dispersion and bubble-to-emulsion phase mass exchange in a gas-solid bubbling fluidized bed: a computational and experimental study. *Int. J. Chem. React. Eng.* 1, 1–20.

Patil, D.J., van Sint Annaland, M. & Kuipers, J.A.M. 2004 Critical comparison of hydrodynamics models for gas-solid fluidized beds- partii: freely bubbling gas-solid fluidized beds. *Chem. Eng. Sci.* 60, 73–84.

Raffel, M., Willert, C. & Kompenhans, J. 1967 The rising velocity of bubbles in two-dimensional fluidized beds. *Chem. Eng. Sci.* 22, 531–53.

Rosenweig, R.E. 1979 Fluidization: hydrodynamic stabilization with a magnetic field. *Science* 204, 57–60.

Rowe, P.N. & Nienow, A.W. 1976 Particle mixing segregation in gas fluidised beds. a review. *Powder. Technol.* 15(2), 141–147.

Roy, R., Davidson, J.F. & Tuponogov, V.G. 1990 The velocity of sound in fluidised beds. *Chem. Eng. Sci.* 45, 3233–3245.

Rubin, E. 1968 Behavior of gas bubbles in vertically vibrating liquid columns. *Can. J. Chem. Eng.* 46, 145–149.

Sadiq, S.A. & Asif, M. 2012 Fluidization of nano-powders: Effect of flow pulsation. *Powder Technol.* 225, 86–92.

Sánchez-Delgado, S., Marugán-Cruz, C., Acosta-Iborra, A. & Santana, D. 2010 Dense-phase velocity fluctuation in a 2-d fluidized bed. *Powder Technol.* 200, 37–45.

Sano, O. 2005 Dilatancy, buckling, and undulations on a vertically vibrating granular layer. *Phys. Rev. E.* 72, 051302.

Santana, D., Nauri, S., Acosta, A., Garcia, N. & Macias-Machín, A. 2005 Initial particle velocity spatial distribution from 2-d erupting bubbles in fluidized bed. *Powder Technol.* 150, 1–8.

Sasic, S., Leckner, B. & Johnsson, F. 2005 Fluctuations and waves in fluidized bed systems: The influence of the air-supply system. *Powder Technol.* 153, 176–195.

Sasic, S., Leckner, B. & Johnsson, F. 2007 Characterization of fluid dynamics of fluidized beds by analysis of pressure fluctuations. *Prog. Energy Combust. Sci.* 33, 453–496.

van der Schaaf, J., Schouten, J.C. & van den Bleek, C.M. 1998 Origin, propagation and attenuation of pressure waves in gas-solid fluidized beds. *Powder Technol.* 95, 220–233.

Schaeffer, D.G. 1987 Instability in the evolution equations describing incompressible granular flow. *J. Diff. Eqns.* 66, 19–50.

Sette, E., Pallarès, D., Johnsson, F., Ahrentorp, F., Ericsson, A. & C., Johansson 2015 Magnetic tracer-particle tracking in a fluid dynamically down-scaled bubbling fluidized bed. *Fuel Process. Technol.* 138, 368–377.

Sharma, A.K., Tuzla, K., Matsen, J. & Chen, J.C. 2000 Parametric effects of particle size and gas velocity on cluster characteristics in fastfluidized beds. *Powder Technol.* 111, 114–122.

Shen, L., Johnsson, F. & Leckner, B. 2004 Digital image analysis of hydrodynamics two-dimensional bubbling fluidized beds. *Chem. Eng. Sci.* 59, 2607–2617.

Sobrino, C., Almendros-Ibáñez, J.A., Santana, D. & de Vega, M. 2008 Fluidization of group b particles with a rotating distributor. *Powder Technol.* 181, 273–280.

Solimene, R., Marzocchella, A., Passarelli, G. & Salatino, P. 2006 Assessment of gas-fluidized beds mixing and hydrodynamics by zirconia sensors. *AIChE Journal* 52, 185–198.

Soria-Verdugo, A., García-Gutíerrez, L.M., Sánchez-Delgado, S. & Ruiz-Rivas, U. 2011 Circulation of an object immersed in a bubbling fluidized bed. *Chem. Eng. Sci.* 66, 78–87.

Squires, A.M. 2004 Chemical process opportunities for vibrated powders: 2. in the field. *Powder Technol.* 147(1-3), 10–19.

Strumillo, C. & Pakowski, Z. 1980 *Drying of granular products in vibrofluidized beds.* in: A.S. Mujumdar (Ed.), Drying'80: Developments in Drying, Hemisphere Publishing Corporation, Montreal.

Strumillo, C. & Pakowski, Z. 2007 *Particle Image Velocimetry, A Practical Guide.* Springer, Berlin.

Sun, J., Battaglia, F. & Subramaniam, S. 2006 Dynamics and structures of segregation in a dense, vibrating granular bed. *Phys. Rev. E* 74, 1–13.

Sun, L., Zhao, F., Zhang, Q., Li, D. & Lu, H. 2014 Numerical simulation of particle segregation in vibration fluidized bed. *Chem. Eng. Technol.* 37(12), 2109–2115.

Sutkar, V.S., Deen, N.G. & Kuipers, J.A.M. 2013 Spout fluidized beds: Recend advances in experimental and numerical studies. *Chem. Eng. Sci.* 86, 124–136.

Sveen, J.K. 1998-2014 Matpiv. In *https://www.mn.uio.no/math/english/people/aca/jks/matpiv/*.

Syamlal, M., Rogers, W. & O'Brien, T.J. 1993 MFIX documentation: Theory guide. *U.S. Department of Energy (DOE), Morgantown Energy Technology Center, Morgantown, West Virginia* .

Taghipour, F., Ellis, N. & Wong, C. 2005 Experimental and computational study of gas-solid fluidized bed hydrodynamics. *Chem. Eng Sci.* 60, 6857–6867.

Taguchi, Y. 1992 New origin of a convective motion: elastically induced convection in granular materials. *Phys. Rev. Lett.* 69, 1367–1370.

Tatemoto, Y., Mawatari, Y., Yasukawa, T. & Noda, K. 2004 Numerical simulation of particle motion in vibrated fluidized bed. *Chem. Eng. Sci.* 59, 437–447.

Third, J.R., Chen, Y. & Müller, C.R. 2016 Comparison between finite volume and lattice-boltzmann method simulations of gas-fluidised beds: bed expansion and particle–fluid interaction force. *Comp. Part. Mech.* 3, 373.

Tsuji, Y., Tanaka, T. & T., Ishida 1992 Lagrangian numerical-simulation of plug flow of cohesionless particles in a horizontal pipe. *Powder Technol.* 71, 239–250.

van Wachem, B.G.M & Almstedt, A.E. 2003 Methods for multiphase computational fluid dynamics. *Chem. Eng. J.* 96, 81–98.

Wang, T.J., Jin, Y., Tsutsumi, A., Wang, Z. & Cui, Z. 2000 Energy transfer mechanism in a vibrating fluidized bed. *Chem. Eng. J.* 78, 115–123.

Wang, T., Jin, Y., Wang, Z. & Yu, Z. 1997 The characteristics of wave propagation in a vibrating fluidized bed. *Chem. Eng. Technol.* 20, 606–611.

Wassgren, C.R., Brennen, C.E. & Hunt, M.L. 1996 Vertical vibration of a deep bed of granular material in a container. *J. Appl. Mech.* 63, 712–719.

Wassgren, C.R., Hunt, M.L., Freese, P.J., Palarma, J. & Brennen, C.E. 2002 Effects of vertical vibration on hopper flows of granular material. *Phys. Fluids* 14, 10.

Wen, C.Y. & Yu, Y.H. 1966 Mechanics of fluidization. *Chem. Eng. Prog. Symp. Ser.* 62, 100–111.

Xiang, L., Shuyan, W., Huilin, L., Goudong, L., Juhui, C. & Yikun, L. 2010 Numerical simulation of particle motion in vibrated fluidized beds. *Powder Technol.* 197, 25–35.

Xu, C. & Zhu, J. 2005 Experimental and theoretical study of the agglomeration arising from fluidization of cohesive particles-effects of mechanical vibration. *Chem. Eng. Sci.* 60, 6529–6541.

Yanagida, T., Matchett, A.J. & Coulthard, J.M. 2002 Damping and elastic properties of binary powder mixtures. *Powder Technol.* 127, 107–115.

Yang, W.C. 2003 *Handbook of fluidization and fluid-particle systems*. Marcel Dekker Inc.

Yang, X., Zhao, Y., Luo, Z., Song, S., Duan, C. & Dong, L. 2013 Fine coal dry cleaning using a vibrated gas-fluidized bed. *Fuel Process. Technol.* 106, 338–343.

Zeilstra, C., van der Hoef, M.A. & Kuipers, J.A.M. 2013 Experimental and numerical study of solids circulation in gas-vibro fluidized beds. *Powder Technol.* 248, 153–160.

Zhang, F., Wang, L., Liu, C., Wu, P. & Zhan, S. 2014 Patterns of convective flow in a vertically vibrated granular bed. *Phys. Lett. A* 378(18-19), 1303–1308.

Zhao, P., Zhao, Y., Chen, Z. & Luo, Z. 2015 Dry cleaning of fine lignite in a vibrated gas-fluidized bed: Segregation characteristics. *Fuel* 142, 274–282.

Zhong, W., Chen, X. & Zhang, M. 2006*a* Hydrodynamic characteristics of spout-fluid bed: Pressure drop and minimum spouting/spout-fluidizing velocity. *Chem. Eng. J.* 118, 37–46.

Zhong, W., Li, Q., Zhang, M., Jin, B., Xiao, R., Huang, Y. & Shi, A. 2008 Spout characteristics of a cylindrical spout-fluid bed with elevated pressure. *Chem. Eng. J.* 139, 42–47.

Zhong, W., Zhang, M. & Jin, B. 2006*b* Maximum spoutable bed height of spout-fluid bed. *Chem. Eng. J.* 124, 55–62.

Zhou, T., Kage, H., Funaoka, S., Ogura, H. & Matsuno, Y. 2001 Fluidization behaviour of glass beads under different vibration modules. *Adv. Powder Technol.* 12, 559–575.

Zhou, T., Kage, H. & Li, H. 2005 Bubble characteristics in a two-dimensional vertically vibro-fluidized bed. *China Partic.* 3, 224–228.

Zhou, T., Ogura, H., Yamamura, M. & Kage, H. 2004 Bubble motion pattern and rise velocity in two-dimensional horizontal and vertical vibro-fluidized beds. *Can. J. Chem. Eng.* 82, 236–242.

Zielinska, M. & Markowski, M. 2007 Drying behavior of carrots dried in a spout-fluidized bed dryer. *Drying Technol.* 25, 261–270.

# List of publications

The work performed in this thesis has been presented in the following papers.

The results shown in Chapter 3 have been reported in:

- E. Cano-Pleite, F. Hernández-Jiménez, A. Acosta-Iborra, Bulk oscillation and velocity wave propagation in a vibrated fluidized bed at minimum fluidization conditions, *Submitted for publication in Powder Technology* 2016.

The isolated bubble analysis carried out in Chapters 4 has been published in:

- E. Cano-Pleite, F. Hernández-Jiménez, M. de Vega, A. Acosta-Iborra, Experimental study on the motion of isolated bubbles in a vertically vibrated fluidized bed, *Chemical Engineering Journal* 255 114-125, 2014.
- E. Cano-Pleite, F. Hernández-Jiménez, A. Acosta-Iborra, Compressible-gas two-fluid modeling of isolated bubbles in a vertically vibrated fluidized bed and comparison with experiments, *Chemical Engineering Journal* 271 287-299, 2015.

The study of the behavior of the bubbling bed of Chapter 6 has been presented in:

- E. Cano-Pleite, Y. Shimizu, A. Acosta-Iborra, Y. Mawatari, Effect of vertical vibration and particle size on the solids hold-up and mean bubble behavior in pseudo-2D fluidized bed, *Chemical Engineering Journal* 304 384-398, 2016.
- E. Cano-Pleite, F. Hernández-Jiménez, A. Acosta-Iborra, Oscillatory behavior of the bed bulk and the bubbles in a vertically vibrated pseudo-2D bed in bubbling regime, *Submitted for publication in Chemical Engineering Journal* 2016.

The results of Chapter 7 were orally presented by the author in the Fluidization XV conference (ECI, 2016 - Fairmont Le Chateau Montebello, Quebec, Canada) and have been presented in the following papers:

- E. Cano-Pleite, F. Hernández-Jiménez, A. Acosta-Iborra, T. Tsuji, C. Müller, Segregation of equal-sized particles of different densities in a vertically vibrated fluidized bed, *Submitted for publication in Powder Technology* 2016.

- E. Cano-Pleite, F. Hernández-Jiménez, A. Acosta-Iborra, C. Müller, Reversal of gulf stream circulation in a vertically vibrated triangular fluidized bed, *Submitted for publication in Powder Technology* 2016.

Other works of the author in the framework of the thesis are:

- F. Hernández-Jiménez, J. Sánchez-Prieto, E. Cano-Pleite, L.M. Garcia-Gutierrez, A. Acosta-Iborra, Development of an empirical wall-friction model for 2D simulations of pseudo-2D bubbling fluidized beds, *Advanced Powder Technology* 27 521-530, 2016.
- F. Hernández-Jiménez, T. Li, E. Cano-Pleite, W. Rogers, A. Acosta-Iborra, Characterisation of the particle-wall frictional forces in pseudo-2D fluidized beds using DEM, *Chemical Engineering Science* 106 136-143, 2014.
- E. Cano-Pleite, J. Gómez-Hernández, J. Sánchez-Prieto A. Acosta-Iborra, Characterization of the bubble behavior in vibrated fluidized beds by means of two-fluid CFD simulations coupled with accelerometry data, *The 14th International Conference on Fluidization - From Fundamentals to Products, ECI Symposium Series*, 2013.